MOLYBDENUM OXIDES AS CATALYST FOR BIOMASS-DERIVED COMPOUNDS: A THEORETICAL APPROACH

Marcos Rellán Piñeiro

UNIVERSITAT ROVIRA i VIRGILI

Molybdenum oxides as catalyst for biomass-derived compounds: a theoretical approach

Marcos Rellán Piñeiro

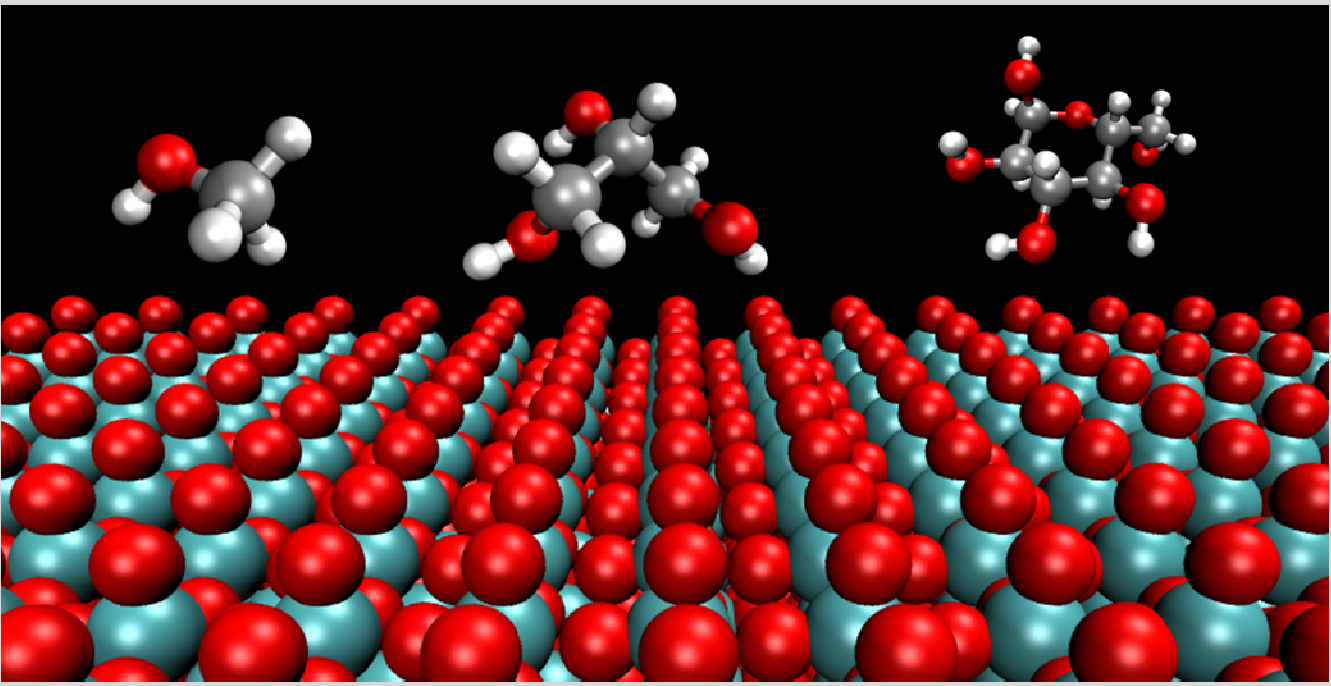

DOCTORAL THESIS
2018

UNIVERSITAT ROVIRA I VIRGILI
MOLYBDENUM OXIDES AS CATALYST FOR BIOMASS-DERIVED COMPOUNDS: A THEORETICAL APPROACH
Marcos Rellán Piñeiro

UNIVERSITAT ROVIRA I VIRGILI
MOLYBDENUM OXIDES AS CATALYST FOR BIOMASS-DERIVED COMPOUNDS: A THEORETICAL APPROACH
Marcos Rellán Piñeiro

Marcos Rellán Piñeiro

Molybdenum Oxides as Catalyst for Biomass-derived Compounds: a Theoretical Approach

DOCTORAL THESIS

Supervised by
Prof. Núria López Alonso

Institute of Chemical Research of Catalonia (ICIQ)
and Rovira i Virgili University (URV)

ICIQ
Institut Català d'Investigació Química

UNIVERSITAT ROVIRA I VIRGILI

Tarragona

2018

UNIVERSITAT ROVIRA I VIRGILI
MOLYBDENUM OXIDES AS CATALYST FOR BIOMASS-DERIVED COMPOUNDS: A THEORETICAL APPROACH
Marcos Rellán Piñeiro

Institut Català d'Investigació Química

Av. Països Catalans, 16

43007 Tarragona (Spain)

Prof. Núria López Alonso, group leader in the Institute of Chemical Research of Catalonia (ICIQ),

I STATE that the present study, entitled "**Molybdenum Oxides as Catalyst for Biomass-derived Compounds: a Theoretical Approach**", presented by Marcos Rellán Piñeiro for the award of the degree of Doctor in Chemical Science and Technology, has been carried out under my supervision at the Institute of Chemical Research of Catalonia, and that it fulfills all the requirements for the award of the distinction of International Doctor.

Tarragona, 5th February, 2018

Prof. Núria López Alonso

UNIVERSITAT ROVIRA I VIRGILI
MOLYBDENUM OXIDES AS CATALYST FOR BIOMASS-DERIVED COMPOUNDS: A THEORETICAL APPROACH
Marcos Rellán Piñeiro

Sponsors

The work presented in this thesis was possible by the economic support and collaboration of the ICIQ Foundation, the Spanish Ministerio de Economía y Competitividad (MINECO) (CTQ 2015-68770-R, Severo Ochoa Excellence Accreditation 2014–2018 SEV-2013-0319, and Severo Ochoa predoctoral grant SVP-2014-068237) and the European Research Council (ERC-2010-StG-258406 Bio2Chem-d and ERC-2015-PoC-680900 BigData4Cat). In addition, we thank BSC-RES for providing computational resources.

UNIVERSITAT ROVIRA I VIRGILI
MOLYBDENUM OXIDES AS CATALYST FOR BIOMASS-DERIVED COMPOUNDS: A THEORETICAL APPROACH
Marcos Rellán Piñeiro

Acknowledgements

No puedo empezar esta página de otro modo que no sea dando las gracias a mis padres. Ellos me educaron para ser lo que soy y sin sus esfuerzos y apoyo jamás hubiera llegado aquí. También tengo mucho que agradecer a mis hermanas, abuelos, tíos, primos y sobrino (ya casi sobrinos); con todos vosotros es muy fácil ser feliz. Y no sabéis cuanto se os echa de menos desde la otra punta del país. Por supuesto, también tengo mucho que agradecerle a Conchi, durante estos cuatro años en Tarragona no se que hubiera sido de mí sin ella.

También tengo que agradecer especialmente a Núria López, quién me dio la oportunidad de realizar esta tesis. Todo lo que he aprendido de ella estos últimos cuatro años es impagable. Admiro muchísimo la pasión que pone en su trabajo, y agradezco enormemente la parte que me ha contagiado. No me quiero olvidar tampoco de darles las gracias a Jesús y Carola, mis supervisores durante las primeras etapas de mi carrera científica y de quienes guardo un magnífico recuerdo, ellos también pusieron su granito de arena para que llegara aquí.

I would also like to thank to Hanne Falsig, to give me the opportunity to spend three months in Haldor Topsøe working with her. Moreover, I want to extend my thanks to all the people that I had the opportunity to know during those three months.

Estos cuatro años en el ICIQ, en los que he tenido la oportunidad de conocer gente de todo el mundo, han sido geniales. Debo agradecerle especialmente a Núria Vendrell todo el tiempo gastado en solucionar mis papeleos y por mantener en funcionamiento todo nuestro despacho. También a Martín, a quién no he parado de darle la lata con mis problemas informáticos a los que siempre encuentra solución. Entre mis compañeros de despacho me gustaría agradecerles especialmente a Rodrigo y Marçal, quienes me han ayudado muchísimo estos años, siempre resolviendo mis dudas, y de los que he aprendido un montón de cosas. También a Qiang, empezamos esto juntos hace cuatro años y todavía no deja de sorprenderme. Me gustaría mencionar a Neyvis y Miquel, con quienes he compartido proyectos de investigación. Aunque no os nombre a los demás (sois muchísimos) os agradezco hasta el infinito la compañía que me habéis dado estos cuatro años, me lo he pasado genial con vosotros y he estado siempre muy a gusto. Compartir despacho con vosotros ha sido un placer. Siempre

me digo que parece mentira que este sea un despacho de químicos teóricos. Y por supuesto quiero darle las gracias a Feliu y Carles, ya que ellos junto con Núria son los encargados de formar y guiar este gran grupo de científicos.

También quiero darle las gracias a toda la gente de Vigo y de Burbia, tenéis parte de culpa de que sea lo que soy y sin vuestro apoyo, vuestra amistad y vuestras vaciladas por whatsapp la vida sería mucho más aburrida.

Mis mejores deseos para todos vosotros. Espero que nunca perdamos el contacto.

"Partido a partido. Final a final. Si miras lejos, no ves el paso inmediato y tropiezas. Hay que ir despacio, que no lento..."
Diego Pablo Simeone

UNIVERSITAT ROVIRA I VIRGILI
MOLYBDENUM OXIDES AS CATALYST FOR BIOMASS-DERIVED COMPOUNDS: A THEORETICAL APPROACH
Marcos Rellán Piñeiro

List of abbreviations

VASP	Vienna *ab initio* simulation package
MGCM	Multigrid Continuum Model
DFT	Density Functional Theory
GGA	Generalized Gradient Approximation
PAW	Projector Augmented Wave
PBE	Perdew–Burke–Ernzerhof functional
HSE	Heyd-Scuseria-Ernzerhof functional
vdW	van der Waals
NEB	Nudge Elastic Band
CI-NEB	Climbing Image - Nudge Elastic Band
MEP	Minimum Energy Path
IDM	Improve Dimer Method
ZPVE	Zero Point Vibrational Energy
CUS	Coordinatively Unsaturated Site
DOS	Density of States
TPD	Temperature Programed Desorption
XPS	X-ray Photoelectron Spectroscopy
IS	Initial State
FS	Final State
TS	Transition State
RDS	Rate Determining Step
HDO	Hydrodeoxygenation
PG	Propylene Glycol
HP	Hydroxypropanal
POM	Polyoxometalate
HAE	Hydrogen Addition Energy
Red.	Reducibility
MAE	Mean Absolute Error

UNIVERSITAT ROVIRA I VIRGILI
MOLYBDENUM OXIDES AS CATALYST FOR BIOMASS-DERIVED COMPOUNDS: A THEORETICAL APPROACH
Marcos Rellán Piñeiro

List of Publications

Publications related with this thesis

1. Marcos Rellán-Piñeiro and Núria López
   The Active Molybdenum Oxide Phase in the Methanol Oxidation to Formaldehyde (Formox Process): A DFT Study
   ChemSusChem, **2015**, 8, 2231–2239

2. Marcos Rellán-Piñeiro, Miquel Garcia-Ratés and Núria López
   A mechanism for the selective epimerization of the glucose mannose pair by Mo-based compounds: towards catalyst optimization
   Green Chem., **2017**, 19, 5932–5939

3. Marcos Rellán-Piñeiro and Núria López
   One oxygen vacancy, two charge states: characterization of reduced α-MoO_3(010) through theoretical methods
   Submitted, **2018**

4. Marcos Rellán-Piñeiro and Núria López
   Propylene production from glycerol: a first principles study of hydrodeoxygenation (HDO) process on MoO_{3-x}
   In preparation

Additional publications

5. Qiang Li, Marcos Rellán-Piñeiro, Neyvis Almora-Barrios, Miquel Garcia-Ratés, Ioannis N. Remediakis and Núria López
   Shape control in concave metal nanoparticles by etching
   Nanoscale, **2017**, 9, 13089–13094

Marcos Rellán performed all calculations of the publications (1), (2), (3) and (4). He carried out the analyses, made the figures and actively participated in the writing of the four publications.

Marcos Rellán performed part of the calculations and took part in the analyses and discussions of the publication (5).

UNIVERSITAT ROVIRA I VIRGILI
MOLYBDENUM OXIDES AS CATALYST FOR BIOMASS-DERIVED COMPOUNDS: A THEORETICAL APPROACH
Marcos Rellán Piñeiro

Abstract

The development of a more sustainable chemical industry requires the upgrading of biomass-derived compounds to valuable chemicals in selective and non-contaminant processes. In this thesis, the catalytic conversion of oxygenated hydrocarbons obtained from biomass by Mo-oxides is studied by means of Density Functional Theory (DFT). In the different chapters the selective conversion of a small alcohol (methanol), a poly-alcohol (glycerol), and one sugar (glucose) is rationalized. In addition, the optimization of the DFT+U method for the study of Mo-oxides and the analysis of the nature of vacancy defects on α-MoO_3(010) surface, a potential catalytic site, is performed.

In Chapter 3 the selective methanol oxidation to formaldehyde is studied. This is an important reaction in chemical industry. The used industrial catalyst is a mixture of MoO_3 and the iron molybdate $Fe_2(MoO_3)_4$. Several issues, regarding the role of each phase, are under discussion. The reaction path is calculated on α-MoO_3(010) and MoO_2(110) surface, and the differences in activity and selectivity of the two surfaces under aerobic and anaerobic conditions are studied. Moreover, the role of the iron in the industrial catalyst is is unraveled by doping of MoO_3.

Most of the applications of MoO_3 are due to its redox properties. Pure DFT methods cannot describe correctly its electronic structure and the correction of GGA functionals by the addition of an extra interelectronic repulsion term, U, is needed. In Chapter 4 the optimization of these parameter is performed by benchmarking with the hybrid HSE06 functional and coupled cluster CCSD(T) method. In addition, vacancies play an essential role in the catalytic activity of MoO_3. With the optimized DFT+U method a complete characterization of the vacancy defects is performed in terms of bond distances, Bader charges, vibrational frequencies, and XPS shifts. Interestingly, two different electronic states closed in energy and dynamically interconnected are found in the vacancy defects; either two polarons corresponding to the reduction of two Mo^{+6} centers to Mo^{+5}, or a single bipolaron corresponding to the reduction of only one Mo center to Mo^{+4}.

It has been experimentally shown that reduced MoO_3 can drive the selective hydrodeoxygenation (HDO) of oxygenated compounds into unsaturated hydrocarbons. Following these observations, the selective reduction of glyc-

erol to propylene is studied in Chapter 5. The study of the reaction network for the selective conversion on oxygen defective MoO_3 has been performed to illustrate the selective C-O bond cleavage over C-C bonds and pave the way to a better understanding of these HDO processes.

Finally, the selective epimerization of glucose to mannose is studied in Chapter 6. This is an important reaction that allow the selective obtaining of rare sugars from their abundant epimers. The reaction path for the inversion of C^2 configuration through a 1,2 C-shift is calculated on Mo-based polyoxometalates and continuous α-MoO_3 surface. It was found that he Mo-centers act as electron buffer in these reactions; and therefore, the reducibility of the Mo-centers can be traced back as the descriptor for catalyst activity. Moreover, a microkinetic model was built in order to obtain the analytical equation for the reaction rate as function of reducibility.

Through these three different reaction: i) oxidation, ii) reduction and iii) isomerization, this work shows Mo-oxides as versatile catalysts for selective biomass-derived conversion. These studies at atomic scale provide some important insights about their catalytic behavior that pave the way for the development of more active, selective, and stable Mo-based catalysts.

Contents

Chapter 1

Introduction

The general objective of this thesis is the study of the upgrading of small alcohols and poly-alcohols derived from biomass catalyzed by molybdenum oxides through theoretical methods. With the knowledge obtained in this work I want to contribute to the development of new catalysts that make possible the building of a more sustainable and environmental friendly chemical industry.

1.1 Biomass to valuable chemicals

Fossil resources are fundamental in our society. They provide most of the energy supply in the world. Moreover, around 90% of the organic chemicals are produced from petroleum and natural gas, which means that most things that we use every day came from fossil feedstock. However, this dependence has an important cost, the global warming, whose effects are obvious nowadays. In addition to the environmental concerns, the depletion of fossil resources and the consequent rising in the crude barrel price force the chemical industry to search for new energy sources and chemical raw materials. In the last decades, biomass has emerged as a green and renewable alternative resource of chemical compounds.[1] It is generated in photosynthesis from CO_2 and H_2O using sunlight. It is estimated that around 170 billion metric tons of biomass are generated per year in nature, and only 3-4% of these compounds are used by humans.[2] Therefore, biomass has a high potential grow as raw material for chemical industry with the added advantage that it is distributed over the entire world.

The use of biomass as transportation fuel is a very attracting industrial challenge, however, its low carbon content (that means low energy density) limits its use for this purpose.[3] Instead, biomass has a much larger potential as renewable feedstock for the production of valuable chemicals. Biomass is formed by highly functionalized molecules with a wide chemical diversity, which coverts it in a excellent raw material for high-value compounds.[4] There

are three main routes to transformation of biomass into chemicals: pyrolysis,[5] gasification[6] and hydrolysis.[7] The main chemicals obtained from biomass are oxygenated hydrocarbons. The Department of Energy of US proposed a list of top value added building blocks obtained from biomass with the purpose of to lead the chemical research efforts to the profitable production of these compounds from biomass.[8] These molecules are chemical intermediates with a structure able to generate a large number of derivatives.[9]

The change in the feedstock implies the use of different catalyst than the petroleum industry, which results in the challenge of the development a new chemistry. This is an opportunity either to develop cleaner processes in order to synthesize from biomass similar products than petroleum derived, or new products with enhanced properties and more environmental friendly, as biodegradable plastics.

A major challenge of the biobased industry is the development of catalysts active, selective, and stables for transformations of biomass-derived compounds into valuable chemicals.[10,11] There are many research works focused to upgrade the biomass-derived molecules,[12,13] and catalysts as metals and metal oxides were reported to perform chemical transformations as, isomerization,[14,15] hydrogenation,[16] dehydrogenation,[17] dehydroxylation/hydrogenolysis,[18] deoxygenation,[19] and oxidation reactions.[20] These processes combine acid/base-catalyzed reactions such as hydrolysis and dehydration reactions to achieve multistep conversion in one-pot processes.

1.2 Catalysis

A catalyst is an external substance that speeds up the chemical reactions and, ideally, after the reaction remains intact and can be reused.[21] The reactants bond to the catalyst and react between them to form the product overcoming lower energy barriers than in the uncatalyzed system. Thereafter, the catalyst and product separate. The energy diagram of Figure 1.1 illustrates how catalyst offers a more complex alternative but less energy demanding. The catalyst affects the kinetics of the system but does not affect its thermodynamic, that is, the overall change in Gibbs free energy is the same in the catalyzed and non-catalyzed systems and therefore, the equilibrium constant is not affected. A good catalyst should be selective, that is, it should not catalyze unwanted reactions, avoiding the formation of side products.

Catalysis is a fundamental part of chemical industry. It is estimated that around the 90% of chemical products have at least one catalytic step in their manufacturing.[22] Catalysts enable to carry out reactions under softer conditions of temperature and pressure, which reduces the economical cost. Moreover, catalysis allows chemical transformations impossible for non-catalyzed systems. Much fundamental and applied research is done to know how catalysts work in order to improve their performance; an improved catalytic activ-

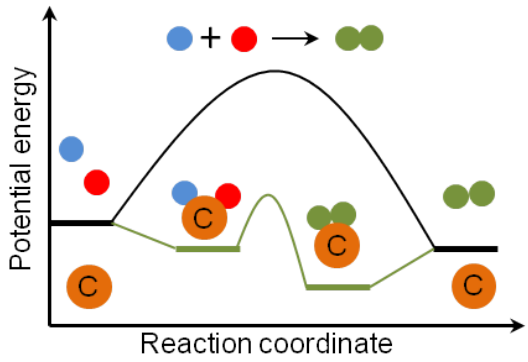

Figure 1.1: Potential energy profile for a uncatalyzed reaction, black line, and the same reaction catalyzed by C, green line.

ity and selectivity reduce the energy consumption and reduce the amount of reactants that are spent in the formation of unwanted side products. Therefore, catalysis contributes to the development of the sustainable chemistry by the reducing the CO_2 emissions produced in the energy generation, reducing waste products and by allowing transformations of the biomass compounds to valuable chemicals impossible for uncatalized systems.

There are three different classes of catalysis: i) homogeneous, where both the catalyst and reactants are in the same phase; ii) heterogeneous, in which the catalyst is a solid that catalyzes reactions of molecules in gas or solution; and iii) biocatalysis, where the reaction are catalyzed by enzymes. Industrially, heterogeneous catalysis is the most utilized, being responsible of the 80% of the global market.[23] As this thesis is focused to develop most efficient and sustainable catalytic processes in industry, heterogeneous catalysis of biomass-derived compounds is studied.

Heterogeneous catalysis

In heterogeneous catalysis the reactions take place in the interface between the solid-phase of the catalyst and the gas- or liquid-phase. The reactions typically occur through a Langmuir-Hinshelwood mechanism:[21] the reactant molecules adsorb on the catalyst surface where they react to form the product that in the following step desorbs, see Figure 1.2. Reactivity is only performed in specific parts of the surface, the active sites.

Figure 1.2: Scheme of a catalytic process through the Langmuir-Hinshelwood mechanism.

The adsorption of molecules on the surface can be classified either as physisorption, if the molecule is bonded to the surface through dispersion forces; or chemisorpcion, if the molecule forms chemical bonds with the surface. The adsorption also can be classified either in molecular adsorption, if the adsorbed molecule keeps intact; or dissociative adsorption, if any of the molecular bonds is broken concomitantly with adsorption. The best catalytic performance is obtained if the interaction between the surface and reactants is neither too weak nor too strong. A weak adsorption would result in a small catalytic effect, whereas in a strong adsorption the reactants and products would not desorb. Both extremes result in a poor catalytic performance. This is known as the Sabatier's principle.[24]

Typical heterogeneous catalyst are pure metals[11] and metal oxides.[25] Their properties can be enhanced by mixing pure metals, forming alloys,[26] mixing oxides,[27] or by adding impurities in doping.[28,29]

1.3 Molybdenum (VI) oxide

Reducible transition metal oxides have been widely used in chemical industry as catalysts for obtaining bulk chemical through the selective oxidation of hydrocarbons[30] and alcohols,[31] the reduction of nitric oxides,[32] and other reactions. The redox properties of the metal oxides, that is, the ability of their metal centers to change their oxidation states, are responsible of their catalytic activity. A particular transition metal oxide, MoO_3, has been used as catalyst for formaldehyde[33] and acroleine production,[34] alkene metathesis and hydrocraking[35,36] and hydrodesulfurization.[37] More recently, several studies of MoO_3 as catalyst for hydrodeoxygenation (HDO) of oxygenated biomass derived compounds have been published.[19,38–41] This thesis is focused to the theoretical study of catalytic processes on this oxide since, despite of its wide range of uses, little is known about its behavior at atomic level during reactions.

Molybdenum oxides are earth abundant compounds that present in a wide range of oxidation states and structural forms.[42] As catalyst, the α polymorph of the full oxidized MoO_3 is the most used phase. Stoichiometric α-MoO_3 is a n-type semiconductor with a reported band-gap between 3.0-3.2 eV,[43–45] and a high workfunction, >6.9 eV.[46] The electron affinity is around 6 eV and the ionization energy is higher than 9 eV.[47,48] This band structure, which can be modified by doping,[28,29] or by forming vacancy defects, gives molybdenum oxide unique properties that can be employed, in addition to catalysis, for large number of new physical and chemical applications[49] as electro- and chromic devices, photo-, electro- and thermal catalysis, solar cells and light emitting diodes, photodetectors/sensors, batteries, pseudocapacitors, thermoelectric and ferroelectric materials.

As catalyst, the most important industrial application of α- MoO_3 is the

methanol partial oxidation to formaldehyde, the Formox process,[50] where it is mixed with Fe_2O_3 to form the iron molybdate $Fe_2(MoO_3)_4$.[51] With the addition of an excess of MoO_3 to the catalyst, the reaction is highly active and selective being the most efficient industrial process to obtain formaldehyde.[51,52] Although this reaction has been widely studied by experimentalists, some issues regard unsolved.[53–56] The study at atomic scale of this reaction is the objective of Chapter 3, where the performance of the suboxide MoO_2 is also studied.

Nowadays, α-MoO_3 is also attracting attention due to its catalytic properties to upgrade oxygenated hydrocarbons derived from biomass through hydrodeoxygenation, HDO, processes.[19,38–41] These oxygenated hydrocarbons have a high oxygen content and their removal produce valuable chemicals as olefinic compounds that can be used in polymerizations or as transportation fuel. In these reactions, the oxide is pre-reduced with H_2 that forms vacancy defects on its surface. Then, these defects catalyze the selective C-O bond cleavage over C-C. In the global process, the oxygens of hydrocarbon are removed in the form of water. These HDO processes are studied in Chapter 5 through the reaction network of the glycerol reduction to propylene. Moreover, the nature of the surface vacancies is studied previously in Chapter 4.

Other Mo(VI)-oxide based compounds, as niobium molybdates and Mo-polyoxometalates,[14,57] have shown activity for the biomass conversion. In particular, I focused in the selective C^2 epimerization of aldoses catalyzed by $H_3PMo_{12}O_{40}$, a highly active and selective catalyst for the reaction. This system is studied in Chapter 6.

Several theoretical studies have been performed about the structure and electronic properties α-MoO_3.[58–63] However, despite the interesting catalytic properties of α-MoO_3 there are only a few theoretical studies about reactivity.[64–66] A general objective of this work, is to contribute to obtain a better understanding of α-MoO_3 catalytic behavior allowing the development of more active, selective and stable catalyst based on Mo-oxides.

1.3.1 Structure of MoO_3

The α-MoO_3 polymorph crystallizes in a orthorrombic crystal structure with *Pbnm* symmetry. Its structure is formed by distorted MoO_6 octhaedra ordered in bilayers perpendicular to the y-axis. Weak van der Waals interactions between the bilayers keep packed the structure. Each MoO_6 octhahedra has three crystallographic distinct oxygens atoms: i) three coordinated oxygens, O_{3c}, which are symmetrically placed between two Mo centers of the same sublayer along x-axis and forms a long bond with a Mo center of the other sublayer; ii) asymmetric bridging oxygens, O_b, that form an asymmetric bridge between two Mo centers along z-axis; and iii) terminal oxygens, O_t, coordinated to only one Mo center through a double bond along y-axis; they are

present in the interlayer region. The experimental lattice parameters are a= 3.962 Å, b=13.855 Å and c=3.699 Å.[67]

Due to the layered packed through dispersion forces along y axis the most stable surface is the (010), which is reported as the main surface involved in reactivity.[68] The structure of bulk, (010) surface, and MoO_6 octahedra are shown in Figure 1.3.

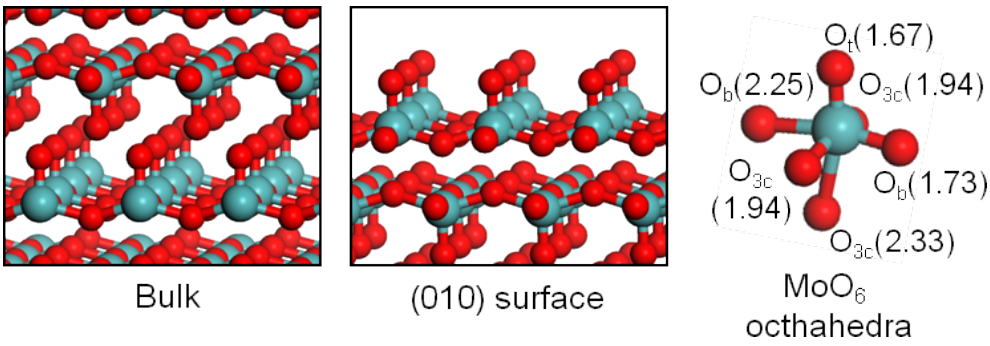

Figure 1.3: Right: Structure of α-MoO_3 bulk; middle: α-MoO_3(010) surface; and left: MoO_6 octhaedra, with experimental bond distances, in Å.[67] Mo atoms in green, O in red.

1.4 DFT calculations

The increase of computational power and the development of Density Functional Theory (DFT) have become possible the calculation of the electronic structure of heterogeneous catalytic systems.[69] Thus, DFT is one of the main tools in heterogeneous catalysis research since the study at atomic scale plays an important role in characterization, understanding and prediction of the catalytic processes.[70] For instance, the description of the chemical bond between reactants and surface is key to understand and predict the catalyst reactivity. The catalysts often present a complex relationship between surface structure and catalytic activity and selectivity that cannot be evident by the experimental studies, but theoretical simulations can give insights about them. Moreover, the calculation of adsorption energies and energy barriers of elementary steps together microkinetic modeling allow the prediction of the kinetic behavior of the catalyst, which is its most important property and the starting point to reactor design. Thus nowadays, it is accepted that the combination of experiments and simulations is the most efficient way to catalysis development.

Simulations on MoO_3 present some challenges. It is a reducible transition metal oxide, and pure DFT cannot reproduce correctly the electron self-interaction of its electrons at 4d orbital. The DFT+U method,[71] which introduces a repulsion term to DFT, has emerged as a possible solution, but its it needs to be improved.[60] Despite the advantages of DFT+U, the fitting of the

U parameter is not straightforward and there is no an accepted value for Mo in literature. As consequence, studies with different U[58,60,62,72] or pure DFT method[66] have been published giving scattered results.

Moreover, due to its layered structure, pure DFT methods cannot reproduce the interaction between layers overestimating the interlayer spacing[59] between other problems. To avoid this problem, some studies fixed the b lattice parameter to the experimental one.[58] A more accurate description can be obtained with the addition of van der Waals interaction in DFT calculations[63] through a semiempirical correction as the Grimme's D2 and D3 methods.[73,74]

The study of biomass derived compounds also presents some issues. Generally, they are large molecules with many functional groups. Computational techniques have their size limitation since, in addition to the extra computational cost, the number of conformations and side reactions increases exponentially with the chain size and number of functional groups, hindering the correct screening of the reaction network. In this work, methanol (C1), glycerol (C3), and monomer glucose (C6) are used as substrate. This molecules can act as probe molecules and the knowledge obtained with them can be extrapolated to larger molecules with the same functional groups.

1.5 Motivation and objectives

The general objective of this thesis is to contribute to the development of a more sustainable and environmental friendly chemical industry through the theoretical study of biomass derived compounds selective conversion catalyzed by metal oxides. In particular, this thesis is focused on the reactivity of oxygenated hydrocarbons, alcohols and polyalcohols, on molybdenum oxides. To date, only few theoretical studies are focused to the study of these catalytic systems. The motivation and objectives for each chapter are detailed in the following:

Chapter 3. The Formox™ process: selective methanol oxidation to formaldehyde

This is an important industrial reaction with an extensive experimental literature. However, several issues regarding the role of the different phases and their oxidation states remain under discussion. The objectives of this chapter are:

- To compute the reaction pathway for methanol oxidation to formaldehyde on Mo-oxides that reproduces the experimental insights.
- To determine of activity and selectivity of the reaction on $MoO_3(010)$ and $MoO_2(110)$ surfaces.
- To determine the role of Fe in the iron molybdate used as catalyst in the industrial formulation.

- To propose a better catalyst composition.

Chapter 4. On the nature of oxygen vacancies on the α-MoO_3(010) surface through an optimized DFT+U method

Vacancies are essential in the catalytic activity of α-MoO_3, and their characterization is a key step to understand the catalytic properties of the oxide. To date, there are no theoretical studies about characterization that reproduce the experimental observations. In addition, an optimized DFT+U method is essential to obtain an accurate description of their properties. In order to contribute to solve these issues, this work was focused on the following objectives:

- To optimize the DFT+U method to obtain correct reaction energies and electron localization in redox reactions.
- To determine what oxygens are removed during α-MoO_3(010) surface reduction.
- To characterize the energetic, electronic and geometrical features of the formed vacancies.
- To study the vacancy energy as function of the coverage.
- To test the influence of the vacancy oxidation state on adsorption energy of methanol and formaldehyde.

Chapter 5. Propylene production from glycerol: a first principles study of the hydrodeoxygenation (HDO) process on MoO_{3-x}.

HDO processes allow upgrading oxygenated biomass molecules by reducing the oxygen contents. Theoretical studies are essential to a complete rationalization of the process for the development of more active and selective catalysts. Moreover, the production of propylene from glycerol is an attractive industrial target. This chapter will be oriented to the following objectives:

- To explain how the HDO works in this catalytic system.
- To study the vacancy formation on the catalyst surface by H_2 adsorption and hydrogen migration over the surface.
- To determine the reaction network for the glycerol reduction to propylene on the base of the intermediates experimentally observed.
- To explore the mechanism of the different reaction types present in the HDO process and to calculate all the elementary steps for them.
- To explain the origin of selectivity towards C-O bond cleavage over C-C.

Chapter 6. Selective C_2 epimerization of aldoses catalyzed by Mo-based compounds

Some rare sugars with important applications can be obtained by the epimerization of their abundant counterpart. Experimentally Mo-based compounds (molecular and solids) have shown a good performance both in activity

and selectivity. Theoretical studies are needed to explain the mechanism and the different activity and stability of the different Mo compounds. The objectives of this chapter are:

- To unravel the reaction mechanism for the C_2 epimerization of aldoses and calculate the reaction path on POMs and bulk MoO_3.
- To test the influence of POM heteroatom and deprotonation grade.
- To study the effects of explicit water molecules in the mechanism.
- To study the influence of side -OH groups in the aldose.
- To explain the different behavior against leaching of the bulk and cluster Mo-based compounds.
- To find a descriptor for the catalytic activity.

With the accomplishment of these objectives, this thesis will display the versatility of Mo-oxides as selective catalyst for biomass conversion. Their special redox properties will be shown through an oxidation reaction, a reduction reaction, and an isomerization. In addition, the optimized DFT+U method will allow to reproduce correctly the molybdenum oxide properties in future studies.

UNIVERSITAT ROVIRA I VIRGILI
MOLYBDENUM OXIDES AS CATALYST FOR BIOMASS-DERIVED COMPOUNDS: A THEORETICAL APPROACH
Marcos Rellán Piñeiro

Chapter 2

Theoretical background

In this chapter I am going to to describe the most important tools of theoretical heterogeneous catalysis that were used during this thesis. I will start the chapter describing the Schrödinger equation, the first mathematical approximation that allows to calculate the energy of chemical systems. After that, I will continue with the Density Functional Theory (DFT), the main method of theoretical heterogeneous catalysis. I will continue describing its fundamentals and how it is applied for the study of solid systems. Finally, the main aspects of microkinetic modeling, a tool that allows the transfer of DFT results to a experiment observables, will be explained.

2.1 From the nuclei and electron configuration to the energy: Schrödinger equation

The fundamental objective of theoretical chemistry is to obtain the energy of a system from the electronic configuration of its atoms and/or molecules. The first step in this direction was done in 1926 with the publication of the time-independent Schrödinger equation,[75] the fundamental equation of quantum physics:

$$\hat{H}\Psi = E\Psi \tag{2.1}$$

where $\hat{H}$ is the Hamiltonian operator that describes the energy of the system, Ψ is the set of solutions of the Hamiltonian (wave functions) that describe the whole system, and E the energy of the system. Solving the Schrödinger equation is possible to obtain the total energy of the system. The Hamiltonian operator contains the operations associated to kinetic, $\hat{T}$, and potential, $\hat{V}$, energy of the system:

$$\hat{H} = \hat{T} + \hat{V} = -\frac{h^2}{2m}\nabla^2 + \hat{V} \tag{2.2}$$

and therefore we can write the Schrödinger equation as:

$$\left[-\frac{h^2}{2m}\nabla^2 + \hat{V}\right]\Psi = E\Psi \tag{2.3}$$

In practice, to solve this equation for a many-body electronic structure is not possible and some approximations are needed. The most important is the so-called Born-Oppenheimer approximation,[76] which separates the electron and nuclei movement in two different mathematical problems. The physical reason behind this assumption is the great difference in their mass. Due to this difference, at the same kinetic energy, the electron movement is much larger; and therefore, the nuclei of the atoms or molecules can be consider static. The nucleus, or nuclei distribution for molecules, then determines the static potential, $\hat{V}$, in which the electrons are moving. Assuming this approximation, for a system of N electrons and described by the wave function $\Psi(\mathbf{r}_1, \mathbf{r}_2, ..., \mathbf{r}_n)$, the many-body Schrödinger equation is written as:

$$\hat{H}_{elec}\Psi = \left[\hat{T} + \hat{V} + \hat{U}\right]\Psi = E\Psi \tag{2.4}$$

and therefore:

$$\left[\sum_{i}^{N} -\frac{h^2}{2m}\nabla_i^2 + \sum_{i}^{N} V(\mathbf{r}_i) + \sum_{i<j} U(\mathbf{r}_i, \mathbf{r}_j)\right]\Psi = E\Psi \tag{2.5}$$

In Eq 2.4, $\hat{T}$ is the kinetic energy, $\hat{V}$ the potential for the interaction electron-nuclei, and $\hat{U}$ the potential for the electron-electron interaction.

There are many methods for to obtain the total energy solving the many-body Schrödinger equation. The most popular is the Hartree-Fock method,[77] which approximates the electron many-body wave function by a single Slater determinant. The accuracy of this method is limited, but some more accurate methodologies have been developed on the base of it, the so-called post-HF methods. These methods have a main problem, they have a high computational cost that limits their application to small systems. Only with the appearance of Density Functional Theory (DFT) the simulation of large systems has become possible.

2.2 From the electron density to the energy: Density Functional Theory (DFT)

Density Functional Theory (DFT) is a methodology that allows the study of the electronic structure of many-body system using the electron density

instead the wave function to describe the system. The computation of the system energy with the many-body Schrödinger equation using the electron density is much more efficient since the wave function depends of 3N variables, $\Psi(\mathbf{r_1}, \mathbf{r_2}, ..., \mathbf{r_n})$, that is, three for each electron in the system; and the whole electron density of the system depends only of 3 variables, $n(\mathbf{r})$.

The electron density can be written in terms of the individual electrons wave function:

$$n(\mathbf{r}) = 2\sum \Psi_i^*(\mathbf{r})\Psi_i(\mathbf{r}) \tag{2.6}$$

and therefore the electron density in $(\mathbf{r})$ is the summation of the probability of an electron in individual wave function $\Psi_i(\mathbf{r})$ is located at position $(\mathbf{r})$. The probability is multiplied by a factor of 2 because of the Pauli exclusion principle that establishes each individual wave function can be occupied by two electrons with opposite spin.

DFT has the roots in the Thomas-Fermi theory,[78] which provided a relationship between the electron density and the corresponding many-body wave function.[79] Based in this relationship Pierre Hohenberg and Walter Kohn postulated their theorems[80] that are the basis of DFT:

- **First theorem:** *"The ground state energy from Schrödinger equation is a unique functional of the electron density."*

This theorem determines a one-to-one mapping between the ground state wave function and the ground state electron density. In practice, this means that the electron density determines all the properties of the ground state, including energy, $\varepsilon[n(\mathbf{r})]$, and wave function, $\Psi[n(\mathbf{r})]$, and it allows solving the many-body Schrödinger equation with a function of only three variables.

- **Second theorem:** *"The electron density that minimizes the energy of the overall functional is the true electron density corresponding to the full solution of Schrödinger equation."*

From this principle an important property can be extracted: if the true functional is known we can apply the variational principle to the electron density until to obtain the exact solution and the exact energy.

Hohenberg-Kohn theorems show that it is possible to use the ground state electron density to calculate properties of the system but they do not provide the way of to find this ground state electron density. This issue was solved by Walter Kohn and Lu Jeu Sham,[81] who showed that solving a set of mono-electron equations for a fictitious system of non-interacting electrons, the electron density can be calculated with the Eq. 2.6. The mono-electronic equations are written as:

$$\left[\hat{T} + \hat{V}_{KS}\right]\Psi_i(\mathbf{r}) = \left[-\frac{h^2}{2m}\nabla^2 + V_{KS}(\mathbf{r})\right]\Psi_i(\mathbf{r}) = \varepsilon_i\Psi_i(\mathbf{r}) \tag{2.7}$$

where $\hat{T}$ represents the kinetic energy of the electron and $\hat{V}_{KS}$ the Kohn-Sham potential, a local effective (fictitious) external potential in which the non-

interacting electrons move. The solution to this equation is a mono-electron wave function that only depends of three spatial variables, $\Psi_i(\mathbf{r})$. The Kohn-Sham potential can be split as:

$$V_{KS}(\mathbf{r}) = V(\mathbf{r}) + V_H(\mathbf{r}) + V_{XC}(\mathbf{r}) \tag{2.8}$$

where $V(\mathbf{r})$ describes the interaction between the electron and the collection of nuclei. $V_H(\mathbf{r})$ is the Hartree potential that describes the Coulomb repulsion between the electron i and the total electron density created by the all electrons of the system. The Hartree potential is defined as:

$$V_H(\mathbf{r}) = e^2 \int \frac{n(\mathbf{r}')}{|\mathbf{r} - \mathbf{r}'|} d^3r' \tag{2.9}$$

The last term in Eq. 2.8, $V_{XC}(\mathbf{r})$, is the exchange correlation potential that accounts all the quantum mechanical effects that are not included in the previous terms, and it is considered as the unknown part as it is a functional derivative of the exchange correlation energy, and the functional that defines this energy is unknown. This potential is defined as:

$$V_{XC}(\mathbf{r}) = \frac{\delta E_{XC}(\mathbf{r})}{\delta n(\mathbf{r})} \tag{2.10}$$

Therefore the expanded Kohn-Sham equation is written as:

$$\left[-\frac{h^2}{2m}\nabla^2 + V(\mathbf{r}) + V_H(\mathbf{r}) + V_{XC}(\mathbf{r}) \right] \Psi_i(\mathbf{r}) = \varepsilon_i \Psi_i(\mathbf{r}) \tag{2.11}$$

Being the energy a functional of the electron density, $\varepsilon_i[n(\mathbf{r})]$, if a initial guess of electron density is made we can solve this equation for each electron and to obtain all the $\Psi_i(\mathbf{r})$ of the system; and using the Eq. 2.6 a new electron density is obtained. Then, the Kohn-Sham equation can be solved iteratively to achieve the self-consistent solution to the system.

2.2.1 Solving the Kohn-Sham equation: Exchange-correlation functional

At this point, through the Hohenberg-Kohn theorems, we know how to transform the many-body Schrödinger equation of 3N spatial variables into a equation of only three. In addition, the Kohn-Sham equations provide us the way for apply the Hohenberg-Kohn theorems. But DFT method still has a problem: the functional for exchange correlation energy, $E_{XC}[n(\mathbf{r})]$, is not known except for the uniform electron gas, where the electron density is constant in all points in the space. This potential should describe the exchange, the energy released when electrons (as they are indistinguishable particles) exchange their positions; and the correlation energy, which arises from the interaction between the electrons of the electronic structure, that is, it is a measure of how

much the movement of one electron is depends on the presence of all other electrons, the so-called electron self-interaction. In order to solve the Konh-Sham equations some approximations to correlation exchange functionals have been developed.

The simplest one is the Local-Density Approximation (LDA).[81,82] In this approximation the energy functional in a given point depends only of the electron density, which is considered constant, in that point:

$$E_{XC}^{LDA}[n(\mathbf{r})] = \int n(\mathbf{r})\varepsilon_{XC}^{LDA}(n(\mathbf{r}))d\mathbf{r} \tag{2.12}$$

This equation could be extended to spin polarized systems. In LDA the exchange-correlation energy for an uniform electron gas is also used for a non-uniform systems, the really interesting systems. Although for some systems LDA has been successful for reactions, either in gas-phase or surface, generally this approximation gives wrong results because of it tends to overestimate binding and cohesive energies.

Increasing the complexity, we found the Generalized Gradient Approximation (GGA) functionals. In this approximation the energy functional in a given point depends of the value and the gradient of electron density in that point:

$$E_{XC}^{GGA}[n(\mathbf{r})] = \int n(\mathbf{r})\varepsilon_{XC}^{GGA}(n(\mathbf{r}), \nabla n(\mathbf{r}))d\mathbf{r} \tag{2.13}$$

The GGA functional equation also could be extended to spin-polarized systems. As there are many ways to include the gradient in the GGA, there are many distinct available functionals. The most commonly used in heterogeneous catalysis are PBE,[83] PW91[84] and RPBE.[85] More recently, the GGA functional Bayesian Error Estimation Functional (BEEF) was generated using several training data sets of quantities representing chemistry, solid state physics and surface chemistry. These pure GGA functionals do not include the van der Waals interaction resulting from dynamical correlations between fluctuating charge distributions, so the can yield wrong results for adsorption and reaction energies with molecules and surfaces where this contribution is important like for α-MoO_3. Some methodologies have been developed to take into account the van der Waals contributions; being the most popular the semi-empirical correction of Grimme[73,74] and the charge density dependent correction developed for Tkatchenko.[86] DFT calculations in the GGA gives good values for thermochemistry, that are improved when dispersion forces are taken into account.

There is another type of functionals, the hybrid functionals, that combines the exchange correlation correction from LDA and GGA methodologies

and add a portion of exact exchange from HF theory. These functionals are more accurate than pure GGAs and they are the most used in simulations of molecules, used to be the most popular B3LYP.[87,88] These functionals can be used in surface simulations, but the computational cost is prohibitive. Typically, they are only used for perform single points calculations; the most popular hybrid functionals for surface simulations are PBE0[89] and HSE.[90]

Heterogeneous catalysis simulations typically involves more than 100 atoms, and therefore solve the many-body Schrödinger equation is prohibitive, being DFT the essential tool for these simulations. Between the approximations of exchange correlation functional, GGA offers the best compromise between computational cost and accuracy.

2.2.2 DFT+U approximation

Although GGA functionals give good results for many system in theoretical heterogeneous catalysis there are a group of surfaces where the application of these functionals to study the reactivity is particularly challenging: the reducible transition metal oxides (RTMOs). Due to the erroneous electron self-interaction approximations, DFT tends to exaggerate the extent of the electron delocalization. This self-interaction errors are most problematic for open shell system, mainly for RTMOs with partially occupied d or f orbitals. In addition, this overdelocalization is different for each oxide.

There are two approaches to mitigate the overdelocalization: the use of hybrid functionals and the DFT+U method. The use of hybrid functionals as common methodology is prohibitive for the computational cost; and therefore, DFT+U is the most used approximation. In DFT+U, an extra interelectron repulsion term $(U - J)$ is introduced. This term measures the strong on-site Coulomb interaction of localized electrons. Thus, the total DFT+U energy is expressed as

$$E_{DFT+U} = E_{DFT} + (U - J)\frac{1}{2}\sum_{lms}(\rho_{lms} - \rho_{lms}^2) \tag{2.14}$$

where U describes the Coulomb potential, J the exact exchange potential, and ρ is the occupation value of an atomic orbital with quantum numbers l, m, and s. The term $(U - J)$ measures the degree of uncanceled electron self-interaction. In a simple approach introduced by Dudarev,[71] the term $(U - J)$ is expressed as a single parameter: $U_{eff} = (U - J)$.

This approximations improves importantly the accuracy of DFT methodology on RTMOs. The main issue of this approximation is to choose the correct value of U_{eff}, which should be optimized for each metal oxide, and in some cases different properties of the same RTMO are correctly reproduces by different values of U_{eff}. Normally the value is chosen to match with a known

experimental property, the band gap being the preferred. Due to the limitations on experimental properties, methodologies to choose the U_{eff} only in base a self-consistent calculations have been developed.[91]

As the work presented on this thesis involves calculations of bulk and surface of α-MoO_3, a RTMO, the chosen functionals are PBE and PBE+U.

2.3 DFT in heterogeneous catalysis: Periodic systems

The best way to reproduce solid systems is using periodic conditions. Normally, to perform simulations we consider that the structure of a solid has the same atom composition and distribution repeated infinitely over each coordinate. Thus, we can describe a solid as a box, where we have this information, that is repeated periodically in the three dimensions. If the box lattice vectors are $\mathbf{a_1}$, $\mathbf{a_2}$, and $\mathbf{a_3}$ the position of each atom is defined by $(\mathbf{r}) = (n_1\mathbf{a_1}, n_2\mathbf{a_2}, n_3\mathbf{a_3})$ for any integer n_1, n_2, and n_3. This boxes are called cells, and the smaller cell that contains all the information in the unit cell. The use of this periodic cells eases the resolution of the Kohn-Sham equation by the application of the Bloch's theorem.

For the cells characterized by the lattice vectors a_i it is possible describe a reciprocal lattice with vectors, b_j. These vectors are defined so that $a_i \cdot b_j = 0$ if $i = j$, and 0 otherwise. Therefore the reciprocal lattice vectors are calculated as:

$$b_1 = 2\pi \frac{a_2 \times a_3}{a_1 \cdot (a_2 \times a_3)} \tag{2.15}$$

$$b_2 = 2\pi \frac{a_3 \times a_1}{a_2 \cdot (a_3 \times a_1)} \tag{2.16}$$

$$b_3 = 2\pi \frac{a_1 \times a_2}{a_3 \cdot (a_1 \times a_2)} \tag{2.17}$$

the space described by these vectors is called reciprocal space or k-space. An important observation is that larger vectors in real space correspond to shorter vectors in reciprocal space. The use of reciprocal space and reciprocal vectors ease the mathematical solution of Kohn-Sham equations.

2.3.1 Wave function description: plane waves basis set

For to solve the Kohn-Sham equations in periodic systems the wave function solutions must satisfy the Bloch's theorem,[92] which states that in a periodic

system the electronic wave functions can be expressed as the product of a cell-periodic part, $e^{i\mathbf{kr}}$, and a plane wave function, $u_n(\mathbf{r})$:

$$\psi_n(r) = e^{i\cdot\mathbf{kr}} f_n(\mathbf{r}) \tag{2.18}$$

The cell-periodic part is defined by a set of plane waves whose wave vectors are reciprocal lattice vectors of the crystal:

$$f_n(\mathbf{r}) = \sum_G c_{n,\mathbf{G}} exp[i\mathbf{G}\cdot\mathbf{r}] \tag{2.19}$$

where G are the reciprocal lattice vectors. This vectors are defined by the lattice vector, l, and an integer: $\mathbf{G} = 2\pi m/\mathbf{G}$. Finally, we can express each electronic wave function as a sum of plane waves:

$$\psi_n(r) = \sum_G c_{n,\mathbf{k}+\mathbf{G}} exp[i(\mathbf{k}+\mathbf{G})\cdot\mathbf{r}] \tag{2.20}$$

To solve the mathematical equations of DFT is much more convenient in terms of $\mathbf{k}$, vectors of reciprocal space, than in terms of $\mathbf{r}$, vectors of the real space. For the electronic wave function at each $\mathbf{k}$ the Bloch's theorem states that it can be expanded in terms of a discrete plane wave basis set. Although, in principle, the electronic wave function must be expanded with an infinite plane wave set, in practice this set can be shortened. The coefficient $c_{n,k+G}$ for plane waves with small kinetic energy are much more important than for plane waves with high kinetic energies. Thus, in practice, the plane wave basis set is truncated and only the plane waves with kinetic energies lower than a particular value are included in the calculation. This maximum value of kinetic energy is the cutoff energy. Therefore, applying the Bloch's theorem and the cutoff energy a finite basis set is produced. The use of a cutoff energy leads to errors in the total energy, lower for higher cutoff value, but it is possible expand the kinetic energy to a value where the relative energies between the different systems converge.

For the wave functions at each $\mathbf{k}$, there are a number of n solutions to the Kohn-Sham equations. These solutions, which have an associated energy, are the so-called bands. The overall energy distributions of bands over all the k-points determines important properties of the solid. The lack of energy gap between bands, band gap (BG) is a property of metallic materials. If there is a energy gap the compound could be a semi-conductor, for small gaps, or insulator, for large gaps, see Figure 2.1.

Bloch's theorem allows to only consider the electrons within the unit cell at an infinite number of k-points within the first Brillouin zone. The occupied electron states of each k-point contributes to the electronic potential, so a infinite number of calculations would be needed to compute the total potential. But in practice, the electronic wave functions of k points that are very close are almost the same. Therefore, it is possible to represent the wave function of a region of the space by the wave function of a single k point. If the

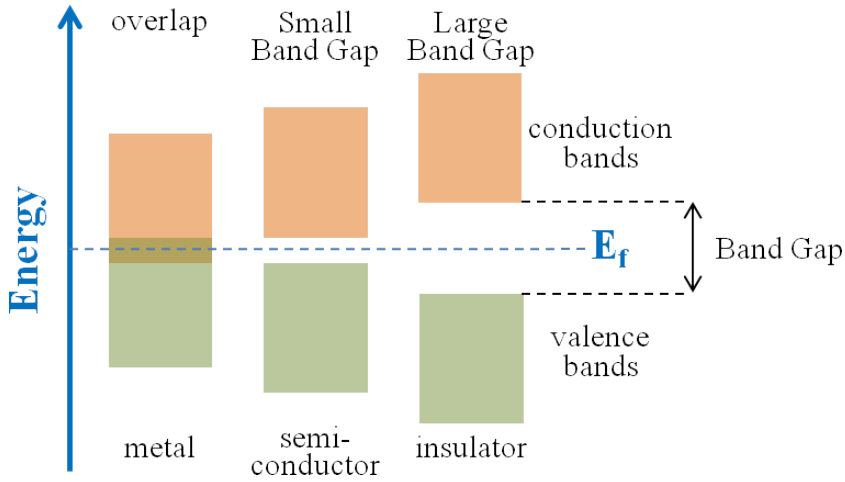

Figure 2.1: Schematic representation of the electronic band structure of a metal, a semiconductor and an insulator.

reciprocal space is correctly sampled it is possible to calculate the electronic potential, and thus the energy of the cell of the solid, using a finite number of k-points. There are several methodologies to sampling the k-points as efficiently as possible, the most widely used is the Monkhorst-Pack method.[93] The use of a k-point sampling produces an error in the total energy. This error can be reduced by the increase of k-point sampling. In practice this error converges as the density of k-points increases, for high k-points density this error tends to zero. As we work on the reciprocal space that is smaller as bigger is the real cell, we can use less density k point sampling as larger is the cell.

2.3.2 Reducing the number of wave functions: pseudopotentials

The substitution of core electron by pseudopotentials is an approximation based on the chemical properties of the atoms are determined only by the valence electrons. The inner electrons do not participate in chemical bonds, they are almost inert and their distribution is practically the same in different chemical environments. In addition, as they are very close to the nuclei they have a strong ionic potential and their wave function have fast oscillations and a large number of plane waves would be necessary to correctly reproduce them. This fast oscillation results in a large kinetic energy for the valence electrons in the core region, which roughly cancels the large potential energy due to the strong Coulomb potential. Thus, the valence electrons are much more weakly bound than the core electrons.

In this approximation, the strong Coulomb potential is replaced by an effective weaker pseudopotential and the valence wave functions by a pseudo wave functions that vary smoothly in the core region and outside they are identical to the original ones, see Figure 2.2. The use of pseudopotentials

allows the utilization of a smaller plane wave basis set to correctly describe the wave function.

The ideal pseudopotential should be soft and transferable. Soft pseudopotential means that the number of plane waves to expand the pseudo wave functions is small . The transferability ensures the pseudopotential is able to reproduce the properties of the atom in different chemical environments. One of the most used pseudopotential methodology, and employed in the whole thesis, is the Projector Augmented Wave (PAW) method.[94,95] In this method, the pseudo wave functions are used to construct the all electron wave functions and the total energy functional is evaluated from the latter.

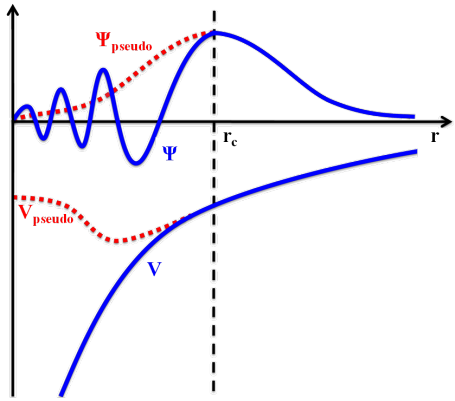

Figure 2.2: Schematic representation of the all electron, continuous blue line, and pseudopotential, dashed red line, wave functions and potentials. r_c is the cutoff radius, that marks the point from the all electron and pseudopotential variables have the same value. Adapted from ref.[96]

2.3.3 Practical application of periodic conditions: Slab models

In the most of heterogeneous catalysis, the catalytic activity takes place on the surface of the catalysis. Surfaces are infinite in two dimensions, and therefore it seems easy to represent the surface using the boundary conditions in two dimensions. However, as the Bloch's theorem applies for periodic conditions in the three dimensions the slab model is used. The idea behind this model is to represent the surface as a slab of few atomic layers and add a vacuum region between slabs. Therefore when the cell is repeated in the three dimensions, it defines a series of stacked slabs of catalyst separated by vacuum regions, as it can be see in Figure 2.3, where a slab model of a metal surface is represented. The surface slab should have several atoms layers in order to correctly mimic the bulk/surface properties. It is important that the vacuum region is large enough to avoid the interactions between slabs, and between adsorbates and the bottom of the next slab.

In practice, for the slab thickness, more atoms layers are better, but more layers means more computational time, and therefore, to choose the number

of layers convergence test should be done. The enough thickness depends on the surface nature and the property of interest. In the same way is better as larger is the vacuum region, but it increases the computational time; typical values are between 10-15 Å. Normally the reactivity is studied only on one side of the slab, and the upper layers of the slab, and the adsorbates, are allowed to relax, keeping on the bulk distribution of the atoms the first layers. Thus, the slabs are asymmetrical, causing spurious terms that are avoided with the use of a dipole correction along z axis.[97]

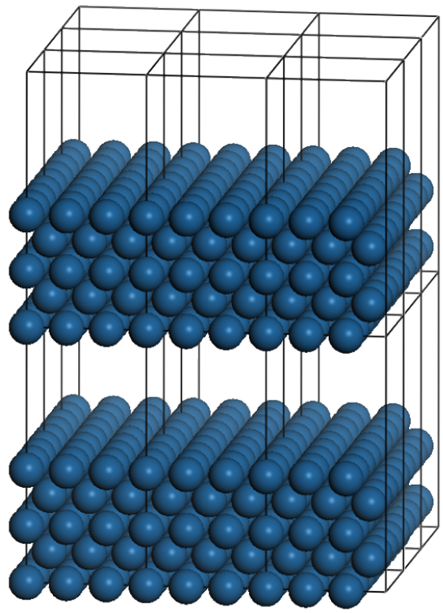

Figure 2.3: Repeated supercell of a metal surface represented by the slab model.

2.4 Finding transition states: NEB, CI-NEB and IDM

In the study of reactivity to allocate the transition states (TS) structures is a essential part. TS are defined as the atomic configuration with the highest potential energy along the reaction coordinate. Mathematicaly they are first order saddle points. The difference in energy between the TS and the initial state (IS) or final state (FS), the forward and reverse activation energy, determines the rate of the reaction. Unfortunately, the numerical methods employed to find minima can not be used to TS since they are developed to minimize the energy. However, some methods have been developed to search TS.

The method most widely used in heterogeneous catalysis is the Nudge Elastic Band (NEB).[98,99] This method is based in to define a minimum energy path (MEP) between the IS and the FS. A initial guess of the MEP is given as a

series of n atomic dispositions, called images, that are linearly interpolated between the two minima. Then, a constrained optimization of the images is done. Spring forces along the path between images are added and the component of the force due to the potential perpendicular to the path is projected out. In other words, each image is optimized taking into account the previous and following one and maintaining equal space to them. Once the forces perpendicular to the path of all structures is zero the MEP is founded. As more images are used to represent the path a better description of the MEP is obtained. The highest energy image is considered the transition state.

However, none of the images represents exactly the transition state structure, see Figure 2.4. Therefore, a modification of the NEB method was developed to find the exact TS structure, the so-called climbing image, CI-NEB.[100] In this method the highest energy image does not feel the spring forces along the path, and it is displaced to the saddle point by the inversion of the true force along the tangent. In others words, the energy is maximized along the path and minimized in all other directions. This image converges at the exact transition state structure. In Figure 2.4 a comparison between NEB and CI-NEB is shown. The highest energy image obtained with NEB method is not on the saddle point of MEP, leading a wrong identification of the TS. However, using the CI-NEB method the structure corresponding to the saddle point is achieved.

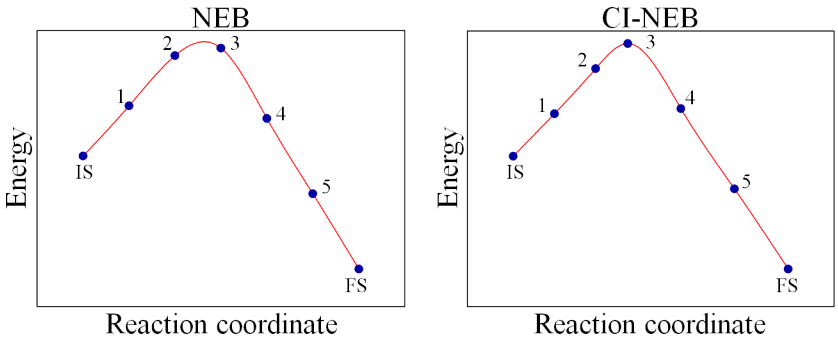

Figure 2.4: Representation of NEB (right) and CI-NEB (left) calculations. Red line represents the MEP and blue points the IS, FS and optimized images.

In practice, the best way to find TS is the combination of NEB methods with the Improved Dimer Method (IDM). The highest energy image from a NEB is used as initial guess of IDM. In this method two images (the dimer) separated to a fixed distance are optimized to maximize the energy along the dimer axis and minimize in all others. Then, the curvature is calculated and the dimer rotated to set the dimer axis parallel to the direction of maximal negative curvature. This cycle is repeated until the dimer converges in the TS structure. The initial dimer axis is provided by a frequency calculation.

2.5 Linking DFT results with experiments: microkinetic modeling

Typical DFT calculations are performed for model systems of isolated molecules, and we need to relate this calculations with experiments. Kinetics provides us the theoretical framework to relate the the thermodynamic values calculated with DFT and the rate of variation of macroscopic parameters as reactant concentration and pressures. In addition, the chemical processes normally are composed of several elementary steps, or even, by complex reaction networks. Microkinetic models[21] couple these elementary steps providing a important tool to understand the chemical processes.

In heterogeneous catalysis the reactants normally adsorbs on the surface. Once all the reactants are adsorbed they react in their chemisorbed state. After that, the products are desorbed. This mechanism is known as Langmuir-Hinshelwood kinetics. The simplest Langmuir-Hinshelwood mechanism is represented in the following reaction scheme model were * represents the free active sites:

R1: A(g) + * $\longleftrightarrow$ A*

R2: A* $\longleftrightarrow$ B*

R3: B* $\longleftrightarrow$ B(g) + *

R1 and R3 describe the elementary step of adsorption/desorption of A and B respectively. R2 describe the chemical reaction to the interconversion between A* and B*. Each step is characterized by a forward, k_i^+, and reverse, k_i^-, kinetic coefficient. They are linked to the thermodynamic constant, K_i, of each reaction through the relationship $K_i = k_i^+/k_i^-$. The corresponding rate for R1-R3 reactions can be written as function of these constants:

$$r_1 = k_1^+ P_A \theta_* - k_1^- \theta_A \tag{2.21}$$

$$r_2 = k_2^+ \theta_A - k_2^- \theta_B \tag{2.22}$$

$$r_3 = k_3^+ \theta_B - k_3^- P_B \theta_* \tag{2.23}$$

where P_i is the pressure of reactant i, θ_i is the coverage of the adsorbed reactant i and θ_* is the fraction of free sites in the surface. The number of active sites on the surface is constant, and the following balance is established:

$$\theta_* + \theta_A + \theta_B = 1 \tag{2.24}$$

The kinetic coefficients k_i^+ and k_i^- are obtained following the Transition State Theory (TST) of Eyring, Evans and Polanyi.[101,102] This theory postu-

lates that the reaction proceeds through an activated complex located at the top of the energy barrier between the reactants and products. This complex is the transition state. DFT calculations are used to calculate the energy barriers and the partition functions needed to solve the TST equations.

R1 reaction describes the adsorption/desorption of A molecule on a free site. The adsorption rate is calculated with the following equation:

$$r_{ads,A} = k_1^+ P_A \theta_* \tag{2.25}$$

$$k_1^+ = \frac{A_{cat}}{\sqrt{2\pi m_A k_B T}} S_0(T) \tag{2.26}$$

The adsorption constant, k_1^+, is calculated using the Hertz-Knudsen equation, where A_{cat} is the area of a free site; m_A is the mass of a single molecule A; k_B is the Boltzmann's constant; T the temperature of the reaction system; and $S_0(T)$ the sticking coefficient that in the most of the cases may be approximated to the unit. An equivalent equation would be used to calculate $r_{ads,B}$ and k_3^-. The reverse reaction, the desorption rate of the molecule A is calculated as:

$$r_{des,A} = k_1^- \theta_A \tag{2.27}$$

$$k_1^- = \frac{k_B T}{h} \frac{q_{des,A}^{\#}}{q_{A*}} e^{\frac{E_{ads,A}}{k_B T}} \tag{2.28}$$

where q_A and $q_{des,A}^{\#}$ are the partition function of the adsorbed molecule A and of the transition state for desorption process; h is the Planck constant and $E_{ads,A}$ the adsorption energy of the A molecule. $r_{desorp,B}$ and k_3^+ are calculated with equivalent reactions. The rate of the elementary step to the interconversion between A* and B* is written as:

$$r_{A^* \to B^*} = k_2^+ \theta_A - k_2^- \theta_B \tag{2.29}$$

$$k_2^+ = \frac{k_B T}{h} \frac{q_{A\#}^{\#}}{q_{A*}} e^{\frac{-E_a^+}{k_B T}} \tag{2.30}$$

In this equation $q_{A\#}$ is the partition function of the transition state to the interconversion between A* and B* and E_a is the activation energy, that is, the energy difference between the transition state and A*. For the reverse reaction the equivalent reaction is applied. There is consistence between thermodynamics and kinetics in all the reaction system so that

$$K_i = e^{\frac{-\Delta G}{k_B T}} = \frac{k_i^+}{k_i^-} \tag{2.31}$$

The total partition function of a molecule is defined as the product of the nuclear, electronic, vibrational, rotational and translational partition functions:

$$q = q_{nucl}\ q_{rot}\ q_{elec}\ q_{vib}\ q_{rot}\ q_{trans} \tag{2.32}$$

q_{nucl} and q_{rot} are simplified to the unit since they keep constant during reactions. In addition, for adsorbed species the rotational and vibrational partition functions are also simplified to the unity since the adsorbed molecules can not rotate or move. Therefore the partition function for adsorbed species is calculated as:

$$q_i = q_{vib,i} = \prod_i \frac{e^{-h\nu_i/2k_BT}}{1 - e^{-h\nu_i/k_BT}} \tag{2.33}$$

where ν_i is the vibrational frequency i. If ZPVE is added to the value of energy barriers, the partition function has the form:

$$q_i = q_{vib,i} = \prod_i \frac{1}{1 - e^{-h\nu_i/k_BT}} \tag{2.34}$$

for the calculation of $q^{\#}_{desorp,i}$ the rotational partition function, $q_{rot,i}$, and translational 2D partition function, $q^{2D}_{trans,i}$, have to be added:

$$q^{\#}_{des,i} = q_{vib,i}\ q_{rot,i}\ q^{2D}_{trans,i} \tag{2.35}$$

$$q_{rot,i} = \frac{1}{\sigma}\left(\frac{8\pi^2 k_B T}{h^2}\right)^{\frac{3}{2}} \sqrt{\pi I_A I_B I_C} \tag{2.36}$$

$$q^{2D}_{trans,i} = A\frac{2\pi m k_B T}{h^2} \tag{2.37}$$

Being σ the symmetry number and I_x the moment of inertia along the three spatial coordinates.

The differential equations for the variation of the coverage for each compound are expressed as the sum of the rate of each elementary step in which it is involved. The differential equations for the mass balance of reactants and products depend of the simulated system. The full set of equations can be solved numerically with a computer to obtain the complete solution, which describes the time dependent evolution of products and intermediates of the reaction. However, if we are only interested on the steady state some approximations can be applied:

- **The steady state approximation.** It is assumed that the steady state was reached and the coverage of all species is a constant value. Therefore, all the differential equations are equal to zero. A constant flow of reactants enter on the reactor leading a constant flow of products.

- **The *quasi-equilibrium* approximation.** One elementary step is considered the rate determining step (RDS) and all the others are assumed to be in equilibrium.

- **The irreversible step approximation.** It is a further approximation of the *quasi-equilibrium* approximation. In addition, the rate for the reverse reaction of one or several steps is set to zero.

The *quasi-equilibrium* approximation

In chapter 6 the *quasi-equilibrium* approximation approximation will be used to compare the catalytic activity of some Mo-based compounds. For the previous reaction scheme R1-R3 this approximation is applied in the following way:

Considering R2 as the RDS:

$$r_1 \cong 0 \; \theta_A = K_1 P_A \theta* \tag{2.38}$$

$$r_3 \cong 0 \; \theta_B = K_3^{-1} P_B \theta* \tag{2.39}$$

$$r = r_2 = k_2^+ \theta_A - k_2^- \theta_B = k_2^+ K_1 P_A \theta_* - \frac{1}{K_3} P_B \theta_* \tag{2.40}$$

and being $K_2 = k_1^+ / k_1^-$ and $K_T = K_1 K_2 K_3$, then

$$r = k_2^+ K_1 P_A \left(1 - \frac{P_B}{K_T P_A}\right) \theta_* \tag{2.41}$$

As for the principle of conservation of sites $\theta_A + \theta_B + \theta_* = 1$ using the Eq. 2.42 and 2.43 the fraction of free sites can be expressed as

$$\theta_* = \frac{1}{1 + P_A K_1 + P_B \frac{1}{K_3}} \tag{2.42}$$

With these equations we can express the overall reaction rate in function of equilibrium constants of the steps in *quasi-equilibrium*, the rate constant of RDS and pressure of reactants:

$$r = k_2^+ K_1 P_A \left(1 - \frac{P_B}{K_T P_A}\right) \frac{1}{1 + P_A K_1 + P_B \frac{1}{K_3}} \tag{2.43}$$

Chapter 3

The Formox™ process: selective methanol oxidation to formaldehyde

In this chapter I will explain the study of the selective methanol oxidation to formaldehyde catalyzed by molybdenum oxides, an industrial reaction known as Formox process. This was my first study of catalytic biomass conversion and thus, simple PBE functional was used. Methanol is the smallest oxygenated compound obtained from biomass, and its small size along with its small number of conformation does this molecule the ideal probe molecule to understand the behavior of molybdenum oxides in biomass reactions. This work was published in ChemSusChem journal.[103]

3.1 Introduction

Formaldehyde is an important precursor to many other materials and chemical compounds, it is predicted its production will exceed 52 million tonnes in 2017.[50] The most efficient industrial route to obtain formaldehyde is the oxidation of methanol, $CH_3OH(g) + \frac{1}{2}O_2 \rightarrow CH_2O + H_2O$, through the Formox process, where the catalyst is a mixture of MoO_3 and the iron molybdate $Fe_2(MoO_3)_4$. To obtain a high selectivity an excess of MoO_3 should be added to the reactor. The two phases are essential; some experimental studies have determined that the Fe content promotes the catalyst activity and the Mo-phase promote the selectivity,[56] but the exact role and their synergy are under discussion. In addition, the nature of the active site and its oxidation state also are unknown. The objective of the present work is to clarify these issues. There are many experimental works focused to solve these questions,[52–56] since remove the drawbacks of the process, as the catalyst stability,[104,105] is an important industrial challenge. Before the publication of this work there was not

previous theoretical studies about this reaction, but currently, another study was published.[65]

In this work, the reaction network for methanol oxidation catalyzed by different molybdenum oxides was calculated. In order to determine the influence of molybdenum oxidation state the reaction network was calculated on both α-MoO_3 and MoO_2. As model of α-MoO_3 the most stable (010) surface was used; it was claimed to be the responsible of the production of formaldehyde.[106] In oxygen-depleted environments, vacancies appear in the surface[107] changing the oxidation state of the molybdenum center. The reaction on these defects was also calculated by removing one surface terminal oxygen atom, O_t. These oxygens were reported to be responsible of oxygen depletion on the surface.[58,106] MoO_2 has a monoclinic structure similar to a distorted rutile. To simplify the analysis a rutile structure was used as model of this catalyst; this approximation was used previously with success.[108,109] The reactivity was calculated over the most stable plane (110). In oxygen environments the surface undercoordinated Mo centers, Mo_{cus}, are partially covered by oxygen atoms, and the reaction network was also calculated on this system. The slabs models of these systems are shown in Figure 3.1.

In addition, to determine the role of iron in the industrial catalyst, α-MoO_3(010) was doped with Fe atoms. Vacancy formation and reactant adsorption calculations were done to study the influence of iron atoms in activity and selectivity.

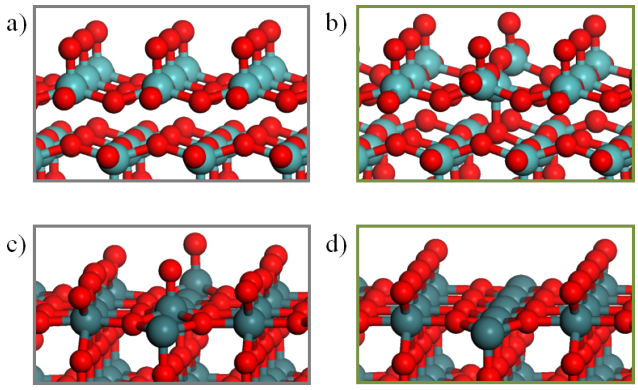

Figure 3.1: Slabs models used in the present study to represent MoO_3 and MoO_2 under aerobic, gray squares, and anaerobic, green squares, conditions. a) α-MoO_3(010) pristine surface. b) O_t defective α-MoO_{3-x}(010) surface. c) r-MoO_{2+x}(110) surface with O atoms adsorbed on Mo_{cus} position. d) Clean r-MoO_2(110) surface.

3.2 Description of the reaction path

For the analysis of activity and selectivity two reactions were studied, the methanol oxidation to formaldehyde (R1) and the further oxidation of

formaldehyde to carbon monoxide (R2):

R1: $CH_3OH + \frac{1}{2}O_2 \xrightarrow{MoO_x} CH_2O + H_2O$

R2: $CH_2O + \frac{1}{2}O_2 \xrightarrow{MoO_x} CO + H_2O$

In the mechanism calculated for R1 the methanol adsorption on catalyst surface is followed by the -OH dissociation by an acid-base pair. In the next step a surface oxygen breaks the C-H bond with the subsequent formation of formaldehyde, which afterwards desorbs:

R1.1: $CH_3OH(g) + * \longleftrightarrow CH_3OH*$

R1.2: $CH_3OH* + * \longleftrightarrow CH_3O* + OH*$

R1.3.A: $CH_3O* + OH* \longleftrightarrow CH_2O* + H_2O*$

R1.3.B: $CH_3O* + * \longleftrightarrow CH_2O* + OH*$

R1.4: $CH_2O* \longleftrightarrow CH_2O(g) + *$

This mechanism for the reaction catalyzed by α-MoO_3 was summarized by Tatibouët[110] and it is supported by several experimental evidences.[111–115] The mechanism for R2 starts with the formaldehyde adsorption and continues with two consecutive C-H bond breaking where the hydrogen atoms are transferred to surface oxygens:

R2.1: $CH_2O(g) + * \longleftrightarrow CH_2O*$

R2.2: $CH_2O* + * \longleftrightarrow CHO* + OH*$

R2.3: $CHO* + * \longleftrightarrow CO* + OH*$

R2.4: $CO* + * \longleftrightarrow CO(g) + *$

Alternatively HCO could also react with another hydroxy fragment to generate CO_2, but this possibility was not considered. The reaction paths for the reaction on the two oxides are shown in Figure 3.2 and 3.3.

During the reaction path, hydrogen atoms are stripped from methanol and formaldehyde by -O_t oxygens of the catalyst forming -O_tH* groups on the surface (R1.2, R1.3.B, R2.2 and R2.3). This is supported by the reported formation of hydroxylated surface in the form of a bronze (H_xMoO_3) during the reaction at temperature of 200^{o}C.[116] These hydroxyl groups recombine to form an adsorbed water molecule, H_2O_t*. Low energy barriers, around 0.7 eV, have been calculated for hydrogen diffusion on the surface. Alternatively, if the whole reactivity takes place on a unique reactive center and two hydrogen atoms are transferred to the same oxygen a water molecule is directly formed (R1.3.B). These water molecules are released from the surface forming a vacancy defect. This is a typical Mars-van Krevelen mechanism,[117] where a reaction product leaves the catalyst surface with some constituent of the catalyst's lattice. In addition, accordingly with the experiments, when there is

a high vacancy concentration on the surface, as in anaerobic experiments, instead of water, H_2 molecules are formed and released to recover the catalyst,[33] due the high energy necessary for to form two nearby vacancies.

For the catalyst recovery the surface vacancies should be healed. Under aerobic conditions O_2 molecules adsorb in vacancy positions very exothermically (-2.14 eV) regenerating the surface O_t. When oxygen is not present in the reaction media, the surface vacancies are healed by bulk oxygens,[106] process favored by the relatively high temperature of the experimental procedure. Experiments in anaerobic conditions have identified the formation of Mo^{4+} and Mo^{5+} bulk centers through X-ray photoelectron spectroscopy (XPS).[33] In addition, a diffusion path for the defects on α-MoO_3 that allows bulk oxygen transport through bulk vacancies with very small energy differences have been identified in the present work.

Kinetics experiments have assigned positive reaction order for methanol and oxygen and negative to water.[111,118,119] This is in agreement with our calculations since adsorption of methanol and oxygen is exothermic in all the systems and their presence favored the reaction. However, the presence of water inhibits the reaction because of water competes with oxygen for the adsorption on vacancy positions preventing a faster catalyst recovering.

3.3 Activity and selectivity

The reaction paths for R1 and R2 shown in Figure 3.2 and 3.3 were analyzed to determine the activity and selectivity towards formaldehyde production of the four catalytic systems. Adsorption energies of reactants, energy barriers for the hydrogen stripping steps, and the products desorption are taken into account in this analysis. To reach selectivity the adsorption energy of formaldehyde should be smaller than for methanol and smaller than C-H activation.[120]

The reaction path shown in Figure 3.2.a corresponds to the decomposition of methanol and formaldehyde in the pristine α-MoO_3(010) surface. The C-H activation and water desorption appears to be the most energy demanding steps, in agreement with experiments.[112,115] The ZPVE corrected activation energy for the methyl H abstraction is 0.92 eV, in good agreement with the apparent activation energy reported between 0.90 and 1.00 eV.[110,118] Low activity is predicted for this surface by two reasons: i) the high energy barrier for water desorption, which is a crucial step for recovery of the catalytic O_t centers; and ii) the methanol weak adsorption, which is in agreement with temperature programed desorption (TPD) experiments.[112] Therefore, high temperatures are needed to remove adsorbed water from the surface and reach a high catalytic activity. On the other hand, the selectivity towards formaldehyde production is expected on this surface. The adsorption of the formaldehyde is only -0.05 eV and thus, the high energy demanding first H abstraction can not compete with desorption. Moreover, the low coverage of methoxy

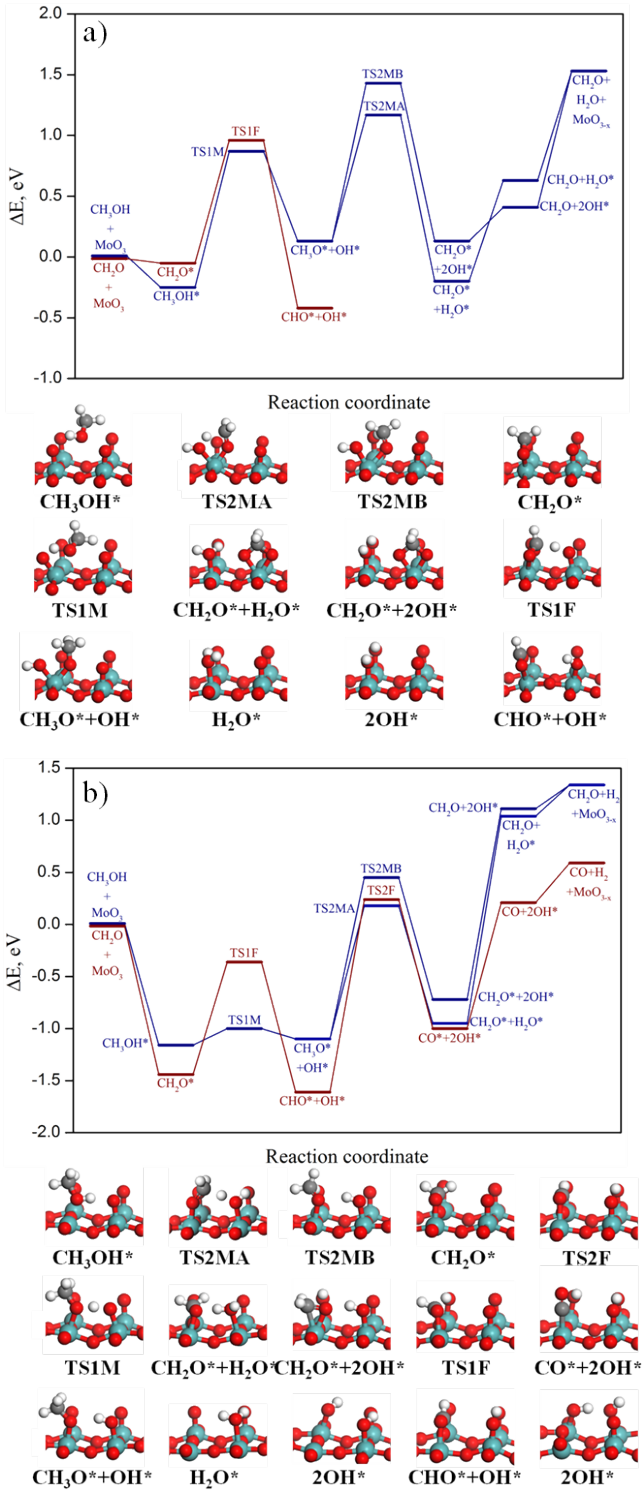

Figure 3.2: Reaction energy profile for the decomposition of methanol on a) α-$MoO_3(010)$ and b) Partially reduced α-$MoO_{3-x}(010)$.

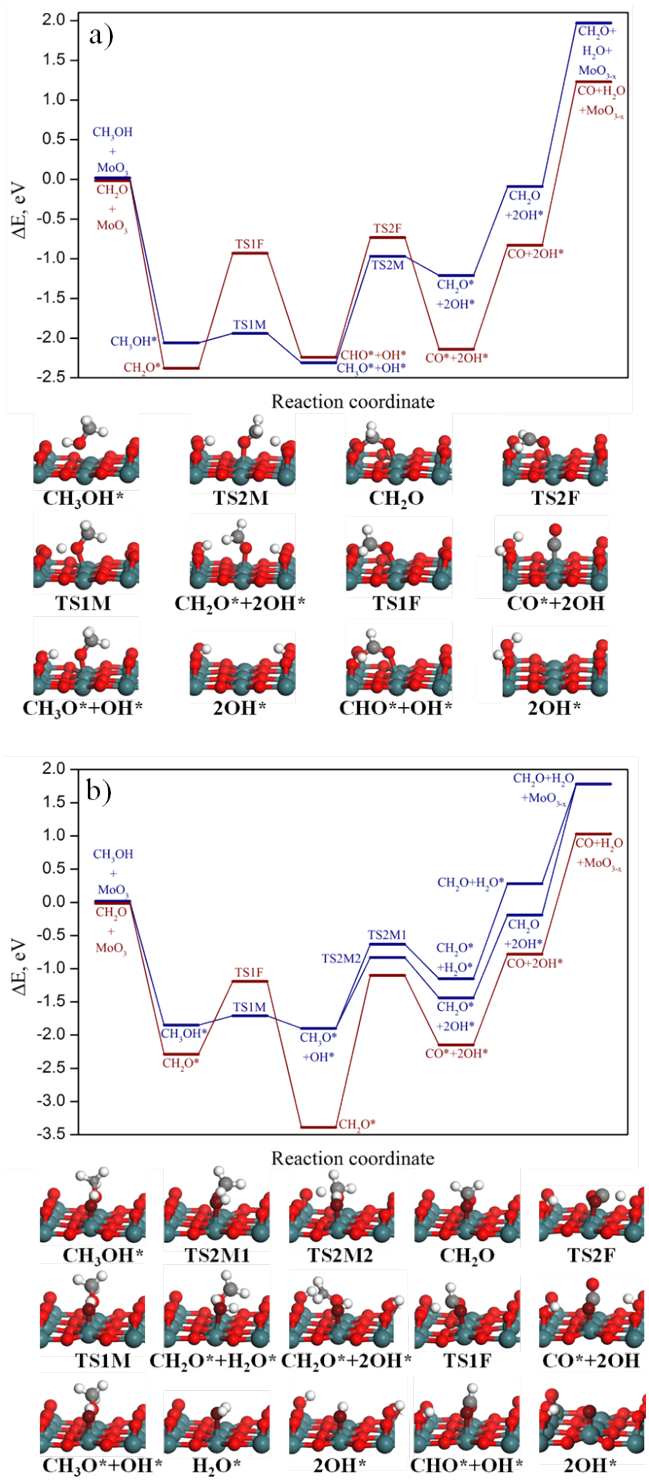

Figure 3.3: Reaction energy profile for the decomposition of methanol on a) r-MoO_2(110) and b) Partially oxygen covered in cus position r-MoO_{2+x}(110).

species induced by its endothermic adsorption energy avoids the formation of dimethyl ether.

Under anaerobic conditions, Figure 3.2.b, the reactants adsorb on vacancy positions strongly. The removal of hydroxyl groups from the surface either in the form of water or H_2 are a high energy demanding steps. Moreover, due the lack of oxygen in the system, the surface oxygens should be replaced by bulk lattice oxygens and this supply is limited a low temperature. Therefore, relevant activity is only expected at high temperatures; even so, it would be conditioned by the reduced availability of oxygen. The formaldehyde adsorption is strongly exothermic, even more than methanol adsorption, and the first H abstraction is an exothermic process with an energy barrier lower than the formaldehyde desorption. Therefore, a complete oxidation of methanol to CO is expected for this system.

The reaction path on r-MoO_2(110) both in stoichiometric and oxidized surface, Figure 3.3 a and b respectively, is very similar. Reactants and products are strongly adsorbed, being the most energy demanding steps the desorption of formaldehyde and water. These high values are the main drawback to the activity on these surfaces. The barriers for the oxidation of formaldehyde are lower than its desorption energy for both surfaces, and thus, selectivity is not expected on both MoO_2 surfaces.

These results are in agreement with experiments on both surfaces.[33] Oxidation of methanol was possible on MoO_3 and MoO_2 indicating that the requirement for the activity is the presence of Mo/O pairs, independently of the Mo oxidation state. However, the presence of a complete layer of Mo^{6+} centers is essential to ensure a selective reaction towards formaldehyde, which explain why the presence of an excess of O_2 in the system is essential. Molecular oxygen, in addition to act as an oxygen reservoir to recover the catalyst, competes with formaldehyde for adsorption on vacancy positions.

3.4 MoO_2/MoO_3

Experiments have shown as the catalytic behavior of MoO_2 changes completely in a second run and it resembles the performance of MoO_3.[33] XPS analysis of post reaction MoO_2 showed as its surface was completely oxidized to Mo^{6+} state. Previously, it had been reported that under reaction conditions MoO_2 can be oxidized to MoO_3 at temperatures above 300ºC.[121] In addition, the methanol conversion over this oxidized surface is higher than on MoO_3, which may be due the larger surface area of the MoO_2.

Due to the good performance of the oxidized surface over the MoO_2 bulk, the reaction on a MoO_3 layer on top of MoO_2 slab was studied. A monolayer of MoO_3(010) was placed over r-MoO_2(110) surface. The adhesion of this epitaxial layer was exothermic, -0.25 eVÅ^{-2}. The reaction path calculated

over this surface shows that the methanol conversion is feasible; however, it was not possible to reproduce the selectivity. This result indicates that a well developed MoO_3 surface structure is needed for an active and selective behavior.

3.5 The role of iron

The role of iron in the industrial formulation was also studied in this work. Both calculations of this work and previous experiments[33] have shown as the MoO_3 phase can catalyze selectively the reaction. However, the reaction profile of Figure 3.2.a shows a weak adsorption energy for methanol and high energy barriers for redox steps, C-H bond break and vacancies formation, which predict a low conversion of methanol on this surface. In addition, the presence of vacancies on the surface was demonstrated as detrimental for the formaldehyde selectivity, and therefore, the vacancy formation energy can be consider as a single descriptor of activity and selectivity for methanol decomposition.

The role of the iron was analyzed by the doping of the α-$MoO_3(010)$ surface. Two models were studied, in the first one a surface molybdenum was substituted by an iron and in the second one the substituted was a subsurface molybdenum. These two doped structures are almost isoenergetics. The vacancy formation energy, calculated for the formation of $\frac{1}{2}O_2$, and adsorption of methanol and formaldehyde was calculated for these models and compared with the native α-$MoO_3(010)$, see Figure 3.4.

Vacancy formation on the native surface is a process very endothermic,

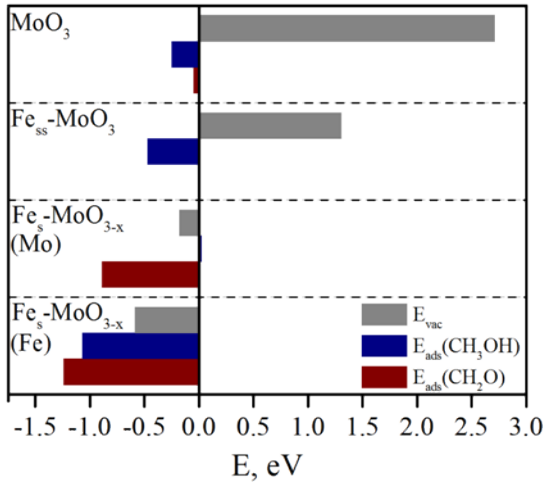

Figure 3.4: Vacancy formation energy to form $\frac{1}{2}O_2$, E_{vac}, and adsorption energy, E_{ads}, of methanol and formaldehyde on α-$MoO_3(010)$ clean and iron doped in subsurface, Fe_{ss}, and in surface, Fe_s. For Fe_s-MoO_3 the adsorption is on a vacancy position; between brackets the atom on which the vacancy is formed.

2.71 eV, but this energy is halved for the system with iron in subsurface, 1.30 eV. For the system with the iron placed on the surface this process turns exothermic, either the vacancy is formed on a Mo-O_t center, -0.18 eV, or on the Fe-O_t center, -0.59 eV. Therefore, if the iron is placed on the surface the vacancies are formed spontaneously, which is detrimental to the selectivity.

In pure α-$MoO_3(010)$ the vacancy formation leaves two additional electrons on the surface that are accepted by the molybdenum atom and in a lesser extent by the surrounding oxygen atoms, which reduce their distance to Mo. This generates a large rearrangement of the first coordination sphere of oxygen that results in a high vacancy formation energy. The vacancy formation in subsurface doped oxide is less energetic. The analysis of magnetization variation shows as iron accepts one electron since magnetization rises from 1.29 to 2.32 μ_B. Analysis of the density of states (DOS) leads to the same conclusion. Therefore, when a vacancy is formed on the doped surface, one electron is accepted by the Fe atom buffering the large oxygen rearrangement and favoring the vacancy formation.

Adsorption energies were calculated, therefore, on the pristine Fe_{ss}-$MoO_3(010)$ and in the defective Fe_s-$MoO_{3-x}(010)$ surface. For the last one, the molecules are adsorbed defective center, either on a Mo or on a Fe. The selectivity of the native surface is determined partially for the competitive adsorption of methanol and formaldehyde where both compounds are adsorbed weakly, -0.25 and -0.05 eV respectively. If the Fe dopant is in a subsurface position the adsorption energies are -0.47 and -0.01 eV for methanol and formaldehyde respectively, so the selectivity is even enhanced. However, if the Fe is placed on surface the selectivity disappears since the adsorption of formaldehyde is favored either on a Mo vacancy position, 0.02 versus -0.89 eV, or on a Fe vacancy position, -1.07 versus -1.24 eV.

Then, the best performance is obtained with iron atoms placed on the subsurface, see Figure 3.5, which increase the activity by the reduction of the energy cost of surface reduction and keeps the selectivity of the native surface. Conversely, iron atoms on surface force the presence of oxygen vacancies avoiding the selectivity. These results explain the experimental observations;[51] the presence of iron increases the overall activity, but the iron atoms on the catalyst surface decrease the selectivity, and this is the reason why an excess of MoO_3 is needed in the industrial formulation. Therefore, the active and selective phase is MoO_3 and the role of Fe atoms is to act as electron acceptor in redox steps, reducing the energy cost and increasing the activity.

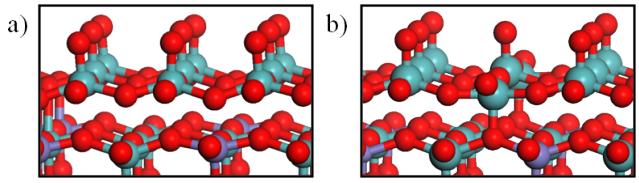

Figure 3.5: Doped Fe_{ss}-$MoO_3(010)$ surface. a) Clean surface. b) Defective surface.

3.6 Conclusions

The selective methanol oxidation towards formaldehyde on Mo-based oxides was studied by means of DFT. The reaction is possible on both Mo^{6+} and reduced centers, only the presence of the Mo/O pair is needed; and the catalytic activity is linked to fast the recovery of the catalyst forming vacancies, by water desorption, and healing them, either with environmental O_2 or bulk lattice oxygens. Differently, for a selective process the presence of reduced centers is detrimental, since formaldehyde adsorbs strongly on them. The role of iron oxide of the industrial Formox formulation was also rationalized by the study of the Fe doped α-MoO_3(010). Iron atoms in subsurface halves the energy cost to form a vacancy, which increases the activity, and enhances the selectivity. With Fe atoms in surface vacancies are formed spontaneously reducing the selectivity. Therefore, in the industrial catalyst MoO_3 is the catalytic phase, and the role of Fe atoms is to increase the activity by the reducing of reaction energy in redox steps. An excess of MoO_3 is needed to avoid the presence of Fe atoms in the catalyst surface, which is detrimental to selectivity.[†]

[†]A latter study of Choksi *et al.*[65] about the methanol oxidation on α-MoO_3 using the BEEF-vdW functional was published. They propose the same reaction pathway and found the same selectivity towards formaldehyde due the high energy difference between the first C-H scission on CH_2O* and the molecular desorption. As difference, they propose the vacancy positions as active and selective site, differently that is observed in experiments. Finally, they performed a microkinetic study, where the C-H bond cleavage of methanol was found as the rate determining step by the calculation of degree rate control.

Chapter 4

On the nature of oxygen vacancies on the α-MoO_3(010) surface through an optimized DFT+U method

This chapter is divided in two parts: i) the optimization of the U_{eff} for the PBE+U method, and ii) the study of the vacancy natur at the α-MoO_3(010) surface. Vacancies play an important role in the catalytic activity of MoO_3, and the correct characterization of them is essential. Searching in literature can be found studies with pure DFT or DFT+U approximation, for which several values of U_{eff} (from 2.0 to 8.6 eV) have been reported. Due to the scattered results obtained with the different U_{eff}, an in-depth optimization of U_{eff} was performed in this study. To date, there are no studies that describe correctly the vacancy nature on α-MoO_3(010). Only a recent study found the correct electronic states, but they are briefly described.[122] The manuscript of this work has been submitted.[123]

4.1 Introduction

In the last years, molybdenum oxides, mainly α-MoO_3, have become the catalyst of choice for a wide range of applications.[38,40,56] In addition to its catalytic properties, a wide range of chemical and physical applications have been reported for them.[49] The most of these properties are due to their redox properties, that can be fine-tuned by addition of cations,[124] hydrogen[125] or by oxygen removal.[126] Specifically, in catalyst, most of the reactions are carried out in the reduced oxide, being vancies the reactive center. The vacancy formation modifies the properties of the oxide, as two electrons are kept at the surface. The electrons could be either accommodate in one[127] or two[128] surface

cations, or even they could be delocalized.[129] Therefore, a characterization of the structural and electronic properties of the vacancies is essential to predict and to control the properties of the material.

This work is focused to the study of the nature of vacancies on the α-$MoO_3(010)$ surface; where is carried out the most of the catalytic reactivity with this oxide. This surface has three different types of oxygens bonded to one, two and three molybdenum centers. It is important to know which type of oxygen is removed during reduction and the electronic structure of the reduced surface, as they affect the catalytic properties of the oxide. Experimentally the formation of Mo^{5+} centers at low vacancy concentration has been observed, whereas at high vacancy concentration the formation of Mo^{4+} centers was also reported.[46,130]

Previously, pure DFT calculations have been performed to characterized the vacancy formation on MoO_3 where O_t and O_b were reported as the easiest oxygen to remove;[58,64,65] but the overdelocalization of the electrons by pure GGA functionals did not allow the assignment of the oxidation states. PBE+U calculations have also been performed for a scattered U_{eff} and they report either no localization,[62] or the formation of Mo^{4+} centers[58,72] after O_t removal. However, a recent study using an U_{eff}= 6.0 eV pointed out the formation of two different states after O_t removal, but no characterization was performed and low vacancy formation energies were reported.[122] The different U_{eff} results in a wide range of reaction energies and electron localization and so, the results are not comparable. Therefore, a more thorough investigation of the dependence of the chemical properties with U_{eff} is thus necessary.

In this work the U_{eff} was optimized by fitting with HSE06 and CCSD(T) benchmarks. PBE+U thus allow the correct description in terms of energy and electronic structure of the vacancy formation. The easiest oxygen to remove was identified and a detailed description and characterization of the formed vacancies was performed.

4.2 U_{eff} optimization

The effects of U_{eff}[71] in reaction energies and electron localization for calculations on α-MoO_3 were studied. The results were benchmarked with the hybrid HSE06[90] functional and the U_{eff} that gave better performance in terms of reaction energies and electron localization was chosen. The methanol oxidation to formaldehyde on $MoO_3(010)$ was used as example.[65,103] Finally, the performance of the optimized PBE+U and other DFT functionals was benchmarked with a reference value calculated with CCSD(T), a highly accurate calculation level, for the 1,3-propanediol oxidation to hydroxypropanal on the cluster Mo_3O_9.[131]

4.2.1 ΔE *vs* U_{eff} and HSE06 benchmarking

The following three reactions of the methanol oxidation to formaldehyde were considered for the analysis:

R1: $CH_3OH(g) \xrightarrow{\alpha-MoO_3} CH_3O^* + OH^*$

R2: $CH_3OH(g) \xrightarrow{\alpha-MoO_3} \frac{1}{2}CH_2O(g) + OH^*$

R3: $CH_3OH(g) \xrightarrow{\alpha-MoO_3} CH_2O(g) + 2OH^*$

R1 is the dissociative adsorption of methanol, and thus an acid-base reaction. R2 and R3, the formation of $\frac{1}{2}$formaldehyde and formaldehyde respectively, are redox process that leave one and two hydrogen on the surface, respectively, with the concomitant one and two-electrons surface reduction. In Figure 4.1, the reaction energy, ΔE, and electron localization are represented as function of U_{eff} for the range U_{eff}= 0-7.0 eV. For the acid base system, ΔE is almost constant and no magnetization is observed in all the U_{eff} range. However, the two redox reactions, R2 and R3, show a different behavior: ΔE keeps constant and no magnetization is observed until U_{eff}= 3.0 eV; for higher values ΔE decreases linearly with U_{eff} and the electron localization is close to 1 and 2 for R2 and R3, corresponding to a reduction of one and two Mo centers to Mo^{5+}. The linear regression of the energy shows as the slope depends on the number of electrons localized in the surface, in agreement with previous observations.[91] For U_{eff} between 3.0 and 7.0 eV ΔE decreases by 0.65 and 1.30 eV for R2 and R3 respectively, changing the thermodynamics of the system. These results display the dramatic consequences of to choose an incorrect U_{eff} value.

For the benchmark against the hybrid HSE06 functional single points on PBE+U at U_{eff}= 0, 3.5 and 7.0 eV geometries were performed. The results are shown in Figure 4.1. For R1 HSE06 gives ΔE between 0.43 and 0.54 eV, slightly higher than PBE+U in all U_{eff} range. For both redox systems HSE06 gives reaction energies similar to PBE with intermediate U_{eff} values. Instead, the PBE+U results with high U_{eff} are very different, even for structures optimized with U_{eff}=7.0 eV. For R2 and R3 a electron localization close to 1 and 2 was obtained respectively, since one and two Mo^{6+} were reduced to Mo^{5+}. Thus, intermediate values of U_{eff} should be used to fit the HSE06 reaction energies; and, a U_{eff} higher than 3.0 eV should be used to reproduce the correct electron localization. Therefore, in this analysis it was conclude that the better performance is obtained with U_{eff}= 3.5 eV, that fit both ΔE and electron localization of the more accurate HSE06 functional.

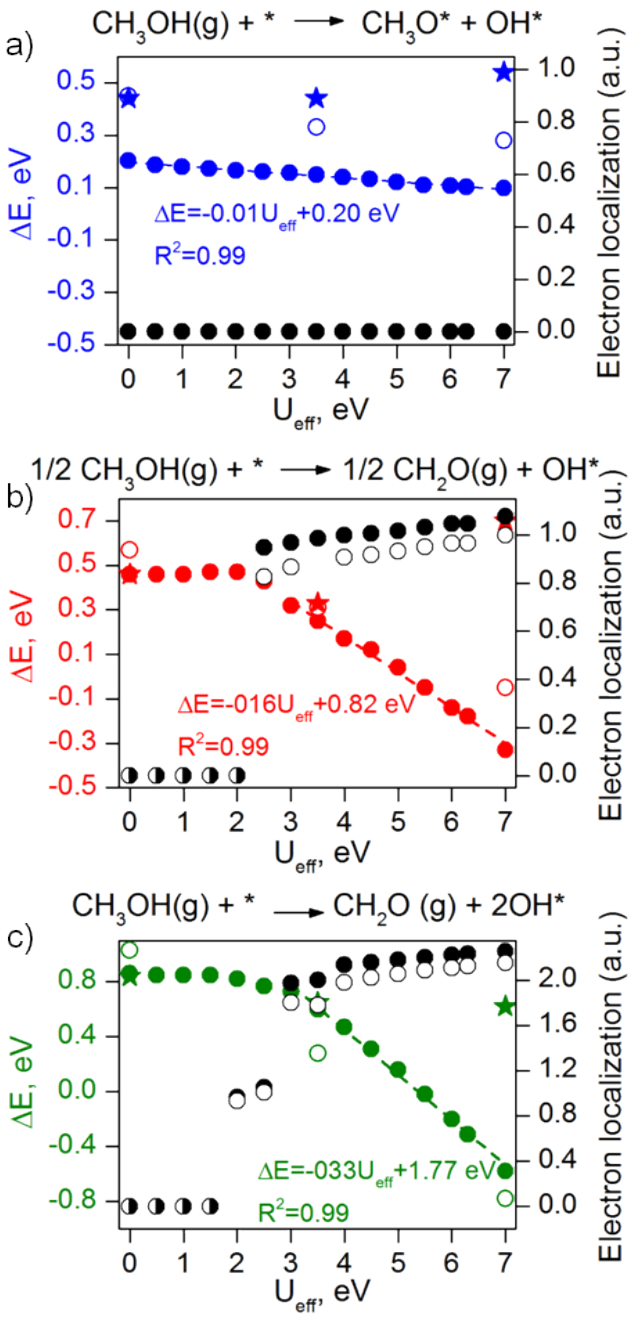

Figure 4.1: Reaction energy, ΔE, as function of U_{eff} for: a) acid-base dissociative adsorption of methanol, b) one electron reduction of the surface by de adsorption of one hydrogen atom, and c) two electron reduction of the surface for the addition of two hydrogen atoms. Colored filled circles are PBE+U values at 5×5×1 k-point sampling. Colored circles are PBE+U energies at Γ-point. Colored stars are HSE06 reaction energies calculated as single points at the corresponding PBE+U geometries. Electron localization: Black circles are the total magnetization and white circles the magnetization of reduced Mo centers.

4.2.2 CCSD(T) benchmarking

In addition, benchmark calculations for the 1,3-propanediol oxidation to hydroxypropanal on the cluster Mo_3O_9 were performed, see Figure 4.2. The CCSD(T)/aug-cc-pVDZ-pp reaction energy,[131] 1.00 eV, was used as reference. Calculations were performed for PBE, PBE+U, BEEF-vdW and HSE06 functionals. For PBE+U the above chosen U_{eff}= 3.5 eV and the most utilized, 6.3 eV, were assessed. In addition, a B3LYP/aug-cc-pVDZ-pp calculation was performed in Gaussian 09[132] . The best results are obtained with the hybrid functionals 1.05 and 1.11 eV for B3LYP and HSE06. PBE an BEEF-vdW overestimate ΔE by $\sim$0.25 eV. PBE+U with U_{eff}=3.5 eV leads to a good result of 1.13 eV, very similar to HSE06 again, and not far of CCSD(T). In contrast, PBE+U with U_{eff}=6.3 eV gives 0.66 eV.

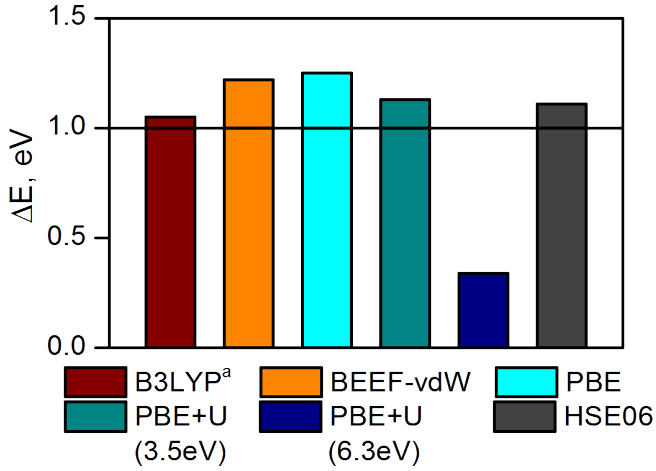

Figure 4.2: Reaction energy for $C_3O_2H_8$(g) + Mo_3O_9 $\rightarrow$ $C_3O_2H_6$ + $Mo_3O_9H_2$ with different functionals. The horizontal line marks the value for the CCSD(T)/aug-cc-pVDZ/aug-cc-pVDZ-pp method.[131] [a]B3LYP calculations were performed with Gaussian 09 software.[132]

With the previous analyses can be concluded that U_{eff}= 3.5 eV gives accurate results for reaction energies and electron localization. Conversely, the previous reported U_{eff}= 6.3 eV results in a larger error estimation of reaction energies.

4.3 Vacancies on MoO_3(010)

The three different oxygen (O_t, O_b, and O_{3c}) are exposed in the surface and could be removed in vacancy formation. Previous calculations with pure DFT reported O_t and O_b as the easiest oxygens to remove with similar vacancy formation energies. The optimized structures were very similar with one oxygen in an intermediate position.[58,64,65] However, in the PBE+U calculations of the present work, when the O_t is removed, the two neighboring O_b remain in

the surface plane. In addition, all the attempts to converge the O_b vacancy leaded to the displacement of the O_t to the O_b position, resulting in the same geometry of the O_t vacancy. For O_{3c} the calculated vacancy formation energy was around 1.80 eV higher than for O_t. Therefore, can be concluded that on the α-MoO_3(010) surface vacancies are exclusively produced in O_t positions.

4.3.1 Vacancies characterization

The vacancy formation leaves two electrons on the surface that are accomodated on the surface cations. For the O_t vacancy formation were isolated two different electronic states: either i) the two electrons are localized in two neighboring Mo centers along z axis that are reduced to Mo^{5+}: Mo^{5+}(□)-O-Mo^{5+}(=O); or ii) the two electrons are accommodate on the undercoordinated Mo center that is reduced to Mo^{4+}: Mo^{4+}(□), see Figure 4.3. For simplicity, the vacancies will be named as 2×Mo^{5+} and Mo^{4+}. Only a previous theoretical work had been reported the existence of these two states.[122] Other PBE+U studies have only reported the formation of the Mo^{4+},[58,72] or could not determine the oxidation state.[62] The coexistence of these two electronic states is in agreement with experiments.[46,130] The following analyses of the vacancies features were performed:

- **Density of states, DOS:**

  -2×Mo^{5+}: each electron is localized in a *d*-orbital of each reduced Mo, being lower in energy the *d*-orbital of the undercoordinated Mo, Figure 4.3.b.

  -Mo^{4+}: the two electrons are in *d*-orbitals of the undercoordinated Mo, Figure 4.3.c.

- **Mo-O bond distances:**

  -2×Mo^{5+}: the Mo-O bonds are shorter for the Mo^{5+}(□) center than in the pristine surface and longer for the Mo^{5+}(=O).

  -Mo^{4+}: the Mo-O plane-surface bonds are similar than for the pristine surface, only the bond with the O_{3c} of the sublayer is shortened.

- **Bader charges:**

  -Clean surface: 2.67 $|e^-|$.

  -2×Mo^{5+}: 2.48 $|e^-|$.

  -Mo^{4+}: 2.24 $|e^-|$.

- **Magnetization:**

  -2×Mo^{5+}: 0.96 μ_B for Mo^{5+}(□) and 0.83 μ_B for Mo^{5+}(=O).

  -Mo^{4+}: 1.70 μ_B.

These configurations can be identified as two polarons that localize two electrons in neighboring Mo centers, see Figure 4.3.b; and as a single dipolaron that localizes two electrons in the same Mo center, see Figure 4.3.c. The Raman fingerprint and XPS shifths was calculated for the pristine surface and the two vacancy electronic configurations. The differences in Raman vibrations[133,134] and the trends in XPS shifts[39,46,130] are in agreement with the experiments.

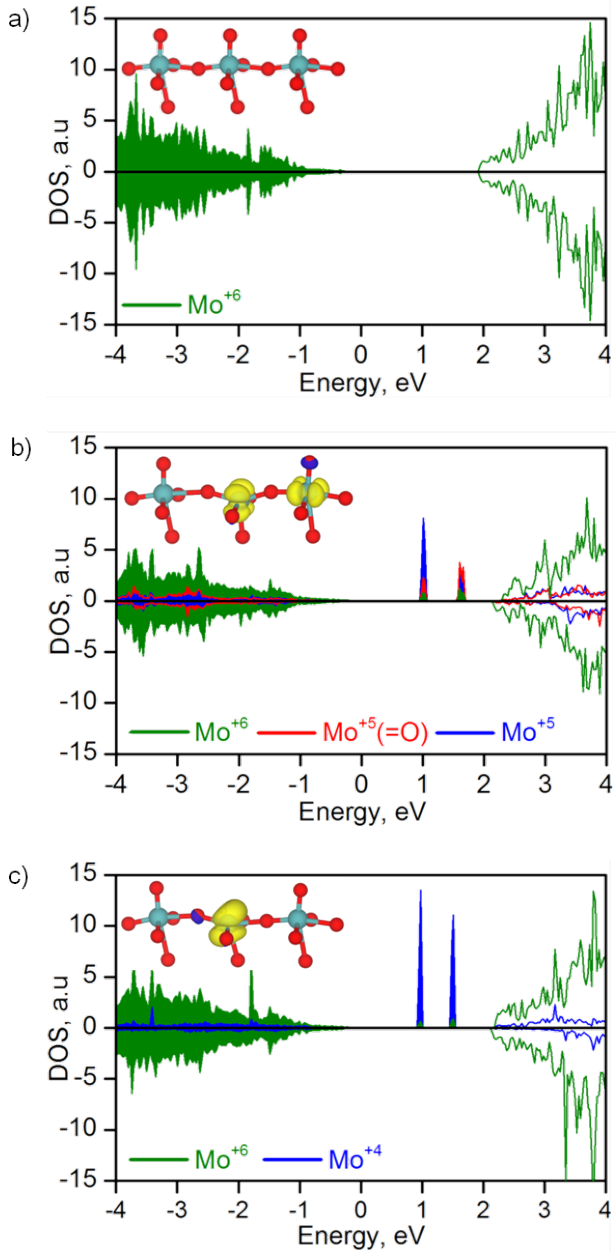

Figure 4.3: Density of states, DOS, and spin-density at $0.01|e^{-}|Å^{-3}$ for: a) pristine surface, b) $Mo^{5+}(\square)$-O-$Mo^{5+}(=O)$ vacancy, and c) $Mo^{4+}(\square)$ vacancy.

4.3.2 Energy differences between electronic configurations

It was found that the two electron configurations are close in energy, see Figure 4.4.a, being the 2×Mo^{5+} the most stable. Its vacancy formation energy for the reaction $MoO_3 \rightarrow \frac{1}{2}O_2 + MoO_{3-x}$ is 2.62 eV in the (3×3) supercell, 0.22 eV lower than for Mo^{4+}. In a (2×2) supercell the vacancy formation energy of the two polarons configuration is increased by 0.11 eV; whereas it remains almost constant for the single dipolaron configuration. Hybrid single points calculations results in higher vacancy formation energies, 2.82 and 3.18 eV for 2×Mo^{5+} in the (3×3) and (2×2) supercell, respectively. In the previous study with an U_{eff}=6.0 eV the reported formation energy was 1.51 eV, highlighting the importance of to use the correct U_{eff} value. The energy difference between the two configurations is increased to 0.35 eV in the higher cell whereas remain constant for the (2×2).

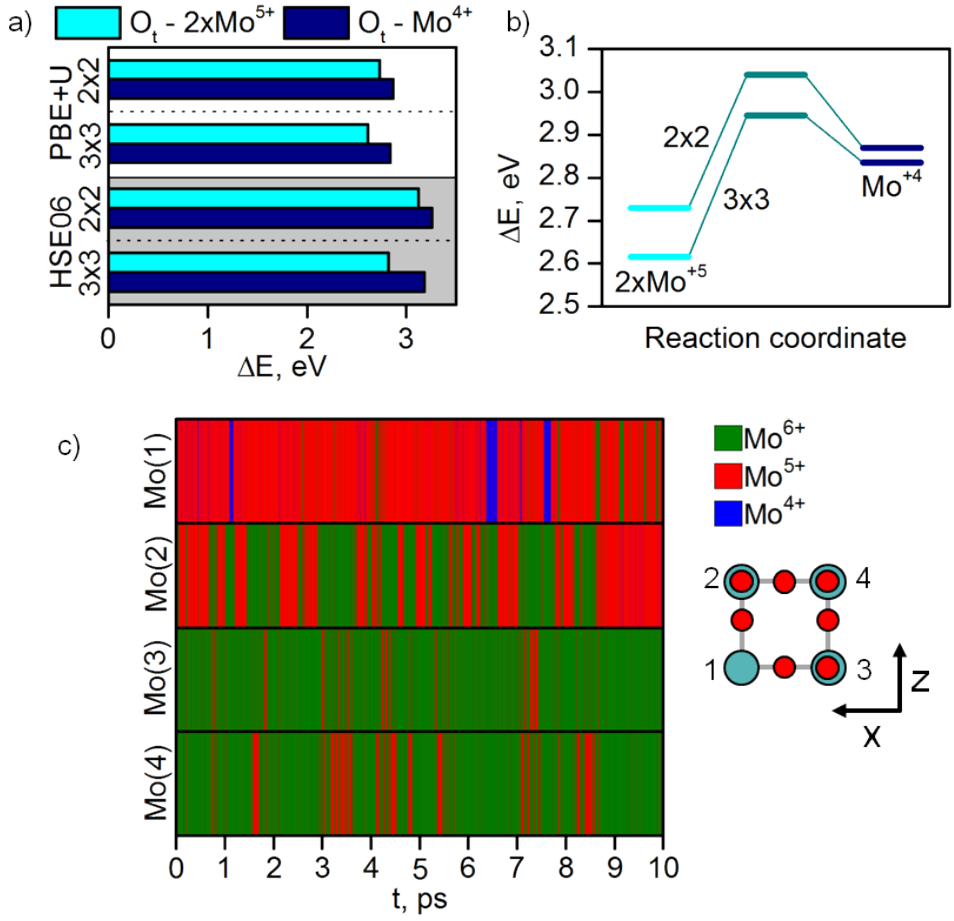

Figure 4.4: a) Vacancy formation energy, ΔE, according to the reaction $MoO_3 \rightarrow MoO_{3-x} + \frac{1}{2}O_2$(g) calculated on (2×2) and (3×3) supercells with PBE+U and HSE06 functionals. b) Energy profile of the electron hopping for the conversion 2×Mo^{5+} → Mo^{4+} on (2×2) and (3×3) supercells.

The energy barrier for the conversion between the two electronic states through electron hopping was calculated on the two supercells. Low energy barriers, ∼0.30 eV, were found for the two supercells, see Figure 4.4.b. This energy barrier is easily overcome at typical reaction temperatures, between 300 and 400ºC, and therefore, a thermodynamic equilibrium between the two electronic states is expected. For instance, at 300ºC the relative Boltzmann population at medium vacancy coverage is around 93:7 for Mo^{5+}:Mo^{4+}, in agreement with the quantification through XPS experiments at similar temperature.[130] A Molecular Dynamics, MD, trajectory of 10 ps for a vacancy coverage of θ_{vac}= 0.25 ML was simulated at 300ºC to illustrate the dynamic nature of the vacancy at reaction temperatures, see Figure 4.4.c. The undercoordinated Mo center has 5+ oxidation state almost all the time, sampling also Mo^{4+}. The second polaron is localized preferentially in the neighboring Mo along z axis. The less favorable localization for the polaron is the vicinal Mo along x axis.

In order to test the effects of electron configuration in the adsorption of molecules, methanol and formaldehyde were adsorbed in the two configurations. The adsorption of methanol was isoenergetic in the two configurations, -1.55 eV. However, the adsorption of formaldehyde is 0.23 eV stronger at the Mo^{4+} center. The two molecules interact differently with the surface: methanol only interacts with the Mo center but formaldehyde also forms a bond with a neighboring O_b. The strong of Mo-O bonds is different in the two configurations, explaining the different behavior in the formaldehyde adsorption.

4.3.3 Vacancy accumulation

The vacancy formation energy as function of the coverage was studied. On the one hand, the formation energy of 2×Mo^{5+} vacancies increases linearly with the vacancy coverage, Figure 4.6 a. In this configuration the two reduced Mo^{5+} are placed along the z axis, therefore the formation of two consecutive vacancy position along this axis is not possible. For high coverages, the formation of vacancies with the 2×Mo^{5+} configuration in alternative Mo positions along the z axis form a continuous row of Mo^{5+}. The formation of a vacancy in a consecutive position along the x axis, where the undercoordinated Mo share an O_{3c}, has an energy cost ∼0.35 eV higher than the formation on any other position. On the other hand, the vacancy formation energy of Mo^{4+} is constant until a vacancy coverage θ_{vac}= 0.5 ML, see Figure 4.5 a. The formation of a second vacancy along the z axis in the neighboring Mo center has the same energy cost as the first one. However, the formation of a consecutive vacancy along x axis has an energy cost ∼0.25 eV higher than in the any other positions. Therefore, for both 2×Mo^{5+} and Mo^{4+} electronic configurations the accumulation of vacancies along x axis is avoided, which results in the formation of Magnéli phases (crystal shears).[126] This analysis is in agreement with the MD simulation The quantification of each Mo^{n+} species on the surface

for different coverage was performed for the Boltzmann distribution at 350 ºC and represented as XPS, Figure 4.5 b.

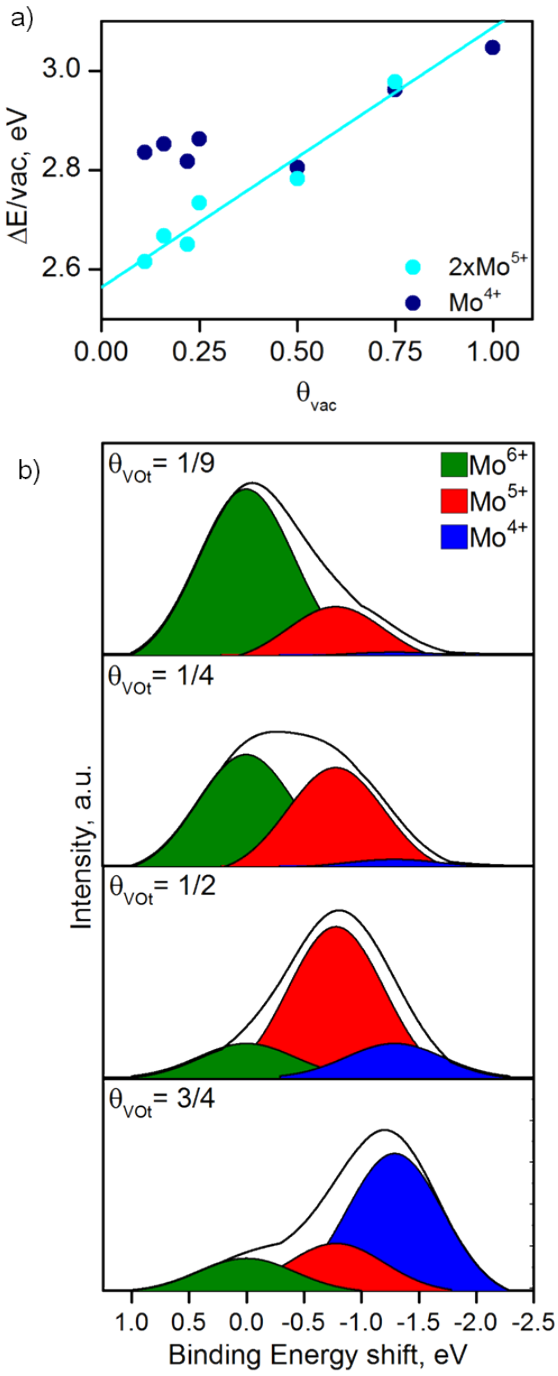

Figure 4.5: a) Average vacancy formation energy of the most stable configuration as function of the coverage, θ_{vac} in ML. b) Calculated XPS at different θ_{vac} at 350 ºC.

4.4 Conclusions

In this work the vacancy formation on α-MoO_3(010) was studied through PBE+U. The U_{eff} was previously optimized to 3.5 eV by fitting with the HSE06 hybrid functional and CCSD(T). This value resulted in accurate reaction energies an electron localization. HSE06 and CCSD(T) benchmarks show that the previously most used value, U_{eff}=6.3 eV, strongly underestimates the reaction energies. Using this optimized value was found that on α-MoO_3(010) surface vacancies are only produced in O_t positions. The formation of vacancies reduces the surface in two different ways: i) forming two Mo^{5+} polarons in the undercoordinated Mo and in a neighboring Mo center; and ii) forming a single Mo^{4+} dipolaron in the undercoordinated Mo. The two configurations are close in energy, with the double polaron more stable by 0.22 eV at low coverage. The conversion between the two electronic states through an electron hopping has a low barrier of $\sim$0.30 eV that can be overcome easily at typical reaction temperatures. It was shown that the electronic configuration can be effects in adsorption energy of molecules. Moreover, the coverage influence was studied, and a inversion of stability at high coverages was found. Finaly, the formation of Magnéli phases could be explained by the impossibility of the vacancy accumulation through x axis.

UNIVERSITAT ROVIRA I VIRGILI
MOLYBDENUM OXIDES AS CATALYST FOR BIOMASS-DERIVED COMPOUNDS: A THEORETICAL APPROACH
Marcos Rellán Piñeiro

Chapter 5

Propylene production from glycerol: a first principles study of hydrodeoxygenation (HDO) process on MoO_{3-x}

In the present chapter I will explain the reduction of glycerol to propylene, an attractive reaction for the biomass upgrading. This conversion is produced through a hydrodeoxygenation, HDO, process. In this catalytic process the hydrocarbons are selectively deoxygenated whereas their carbon chain is maintained. This is an interesting catalytic process since adding H_2 to the system the molecular oxygens are eliminated in the form of water, being therefore, an environmental friendly process. The selected compound is the glycerol, a molecule with three carbons and three hydroxyl groups, which is transformed to propylene through a complex reaction network. In addition to be a good example of HDO, this reaction is important by itself because of the overproduction of glycerol and the forecasted shortage in propylene supply. In this work the DFT+U method developed in the previous chapter is used. The manuscript of this work is under preparation.

5.1 Introduction

Biomass is a complex material and includes a wide range oxygenated as alcohols, aldehydes, ketones, carboxylic acids and phenols.[135] Therefore, the preferential C-O bond cleavage over the other bonds C-C and C-H is a must to the upgrading of these molecules. In this direction one of the most viable processes to reduce the oxygen content, is hydrodeoxygenation, HDO,[136–138] that achieves the reduction of the oxygen content in biomass-derived molecules by its reaction with H_2 at high temperatures, producing water as side prod-

uct. Therefore, HDO is a green process that allow to obtain key chemical intermediates from biomass-derived compounds.

Potential HDO catalysts include noble (Pd, Pt, Ru, Ag and Rh)[139–144] and non-noble metals (Cu and Ni),[145,146] molybdenum sulfides and carbides.[147–149] More recently, metal oxides have also been proposed. For instance, molybdenum oxides showed good selectivity in HDO of alcohols,[150–152] linear ketones and cyclic ethers to produce olefins and cyclic ketones and phenols to form aromatic hydrocarbons.[19,38] In these reactions, α-MoO_3 presents a preferential C-O bond cleavage pattern leading the formation of hydrocarbons and olefins while keeping of the carbon chain.

Among the biomass derivatives glycerol plays an important role since it is a by-product in the transesterification of vegetal oils for biodiesel production. Around 10 tonnes are produced per 100 tonnes of biodiesel.[153] Due the increase in biodiesel production, glycerol is an abundant and cheap compound,[154] and finding new efficient and environmental friendly routes to transform it in most valuable compounds is a challenging industrial target. Therefore, it was included as one of the top twelve building blocks by DOE.[8,155] The deoxygenation of glycerol can be a source for propanediols and propanols and more interestingly propylene. Propylene is the precursor to polypropylene, acrylonitrile, propylene oxide, oxo-alcohols, cumene, isopropyl alcohol, and others.[156] The current propylene production is around 90 million tons and it is forecasted to grow up to 130 million tonnes worldwide by 2023.[157] Nowadays, it is mainly obtained as by-product of naphtha steam cracking,[156] but the emergence of shale-gas feedstocks will likely produce a shortage in the next years in particular geographical areas, mainly in US. Therefore, an on-purpose technology for propylene production is and attractive industrial target and its production from glycerol remains a promising route.

The production of propylene from glycerol was first reported in a two-steps system using Ir/ZrO2 to catalyze the glycerol hydrogenolysis to 1-propanol, and H-ZSM-5 to catalyze its dehydration to propylene.[158] The conversion in one-step catalyzed by molybdenum oxide, Mo/C, and iron molybdate, Fe-Mo/C, was reported both in gas[159] and liquid-phase.[40] The conversion in gas-phase can reach 100% with 90% of selectivity. The reaction pathway was studied and the path through acetol, propylene glycol, acetone and 2-propanol was proposed.[160] In liquid-phase the reported conversion on Mo/C was 70% with 70% of selectivity. The main by-products were C3 compounds: 2-propenol, 1-propanol and propylene glycol, 2-propanol, acetol and 1,2-propanediol. A small portion, 2.5%, of C2 and C1 compounds were also obtained: methanol, ethanol and ethylene glycol. The studied reaction pathway suggested propylene is formed via 2-propenol, with 1- and 2-propanol dehydration as secondary routes.[130]

For a complete rationalization of HDO processes first principles studies are needed, but only a small number of studies have been reported. The mechanism for alcohols dehydration[150,151] and HDO for acrolein to propylene[161]

were studied on $(MoO_3)_3$ cluster models, which cannot reproduce the bulk properties giving incorrect kinetic and thermodynamic parameters. Moreover, two studies were performed on α-MoO_3(010) surface using periodic slab models: the HDO of acetaldehyde[64] and acetone.[66] The vacancy formation and the HDO mechanism were reported in both studies. They were performed with pure DFT that, as we have seen in Chapter 4, produces incorrect estimations of reaction energies and activation barriers.[123]

In this work, Density Functional Theory has been employed to unravel the mechanism for the conversion of glycerol to propylene on α-MoO_3(010) representing molybdenum oxide. The reaction energies and activation barriers were computed for all the elementary steps of the reaction network. The mechanism for hydrogen adsorption and vacancy formation was also studied.

5.2 Computational methods

Density Functional Theory (DFT) calculations performed on slab models with the VASP 5.3.3 package[162,163] were employed to obtain the thermodynamic and kinetic parameters for the reactions. The generalized gradient approximation (GGA) in the form of the Perdew-Burke-Ernzerhof (PBE) functional[83] was chosen to describe the exchange correlation energy. To introduce the van der Waals contributions the Grimme's semiempiric correction vdW-D2[73] was used. The core electrons were replaced by the projector-augmented wave (PAW) pseudopotentials;[95] and, the valence electrons were expanded in plane-waves with a kinetic cut-off energy of 450 eV. The Hubbard U[71] correction was applied to describe the $4d$ electrons of molybdenum atoms with an U_{eff}= 3.5 eV.

The HDO process was studied on the (010) surface, Figure 5.1, the lowest energy facet of α-MoO_3. This surface model was previously used to study oxidation to formaldehyde[65,103] and the HDO of acetaldehyde[64] and acetone.[66] The fully oxidized surface can only perform acid-base reactivity but the HDO process involves redox steps, therefore, a reduced Mo center is needed for the reaction to occur.[38] Molybdenum oxides accommodate a certain degree of reduction and out of the oxygens in the lattice, the O_t are the easiest to remove.[58,64,72,123] These vacancy positions are the preferential adsorption sites for oxygenated intermediates.

The α-MoO_3(010) surface was represented with a slab model contained two bilayers in a (3×3) supercell with a 3×3×1 k-point sampling. The upper bilayer and the adsorbates were allowed to relax. A vacuum gap of 15 Å between slabs and a dipole correction along z-axis were added to avoid the interaction between slabs and the spurious terms arising from the use of asymmetric arrangement of the slabs.[97] The reaction network was studied in this slab model with one O_t defect simulating surface reduction, Figure 5.1. The corresponding undercoorditaed molybdenum center is labeled as Mo_{cus}. The transition states

were located with the climbing image version of the nudge elastic band (CI-NEB) method[98–100] and refined with the improved dimer method.[164,165] All relevant configurations in the potential energy surface were confirmed through vibrational analysis and the reported energies are ZPVE corrected.

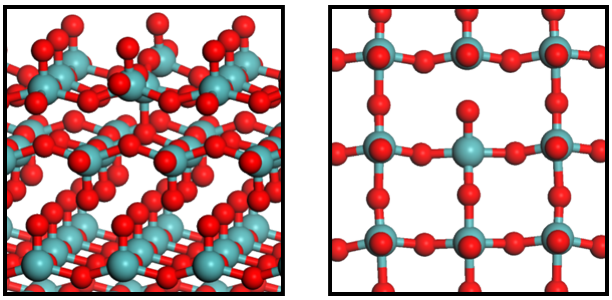

Figure 5.1: Side and top views of the reduced α-MoO_3(010) surface used as catalyst. Green atoms represent Mo, red stand for O.

5.3 Results and discussion

HDO processes are composed by two combined cycles: i) the hydrogen adsorption and vacancy formation through water formation and release; and ii) adsorption and deoxygenation of hydrocarbonated compounds on vacancy a position. The second one heals the vacancy and closes the catalytic cycle. The two cycles were studied in this work. Experimentally, a pre-reduction of the catalyst with H_2 is carried out to form defects on the surface.[19,40] Moreover, the presence H_2 in the reaction media is essential to maintain the catalytic activity.[19,40]

5.3.1 Vacancy formation and hydrogen migration

Hydrogen molecules dissociatively adsorb forming two -OH groups that can be either two terminal -O_tH groups, with an energy barrier for the adsorption of 1.63 eV, or one -O_tH and one -O_bH group, with an energy barrier of 1.46 eV, see Table 5.1. The adsorption energies for the two configurations are -0.60 and -0.69 eV respectively. Once the -OH groups are created the hydrogen atoms can be transferred from a hydroxyl group to a neighboring surface oxygen and diffuse over the surface with relatively low energy barriers, *ca.* ∼0.4-0.8 eV, see Table 5.1.

The formation of water molecules by the recombination of two neighboring -OH groups has low energy barriers: 0.14 and 0.22 eV for the recombination from two -O_tH and from one -O_tH+-O_bH, respectively. Thus, H_2O_t molecules binding to the Mo center are formed at catalyst surface. The energy needed for water molecules to desorb is 1.22 eV, and therefore, they are released under reaction conditions. The reaction energy for the total process is only

Table 5.1: Adsorption energies, E_{ads} in eV, of H_2 molecules, using as reference clean surface and gas-phase H_2 molecule, and energy barriers, E_a in eV, for H_2 adsorption and proton diffusion on the surface.

Adsorption		**Diffusion**	
Site/Path	$\mathbf{E_{ads}/E_a}$	**Path**	$\mathbf{E_a}$
$H_2 \rightarrow O_tH{+}O_tH$	1.63	$O_tH(a) \rightarrow O_tH(b)$	0.40
$H_2 \rightarrow O_tH{+}O_bH$	1.46	$O_bH \rightarrow O_tH$	0.77
$O_tH{+}O_tH$	-0.60	$2O_tH \rightarrow H_2O_t$	0.14
$O_tH{+}O_tH$	-0.69	$O_bH{+}O_tH \rightarrow H_2O_t$	0.22
H_2O_t	-0.92		
V_{Ot}	0.30		

0.30 eV. The highest energy barrier was founded for the hydrogen adsorption, which explains why high hydrogen pressure is needed to obtain high reactant conversion.

5.3.2 HDO network

The decomposition of glycerol in HDO process comprises a competition between sequential and parallel dehydrations, keto-enol equilibra, and hydrogenations that are grouped in the reaction network presented in Figure 5.2. General mechanisms for each process are shown in Figure 5.3.

The first step in HDO is glycerol dehydration to form the corresponding alkenol. For this step we follow the mechanism proposed previously for the dehydration of alcohols in molybdenum oxides,[151]Figure 5.3.a. Glycerol adsorbs on a vacancy site through one of its oxygens forming a Mo-O bond. After that, the hydroxyl proton is transferred to a terminal oxygen forming an $-O_tH$ group. Then, in a concerted step, a β-hydrogen is stripped by a O_b and concomitantly the C-O bond breaks. This step involves the formation of the C=C double bond of the alkenol.

As glycerol has two different OH types, adsorption by the terminal OH triggers the formation of 1,2-Enol whereas the secondary hydroxyl would drive the formation of 1,3-Enol. The enolates formed are in equilibrium with their keto tautomer, acetol, and hydroxypropanal (HP), respectively. These equilibria are thermodynamically displaced towards the keto form by -0.65 eV to acetol and -0.15 eV to HP. The mechanism of the keto-enol interconversion is shown in Figure 5.3.b. The first elementary step in tautomeric isomerization is the enolate adsorption on vacancy positions. They adsorbs through their enolic –OH group that interacts with the undercoordinated Mo center. Then, the –OH group dissociates transferring a hydrogen atom to an O_t. Finally, the hydrogen of -OtH group is transferred either to the methylene group ($H_2C=$) of the 1,2-Enol to form acetol, or to methine group (=CH-) of the 1,3-Enol to

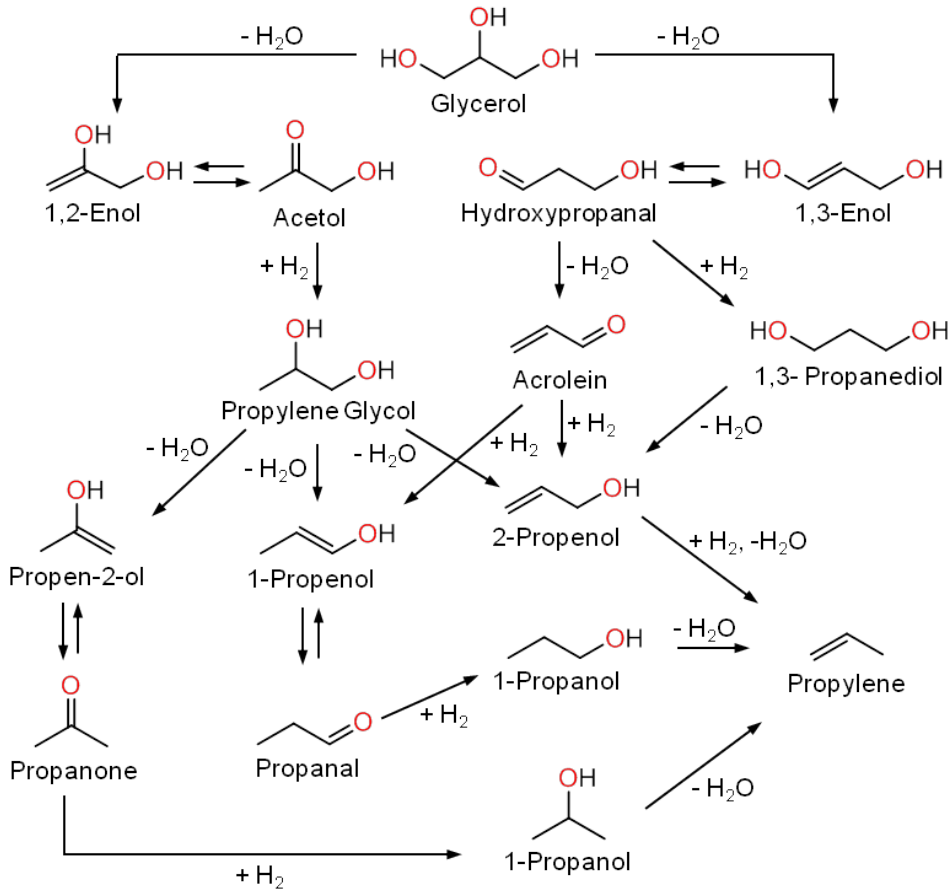

Figure 5.2: Reaction network for the complete hydrodeoxygenation, HDO, of glycerol to propylene. Double arrows indicate keto-enolic equilibria.

form HP. After that, the ketones can either desorb or remain bonded to the vacancy to react further.

In the next step, acetol and HP are hydrogenated to form propylene glycol (PG) and 1,3-propanediol, respectively. The mechanism for these hydrogenations is shown in Figure 5.3.c. Acetol and HP adsorb on undercoordinated Mo site through the ketone group and a hydrogen atom is transferred from a neighboring -O_tH group to the carbon atom of the ketone group to form a deprotonated diol. These diols could be protonated by other surface hydroxyls, and desorb or experiment further dehydration. In parallel, HP could suffer another dehydration to form acrolein repeating the steps described previously. This is not possible for acetol because its -OH group does not have any β-hydrogens to be stripped off.

The PG and 1,3-propanediol adsorption on Mo_{cus} can result in further dehydrations. PG adsorption trough its primary hydroxyl group leads the dehydration to propen-2-ol, whereas the adsorption through the secondary hydroxyl results in the dehydration to either 1-propenol, if during the reaction the β-

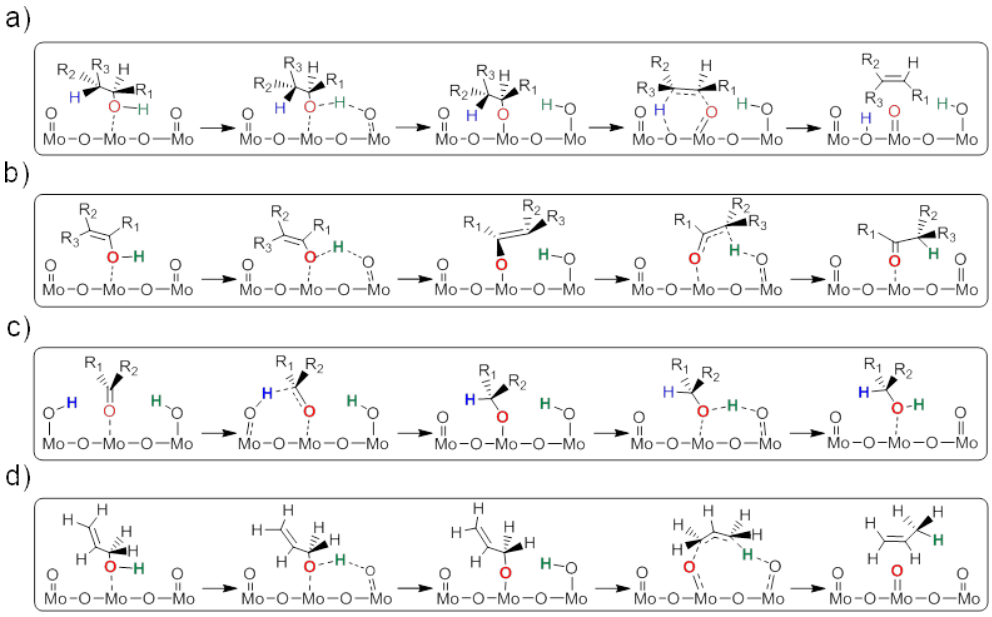

Figure 5.3: Reaction mechanism of the reactions in reaction network. a) Dehydration, b) keto-enol equilibrium, c) hydrogenation, and d) 2-propenol conversion to propylene.

hydrogen of C_1 is transferred to the surface; or 2-propenol, if the β-hydrogen of C_3 is stripped. 1,3-propanediol dehydration only can result in 2-propenol. Acrolein is hydrogenated either at the ketonic carbon to form 2-propenol, like 1,3-propanediol, or at the methylene carbon to form 1-propenol. Propen-2-ol and 1-propenol are enolates and therefore they are in equilibrium with the corresponding keto tautomer: propanone and propanal respectively. The keto tautomers, propanone and propanal, are more stable than the corresponding enol form by -0.53 and -0.35 eV, respectively.

In turn, propanone and propanal adsorbed at Mo_{cus} are hydrogenated to 2-propanol and 1-propanol respectively. These two compounds are dehydrated on the vacancy position to form the final product: propylene. 2-propenol adsorption on under-coordinated Mo also leads to propylene. The molecule adsorbs though the –OH group, which is dissociated by an $-O_t$ forming a surface hydroxyl. Then, the hydrogen is transferred back from the surface hydroxyl to the methylene group ($H_2C=$) of the adsorbed 2-propenol at the same time that C-O bond breaks results in the propylene physisorbed on the surface. A similar mechanism to the formation of propylene from 2-propenol on Mo_3O_9 cluster has been proposed previously.[161]

Reaction and activation energies for each elemental reaction step in glycerol HDO are shown in Figure 5.4. An analysis of the data shows and alcohol deprotonations are always endothermic steps with energy barriers lower than 0.75 eV. The C-O bond breaking steps in hydrogenations are slightly endothermic with a high energy barriers, between 1.00 and 1.50 eV. The formation of

C-H bonds in keto-enol equilibria are highly exothermic steps with a very low energy barrier. Finally, the C-H formation in hydrogenations are slightly endothermic steps with similar energy barriers as C-O bond breaking.The reported experimental temperature is 300ºC,[40,130] high enough to ensure that the barriers can be overcome

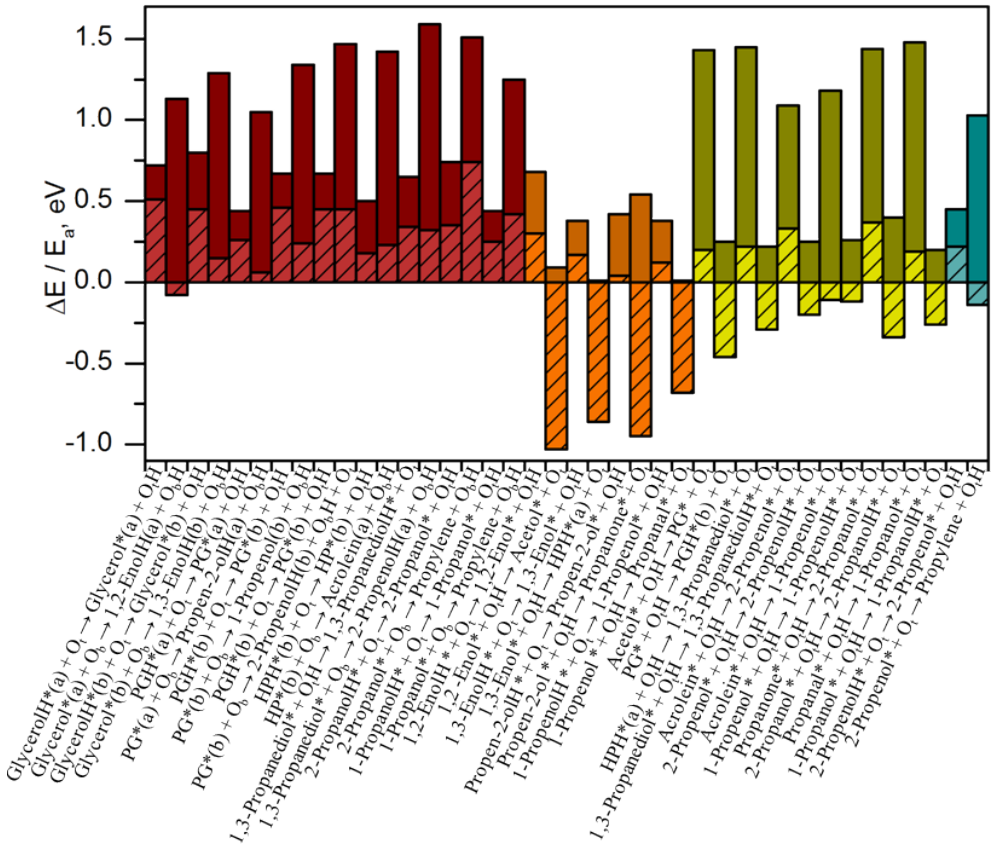

Figure 5.4: Reaction energy, ΔE (striped bars), and activation energy, E_a (plain bars), for all direct elementary steps of the reaction network. Wine color bars correspond to dehydration reactions, orange bars to keto-enol equilibrium, yellow bars to hydrogenation reactions and turquois bars to 2-propenol-Propylene reaction. All the energies are in eV.

5.3.3 C-C bond cleavage

The fact that C-O bond breaking prevails does not completely overrule C-C bond cleavage. Indeed some methanol, ethanol and ethylene glycol (EG) were detected as minor reaction products, about 2.5% in total, for the reaction catalyzed by the iron molybdate catalyst.[40] Ethylene glycol and ethanol could be produced from C-C bond cleavage in glycerol and propylene glycol respectively, which also gives methanol in both cases by the pathway showed in Figure 5.5.

For to take place the reactions proposed in Figure 5.5 glycerol and PG have to be bonded to two neighboring Mo_{cus} through the two hydroxyl groups of the broken C-C bond. The two reduced Mo act as electron buffer allowing the bond breaking. The formation of a neighboring vacancy along z axis has not an extra formation energy[123] and, therefore, at medium vacancy coverage they appear. Then, glycerol and PG can adsorb directly to two undercoordinated $(Mo_{cus})_2$ centers through two OH groups. Once the molecules are adsorbed they are dissociated easily forming two -OH_t groups and two Mo-O covalent bonds with the surface. In this step each Mo_{cus} is one-electron oxidized. The adsorption energy for the dissociated molecules are -2.37 and -2.43 eV for glycerol and PG respectively. The dissociated glycerol double bonded to $(Mo_{cus})_2$ can undergo the C-C bond breaking that results in the formation of a ketone group in each fragment and the one-electron reduction of the Mo_{cus} centers leading the formation of of glycoaldehyde (GA) and formaldehyde. The energy barrier for this step is 1.66 eV. The same elementary step can occur for PG with an activation energy of 1.65 eV, and resulting in the formation of formaldehyde again and acetaldehyde (AA). These compounds are further hydrogenated to methanol, EG, and ethylene.

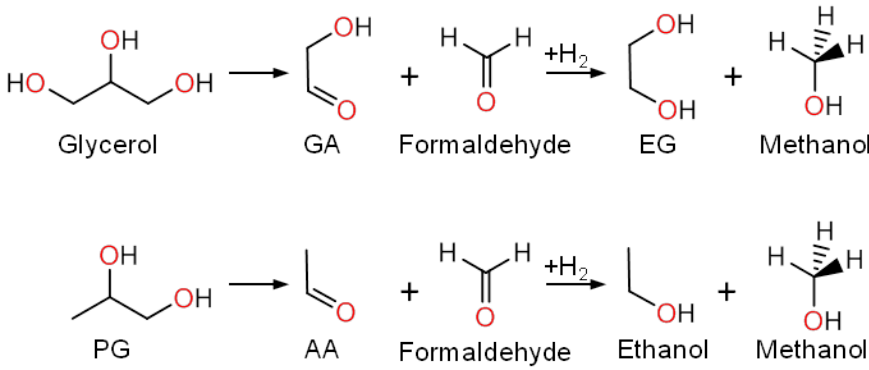

Figure 5.5: Reaction for C-C bond cleavage in glycerol and PG for the formation of methanol, ethanol and ethylene glycol.

The high energy barrier calculated for the C-C bond cleavage and the necessity of two neighboring empty vacancies explain the selectivity to three-carbon products observed experimentally. In the reaction network there are no more compounds with -OH groups in adjacent carbons and, therefore, these are the only one and two-carbon formed products.

5.4 Conclusions

The glycerol conversion to formaldehyde catalyzed by MoO_3 was studied by means of density functional theory, DFT. The conversion is produced through a hydrodeoxygenation, HDO, process that takes place on surface vacancy defects. The highest energy barrier in the vacancy formation cycle is the hydro-

gen dissociative adsorption. This explains why high H_2 pressure is needed in experiments. The adsorbed hydrogen atoms can move over the surface with low energy barriers and to form water molecules that are released. Vacancies play a central role in the HDO process. Oxygenated compounds adsorb on surface through Mo-O bond with an undercoordinated Mo center; after that, a selective C-O bond cleavage produces the deoxygenated compound while the oxygen atom remains bonded to Mo center healing the vacancy.

The complete HDO cycle is composed by three different reactions: i) dehydrations, ii) keto-enol equilibria, and iii) hydrogenations. The combination of these three reactions on vacancy positions results in a reaction network with 14 intermediates connected by 20 reactions where all the side products experimentally reported are in our reaction network. The high reaction barrier for the C-C bond cleavage and the necessity of two neighboring empty vacancies explain the selectivity to C-O bond cleavage. The reaction mechanism in this work can be applied to the HDO of any polyalcohol. The results shown in this study pave the way to a better understanding of HDO process giving insights to a development of more active and selective catalyst.

Chapter 6

Selective C_2 epimerization of aldoses catalyzed by Mo-based compounds

In this chapter, the selective epimerization of glucose to mannose catalyzed by Mo-based compounds will be explained. In this reaction the redox properties of the Mo are employed to catalyze the isomerization of chiral centers. This is an appealing reaction that allows obtaining valuable and non-abundant aldoses from their nature abundant epimers. However, to date, there is no a heterogeneous catalyst that allow an easy implementation of this process in industry. This work has been already published.[166]

6.1 Introduction

Epimers are a steroisomers pair with several quiral center that differ in the configuration at only one. Typical molecules with epimer pair are monosaccharides, more commonly called sugars, a renewable biomass source.[167] Some of them, as mannose, lyxose and ribose, appear in small quantities in nature and, thus, are known as rare sugars. Epimerization can be used to obtain these rare sugars from their more abundant epimers; glucose, xylose and arabinose. Rare sugars have a high potential in the chemical industry, as they can be employed as chemical platforms to synthesize complex compounds with the same local configuration.[144] Therefore, the development of a catalyst for the selective transformation of abundant natural sugars in their rare counterparts constitutes an important industrial goal.

Epimerases are the most powerful catalyst for the reaction,[168,169] however, their application in industry presents important drawbacks.[170] Inorganic catalyst as bases,[171] lewis acids,[172–174] and zeolites[175–178] have been reported as active catalyst for epimerization reactions, but they offer a poor selectivity.

The best performance for activity and selectivity is obtained with Mo-based compounds. In the 1970s, Bilik and coworkes reported molybdates as highly selective catalyst for the epimerization reaction at C^2 position.[179,180] This reaction was experimentally studied[181–184] and a mechanism, where the epimerization is produced through a 1,2 C-shift, was proposed.[185] The apparent activation energy was reported to 126 kJ/mol. Since then, epimerization reactions through 1,2 C-shift are known as Bilik reactions. More recently, the Mo-based polyoxometalate (POM), the Keggin cluster $H_3PMo_{12}O_{40}$,[14] and niobium molybdates[186] have also been reported as active catalysis, showing a better performance than molybdates.

The Keggin cluster $H_3PMo_{12}O_{40}$ has been reported as a highly active and selective catalyst.[14] Apparent activation energies were reported between 95 and 100 kJ/mol, lower than those reported for molybdates, and selectivity reached more than 90%. In addition, it has shown another advantages for an industrial use. It can be easily filtered and recycled, and more interestingly, it can be supported on carbon or resins and used in flow reactors.[144] The same 1,2 C-shift reported for molybdates was found by ^{13}C NMR studies. However, due its structure, the mechanism should be diferent to the proposed for molybdates.

In this chapter, a reaction mechanism for the epimerization of glucose to mannose on the Keggin cluster $H_3PMo_{12}O_{40}$ was investigated. The influence of the heteroatom and the presence of water in the reaction performance, and the substrate requirements were studied. The reaction mechanism was also calculated on the compounds shown in Figure 6.1. Finally, the reducibility, calculated as H-addition energy (HAE), of the Mo centers was founded as the single descriptor for the catalytic activity. This result shows as irrespectively of their molecular or bulk nature the use of the same method allows establishing a correspondence between the catalytic properties of homogeneous and heterogeneous catalyst.

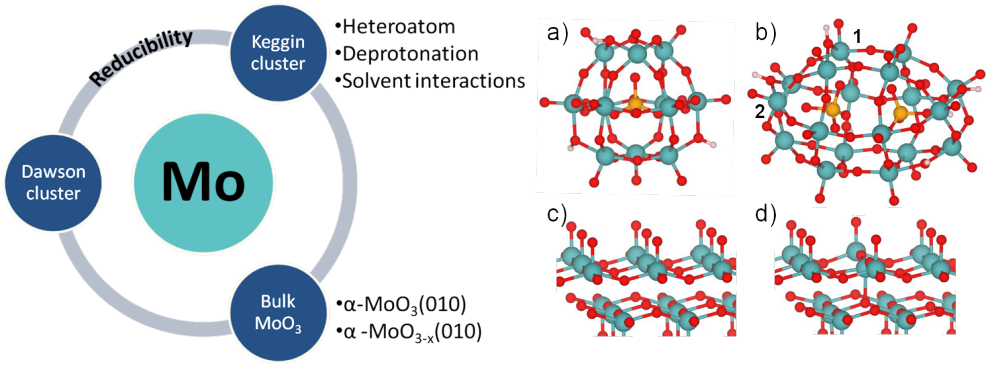

Figure 6.1: Scheme of the studied factors and Mo-based systems where the Bilik reaction was studied: a) Keggin POM $H_3PMo_{12}O_{40}$; b) Dawson POM $H_6PMo_{18}O_{62}$, two different types of Mo centres are indicated by 1 and 2; c) α-$MoO_3(010)$; d) α-$MoO_{3-x}(010)$. Mo atoms in green, O in red, P in orange and H in white.

6.2 Mechanism and energy profiles

The bonding of the aldose to two neighboring Mo atoms is hindered by the coordination environment of Mo centers. Therefore, the Bilik mechanism proposed for molybdates is not possible on Keggin structure. In this work a different mechanism with a single Mo coordination has been evaluated. It is similar to the previous mechanism proposed for metal chlorides.[174] The mechanism starts with the open-chain form of glucose and it is composed by three steps, glucose dissociative adsorption (R1), the epimerization through 1,2 C-shift (R2), and mannose associative desorption (R3):

$$\text{R1: } \mathrm{G(g) + * + O_t* \xrightarrow{H_3PMo_{12}O_{40}} G_{diss}* + O_tH*}$$

$$\text{R2: } \mathrm{G_{diss}* + O_tH* \xrightarrow{H_3PMo_{12}O_{40}} M_{diss}* + O_tH*}$$

$$\text{R3: } \mathrm{M_{diss}* + O_tH* \xrightarrow{H_3PMo_{12}O_{40}} M(g) + * + M(g)}$$

The mechanism scheme and the optimized structures are shown in Figure 6.2 a and b. In aqueous solution only the 0.25% of glucose molecules are in the open-chain form and around 99% exist in their pyranose configuration. The non-catalyzed glucose ring-opening is a high energy demanding step,[187] but it can be also catalyzed by the POM. This path was calculated and relatively low energy barriers were obtained.

In addition to the Keggin structure, the mechanism was also calculated on the Dawson cluster $H_6PMo_{18}O_{62}$, and on the pristine α-$MoO_3(010)$ and defective α-$MoO_{3-x}(010)$ surfaces. On the defective surface the mechanism is slightly different; the glucose and mannose adsorption is non-dissociative, and it is strongly exothermic, -1.26 and -1.40 eV respectively. Afterwards, the aldoses are deprotonated by the surface and suffer the epimerization. The reaction energy profile for all the catalysts is shown of Figure 6.2.c. The energy barrier for the uncatalyzed 1,2 C-shift is 1.37 eV. This value is reduced to 0.99 eV on the Keggin cluster, and 1.10 eV on the Dawson structure. However, the lowest barriers are obtained for the bulk catalyst, 0.85 and 0.94 eV for the defective and pristine surface, respectively.

Even if the lowest energy barrier for the 1,2 C-shift is on the defective surface, its use as catalyst has two drawbacks: i) the aldoses are adsorbed strongly, being the desorption of glucose/mannose the most energy demanding step. ii) α-MoO_{3-x} has been reported as an active catalyst for hydrodeoxygenation, HDO, reactions of oxygenated hydrocarbons where Mo-O bonds are broken.[19,38,40] A typical HDO reaction is the dehydration of alcohols. The Mo-O bond break step was calculated for the -O^5H group, being the energy barrier 1.01 eV. Glucose has five -OH groups that can suffer this reaction and similar values are expected for other alcohol groups, an therefore, the selectivity towards epimerization reaction would be compromised discarding the defective surface as a catalyst for the reaction.

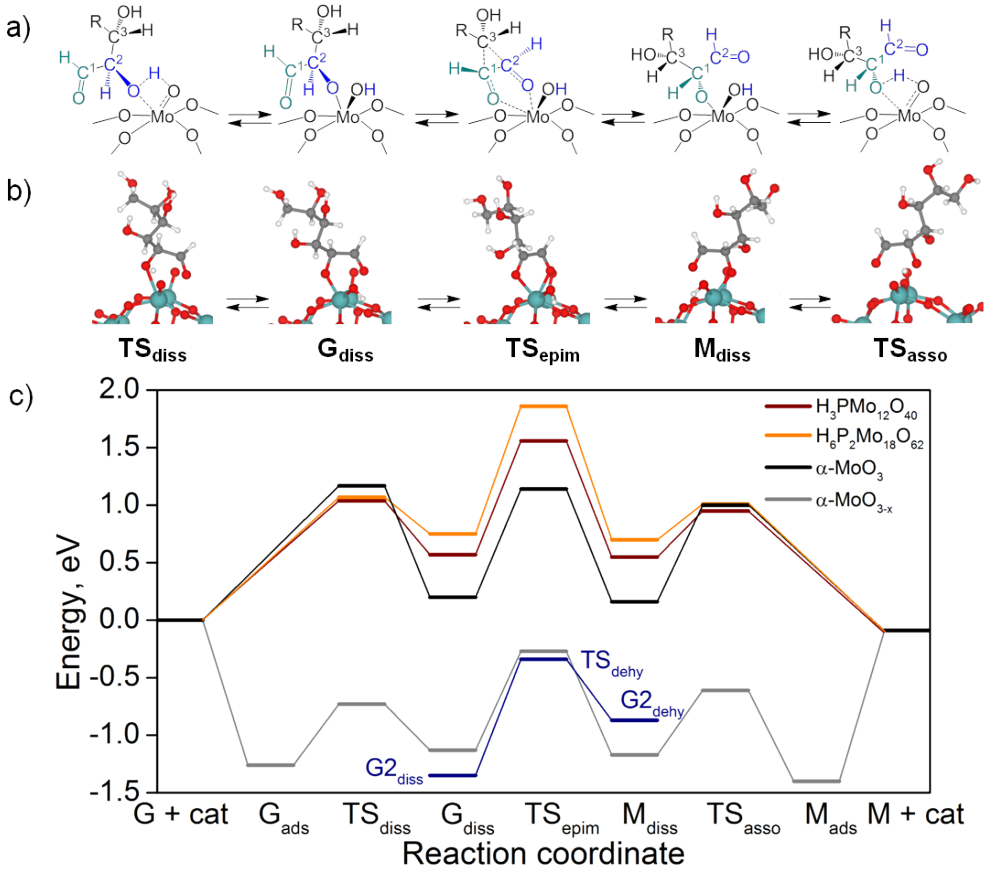

Figure 6.2: a) Proposed mechanism for the epimerization reaction on $H_3PMo_{12}O_{40}$. b) Optimized structures for reaction on $H_3PMo_{12}O_{40}$ starting from glucose. c) Reaction profile for the Bilik reaction for glucose on $H_3PMo_{12}O_{40}$, $H_6PMo_{18}O_{62}$, α-$MoO_3(010)$ and α-$MoO_{3-x}(010)$. The dehydration step on α-$MoO_{3-x}(010)$ is represented by the blue line. Taken from ref.[166]

Experiments for the reaction carried out in aqueous solution have reported a better performance for $H_3PMo_{12}O_{40}$ catalyst than for MoO_3.[144] This was due the leaching suffered by the bulk compound.[144,186] It forms a solution of active molybdates that have been reported to have a higher apparent activation energy than POM and it complicates the recycling of the catalyst. However, in a tandem catalyst, where the bulk and POM compounds were used as epimerization catalyst in ethanol, α-MoO_3 did not suffer leaching and it showed a slightly better performance.[15] Therefore, when the crystalline structure is maintained the bulk compound shows a higher activity, in agreement with our calculations. However, the low solubility of sugars in alcohols limits the use of α-MoO_3 as catalyst for the reaction.

In order to understand the different crystalline stability in aqueous solution of the bulk α-MoO_3 and the aqueous species of the POM, $[PMo_{12}O_{40}]^{3-}$, their cohesive energy, the energy required to separate the crystalline structure

into isolated molecular units, was calculated. The molybdic acid, H_2MoO_4, was used as Mo-reference unit, as it is the smallest molybdenum compound present in aqueous solution. A cohesive energy of 1.06 and 1.78 eV/MoO_3 was calculated for α-MoO_3 and $[Mo_{12}O_{40}]^{3-}$ respectively. The high difference in their cohesive energies explains the different behavior against leaching in aqueous solution. The higher value for the POM is due the electrostatic interactions between the encapsulated anion and the $Mo_{12}O_{36}$ framework that stabilizes the structure.

6.2.1 Effects of the heteroatom

Due to the good performance of the Keggin cluster, the effects of the heteroatom in the POM performance were studied. Although the heteroatom does not take part directly in the reactivity, due to its electronic structure and formal charge, it influences the charge distribution over the POM and modifies the redox properties of the $Mo_{12}O_{36}$ framework.[188,189] Intermediates and transition states for the 1,2 C-shift were calculated on $H_nXMo_{12}O_{40}$ (X= S, P, As, Si, Ge). Slightly differences were found, binding energies are between 0.51 and 0.67 eV for glucose, and between 0.49 to 0.62 eV for mannose. The energy barriers ranging from 0.95 to 1.07 eV. Binding and activation energies increases with the negative formal charge of heteroatom, and for a given charge with the heteroatom size: S < P < As < Si < Ge.

6.2.2 Influence of the functional groups

The presence of the functional groups of the aldoses has a big influence on the activity the Bilik reaction catalyzed by molybdates:[185] i) the presence of an aldehyde group in C^1 position and alcohol groups in C^2 and C^3 position have been shown to be essential, ii) the lack of alcohol in C^4 position results in a lower activity.

The influence of these groups in the mechanism calculated in the present work was analyzed using as model the reaction on $H_3PMo_{12}O_{40}$. Additional calculations of intermediates and transition state for 1,2 C-shift step with glucoses without -OH group at C^3 and C^4 position were performed. The following conclusions could be obtained from the mechanism:

- **$C^1H(=O)$ and C^2OH:** their influence is evident since they take part directly in the reaction mechanism. Glucose adsorbs on a Mo center through the C^2 alcohol group and its transformation on a ketone together the transformation of the C^1 aldehyde group allow the carbon chain arrangement with the consequent epimerization.
- The presence of a ketone group in other carbon positions could allow the C-shift but it does not result in a epimerization; it would result in a structural isomer.

And from the calculations without -O^3H and -O^4H groups:

- **C^3OH:** without this group the the activation energy reaches 1.23 eV. This increment is due the formation of a partial double C^3=O^3H stabilizes the transition state.
- **C^4OH:** the lack of this group increases the energy barrier to 1.08 eV. A hydrogen bond is formed between -O^3H and -O^4H; in the transition state this bond is reinforzing stabiling the transition state.

6.3 Solvation effects

As the reaction is performed on aqueous solution the influence of the presence of water in the system was studied for the $H_3PMo_{12}O_{40}$ system. Analysis were performed for a implicit solvent, through the continuous solvent model VASP-MGCM,[190,191] and with the addition of one or two explicit water molecules.

The Keggin cluster has a high solubility in water and it is a strong acid that is completely deprotonated.[192] The use of the implicit model allow the analysis of the deprotonation effects, which were studied for the 1,2 C-shift elementary step. Intermediates and transition state were calculated on $[H_{3-n}Mo_{12}O_{40}]^{n-}$ clusters. For the completely protonated POM the dissociative binding energy of the aldoses is not influenced by the presence of solvent; however, the polarity of water stabilizes the transition state and the energy barrier is reduced by 0.24 eV. A linear increase with the overall charge of the POM is observed for binding and activation energies. The solvent stabilizes the charge of deprotonated POMs smoothing this effect. The binding and activation energy values for the fully deprotonated POM, $[PMo_{12}O_{40}]^{3-}$, are 1.05 and 1.00 eV.

In addition, a set of calculations with one or two explicit water molecules were done for each elementary step in order to know the exact role of each water molecule. In the first step of the reaction path in gas-phase, sugars dissociatively adsorb on a Mo center with an activation energy of 1.04 eV for both aldoses. A explicit water molecule was placed between the aldoses and the POM, and acting as proton shuttles reduces the energy barrier to 0.54 and 0.55 eV for glucose and mannose respectively. In the 1,2 C-shift step the influence of two water molecules has been shown significant. On the one hand, one water molecule interacts with the -O_tH group bonded to the reactive Mo center after the dissociative adsorption. This interaction weakens the Mo-O_t bond allowing a better stabilization of the transition state by the Mo center, reducing the energy barrier by 0.12 eV. On the other hand, a second water molecule was placed between the -O^3H and -O^4H group. This water molecule assists the formation of the partial double bond C^3=O^3H and diminishes the activation energy by 0.10 eV. In the system with the two explicit molecules, the energy barrier is reduced by 0.19 eV, almost reproducing the value obtained with the implicit model.

6.4 Descriptor analysis

Adsorption and reactivity can be described as function of one or several electronic or geometrical properties of the catalyst.[193,194] In the epimerization reaction, reducibility was found as a single descriptor that correctly describes adsorption and activation energies for this process for both cluster and surface catalysts.

6.4.1 BE and E_a in Keggin cluster

The redox properties of the $Mo_{12}O_{36}$ framework of the POM can be tunned by the heteroatom and protonation grade, which modify the charge density in the POM skeleton. The influence of these parameters on adsorption and activation energies was studied.

Heteroatom

The encapsulated anion, XO_4^{n-}, of the POM transfers part of its charge to the framework. The extent of this charge transfer depends of the nature of the heteroatom. In this work, it was measured as the variation between the formal charge of the heteroanion and the calculated Bader charge on it. Both binding energies of aldoses and activation barriers for 1,2 C-shift calculated for different heteroatom increase linearly as function the value of the transferred charge, see Figure 6.3.

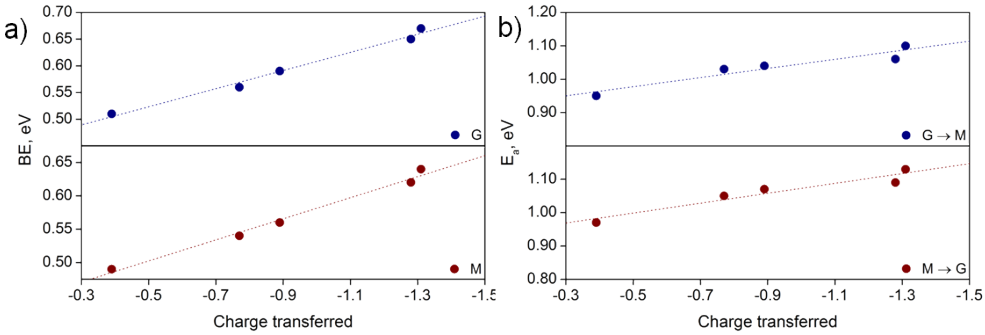

Figure 6.3: a) Binding energies, BE, of dissociated glucose and mannose and b) activation energy for the 1,2 C-shift as function of charge transferred, CT in $|e^-|$, to $H_nXMo_{12}O_{40}$ (X= S, P, As, Si, Ge). BE(G)= -0.17CT + 0.44, R^2= 0.99, MAE= 0.01 eV. BE(M)=-0.13CT + 0.53, R^2= 0.93, MAE= 0.01 eV. Ea(G→M)=-0.11CT + 0.91, R^2= 0.87, MAE= 0.01 eV. Ea(M→G)= -0.14CT + 0.90, R^2= 0.95, MAE= 0.03 eV.

Deprotonation degree

Each deprotonation leaves one additional electron on the Mo-framework increasing its electron density. The analysis of the binding and activation energies as function of the POM charge shows a linear correlation between them,

see Figure 6.4. The same trend was experimentally observed for the reduction potential, which decrease linearly with the POM deprotonation.[189,195,196] This behavior can be rationalized, since a higher electron density on Mo centers results in a more difficult addition of an electron.

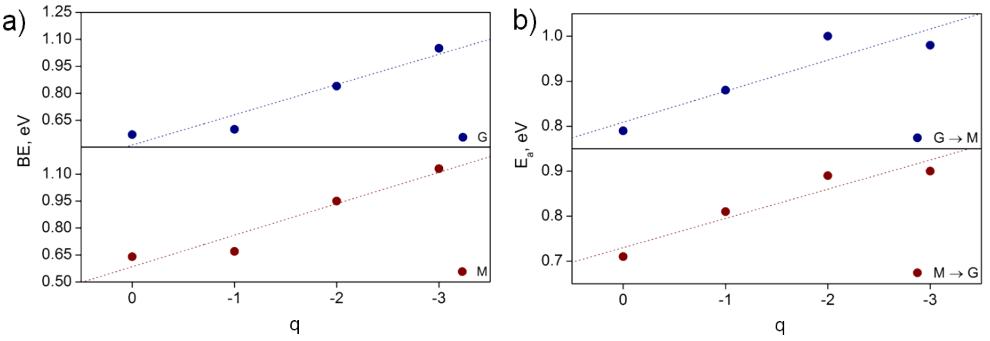

Figure 6.4: a) Binding energy, BE, of dissociated glucose and mannose and b) activation energy for the 1,2 C-shift as function of charge, q in $|e^-|$ on $[H_{n-x}XMo_{12}O_{40}]^{x-}$ (x between 0 and 3). BE(G)= -0.17q + 0.51, R2= 0.93, MAE= 0.05 eV. BE(M)=-0.17q + 0.57, R2= 0.93, MAE= 0.04 eV. Ea(G→M)=-0.08q + 0.80, R2= 0.91, MAE= 0.02 eV. Ea(M→G)= -0.07q + 0.72, R2= 0.98, MAE= 0.01 eV.

Charge density

In addition, during the 1,2 C-shift the C^1 aldehyde is transformed in an alkoxy group and the C^2 alkoxy group in an aldehyde leading a large electronic rearrangement assisted by the Mo centers. The transition state of this elementary step was studied by the calculation of the charge density difference of the transition state TS_{epim} with respect to the anion $[C_6H_{11}O_6]^-$ and the protonated POM, Figure 6.5. This analysis shows as the charge density of the lone pairs of the isolated glucose is accepted by the Mo center.

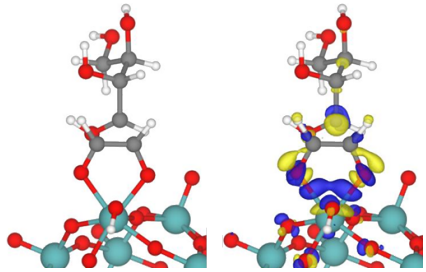

Figure 6.5: Structure of the TS_{epim} for $H_3PMo_{12}O_{40}$ (left) and TS_{epim} charge density difference (right). The charge density difference was calculated with respect to the $[C_6H_{11}O_6]^-$ anion and the $(H_4PMo_{12}O_{40})^+$ cation at the TS_{epim} geometry. Same colour code as Figure 6.1. Blue colour means depletion of charge density and yellow colour stands for accumulation.

These analysis shows as the redox properties of the Mo centers governs the catalytic activity of the Keggin cluster.

6.4.2 HAE descriptor

Reducibility is a property that allows measuring the redox character of the reactive. This property has the advantage that can be also measured on the bulk catalyst and therefore, it can be used as descriptor for the reaction.

The most direct way to calculate the reducibility is the addition and localization of a single electron in the reactive center. However, the direct calculation of single atom reducibility on α-MoO_3 surfaces was elusive, and therefore an alternative way to calculate the reducibility was chosen. Previously, the H-atom addition energy (HAE) had been proposed as descriptor for C-H activation for methanol oxidation on POM.[57,197] This HAE parameter is calculated as the energy of to add one hydrogen atom to an oxygen of the catalyst:

$$\mathrm{HAE} = E_{cat+\mathrm{H}\cdot} - E_{cat} \tag{6.1}$$

This parameter simultaneously measures the reducibility of the metal center, by the addition of one electron, and the basicity, by the adsorption of the proton on a neighboring oxygen. As is shown in Figure 6.6 the binding and activation energies for 1,2 C-shift elementary step correlate with the HAE parameter. Only the binding energy on the defective surface does not fit correctly due electrostatic effects.

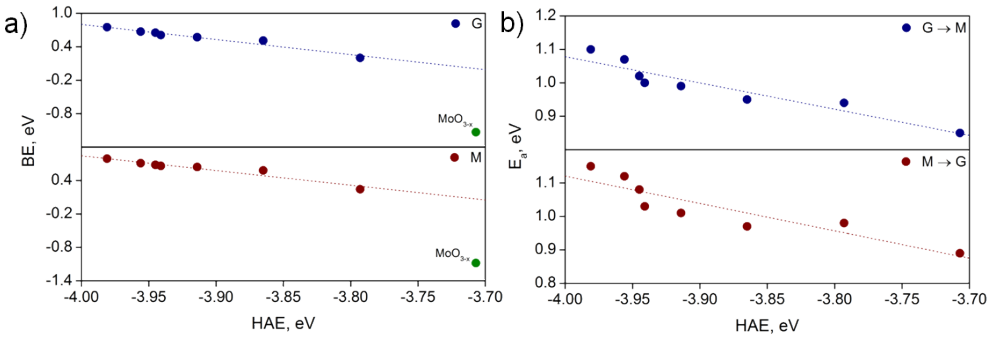

Figure 6.6: a) Binding energy, BE, of dissociated glucose and mannose as function of HAE. BE(G)=-2.72HAE-10.08 eV, R^2= 0.96, MAE= 0.03 eV. BE(M)=-2.65HAE-9.74 eV, R^2= 0.93, MAE= 0.03 eV. Adsorption on defective MoO_{3-x}(010) surface is not included in the fittings. b) Activation energy, E_a, of TS_{epim} as function of HAE. E_a(G→M)=-0.79HAE-2.06 eV, R^2= 0.88, MAE= 0.02 eV. E_a(M→G)=-0.81HAE-2.13 eV, R^2= 0.81, MAE= 0.03 eV.

The reducibility can be calculated from the HAE by the removing of the basicity contribution, calculated as energy of to adsorb a proton on a neighboring oxygen:

$$\mathrm{Red} = \mathrm{HAE} - (E_{\mathrm{cat}+\mathrm{H}^+} - E_{cat}) \tag{6.2}$$

This reducibility was calculated for $H_nXMo_{12}O_{40}$ (X= S, P, As, Si, Ge) and $H_6PMo_{18}O_{62}$. The binding and activation energies correlate with the reducibility, showing as a higher reducibility results in lower binding and activation energies, see Figure 6.7.

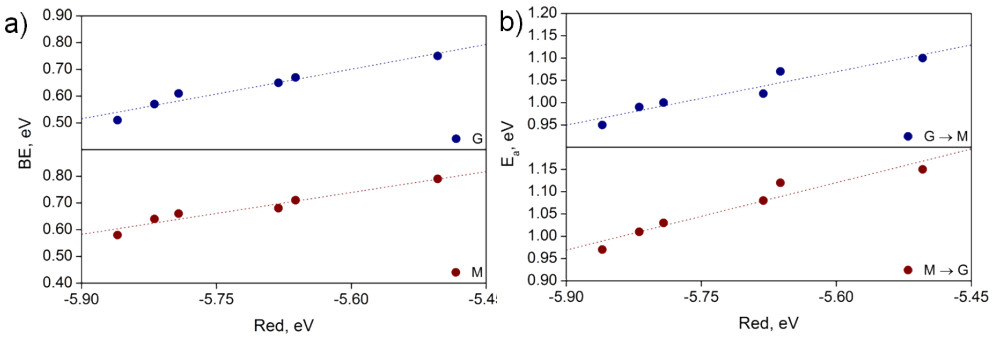

Figure 6.7: a) Binding energy, BE, of dissociated glucose and mannose on $H_nXMo_{12}O_{40}$ (X= S, P, As, Si, Ge) and on $H_6P_2Mo_{18}O_{62}$ and b) activation energy of the 1,2 C-shift as function of reducibility, Red, of the Mo center. BE(G)= 0.63Red + 4.29, R^2= 0.96, MAE= 0.01 eV. BE(M)=0.54Red +3.76, R^2= 0.93, MAE= 0.02 eV. Ea(G→M)=0.41Red +3.36, R^2= 0.92, MAE= 0.01 eV. Ea(M→G)= 0.51Red +3.99, R^2= 0.94, MAE= 0.01 eV.

These results display that the catalytic performance depends of the redox properties of the catalyst and, therefore, the reducibility can be used as single descriptor of the activity of different catalysts. This descriptor can be experimentally measured by cyclic voltammetry, and thus, this work provides a easy way to predict the activity of catalysts for this process.

6.4.3 Reaction rate and volcano plot

A microkinetic model was built in order to obtain the analytical equation of the reaction rate. From the reaction profiles, Figure 6.2, the 1,2 C-shift can be assumed as the rate-determining step, and therefore, the quasi-equilibrium approximation can be used to obtain the equation for the reaction rate. Binding energies for the dissociative adsorption of aldoses and the energy barrier for the C-shift are obtained from the linear fittings of Figure 6.6 and therefore the rate can be written in terms of HAE:

$$r(HAE) = k_2 k_G[G]\left(1 - \frac{[M]}{K_{global}[G]}\right)\frac{1}{1 + K_G[G] + \frac{1}{K_M}[M]} \tag{6.3}$$

Where K_i are the adsorption constants for glucose and mannose, i=G,M; k_2 the coefficient for epimerization starting from glucose, K_{global} the constant for the epimerization reaction, and [M] and [G] the corresponding concentrations of glucose and mannose. In Figure 6.8 the normalized reaction rate is plotted as function of HAE. The reaction rate shows a volcano shape with the maximum placed at HAE=-3.72 eV and only a narrow zone of reducibility in which Mo-based catalyst are actives for epimerization. With reaction rates obtained through Eq. 6.3 the apparent activation energies, E_{app}, were calculated. For

$H_3PMo_{12}O_{40}$ E_{app} is 1.04 eV, in good agreement with the experimental value: 0.99±0.04 eV.[14] For $H_2SMo_{12}O_{40}$ the apparent activation energy is 1.00 eV, being the catalyst with lowest E_{app}. As POMs are in the upper end of the narrow zone, more active catalysis could be developed.

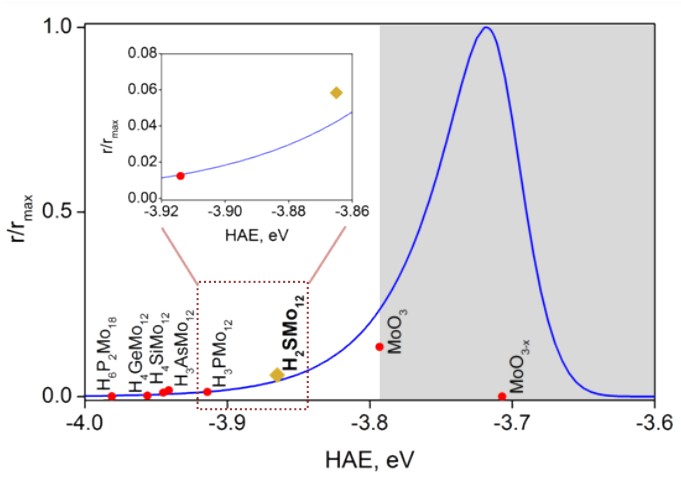

Figure 6.8: Volcano plot of the normalized reaction rate as function of the HAE. Conditions: T=100ºC, [G]=0.90M, [M]=0.10M. Red points correspond to the calculated rate with Eq. 6.3 for the catalyst used in the analysis. Catalysts in the shaded region present drawbacks for epimerization reaction.

6.5 Conclusions

In this chapter the mechanism for the selective C^2 epimerization of aldoses catalyzed by Mo-based compounds has been identified. This mechanism explains the selectivity to C^2 epimerization experimentally observed. The influence of the heteroatom and deprotonation grade were studied. The key step of the mechanism is the carbon chain rearrangement through 1,2 C-shift. Reducibility, calculated as H-addition energy (HAE), was found as the unique descriptor for binding and activation energies for this process, independently of the cluster or bulk nature of the catalyst. A microkinetic model was built and the reaction rate was represented as function of HAE obtaining a volcano-plot, which maximum indicates the HAE for the maximum activity and shows as more active catalysts could be developed. Finally, the different behavior against leaching observed for bulk and cluster catalyst is explained for the electrostatic interaction between encapsulated anion and $Mo_{12}O_{36}$ framework in POM, which increase the stability of the structure.

UNIVERSITAT ROVIRA I VIRGILI
MOLYBDENUM OXIDES AS CATALYST FOR BIOMASS-DERIVED COMPOUNDS: A THEORETICAL APPROACH
Marcos Rellán Piñeiro

Chapter 7

Concluding remarks

The biomass-derived compounds conversion catalyzed by Mo-oxides was studied by means of density functional theory, DFT. Three interesting reactions were studied: i) the oxidation of methanol to formaldehyde (Chapter 3), ii) the glycerol reduction to propylene (Chapter 5), and iii) the glucose epimerization to mannose (Chapter 6). In addition, the optimization of DFT+U method and the study of the nature of vacancy defects on α-$MoO_3(010)$ surface were performed (Chapter 4). Therefore, the studies reported in this thesis pave the way for a better understanding of Mo-oxides catalytic behavior that will allow the development of more active, selective, and stable catalysts. The detailed conclusions of each chapter are detailed in the following:

Chapter 3. The Formox™ process: selective methanol oxidation to formaldehyde

- The reaction pathway for the methanol oxidation to formaldehyde is the following:

  $CH_3OH \rightarrow CH_3OH^* \rightarrow CH_3O^* \rightarrow CH_2O^* \rightarrow CH_2O$

- The catalytic activity is determined by the vacancy formation, the highest point in reaction profiles, and the catalyst recovery.

- Both surfaces α-$MoO_3(010)$ and r-$MoO_2(110)$ are actives for the oxidation of methanol, but the only selective surface is α-$MoO_3(010)$. The presence of reduced Mo centers on this surface is detrimental to selectivity.

- The presence of iron as dopant reduces the vacancy formation energy, which increases the activity. This reduction is due to one electron is accommodated in the iron during the vacancy formation.

- The presence of iron in the surface layer forms vacancies spontaneously, reducing the selectivity. However, iron placed in subsurface layer does not form spontaneous vacancy defects and keeps the selectivity.

- In the industrial catalyst, MoO_3 is the catalytic phase and the role of Fe is to increase the activity by reducing the reaction energy of redox steps.
- The best performance can be obtained with the selective iron doping in subsurface positions. Surface layer of MoO_3 selectively catalyzes the reaction whereas the subsurface iron increases the activity without affecting the selectivity.

Chapter 4. On the nature of oxygen vacancies on the α-MoO_3(010) surface through the optimized DFT+U method

- The U_{eff} of DFT+U method was optimized to a value of 3.5 eV by fitting reaction energies and electron localization with the HSE06 hybrid functional and CCSD(T) method. The mostly used value, U_{eff}=6.3 eV, strongly underestimates the reaction energies.
- During α-MoO_3(010) surface reduction vacancies will be produced only in terminal positions.
- The reduced surface can be in two different local electronic configurations: i) two Mo^{5+} polarons placed in the undercoordinated Mo and in a neighboring Mo center along x axis; and ii) a single Mo^{4+} dipolaron placed in the undercoordinated Mo.
- The two electronic configurations were characterized in terms of bond distances, magnetization, Bader charges, Raman frequencies and XPS.
- The two electronic configurations are close in energy; being the two Mo^{5+} polarons the most stable. The conversion between the two electronic structures through an electron hopping has an energy barrier of $\sim$0.30 eV, easily overcomed at typical reaction temperatures. Therefore, the two oxidation states will be present during catalytic activity.
- The vacancy formation energy of $2\times Mo^{5+}$ configuration increases linearly with the coverage. Whereas, the vacancy formation energy of Mo^{4+} is constant until a coverage of 0.5 ML. At high coverage the inversion of the stability between the two electronic states was found.
- The formation of Magnéli-phases is explained by the impossibility of the vacancy accumulation along x axis.
- The adsorption energy of molecules on vacancy positions can be influenced by the electronic state.

Chapter 5. Propylene production from glycerol: a first principles study of hydrodeoxygenation (HDO) process on MoO_{3-x}

- Hydrogen molecules dissociatively adsorb on surface and they can diffuse over the surface with low energy barriers. The surface hydrogens can recombine with a surface oxygen to form water molecules that are released generating vacancy defects on the surface.

- The high energy barriers for hydrogen adsorption explains why high H_2 pressure is needed in experiments to reach high activity.
- The hydrocarbons are deoxygenated on vacancy defects. They adsorb forming a Mo-O bond. A selective C-O bond cleavage produces the deoxygenated compound while the oxygen atom remains bonded to Mo center healing the vacancy and closing the catalytic cycle.
- Glycerol is reduced to propylene through a reaction network with 16 intermediates interconnected by 20 reactions. All the intermediates experimentally observed are accessible in the reaction network.
- In the reaction network there are three types of reactions: i) dehydrations, ii) keto-enol equilibria, and iii) hydrogenations. The mechanism was elucidated for the three reaction types and all the elementary steps of reaction network were calculated.
- The high reaction barrier and the necessity of two neighboring empty vacancy defects for the C-C bond cleavage explain the selectivity for this HDO process.

Chapter 6. Selective C_2 epimerization of aldoses catalyzed by Mo-based compounds

- The mechanism for the epimerization of aldoses on $H_3PMo_{12}O_{40}$ was unraveled. The epimerization encompasses three elementary steps through a single Mo coordination: i) dissociative adsorption, ii) 1,2 C-shift, and iii) associative desorption.
- During 1,2 C-shift step C^1 and C^2 exchange its functional groups, aldehyde and alkoxy. This large electronic rearrangement is assisted by the Mo centers.
- The same mechanism can be applied to the catalyzed epimerization on larger POMs and α-$MoO_3(010)$ surface.
- The presence of water as solvent reduces the energy barrier of the three elementary steps. In dissociative adsorption and associative desorption one water molecule acts as proton shuttle. During the 1,2 C-shift two water molecules assist the carbon chain rearrangement by the interaction with -OH groups.
- Different heteroatom and protonation grades in the Keggin cluster have an influence in the charge transfer between the heteroanion and the $Mo_{12}O_{36}$ framework. This charge transfer modifies the redox properties of the Mo atoms influencing the barrier for the 1,2 C-shift.
- Regarding the POM stability, the electrostatic interactions between the heteroanion and the $Mo_{12}O_{36}$ framework avoid the leaching observed in the bulk catalyst.

- Reducibility, calculated as hydrogen addition energy (HAE), is an electronic descriptor for adsorption energies and 1,2 C-shift energy barrier. The representation of the rate as function of hydrogen addition energy (HAE) is a volcano plot. Its maximum indicates the HAE of the compound that would have the highest rate.

Chapter 8

Included papers

UNIVERSITAT ROVIRA I VIRGILI
MOLYBDENUM OXIDES AS CATALYST FOR BIOMASS-DERIVED COMPOUNDS: A THEORETICAL APPROACH
Marcos Rellán Piñeiro

ChemPubSoc Europe
DOI: 10.1002/cssc.201500315
CHEMSUSCHEM Full Papers

The Active Molybdenum Oxide Phase in the Methanol Oxidation to Formaldehyde (Formox Process): A DFT Study

Marcos Rellán-Piñeiro and Núria López*[a]

Methanol is oxidised to formaldehyde by the Formox process, in which molybdenum oxides, usually doped with iron, are the catalyst. The active phase of the catalysts and the reasons for the selectivity observed are still unknown. We present a density functional theory based study that indicates the unique character of Mo^{VI}–Mo^{IV} pairs as the most active and selective sites and indicates the active sites on the surface, the controlling factors of selectivity, and the role of the dopant. Iron reduces the energy requirements of the redox Mo^{VI}–Mo^{IV} pair by acting as an electron reservoir that sets in if required. Our present study paves the way towards a better understanding of the process.

Introduction

Nowadays, formaldehyde is one of the top chemical products with 46.4 million tons produced yearly as of 2012.[1] Industrially, two catalytic processes based on the oxidation of methanol have been put forward: $CH_3OH + {}^1/_2 O_2 \rightarrow H_2CO + H_2O$. The first one relies on the use of silver and occurs at high temperatures (between 560 and 600 °C).[2] The second is based on a mixture of reducible oxides including molybdenum, iron and/or vanadium, in the so-called Formox process.[3] The reaction takes place at $T = 250$–400 °C and one of its major drawbacks is the stability of the catalyst (which lasts for about one year).[4] Although the ferric molybdate catalyst was reported in 1931 by Adkins and Peterson,[5] it was not available industrially until the 1960s.[6] In the Mo-containing formulations, Mo sites play an active role[7] and the reaction begins simultaneously with the reduction of the material.[8] However, both the nature of the active site and its particular oxidation state remain under discussion.[9] Given the extensive use of molybdenum oxide based catalysts in methanol and other selective oxidations, such as propene to acrolein ($BiMoO_4$), propane (MoTeVNbO)[9,10] and the hydrodeoxygenation of biomass compounds,[11] an understanding of the nature of the active site is crucial to fine tune it. However, the difficulties to address the nature of these catalysts under true reaction conditions arise from the fact that they are structurally complex and present variable stoichiometries, as well as, in some cases, mixed oxidation states that facilitate their redox chemistry. Computational techniques based on the use of density functional theory can be used to elucidate the active site of the catalyst. For instance, experiments on molybdenum oxide trimers[12] $(MoO_3)_3$ combining temperature-programmed desorption and molecular gas-phase density functional theory have been reported. These works have illustrated the potential paths for oxidation, reduction and condensation of alcohols, which indicate a prominent role for the Mo=O terminal bonds in alcohol activation and in α-and β-hydrogen elimination leading to dehydrogenation and dehydration, respectively. However, these studies have not yet been extrapolated to the bulk phases of molybdenum oxides, so this is the precise aim of the present work.

The high degree of complexity of the molybdenum phases is the main reason why academic studies have focused on the so-called "parent oxides".[13,14] Experiments on different phases of molybdenum oxide under aerobic and anaerobic conditions have demonstrated different selectivities.[14] MoO_3 produces high yields of formaldehyde, in contrast to the behaviour of MoO_2. Under anaerobic conditions on MoO_3, the reaction starts at about $T = 250$ °C and the selectivity, which is quite high at low conversions (around 90%), is severely reduced above 340 °C, at which point CO becomes the major product. It was claimed that this selectivity decreases as a result of surface reduction. The low activity for the anaerobic process was ascribed to the reduced amount of oxygen available. The same experiments indicate the need to retrieve the oxygen from the bulk phase with concomitant formation of the Mo^{4+} and Mo^{5+} species identified by X-ray photoelectron spectroscopy.[14] These species are detrimental to selectivity. By contrast, MoO_3 is very selective under aerobic conditions and activity appears at temperatures higher than 220 °C. The selectivity is retained, even at very high conversions. The side products observed are dimethyl ether and CO_2 (about 8%) in the medium temperature range (360 °C).

In turn, aerobic experiments run on MoO_2 show activity at even lower temperatures ($T = 180$ °C) with high selectivity (around 90%), but the selectivity drop is fast and it is already below 70% at $T = 240$ °C; the secondary product is CO. Significantly, the performance of the MoO_2 catalyst is better in the second run[14] of experiments, in which the activity and selectivity profiles resemble those of the aerobic performance of MoO_3. The large oxygen uptake of the MoO_2 sample at $T =$

[a] M. Rellán-Piñeiro, Prof. N. López
Institute of Chemical Research of Catalonia (ICIQ)
Avinguda Països Catalans, 16, 43007 Tarragona (Spain)

Supporting Information for this article is available on the WWW under http://dx.doi.org/10.1002/cssc.2.201500315.

ChemPubSoc Europe
CHEMSUSCHEM Full Papers

280 °C and the X-ray diffraction analysis indicate the formation of MoO_3 and X-ray photoelectron spectroscopy shows that surface Mo is in the 6+ state. Therefore, these authors identified Mo^{6+} species as the key for the high yield.

A recent structural deep in situ multi-technique analysis[13] of MoO_3 under real anaerobic reaction conditions illustrated the consumption of oxygen from the bulk of the material in what was identified as a Mars–van Krevelen mechanism. According to these experiments, the basal (010) plane is responsible for producing formaldehyde.[13] Geometric rearrangements of the Mo–O structures were reported upon reaction and upon increases in the temperature. Whereas the terminal O_t atoms were closer to the Mo centres, the other oxygen atoms increased in distance from the neighbouring Mo centres.

It has been claimed that the M=O bond length and strength are both fundamental to derive the activity and selectivity of oxide materials in oxidation processes.[12,15] For MoO_3, this argument would imply that the terminal O_t atom would be active, both in terms of activity and selectivity.[6,12,15a,b,16] Although the argument seems intuitive, there is some controversy because no direct correlation is obtained from experimental results. For instance, Routray et al.[17] suggested that there is no relationship between the effectiveness of bulk oxygen and surface reactivity. Through a comparison of these results with the dynamic character of the coordination spheres reported in Ref. [13], it becomes clear that such a simple descriptor might not be practical for large lattice rearrangements. O'Brien et al.[13] indicated that the most labile oxygen atoms in the bulk might be crucial to maintain catalytic activity in oxygen-depleted environments. However, the geometric distortions induced by defect formation might hinder the identification of the species responsible for activity.

With regard to phase control, the MoO_2–MoO_3 equilibrium appears at experimental temperatures around 400 °C and a solid-state reaction between MoO_2 and MoO_3, Mo_4O_{11}, has been proposed.[18] Moreover, vacancy diffusion in MoO_3 was reported at above $T = 300$ °C, which gives further support to the Mars–van Krevelen[13] mechanism. The Formox process[3b,19] uses formulations for which ferric molybdates[19a] with excess MoO_3 are the real catalyst of choice. The particular role of iron is unknown. Moreover, doped molybdenum oxides have been reported to be active and selective catalysts for higher alcohols derived from biomass,[11a] which thus opens a broad field for such catalysts.

The aim of the present work is to use density functional theory to illustrate the reaction network that drives the conversion of methanol to formaldehyde and to determine the active site and how the properties can be fine tuned by doping.

Results and Discussion

Molybdenum oxides present a wide structural and compositional diversity[20] (Tables S1 and S2 in the Supporting Information). The most common oxidised polymorph corresponds to α-MoO_3, which presents an orthorhombic unit cell. This structure consists of bilayers of distorted MoO_6 (Figures S1 and S2 in the Supporting Information) packed through van der Waals forces along the *y* axis, with (010) as the lowest energy surface. The structure contains three crystallographically inequivalent oxygen sites: 1) O_b, an asymmetric bridging of two Mo atoms with one short and one long distance; 2) O_{3c}, with two equal bonds to two Mo atoms of the same sublayer and a long bond to another centre in the other sublayer; and 3) O_t, the terminal oxygen atom capping the Mo centre with the shortest distance (Table S3 in the Supporting Information). This terminal oxygen atom appears between the α-MoO_3 bilayers. In turn, the Mo centres are reported to be either four- or six-fold coordinated depending on the definition used in the experiments.[21]

MoO_2 crystallises in a monoclinic structure, which can be considered as a distorted rutile. This structure is formed by chains of MoO_6 octahedra that share opposite edges along the crystallographic *c* axis. Each oxygen atom is bound to three metal centres and each metal is surrounded by six oxygen atoms. There are two distinct Mo–Mo distances alternated along the *c* axis and two different coordination oxygen atom environments, each with three different bond lengths. In the parent tetragonal rutile structure, there is only one metal–metal distance (the lattice parameter *c*) and all of the metals have the same octahedral coordination (Figures S1 and S2 in the Supporting Information), with two different M–O bond lengths (Table S3 in the Supporting Information). To simplify the analysis, we used the non-distorted high-symmetry-phase rutile, r-MoO_2. Similar strategies have been put forward to analyse scaling relationships for adsorption properties.[22]

Slab models representing different molybdenum oxides are presented in Figure 1. For each of them, the reaction under aerobic and anaerobic conditions was studied with the PBE functional and van der Waals dispersion contributions for the layered compounds (Tables S4 and S5 in the Supporting Information). It is worth noticing that the layered structure of α-MoO_3 is weakly bound along the *y* direction: the interaction energy between the bilayers is only 8 meV Å^{-2}. In addition, we have identified a diffusion path for the defects that allows tridimensional transport mediated by vacancies with very small energy differences (Figure S3 in the Supporting Information).

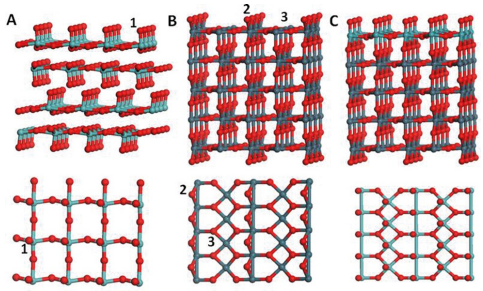

Figure 1. Schematic representation of the slab models in the present study. Top: side view; bottom: top view. A) α-MoO_3(010); 1: terminal oxygen atom, O_t. B) r-MoO_2(110); 2: bridge oxygen atom, O_b; 3: Mo_{cus} atom. C) r-MoO_2 with the outermost layer oxidised to α-MoO_3(010). Colour code: red: oxygen; light grey: Mo^{VI}; dark grey: Mo^{IV}.

On the r-MoO_2(110) layer, oxidation can lead to the formation of α-MoO_3. We have examined this particular aspect by growing a single layer of the α-MoO_3 compound epitaxially along the (010) direction that interacts directly with the r-MoO_2(110) layer (Figure 1C).

The reaction mechanism for the oxidation of methanol on molybdenum oxides has been summarised in the literature by Tatibouët[6] to occur by first stripping of the acid proton by an acid–base pair[23] with the subsequent C–H bond breaking by a nearby basic centre.[16a,24] This reaction scheme, supported by numerous experimental evidences[25] and revised in Ref. [6], will be analysed for the different potential oxide surfaces by following the experimental strategy suggested by Farneth et al.[16b] The analysis over different oxides and stoichiometric terminations can be taken then to infer the nature of the active site because neither the experimental and computational determination of the mixed phases under the reaction conditions is reachable with the required level of detail.

α-MoO_3(010)

The investigated path (Figure 2) follows the experimental indications that suggest that oxidation takes place through the formation of methoxy and hydroxy intermediates that then proceed to form formaldehyde (Table S6 in the Supporting Information).[14,25,26] Methanol adsorbs exothermically on the α-MoO_3(010) layer through a hydrogen bond with a terminal oxygen O_t atom to form the **CH_3OH*** structure. The adsorption energy is −0.25 eV and is thus in the range of typical hydrogen bonds. This is the initial configuration that leads to the methanol oxidation pathway by H abstraction to a terminal oxygen atom of the surface through the transition state **TS1M**, with an activation barrier of 1.13 eV. This acid–base activity is common to all oxides.[27] The final dissociated structure, **CH_3O*+OH***, lies 0.38 eV above the molecular adsorption structure. In this step, the terminal oxygen atom loses part of its bond to the Mo centre and the methoxy fragment bonds covalently to the same surface molybdenum atom.

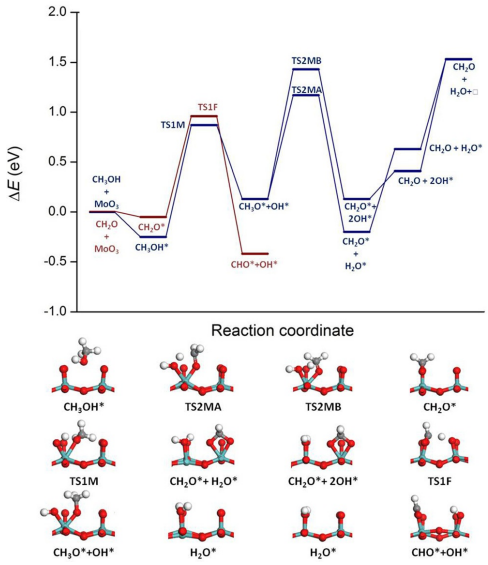

Figure 2. Reaction energy profile for the decomposition of methanol on α-MoO_3(010). Blue lines correspond to methanol and red lines to formaldehyde. The newly formed oxygen vacancy is marked as □. The same colour code as in Figure 1 is used for the structures.

The transfer of the methyl H atom to an O_t atom can lead to the desired product. One of the possibilities consists of the transference of the H atom to the already formed O_tH; that is, the whole reaction takes place on a unique centre on the surface and generates water. This process occurs through the transition state **TS2MA** with an activation barrier of 1.04 eV and leads to a configuration that is placed 0.13 eV below **TS2MA** (not shown in the figure) that presents water and formaldehyde sitting on the same Mo centre. From this structure, formaldehyde can interact with another O_t atom, which leads to a final configuration, **CH_2O*+H_2O***, which is 0.33 eV more stable than the methoxy adsorption state. Desorption of formaldehyde from this configuration is endothermic by $\Delta E=$ 0.83 eV. The water remains bonded to the Mo site in structure **H_2O***. Finally, the release of water from the structure is endothermic by $\Delta E=0.90$ eV. The removal of the last ligand is more endothermic because it encompasses the formation of a vacancy on the surface.

Alternatively, the methyl H atom can be transferred from **CH_3O*+OH*** to any of the O_t surfaces, which thus results in two hydroxy groups. This agrees with the formation of a hydroxylated surface in the form of a bronze of H_xMoO_3 stoichiometry reported[28] if the surface reacts only with methanol at $T=200\,^{\circ}C$. In this path, the H atom is transferred through **TS2MB** with an activation barrier of 1.30 eV. In the final structure, **CH_2O*+2 OH***, the carbon atom from the formaldehyde interacts with a third O_t atom. This configuration is isoenergetic with the previous methoxy adsorption. Desorption of formaldehyde from this structure is slightly endothermic by 0.28 eV. The recombination of hydroxy groups, which is followed by water desorption to the gas phase, again endothermic by 1.12 eV.

The stoichiometric surface is not so effective in the activation of formaldehyde, as the red line in Figure 2 shows. Adsorption of formaldehyde in the form of an oxirane species with $\eta_{2O,O}$ coordination to the Mo centre is weak, with only $\Delta E=-0.05$ eV. The further decomposition, driven by H abstraction, through transition state **TS1F**, cannot compete with desorption.

These results agree with different experimental observations: for instance, the MoO_3(010) surface is known to adsorb methanol weakly according to the temperature-programmed desorption experiments by Sleight and co-workers.[16a,b,29] IR and temperature-programmed reduction analyses performed by Briand et al.[7d] indicated that methanol was dissociatively chemisorbed and was employed for the titration of the active sites.[30] Therefore, under anaerobic conditions, the

ChemPubSoc Europe
CHEMSUSCHEM Full Papers

α-MoO_3(010) surface could strip hydrogen atoms from the methanol but the process is then non-stoichiometric because the terminal oxygen atoms from the surface are consumed. Vacancy formation and replenishing through oxygen is needed for the process to be catalytic. However, vacancy formation, even from water, is endothermic and shows large barriers. This observation is in agreement with the relatively high temperature (close to the MoO_3–MoO_2 transition one) required for the reaction to occur.[18] Therefore, both the relatively low methanol adsorption capacity and vacancy formation are responsible for the poor activity. High temperatures are needed to reach activity and to facilitate oxygen removal. The stoichiometric surface is thus selective.

In situ experiments by Gai and Labun[31] have identified suboxide regions of ordered vacancies, even under reaction mixture conditions. If vacancies appear on the surface (Table S7 in the Supporting Information) of the molybdenum (VI) oxide, the reaction profile changes radically (Figure 3). Adsorption of methanol at the vacancy site is very exothermic ($\Delta E = -1.16$ eV) and the stripping of the hydroxylic proton by a neighbouring O_t atom is very easy: it needs only 0.16 eV (energy barrier). The product is only $\Delta E = 0.07$ eV above the energy of adsorbed methanol. Abstraction of the methyl H atom can occur, either by transfer of the H atom to the already formed O_tH hydroxy group, which results in water, or by transfer of the H atom to another O_t atom, which thus creates two O_tH groups. The energetic barrier to the first path is 1.28 eV,

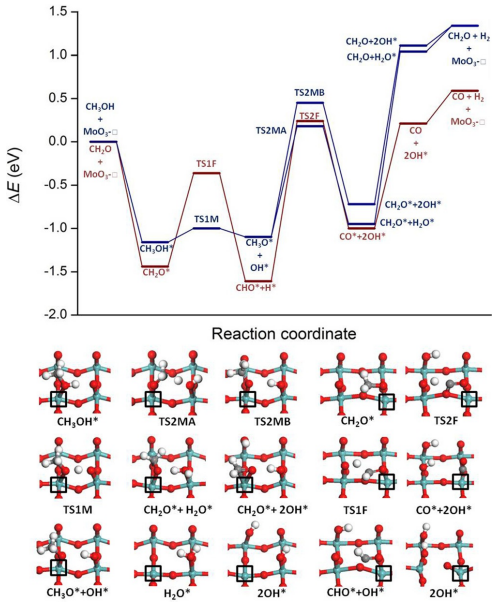

Figure 3. Reaction energy profile for the decomposition of methanol on oxygen-lean α-MoO_3(010)–vacancy. The oxygen vacancy is marked as □. The same colour code as in Figure 2 is used.

via **TS2MA**, and leads to a configuration with the formaldehyde adsorbed through the O atom on the Mo atom of the vacancy and water adsorbed on its Mo centre. This structure is $\Delta E = 1.14$ eV above the methoxy adsorption state but can rotate and contact an O_b atom through the methylene group, to end in a **CH_2O*+H_2O*** structure; the total step is endothermic by $\Delta E = 0.15$ eV. The release of formaldehyde from this structure is too energetically demanding ($\Delta E = 1.99$ eV). In the alternative path, stripping of the methyl H atom occurs through **TS2MB**, with a higher energetic barrier of 1.54 eV. In the final configuration, **CH_2O*+2 OH***, the formaldehyde interacts with the molybdenum atom of the vacancy. The energy of this configuration is 0.38 eV above that of the previous methoxy intermediate. The desorption of formaldehyde is largely endothermic ($\Delta E = 1.83$ eV). The formation of a second vacancy in this system is very large, with $\Delta E = 1.60$ eV from H_2O_t and 2 OH_t. Another possibility is the formation and release of a H_2 molecule. The movement of H atoms over the surface has low energy barriers of around 0.70 eV. The interaction between a hydrogen atom and Mo^{IV} atom presents a hydride character, which could recombine with a proton to create a H_2 molecule as found for other oxides.[32] The total process to create and to release a H_2 molecule is endothermic by $\Delta E = 0.30$ eV in the first path, and by $\Delta E = 0.23$ eV in the second one. This formation of H_2 is in agreement with the experiments.[14]

However, vacancies adsorb oxygen strongly in any form. Therefore, formaldehyde is adsorbed dihapto through an O–Mo contact and the C atom in the methylene bonds with an O_b atom. The corresponding adsorption energy is large −1.44 eV. The barrier for CHO formation, through **TS1F**, is now 1.08 eV, which is lower than that for formaldehyde desorption (in contrast to what happens for the stoichiometric surface). With the final configuration, **CHO*+OH***, this step is exothermic by −0.17 eV. In this step, the H atom is transferred to an O_t atom to form an O_tH group. This proton could be transposed from the O_t atom to another O_t atom with an energy barrier of around 0.70 eV. Finally, the last H atom is transferred to an O_t atom through **TS2F**, with an energy barrier of 1.45 eV. In the final configuration, **CO*+2 OH***, CO is adsorbed carbon down onto a Mo^{IV} centre; this state is 0.62 eV above **CHO*+OH***. CO desorption is endothermic by $\Delta E = 1.21$ eV, whereas hydrogen release is endothermic by $\Delta E = 0.38$ eV. The energy barrier to abstraction of the first H atom of formaldehyde is lower than the energy required to desorb formaldehyde, and, therefore, a complete oxidation of methanol to CO is expected if vacancies appear on the surface. Alternatively, HCO can also react with other hydroxy fragments to generate CO_2 (not shown in Figure 3).

As for the reoxidation of the surface, oxygen vacancies on the α-MoO_3(010)+vacancy surface can trap O_2 molecules and heal.[33] The adsorption energy is −2.14 eV and the oxygen molecule is dihapto coordinated ($\eta_{2O,O}$) with an internal O–O distance of 1.433 Å. Finally, on α-MoO_3(010), the lack of dimethyl ether and CO_2 compounds observed in the experiments[14] is due to the low coverage induced by the endothermic adsorption energy of methoxy compounds on the surface.

ChemPubSoc Europe
CHEMSUSCHEM Full Papers

r-MoO_2(110)

On the r-MoO_2(110) surface, adsorption of methanol (Table S6 in the Supporting Information) through the interaction between a hydroxy group with the Mo_{cus} (undercoordinated site) centre is very exothermic, with a ΔE value of more than 2 eV (Figure 4). The molecular state can easily evolve to the dissociated hydroxy O_bH group and the methoxy group adsorbed on the under-coordinated Mo_{cus} site through **TS1M**, with an energy barrier of only 0.12 eV. The final configuration, **CH_3O*+OH***, lies 0.25 eV below the molecular adsorption state. Therefore, under real typical reaction conditions, all active sites on the surface would be covered by these fragments. Further activation of the methyl H atom is not so straightforward. The process presents an energy barrier of 1.34 eV, which would result in the formation two hydroxy groups on the bridge positions and adsorbed formaldehyde in **CH_2O*+2 OH***. This step is endothermic by $\Delta E = 1.09$ eV. Desorption of the organic compound from the surface is hindered by a sizeable energy barrier of about 1.12 eV. Water evolution is even more hampered because vacancy formation requires more than $\Delta E = 2$ eV for this surface.

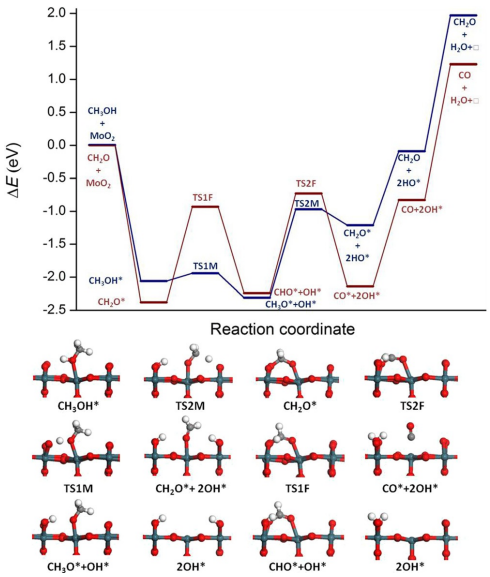

Figure 4. Reaction energy profile for the decomposition of methanol on r-MoO_2(110). The oxygen vacancy is marked as □. The same colour code as in Figure 2 is used.

Unlike the situation with α-MoO_3(010), formaldehyde is more strongly bonded to the surface than the methanol reactant and even the hydroxy–methoxy pair. The most stable configuration, **CH_2O***, has an adsorption energy of −2.38 eV. In this configuration, the O atom interacts with the Mo_{cus} site and the methylene group interacts with a bridging oxygen atom. The activation of formaldehyde is difficult; there is an energy barrier of 1.45 eV to transfer the first H atom. The large residence time of formaldehyde on the surface would compromise activity.

The next step in the decomposition path corresponds to **CHO*+OH*** formation, with one O_bH group whereas the CHO continues to interact with the O_b and Mo_{cus} atoms. Through **TS2F**, the second H atom is transferred to the surface with an energy barrier of 1.51 eV. In the final configuration, there are two O_bH groups and CO is bound to the Mo_{cus} site. Desorption of CO is endothermic by $\Delta E = 1.30$ eV. In comparison, water evolution with concomitant vacancy formation requires $\Delta E =$ 2.07 eV. Therefore, the reaction under anaerobic conditions would likely end with a full surface covered by CO and hydroxy groups.

The reactivity of r-MoO_2(110) at low oxygen exposures will take place as follows. Oxygen is easily split on the r-MoO_2(110) surface and the O atoms in the cus position (Table S8 in the Supporting Information) can then act as stripping agents for the H atom in methanol. The adsorption energy of this O_{cus} atom with respect to gas-phase molecular oxygen is −2.96 eV. The reaction paths are illustrated in Figure 5. Methanol adsorption is very exothermic with $\Delta E = -1.85$ eV. In **CH_3OH***, the hydroxy group interacts with the Mo_{cus} site through the oxygen atom, whereas the hydrogen atom is pointed to the O_{cus} atom. This structure can evolve to **CH_3O*+OH*** with a low energy barrier of 0.14 eV. In this structure, the OH group is dissociated, the methoxy group is bound to the Mo_{cus} centre and the $O_{cus}H$

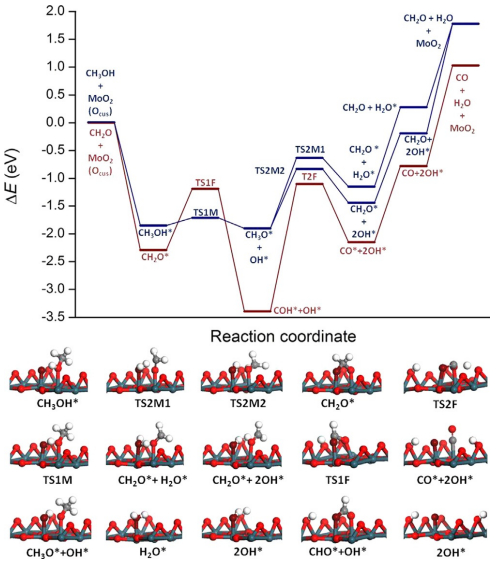

Figure 5. Reaction energy profile for the decomposition of methanol on a partially oxygen-covered MoO_2(110)–O_{cus}. The same colour code as in Figure 2 is used.

group is formed. A second H atom could be transferred to the surface in two different ways, either as a water molecule adsorbed on the Mo_{cus} site or through the formation of an OH group in a bridge position. The first one presents a barrier of 1.27 eV, through **TS2M1** and the second one of 1.07 eV, through **TS2M2**. As with r-MoO_2(110), with these barriers and under real typical reaction conditions, all active sites on the surface would be covered by intermediates. In the first path, once the methylenic hydrogen atom is transferred to the O_{cus} atom, the water molecule and formaldehyde start interacting with the Mo_{cus} centre, in a **CH_2O*+H_2O*** configuration. The reaction energy for this step is 0.75 eV and the desorption of formaldehyde costs $\Delta E = 1.43$ eV. In the second path, the configuration with two O_bH groups and formaldehyde interacting with the Mo_{cus} site, **CH_2O*+2 OH***, lies $\Delta E = 0.46$ eV above the methoxy adsorption. Energy of 1.26 eV is needed to release the formaldehyde from this configuration. Desorption of the O_{cus} atom as a water molecule requires $\Delta E = 1.50$ eV from **CH_2O+H_2O***. After formaldehyde is desorbed from **CH_2O*+2 OH***, the total process to create the H_2O_{cus} molecule and release it is endothermic by $\Delta E = 1.96$ eV.

The red line in Figure 5 represents the path to formaldehyde oxidation on this oxidised surface. The adsorption of formaldehyde is very exothermic with $\Delta E = -2.29$ eV. The oxygen atom interacts with the Mo_{cus} centre and the methylenic group is bound to the O_{cus} atom to form **CH_2O***. The first H atom is transferred to the surface with an energy barrier of 1.10 eV. The resulting structure, **CHO*+OH***, is very stable, with an interaction energy that is 1.10 eV lower than the molecular adsorption state. Stripping of the second H atom is very energy expensive because the energy barrier is 2.28 eV, but the transition state is still below the energy of the reactants by 1.10 eV. In the obtained structure, two O_bH groups are formed and CO is bonded to the Mo_{cus} site; its desorption requires $\Delta E = 1.38$ eV. The recombination of hydrogen atoms with the O_{cus} atom to form water and the subsequent desorption is endothermic by $\Delta E = 1.81$ eV.

The desorption energies of formaldehyde for both MoO_2 surfaces are higher than the barriers needed to completely oxidise formaldehyde. Therefore, selectivity is not expected in either the r-MoO_2(110) stoichiometric or oxidised surfaces.

MoO_3/MoO_2

The oxidation of MoO_2 to MoO_3 can occur under excess oxygen. Experiments indicate that MoO_2 oxidation in 5 vol% of oxygen starts at around $T = 300\,^{\circ}C$.[18] We have investigated the potential growth of an oxidised MoO_3 layer on top of the MoO_2 slab (Figure 1C). This kind of epitaxial registry has been successfully applied to other rutile-based catalysts.[34] Actually, the surface structure of MoO_2 can keep a reasonably good registry between the (110) surface of the reduced system and the (010) surface of the oxidised system. The adhesion of the epitaxial layer to the reduced one accounts for $\Delta E = -0.25$ eV Å^{-2}. This is larger than the bilayer–bilayer interaction of $\Delta E = -0.01$ eV Å^{-2} and even the intra-bilayer value of $\Delta E = -0.03$ eV Å^{-2} for MoO_3.

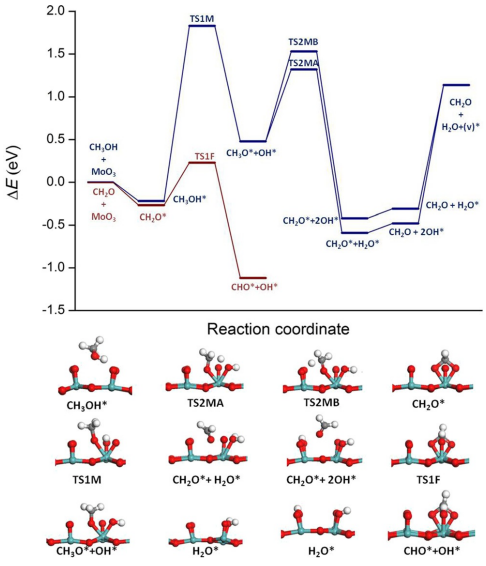

Figure 6. Reaction energy profile for the decomposition of methanol on the epitaxially oxidised MoO_3(010)/MoO_2(110). The same colour code as in Figure 2 is used.

On this system, we have evaluated again the reaction profile for methanol oxidation which is shown by the blue line in Figure 6. Following the same path as that with α-MoO_3(010), the methanol adsorption, **CH_3OH***, is exothermic by $\Delta E = -0.22$ eV, which is practically the same value as with α-MoO_3(010). The stripping of the hydroxy proton through **TS1M** is then an endothermic process by $\Delta E = 0.70$ eV with an energy barrier of 1.77 eV. This is due to the compression of the lattice induced by epitaxial growth. Transfer of the second H atom to the surface presents an energy barrier of 0.84 eV for **CH_2O*+H_2O*** formation and of 1.05 eV to obtain **CH_2O*+2 OH***. These two reaction steps are exothermic by 1.07 and 0.90 eV, respectively. Desorption of the organic species requires about $\Delta E = 0.10$ eV. The vacancy formation and release of water is again endothermic by $\Delta E = 1.62$ and 1.45 eV, respectively. Although the energy barriers are higher than for the α-MoO_3(010) system, this process can occur under the temperatures required for the MoO_3/MoO_2 equilibrium.

For this surface, the adsorption of formaldehyde would compete with the adsorption of methanol. In addition, the energy barrier to strip the first methylene H atom is only 0.50 eV. Therefore, for the MoO_3/MoO_2 oxidised surface, we cannot trace back the selectivity reported in the experiments.[14] As a consequence, a well-developed MoO_3 structure is needed for an active and selective molybdenum catalyst in the methanol to formaldehyde conversion. This agrees with the experimental observation that the catalyst works best during the second cycle.[15]

Comparison to available kinetic measurements

Extensive kinetic tests have demonstrated that the apparent kinetic orders for oxygen and methanol are positive,[23b,35] whereas water inhibits the process.[35c,d,36] These observations completely agree with the mechanistic insight obtained from the calculations, in which the adsorption of both methanol and oxygen is exothermic and thus promotes the reaction and which reveal that water adsorption on the active site is the origin for the observed inhibition. As for the rate-determining step, experiments have identified the C–H activation of the methoxy group[16a,24] that leads to formaldehyde as the crucial elementary step. In our case, this transition state is the highest configuration in the energy profile, which is thus in agreement with the experiments. Moreover, the apparent activation energy was reported to be close to 0.87 eV[23b,35,37] for all catalysts. Our value, with consideration of the zero-point vibrational energy, leads to an apparent activation energy of 0.92 eV. Experiments have also indicated that long residence times of formaldehyde intermediates would result in a lack of selectivity by parallel reactions, as proposed by Busca et al.[38] This correlates with the comparison between adsorption energies and further dehydrogenation reactions described in our methodology.

Role of Fe as dopant

As indicated in the Introduction, the present formulations in the Formox process use Fe-containing molybdenum oxides. As we have seen in the analysis of the pure compounds, the activity of α-MoO_3 is poor as a result of a weak trapping of methanol and the overall activity is controlled by the easy formation of the vacancy on the surface, which is the highest point in the energy profile presented in Figure 2. Thus, the crucial step in the activity of molybdenum oxide is a fast release and regeneration of oxygen in the lattice. In addition, to reach selectivity, the adsorption of formaldehyde needs to be smaller than that of methanol (thermodynamic competitive selectivity)[39] and smaller than the H–C activation in H_2CO, as discussed earlier for CeO_2.[40] The most stable adsorption of formaldehyde involves a vacancy site (bound to the O atom) and an oxygen atom from the lattice that forms a C–O bond in a dioxirane configuration (Figure 3, **CH_2O***). As formaldehyde occupies the position of the O_t atom, selectivity is controlled by how stable this species is. The easier that vacancy formation in α-MoO_3(010) is, the lower the stabilisation of formaldehyde will be. Therefore, the vacancy formation energy is the single descriptor for activity and selectivity of methanol oxidation on molybdenum oxide compounds. A similar reasoning was used as a descriptor for the activity of oxidative dehydrogenation reactions.[15c]

To analyse the role of iron, we have set up a model that contains an α-MoO_3(010) surface in which either a surface or a subsurface Mo atom has been replaced by iron. The energy difference between these two structures is rather small ($\Delta E =$ 0.02 eV) and favours the surface Fe atom. The interpretation of these results is that iron can be in either place without a significant energy cost. We have tested the vacancy formation energies for both structures and compared them with those of the parent compound α-MoO_3(110). Although the value is rather high for the native α-MoO_3(010) ($\Delta E = 2.71$ eV), it is reduced if iron is in the proximity of the Mo–O_t bond, with values of $\Delta E = -0.18$ eV if the Fe atom is on the surface and $\Delta E =$ 1.30 eV if the Fe atom sits in the subsurface region. For the sake of comparison, the formation energy of a defect on the Fe–O_t structure is more exothermic -0.59 eV. The easy formation of vacancies on the surface if Fe is located there actually compromises selectivity.

The reason for such a decrease can be traced back to the geometric reorganisations upon reduction of the surface (Figure 7). In fact, vacancy formation on the pure α-MoO_3(010) surface induces a large rearrangement of the first coordination sphere of oxygen atoms around the under-coordinated Mo centre. In this way, the surrounding oxygen atoms can accept (by reducing the distance to the Mo atom) part of the electronic density that has been left on the defective Mo centre. The resulting elastic relaxation is very large and, thus, the lattice responds by hindering vacancy generation. For the Fe-doped system, the electron storage occurs in a different position instead because the initial Fe^{3+} centre in the lattice can accept part of the electronic excess. The Fe magnetisation rises from 1.29 to 2.33 μ_B (Tables S7–S9 and Figure S4 in the Supporting Information). Therefore, our results show that the system can work through an electron-donor pair, which thus allows a buffering effect on the oxygen content at the molybdenum centre, in a very similar way to doping in CaO.[41]

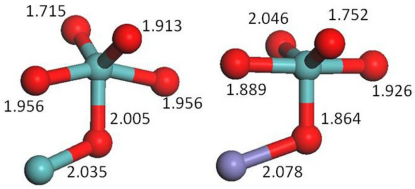

Figure 7. Local structure of the surface vacancy on α-MoO_3(010) and Fe-MoO_3(010) with Mo–O and Fe–O distances given in Å.

These electronic structure properties can then be transferred to the chemical behaviour of the catalyst. On the one hand, activity occurs through the easy formation of vacancies. On the other hand, selectivity is at least partially governed by the competitive adsorption of methanol and formaldehyde. For the native stoichiometric α-MoO_3(010), methanol adsorbs weakly ($\Delta E = -0.25$ eV) and formaldehyde even more weakly ($\Delta E = -0.05$ eV). The situation is reversed if a vacancy exists on this surface because then the adsorption values are $\Delta E =$ -1.16 and -1.44 eV, respectively, which shows the marked preference for formaldehyde that is detrimental to selectivity. If the Fe dopant is in a subsurface position, the adsorption energies are -0.47 and -0.01 eV, respectively. Therefore, the doped system retrieves the thermodynamic selectivity ob-

served for the clean stoichiometric α-MoO_3(010). Finally, if Fe is present on the surface layer, selectivity disappears because vacancy generation is favoured (exothermic processes) and, moreover, these sites then prefer to trap formaldehyde ($\Delta E = -1.44$ versus -1.40 eV; $\Delta E = -1.19$ eV is gained by trapping oxygen; Table S4 in the Supporting Information). This explains why excess MoO_3 is needed in the Formox process.[3b,19b,c]

Conclusions

We have investigated the activity and selectivity of molybdenum-based oxides on the formation of formaldehyde from methanol by means of density functional theory. Our results indicate that MoO_3 activity is linked to the possibility of it forming oxygen vacancies at reasonable energy costs. The active site is a Mo^{VI} centre that cycles to the Mo^{IV} state if forming the vacancy. Therefore, on the MoO_2 surface, an excess of oxygen can generate local species with a Mo^{VI} character, Mo_{cus}, that can also be active. However, the interplay between both oxides is complex and the r-MoO_2(110) surface can form an epitaxial α-MoO_3(010) under oxidation conditions; this surface is not very selective when formed only by an ultra-thin layer. We have also rationalised the role of Fe in the activity and selectivity of the Formox catalyst. We have found that Fe doping in subsurface positions increases the activity and keeps the selectivity of the α-MoO_3(010) by placing the energy cost of vacancy formation in the right window for activity and enhancing the thermodynamic selectivity towards formaldehyde. Moreover, the large relaxations found for the formation of vacancies prevent the use of geometric descriptors as indicative for the activity, as proposed earlier in the literature.

The present results pave the way for a tailored design of new catalytic formulations that can address the stability issues found in the industrial implementation of this catalyst but can retain the activity and selectivity.

Computational Methods

Density functional theory calculations on slab models representing the different potential active phases were carried out with the VASP 5.3.3 package.[42] PBE was the chosen functional,[43] including Grimme's semiempiric correction vdW-D2[44] to reproduce the van der Waals interactions. Projector-augmented wave (PAW) pseudopotentials[45] were used to reproduce the atomic core shells; valence electrons were expanded in plane-waves with a kinetic cutoff energy of 450 eV. The bulk crystals were optimised (Table S1 in the Supporting Information). The reaction network was studied on slab models representing the lowest energy facets. The r-MoO_2(110) model slab contained five trilayers in a supercell that was three times the unit-cell area, with a k-point sampling of $5\times7\times1$. To represent α-MoO_3(010), the slab model contained two bilayers in a (2×2) supercell with a $5\times5\times1$ k-point sampling. The topmost atoms were allowed to relax together with the adsorbates (the upper bilayer for α-MoO_3(010), and the two topmost trilayers for r-MoO_2(110)). To avoid the spurious terms arising from the asymmetry of the slabs, a vacuum gap of 15 Å was added between the slab and its periodic image and a dipole correction along the *z* axis was included.[46] Tests on a model system representing the initial epitaxial oxidation of the topmost r-MoO_2(110) layer are also presented. The calculation setup then follows that of r-MoO_2(110). Tests with a larger energy cutoff demonstrate the stability of the adsorption energy values (Table S5 in the Supporting Information). To allocate the transition-state structures, the nudge elastic band method[47] was used in combination with the so-called climbing image.[48] All stationary points were confirmed through vibrational analysis by diagonalisation of the numeric hessian matrix obtained with 0.02 Å steps.

Acknowledgements

This research has been supported by an ERC Starting Grant (ERC-2010-StG-258406) and MINECO (SVP-2014-068237). We acknowledge BSC-RES for providing generous computational resources.

Keywords: density functional calculations · iron · molybdenum · oxidation · reaction mechanisms

[1] a) G. Reuss, W. Disteldorf, A. O. Gamer, A. Hilt in *Ullmann's Encyclopedia of Industrial Chemistry (Vol. 15)*, Wiley-VCH, Weinheim, **2000**, p. 735; b) http://mcgroup.co.uk/news/20140627/formaldehyde-production-exceed-52-mln-tonnes.html, accessed June 2015.
[2] a) Y. Cao, W.-L. Dai, J.-F. Deng, *Appl. Catal. A* **1997**, *158*, L27 – L34; b) M. Qian, M. A. Liauw, G. Emig, *Appl. Catal. A* **2003**, *238*, 211 – 222.
[3] a) http://www.formox.com, February **2015** ; b) C. Brookes, P. P. Wells, G. Cibin, N. Dimitratos, W. Jones, D. J. Morgan, M. Bowker, *ACS Catal.* **2014**, *4*, 243 – 250.
[4] a) K. I. Ivanov, D. Y. Dimitrov, *Catal. Today* **2010**, *154*, 250 – 255; b) A. Andersson, M. Hernelind, O. Augustsson, *Catal. Today* **2006**, *112*, 40 – 44.
[5] H. Adkins, W. R. Peterson, *J. Am. Chem. Soc.* **1931**, *53*, 1512 – 1520.
[6] J. M. Tatibouët, *Appl. Catal. A* **1997**, *148*, 213 – 252.
[7] a) M. Niwa, M. Mizutani, M. Takahashi, Y. Murakami, *J. Catal.* **1981**, *70*, 14 – 23; b) B. I. Popov, A. V. Pashis, L. N. Shkuratova, *React. Kinet. Catal. Lett.* **1986**, *30*, 129 – 135; c) A. P. Vieira Soares, M. Farinha Portela, A. Kiennemann, L. Hilaire, *Chem. Eng. Sci.* **2003**, *58*, 1315 – 1322; d) L. E. Briand, A. M. Hirt, I. E. Wachs, *J. Catal.* **2001**, *202*, 268 – 278.
[8] T. Ressler, J. Wienold, R. E. Jentoft, F. Girgsdies, *Eur. J. Inorg. Chem.* **2003**, 301 – 312.
[9] A. P. V. Soares, M. F. Portela, *Catal. Rev. Sci. Eng.* **2005**, *47*, 125 – 174.
[10] a) P. Botella, J. M. Lopez Nieto, B. Solsona, A. Mifsud, F. Marquez, *J. Catal.* **2002**, *209*, 445 – 455; b) W. Ueda, D. Vitry, T. Katou, *Catal. Today* **2005**, *99*, 43 – 49.
[11] a) V. Zacharopoulou, E. S. Vasiliadou, A. A. Lemonidou, *Green Chem.* **2015**, *17*, 903 – 912; b) T. Prasomsri, T. Nimmanwudipong, Y. Roman-Leshkov, *Energy Environ. Sci.* **2013**, *6*, 1732 – 1738; c) T. Prasomsri, M. Shetty, K. Murugappan, Y. Roman-Leshkov, *Energy Environ. Sci.* **2014**, *7*, 2660 – 2669; d) J. Guan, G. Peng, Q. Cao, X. Mu, *J. Phys. Chem. C* **2014**, *118*, 25555 – 25566; e) D. Mei, A. M. Karim, Y. Wang, *J. Phys. Chem. C* **2011**, *115*, 8155 – 8164.
[12] a) Z. Li, Z. Fang, M. S. Kelley, B. D. Kay, R. Rousseau, Z. Dohnalek, D. A. Dixon, *J. Phys. Chem. C* **2014**, *118*, 4869 – 4877; b) R. Rousseau, D. A. Dixon, B. D. Kay, Z. Dohnalek, *Chem. Soc. Rev.* **2014**, *43*, 7664 – 7680; c) Z. Fang, Z. Li, M. S. Kelley, B. D. Kay, S. Li, J. M. Hennigan, R. Rousseau, Z. Dohnalek, D. A. Dixon, *J. Phys. Chem. C* **2014**, *118*, 22620 – 22634.
[13] M. G. O'Brien, A. M. Beale, S. D. M. Jacques, T. Buslaps, V. Honkimaki, B. M. Weckhuysen, *J. Phys. Chem. C* **2009**, *113*, 4890 – 4897.
[14] M. Bowker, A. Carley, M. House, *Catal. Lett.* **2008**, *120*, 34 – 39.
[15] a) R. K. Grasselli, *Top. Catal.* **2002**, *21*, 79 – 88; b) J. Ziolkowski, *J. Catal.* **1983**, *84*, 317 – 332; c) M. V. Ganduglia-Pirovano, C. Popa, J. Sauer, H. Abbott, A. Uhl, M. Baron, D. Stacchiola, O. Bondarchuk, S. Shaikhutdinov, H.-J. Freund, *J. Am. Chem. Soc.* **2010**, *132*, 2345 – 2349.
[16] a) W. E. Farneth, F. Ohuchi, R. H. Staley, U. Chowdhry, A. W. Sleight, *J. Phys. Chem.* **1985**, *89*, 2493 – 2497; b) W. E. Farneth, E. M. McCarron III, A. W. Sleight, R. H. Staley, *Langmuir* **1987**, *3*, 217 – 223; c) J. M. Tatibouet, J. E. Germain, *J. Catal.* **1981**, *72*, 375 – 378; d) J. M. Tatibouet, J. E. Germain, J. C. Volta, *J. Catal.* **1983**, *82*, 240 – 244.

[17] K. Routray, L. E. Briand, I. E. Wachs, *J. Catal.* **2008**, *256*, 145 – 153.
[18] T. Ressler, J. Wienold, R. E. Jentoft, T. Neisius, *J. Catal.* **2002**, *210*, 67 – 83.
[19] a) V. Massarotti, G. Flor, A. Marini, *J. Appl. Crystallogr.* **1981**, *14*, 64 – 65; b) E. Söderhjelm, M. P. House, N. Cruise, J. Holmberg, M. Bowker, J.-O. Bovin, A. Andersson, *Top. Catal.* **2008**, *50*, 145 – 155; c) G. Jin, W. Weng, Z. Lin, N. F. Dummer, S. H. Taylor, C. J. Kiely, J. K. Bartley, G. J. Hutchings, *J. Catal.* **2012**, *296*, 55 – 64.
[20] N. N. Greenwood, A. Earnshaw, *Chemistry of the Elements (Chapter 23)*, Elsevier, **1997**.
[21] a) M. Dieterle, G. Weinberg, G. Mestl, *Phys. Chem. Chem. Phys.* **2002**, *4*, 812 – 821; b) M. Labanowska, *Phys. Chem. Chem. Phys.* **1999**, *1*, 5385 – 5392; c) G. Mestl, P. Ruiz, B. Delmon, H. Knozinger, *J. Phys. Chem.* **1994**, *98*, 11283 – 11292.
[22] a) E. M. Fernández, P. G. Moses, A. Toftlund, H. A. Hansen, J. I. Martinez, F. Abild-Pedersen, J. Kleis, B. Hinnemann, J. Rossmeisl, T. Bligaard, J. K. Nørskov, *Angew. Chem. Int. Ed.* **2008**, *47*, 4683 – 4686; *Angew. Chem.* **2008**, *120*, 4761 – 4764; b) J. I. Martinez, H. A. Hansen, J. Rossmeisl, J. K. Nørskov, *Phys. Rev. B* **2009**, *79*, 045120.
[23] a) M. Ai, *J. Catal.* **1978**, *54*, 426 – 435; b) N. Pernicone, F. Lazzerin, G. Liberti, G. Lanzavecchia, *J. Catal.* **1969**, *14*, 293 – 302.
[24] a) T. J. Yang, J. H. Lunsford, *J. Catal.* **1987**, *103*, 55 – 64; b) C. J. Machiels, A. W. Sleight, *J. Catal.* **1982**, *76*, 238 – 239.
[25] J. S. Chung, R. Miranda, C. O. Bennett, *J. Catal.* **1988**, *114*, 398 – 410.
[26] M. Bowker, R. Holroyd, A. Elliott, P. Morrall, A. Alouche, C. Entwistle, A. Toerncrona, *Catal. Lett.* **2002**, *83*, 165 – 176.
[27] H. Metiu, S. Chretien, Z. Hu, B. Li, X. Sun, *J. Phys. Chem. C* **2012**, *116*, 10439 – 10450.
[28] J. Guidot, J. E. Germain, *React. Kinet. Catal. Lett.* **1981**, *15*, 389 – 393.
[29] U. Chowdhry, A. Ferretti, L. E. Firment, C. J. Machiels, F. Ohuchi, A. W. Sleight, R. H. Staley, *Appl. Surf. Sci.* **1984**, *19*, 360 – 372.
[30] a) L. J. Burcham, I. E. Wachs, *Catal. Today* **1999**, *49*, 467 – 484; b) L. J. Burcham, I. E. Wachs, L. E. Briand in *Proceedings of the 16th Meeting of the North American Catalysis Society* **1999**, ACS, Boston, p. 170; c) L. E. Briand, W. E. Farneth, I. E. Wachs, *Catal. Today* **2000**, *62*, 219 – 229.
[31] P. L. Gai, P. A. Labun, *J. Catal.* **1985**, *94*, 79 – 96.
[32] M. García-Melchor, N. López, *J. Phys. Chem. C* **2014**, *118*, 10921 – 10926.
[33] R. Coquet, D. J. Willock, *Phys. Chem. Chem. Phys.* **2005**, *7*, 3819 – 3828.
[34] G. Novell-Leruth, G. Carchini, N. Lopez, *J. Chem. Phys.* **2013**, *138*, 194706/194701 – 194706/194710.
[35] a) J. M. Tatibouet, J. E. Germain, *C. R. Seances Acad. Sci., Ser. C* **1979**, *289*, 305 – 308; b) J.-M. Tatibouet, J.-E. Germain, *C. R. Seances Acad., Sci. Ser. C* **1979**, *289*, 301 – 304; c) N. Pernicone, F. Lazzerin, G. Liberti, G. Lanzavecchia, *J. Catal.* **1969**, *14*, 391 – 393; d) C. J. Machiels, A. W. Sleight, *Proceedings of the Climax Fourth International Conference on the Chemistry and Uses of Molybdenum*, Climax Molybdenum Co., MI, **1982**, pp. 411 – 414.
[36] W.-H. Cheng, *J. Catal.* **1996**, *158*, 477 – 485.
[37] C. Louis, J. M. Tatibouet, M. Che, *J. Catal.* **1988**, *109*, 354 – 366.
[38] a) G. Busca, A. S. Elmi, P. Forzatti, *J. Phys. Chem.* **1987**, *91*, 5263 – 5269; b) G. Busca, *J. Mol. Catal.* **1989**, *50*, 241 – 249; c) A. S. Elmi, E. Tronconi, C. Cristiani, J. P. Gomez Martin, P. Forzatti, G. Busca, *Ind. Eng. Chem. Res.* **1989**, *28*, 387 – 393; d) G. Busca, J. Lamotte, J. C. Lavalley, V. Lorenzelli, *J. Am. Chem. Soc.* **1987**, *109*, 5197 – 5202; e) G. Busca, *Catal. Today* **1996**, *27*, 457 – 496.
[39] Y. Segura, N. López, J. Pérez-Ramírez, *J. Catal.* **2007**, *247*, 383 – 386.
[40] M. Capdevila-Cortada, M. García-Melchor, N. López, *J. Catal.* **2015**, *327*, 58 – 64.
[41] J. Andersin, J. Nevalaita, K. Honkala, H. Hakkinen, *Angew. Chem. Int. Ed.* **2013**, *52*, 1424 – 1427; *Angew. Chem.* **2013**, *125*, 1464 – 1467.
[42] a) G. Kresse, J. Furthmüller, *Phys. Rev. B* **1996**, *54*, 11169 – 11186; b) G. Kresse, J. Furthmüller, *Comput. Mater. Sci.* **1996**, *6*, 15 – 50.
[43] J. P. Perdew, K. Burke, M. Ernzerhof, *Phys. Rev. Lett.* **1996**, *77*, 3865 – 3868.
[44] S. Grimme, *J. Comput. Chem.* **2006**, *27*, 1787 – 1799.
[45] G. Kresse, D. Joubert, *Phys. Rev. B* **1999**, *59*, 1758 – 1775.
[46] G. Makov, M. C. Payne, *Phys. Rev. B* **1995**, *51*, 4014 – 4022.
[47] G. Mills, H. Jonsson, G. K. Schenter, *Surf. Sci.* **1995**, *324*, 305 – 337.
[48] G. Henkelman, B. P. Uberuaga, H. Jonsson, *J. Chem. Phys.* **2000**, *113*, 9901 – 9904.

Received: March 3, 2015
Published online on June 17, 2015

UNIVERSITAT ROVIRA I VIRGILI
MOLYBDENUM OXIDES AS CATALYST FOR BIOMASS-DERIVED COMPOUNDS: A THEORETICAL APPROACH
Marcos Rellán Piñeiro

One oxygen vacancy, two charge states: characterization of reduced α-MoO_3(010) through theoretical methods

*Marcos Rellán-Piñeiro and Núria López**

Institute of Chemical Research of Catalonia, ICIQ, and The Barcelona Institute of Science and Technology, BIST, Av. Països Catalans 16, 43007 Tarragona Spain

AUTHOR INFORMATION

Corresponding Author

*E-mail: nlopez@iciq.es

ABSTRACT

Molybdenum oxides are finding increasing applications that rely on their redox character. On the most common polymorph, α-MoO_3, oxygen vacancy formation leaves two electrons on the surface that can be stored as small polarons. Detailed Density Functional Theory calculations that properly account for the self-interaction term, U_{eff}, show that the vacancy generates two different configurations: either two Mo^{5+} centers (Mo^{5+}□ and Mo^{5+}=O) or a single doubly reduced Mo^{4+}. These states are separated by 0.22 eV with a barrier for interconversion of 0.33 eV, thus both are populated at catalytic temperatures as it is shown by first principles Molecular Dynamics. At higher reduction levels, vacancies can only be accumulated along a preferential direction and the energy difference between the 2xMo^{5+} and Mo^{4+} configurations is reduced. These results point out to the need for a revision of the experimental assignments based on our characterization that includes charges, vibrational frequencies, and XPS signatures.

TOC GRAPHICS

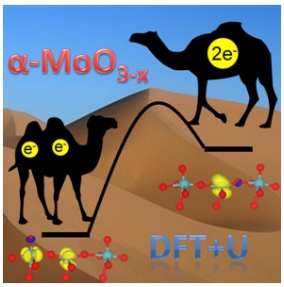

The properties of oxides are dominated by defects, commonly oxygen vacancies.[1-2] Vacancies affect the electronic structure of materials as the two electrons left upon O removal can be: (i) a localized pair at the position of the anion (like for MgO);[3] (ii) separated and localized at the surrounding cations like for TiO_2 and CeO_2 effectively leaving two M^{3+};[4-5] (iii) partially delocalized between a group of metals, like for In_2O_3.[6-7] Recently, Molybdenum oxides have attracted a lot of attention due their large number of new physical and chemical applications as electro- and chromic devices, photo-, electro- and thermal catalysis, in solar cells and as light emitting diodes, photodetectors/sensors, batteries, pseudocapacitors, thermoelectric and ferroelectric materials.[8] All these applications are based on the versatile geometric (with several structure forms)[9,10] and electronic structure linked to the redox character that can be fine-tuned by the addition of cations[11-12] or hydrogen,[13-15] or by oxygen removal,[16] which leads to the formation of Magnéli phases.

In the most common polymorph, α-MoO_3, Mo centers are in the oxidation state, Mo^{6+}, and surrounded by oxygen atoms in octahedral environments with a band gap between 3.0-3.2 eV.[17-19] α-MoO_3 has an orthorhombic unit cell with P*bnm* symmetry where distorted MoO_6 octahedra are ordered in bilayers along the xz plane, see **Figure 1**. Van der Waals interactions hold the layered structure packed. There are three non-equivalent oxygen atoms: (i) three coordinated oxygens, O_{3c}, that form a symmetrical bridge along the x axis between two Mo centers of the same layer and interact with a sublayer Mo; (ii) asymmetric oxygens, O_b, that bridge two Mo centers along the z axis; (iii) terminal oxygens, O_t, double bonded to only one Mo center present in the interlayer region. Oxygen depletion severely affects the electronic structure of the material changing its very large work function (around 6.9 eV) to lower values around 6.5 eV for a 10% oxygen deficient material, introducing donor gap states.[20] Upon reduction, the photoemission

spectra presents additional features: at low vacancy concentrations, these features are assigned to the formation of Mo^{5+} centers, and after a certain concentration, Mo^{4+} features also appear.[20-22] Electron Paramagnetic Resonance, EPR, studies also indicate the formation of structural point defects of Mo^{5+} close to oxygen vacancies which at higher concentrations lead to the formation of other centers associated to extended shear structures.[23] Raman vibrational[24] spectroscopy points out the fingerprints for 996, 823 cm^{-1} (M=O asymmetric and symmetric strechings) and 667 cm^{-1} (asymmetric O-Mo-O). Additional Raman features at 1004 and 1008 cm^{-1} appear at low reduction levels[25] that disappear at longer reduction times, or by hydrogen adsorption and electron beam treatment.[26-27]

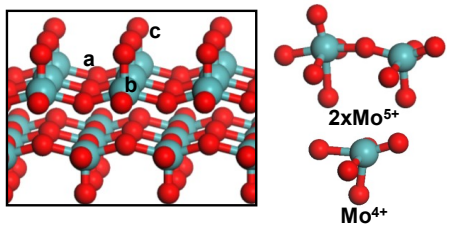

Figure 1. Structures of α-MoO_3(010) pristine surface, left, and local structure of the two possible O_t vacancies, right. a: O_{3c}, b: O_b and c: O_t. Mo: green and O: red.

Understanding the electronic properties of α-MoO_3 from first principles[28] has been hampered by the presence of the layered structure, the semiconductor character of the material, and the reducibility of the cation. Hybrid methods have been applied, for instance, to evaluate the vacancy formation energy in the bulk, which is endothermic by 3.68 eV within HSE06.[29] However, the use of these functionals remains unpractical when exploring complex reaction

networks on the material. Alternatively, DFT Generalized Gradient Approximations, GGA, have been employed. In α-MoO_3 studies with pure GGA functionals[30-33] electron localization is not found, and thus, isolated oxidation states cannot be assigned. The empirical U_{eff} parameter needs to be incorporated to achieve localization.[34] In the literature, scattered U values have been used. Bulk calculations with U_{eff}=5.0 eV were employed to analyze the preferential oxygen eliminated. O_t was identified as the easiest to remove, but the nature of the charge state was not described.[35] With a value of U_{eff}=6.3 eV vacancy formation at O_t atom in the bulk leads to a Mo^{4+} center while removal of the O_b or O_{3c} lattice oxygen ends up in the formation of two Mo^{5+} centers.[27, 36] A recent study with U_{eff}= 6.0 eV suggested the formation of two different states upon reduction, but no characterization was performed, and low vacancy formation energies, ~1.50 eV, were reported.[37]

In surface models, a value of around 6 eV was obtained by fitting to hybrids calculations on cluster structure and it was employed by Chen,[38] Asta,[39] and Willock[40]. The latter reported the formation of a Mo^{4+} center. In turn, Metiu[41-42] and Bell[43-44] proposed a U_{eff} value to match the experimental enthalpy of the reaction $MoO_3 + H_2 \rightarrow MoO_2 + H_2O$, but they reported very different values, 2 and 8.6 eV, respectively. Metiu found out no localization for the O_t removal and two Mo^{5+} when the vacancy is formed at the O_{3c} position. Therefore, the origin of the different oxidation states observed in experiments cannot be assigned from the previous computational studies.

In this work, we reoptimized the U_{eff} value to describe the reactivity on α-MoO_3(010) accurately, following a set of benchmarks that include the comparison to hybrid functionals and CCSD(T) references, see **Section SI1**. Then, we employed PBE+U-D2 to identify the true nature

of vacancies in terms of oxidation state of the cations, and the corresponding spectroscopic fingerprints.

The bulk PBE-D2 calculated lattice parameters are a=3.921, b=14.480 and c=3.708 Å, in agreement with the experimental values: a=3.963, b=13.855 and c=3.696 Å.[45] Because of the layered packing through dispersion forces along the y axis, the (010) surface is the easiest to cleave. The calculated surface energy was 0.01 eVÅ^{-2} within PBE. The density of states (DOS) of the pristine material shows a small band gap of 1.99 eV with the valence band formed by O(2p) and the conduction band by Mo(4d). The Bader charge analysis of the Mo centers provides a value of 2.67 |e$^-$| which is well below the formal charge.

Either the terminal or the two in oxygens plane surface could be the first ones to be removed. Vacancy (V) formation energies for the reaction $MoO_3 \rightarrow MoO_{3-x} + ½\ O_2(g)$ in O_t and O_{3c} position are shown in **Figure 2**. For the O_t-O_b pair it is found that the calculations within PBE result in similar geometries (the remaining oxygen stays at an intermediate position between that of O_t and O_b) and similar formation energies[31-32, 40]. However, in our PBE+U calculations, the converged V_{Ot} geometry keeps the O_b in the surface plane, whereas all our attempts to converge a V_{Ob} resulted in a displacement of the O_t to the O_b position and the convergence in the same O_t vacancy geometry. Therefore, no vacancies appear at O_b positions on the (010) surface. In turn, the formation of O_t vacancies is endothermic, between 2.61 and 2.87 eV, whereas that of O_{3c} requires an additional 1.80 eV, see **Table SI1** and **Table SI2**. The large difference in energy indicates that vacancies are preferentially formed at O_t positions (V_{Ot}), which is in agreement with previous studies.[37, 40]

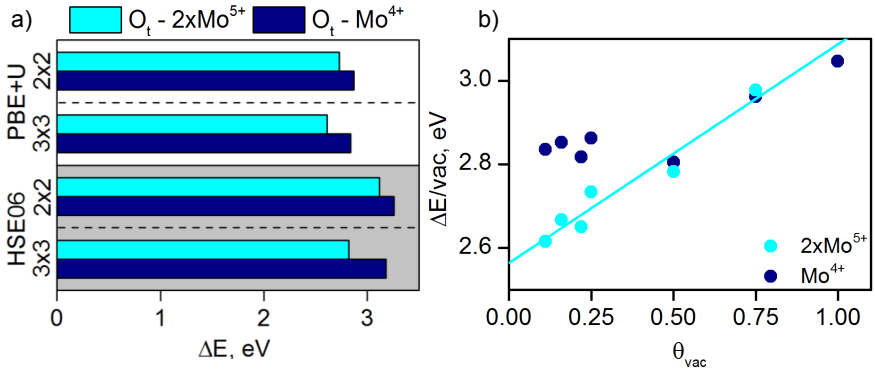

Figure 2. a) V_{Ot} Vacancy formation energy according to the reaction $MoO_3 \rightarrow MoO_{3-x} + ½\ O_2(g)$ calculated on the (2x2) and (3x3) supercells at PBE+U and HSE06 levels. b) V_{Ot} Vacancy formation energy as a function of oxygen depletion for $2xMo^{5+}$ and Mo^{4+} states at PBE+U, U_{eff}=3.5 eV.

V_{Ot} can be present in two different electronic configurations.[37] The ground state has a vacancy formation energy of 2.61 eV (3x3 supercell). In the local geometry of this configuration the undercoordinated Mo (Mo_{cus}) cation shortens the long Mo-O_b and the Mo- O_{3c} sublayer bonds by 0.308 and 0.417 Å, whereas its neighboring Mo (still six-fold coordinated) increases Mo-O_b distances by 0.244 and 0.283 Å, see **Figure 3**. The charge of these two centers differs from that of the pristine surface as 2.48-2.49 $|e^-|$ values are retrieved. The DOS in **Figure 3** shows how one electron is located in a *d*-orbital of each reduced Mo, and the *d*-orbital of the undercoordinated Mo is lower in energy. The electron magnetization is slightly higher in the undercoordinated center: 0.96 vs 0.83 μ_B. Therefore, this configuration corresponds to Mo^{5+}(□)-O-Mo^{5+}(=O), so both Mo, where the vacancy is created (□) and the neighboring cation, have a 5+ character.

A second configuration with a vacancy formation energy of 2.84 eV has also been obtained. In it, the Mo_{cus}-O bond distances with the oxygens of the surface layer are similar to those of the regular surface, but the Mo atom sinks and reinforces its coordination to O_{3c}, the distance is shortened by 0.309 Å, see **Figure 3**. The metal charge is 2.24 $|e^-|$. The DOS clearly shows the localization of the two electrons, with the same spin, in two different *d*-orbitals of the Mo^{4+} center, according with the calculated magnetization of 1.70 μ_B. Therefore, this structure is assigned to the formation of a single double reduced $Mo^{4+}(\square)$ center.

Benchmarks performed with the hybrid functional at this concentration (1/9) and the PBE+U geometries lead to a slightly higher vacancy formation energy range: 2.82 and 3.18 eV. The reoptimized PBE+U (U_{eff}=6.3 eV) energies are much lower, 1.72 and 1.88 eV, but even at these geometries the HSE06 values are 2.93 and 3.30 eV, thus highlighting the critical choice of the U_{eff} when reproducing the formation energies. In summary, the ground state can be identified as a bi-polaron where two electrons are localized on two neighboring Mo centers (Mo^{5+}), whereas the metastable state corresponds to a single dipolaron at the same center (see **Figure 4a)** and the energy difference is well-represented by PBE+U, U_{eff}=3.5 eV.

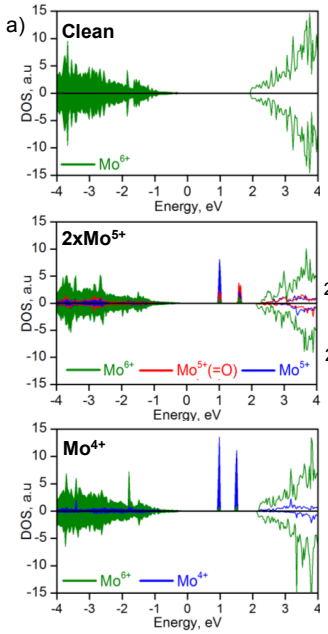

c)

μ	q	XPS
0	2.67	0
υ(Mo=O$_t$)	**υ(Mo-O$_b$)**	**υ(Mo-O$_{3c}$)**
974	875	707

μ	q	XPS
0.96	2.49	-0.94
0.83	2.48	-0.62
υ(Mo=O$_t$)	**υ(Mo-O$_b$)**	**υ(Mo-O$_{3c}$)**
-	840	753
989	776	707

μ	q	XPS
1.70	2.24	-1.29
υ(Mo=O$_t$)	**υ(Mo-O$_b$)**	**υ(Mo-O$_{3c}$)**
-	836	717

Figure 3. a) Projected density of States, b) local geometry with Mo-O bond distances, in Å, and c) fingerprints for the clean surface and the two different states corresponding to the V_{Ot}. Magnetization, μ, in μ_B; Bader charges, q, in $|e^-|$; XPS displacement in eV; and frequencies in cm^{-1}.

We have inspected how concentration affects the V_{Ot} vacancy formation energies, **Figure 2b**. $2xMo^{5+}$-like defects are increasingly more costly (with a linear dependence on concentration), whereas Mo^{4+} ones are independent of the concentration until coverage reaches 0.5. Moreover, vacancies cannot be accumulated through the [100] direction for both configurations, see **Table SI1**. The origin of this vacancy aligment is at the core of the relaxations observed when the

vacancy is formed. When two neighboring vacancies are aligned along [100], the shared O_{3c} sinks towards the subsurface Mo atom (reduces its bond length by 0.1 Å). This ends up increasing the vacancy formation energy. Vacancies would then accumulate on the perpendicular direction generating crystal shears that induce the formation of Magnéli phases.

Next, we analyzed the interconversion between the two vacancy configurations. α-MoO_3 is known to generate small polarons upon electron addition[36, 39] which are highly mobile, with reported barriers of 0.35 eV in the plane and 0.50 eV between bilayers.[36, 39] The CI-NEB results in a barrier for the conversion between oxidation states $2xMo^{5+} \leftrightarrow Mo^{4+}$ of around 0.3 eV. The barrier is low enough to ensure that the two states are in equilibrium even at room temperatures. Therefore, we performed first principles Molecular Dynamics, MD, simulations to illustrate the dynamic nature of the electronic states in V_{Ot}. The local magnetization of the surface centers is shown in **Figure 4b** along the 10 ps trajectory at 300 ºC. The main features are that the Mo_{cus} is preferentially Mo^{5+} but also samples Mo^{4+} states, the second polaron is localized either preferentially along the [001] direction or in zigzag, but not in the nearest neighbor along the [100] direction. At the temperatures at which α-MoO_3 catalyzes reactions take place (around 300ºC), the relative Boltzmann population at low reduction levels (θ_{VOt}=0.25 ML) is around 93% of Mo^{5+} and about 7% of the Mo^{4+} configuration, from our MD trajectory these values are 95 and 5%. This is remarkable as experiments have shown that materials reduced at 350ºC and quantified by the XPS fingerprints provide a 93:7 for Mo^{5+}:Mo^{4+}.[21]

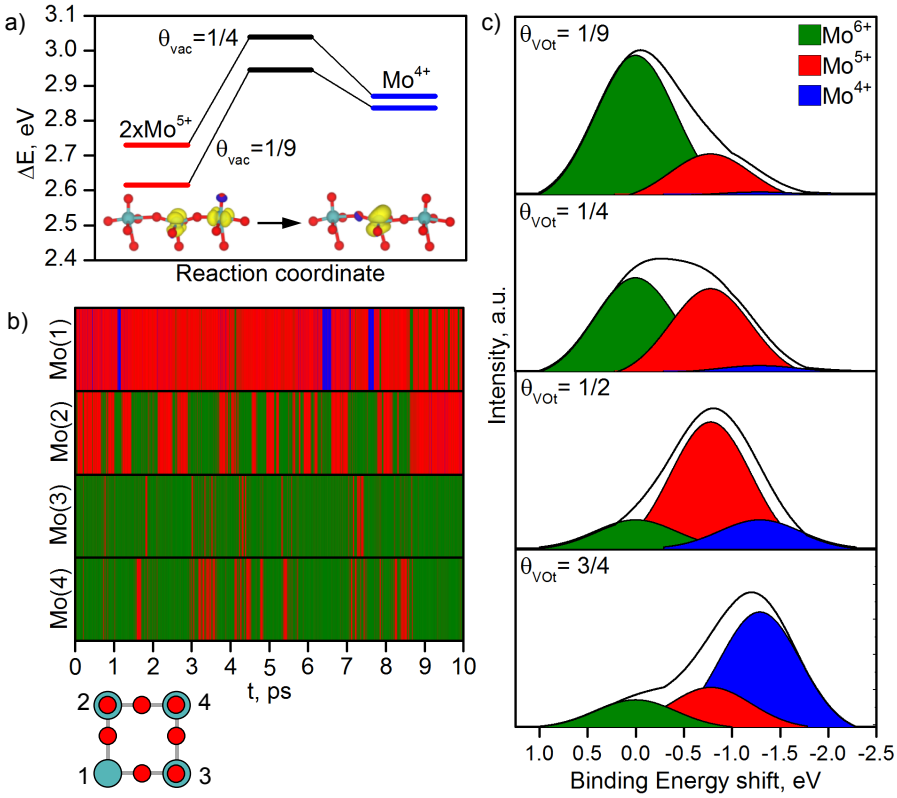

Figure 4. a) Energy profile for the electron hopping for the conversion $2xMo^{5+} \rightarrow Mo^{4+}$ on the (2x2) and (3x3) supercells and calculated spin density for the two surface states at $0.01e^{-}Å^{-3}$. b) Surface Mo local magnetization as a function of time for the Molecular Dynamics run at 300ºC and θ_{VOt}=0.25ML (atom labels shown in the scheme). c) Calculated XPS at different vacancy coverages, θ_{VOt} , at 350ºC. Green Mo^{6+}, red Mo^{5+} and blue Mo^{4+}.

The experimental fingerprints of oxygen deficient α-MoO_3 can then be reanalyzed considering the dual nature of the vacancies. For instance, the Raman fingerprint of α-MoO_3 are three characteristical bands: Mo=O_t and Mo-O_b stretchings, at 996, 823, and Mo-O_{3c} at 667 cm^{-1}, respectively.[46-47] We have calculated the vibrational modes of the different coordination spheres of Mo centers. The reference Mo=O_t is 974 cm^{-1}, which increases by 15 cm^{-1} for the hexacoordinated Mo^{5+} in the Mo^{5+}(□)-O-Mo^{5+}(=O) in agreement with the bands over 1000 cm^{-1} identified in the experiments.[25] In addition, the stretching frequency for Mo-O_b bond is reduced by 35-40 cm^{-1} for undercoordinated cations, and, more importantly, it is reduced by 100 cm^{-1} for the octahedral Mo^{5+}, and therefore could be a fingerprint to this Mo^{5+}(=O) center. The frequency for the Mo-O_{3c} stretching increases for the undercoordinated cations: 10 and 36 cm^{-1} for Mo^{4+} and Mo^{5+} respectively. Thus, this mode can be used to discriminate different states. Complementary, experimental XPS[21-22] on reduced MoO_3 shows the peaks for Mo^{6+}, Mo^{5+} and Mo^{4+} surface centers. For Mo^{5+} the peaks are displaced around -1.80 eV, and for Mo^{4+} -3.0 eV. We calculated the theoretical XPS displacement obtaining values of -0.94 eV and -1.29 eV for Mo^{5+} and Mo^{4+}, respectively. As shown in **Figure 4c** increasing vacancy concentrations would have a dramatic effect on the shape of the XPS spectra.

The ability of the Mo centers to reach different oxidation states can have implications in the chemistry of the oxide. To analyze this we have calculated the adsorption for two key species in the Formox (methanol to formaldehyde) process.[30] While methanol adsorbs through the hydroxyl to the Mo_{cus} by -1.55 eV in both Mo^{4+} and 2xMo^{5+}; formaldehyde bonds to both Mo_{cus} and an O_b by -1.60 and -1.83 eV for the Mo^{5+} and the Mo^{4+} centers, respectively (see **Figure SI3**). The single-site adsorption by lone pair donation of methanol is rather independent of the oxidation state of the metal atom. In contrast, the covalent bifunctional coordination of formaldehyde

perturbs the structure ($2xMo^{5+}$ the Mo_{cus}-O_b-Mo angle changes from 160º to 155º upon adsorption but does not affect Mo^{4+}) thus the adsorption energies for the electronic configurations are different.

In summary, a reaction-thermodynamics adapted PBE+U scheme has been employed to describe the nature of vacancies in α-MoO_3(010). The removal of terminal oxygens generates two different configurations: the ground state configuration is two Mo^{5+}polarons, separated by 0.2 eV of the metastable configuration with a single Mo^{4+}. The interconversion is possible through polaron hopping, and at relevant catalytic temperatures the relative populations are 93:7. Therefore, complex spectroscopic patterns observed for this material might be due to different population of ground and metastable states that correspond to a unique type of atom deficieny. This might have implications in the electronic and transport properties, Magnéli phase formation and chemical properties as, the adsorption from the different states can be different and the phenomenum will appear for oxides in which the cations can adopt multiple low oxidation states.

COMPUTATIONAL METHODS

The Vienna ab Initio Simulation Package (VASP), version 5.3.3, was used to perform the Density Functional Theory (DFT) calculations on slabs models.[48-49] PBE[50] with Grimme's semiempiric D2[51] and U approximation[34] (PBE+U-D2) and BEEF-vdW[52] that contains vdW-DF2[53] nonlocal correlation energy were used in the benchmark. In addition, single points with the hybrid HSE06 functional were performed at PBE+U geometries with U_{eff} = 0, 3.5 and 7.0 eV.[54-55] The core electrons were described by the projector-augmented wave (PAW) pseudopotentials,[56] (with 14 valence electrons for Mo atoms) and valence ones were expanded in

plane waves with a kinetic cut-off energy of 450 eV. Spin polarization was taken into account in all cases.

The bulk was optimized for the PBE functional with a 11x3x11 k-point mesh and a cut-off energy of 600 eV and employed in all calculations. The (010) surface containing two bilayers was cleaved and benchmark calculations were performed on a (2x2) supercell with a 5x5x1 k-point sampling. Vacancy formation was studied on a (2x2), (3x3), (2x3), and (3x2) supercell with a 3x3x1, 5x5x1, 5x3x1 and 3x5x1 k-point sampling respectively. HSE06 single point calculations were performed with 3x3x1 k-point mesh for the (2x2) supercell and Γ-point sampling for (3x3) supercell. During the optimizations, the upper bilayer and adsorbates were relaxed except stated otherwise. A vacuum gap of 15 Å was added to prevent the interaction between slabs together with the dipole correction.[57] Complementary, the first principles Molecular Dynamic run was performed in the Born-Oppenheimer approximation on a (2x2) supercell with one vacancy defect at 300ºC during 10 ps, with 2 ps of equilibration. The most relevant structures have been added to the ioChem-BD database[58] and can be consulted in the following link.[59]

ASSOCIATED CONTENT

The following files are available free of charge.

Supporting_information.pdf (PDF)

AUTHOR INFORMATION

The authors declare no competing financial interests.

ACKNOWLEDGMENTS

We thank the Spanish Ministerio de Economía y Competitividad (MINECO) for financial support (CTQ 2015-68770-R, Severo Ochoa Excellence Accreditation 2014–2018 SEV-2013-

0319, and Severo Ochoa predoctoral grant SVP-2014-068237). In addition, we thank BSC-RES for providing computational resources. We would like to thank Dr. Marçal Capdevila-Cortada for valuable suggestions.

REFERENCES

1. Pacchioni, G. Oxygen Vacancy: The Invisible Agent on Oxide Surfaces. *ChemPhysChem* **2003,** *4* (10), 1041-1047.

2. Henrich, V. E.; Cox, P. A. *The surface science of metal oxides*. Cambridge university press: 1996.

3. Carrasco, J.; López, N.; Illas, F. First Principles Analysis of the Stability and Diffusion of Oxygen Vacancies in Metal Oxides. *Phys. Rev. Lett.* **2004,** *93* (22), 225502.

4. Kowalski, P. M.; Camellone, M. F.; Nair, N. N.; Meyer, B.; Marx, D. Charge Localization Dynamics Induced by Oxygen Vacancies on the TiO_2(110) Surface. *Phys. Rev. Lett.* **2010,** *105* (14), 146405.

5. Ganduglia-Pirovano, M. V.; Da Silva, J. L. F.; Sauer, J. Density-Functional Calculations of the Structure of Near-Surface Oxygen Vacancies and Electron Localization on CeO_2(111). *Phys. Rev. Lett.* **2009,** *102* (2), 026101.

6. Walsh, A.; Da Silva, J. L. F.; Wei, S.-H.; Körber, C.; Klein, A.; Piper, L. F. J.; DeMasi, A.; Smith, K. E.; Panaccione, G.; Torelli, P.; Payne, D. J.; Bourlange, A.; Egdell, R. G. Nature of the Band Gap In_2O_3 Revealed by First-Principles Calculations and X-Ray Spectroscopy. *Phys. Rev. Lett.* **2008,** *100* (16), 167402.

7. Albani, D.; Capdevila-Cortada, M.; Vilé, G.; Mitchell, S.; Martin, O.; López, N.; Pérez-Ramírez, J. Semihydrogenation of Acetylene on Indium Oxide: Proposed Single-Ensemble Catalysis. *Angew. Chem.* **2017,** *129* (36), 10895-10900.

8. de Castro, I. A.; Datta, R. S.; Ou, J. Z.; Castellanos-Gomez, A.; Sriram, S.; Daeneke, T.; Kalantar-zadeh, K. Molybdenum Oxides – From Fundamentals to Functionality. *Adv. Mater.* **2017,** *29* (40), 1701619.

9. 23 - Chromium, Molybdenum and Tungsten. In *Chemistry of the Elements (Second Edition)*, Greenwood, N. N.; Earnshaw, A., Eds. Butterworth-Heinemann: Oxford, 1997; pp 1002-1039.

10. Goodenough, J. B. *Proc. Climax 4th Intern. Conf. Chemistry and Uses of Molybdenum*. Climax Molybdenum Co.: London, 1982.

11. Lee, S.-H.; Kim, Y.-H.; Deshpande, R.; Parilla, P. A.; Whitney, E.; Gillaspie, D. T.; Jones, K. M.; Mahan, A. H.; Zhang, S.; Dillon, A. C. Reversible Lithium-Ion Insertion in Molybdenum Oxide Nanoparticles. *Adv. Mater.* **2008,** *20* (19), 3627-3632.

12. Hu, X.; Zhang, W.; Liu, X.; Mei, Y.; Huang, Y. Nanostructured Mo-based electrode materials for electrochemical energy storage. *Chem. Soc. Rev.* **2015,** *44* (8), 2376-2404.

13. Cheng, H.; Wen, M.; Ma, X.; Kuwahara, Y.; Mori, K.; Dai, Y.; Huang, B.; Yamashita, H. Hydrogen Doped Metal Oxide Semiconductors with Exceptional and Tunable Localized Surface Plasmon Resonances. *J. Am. Chem. Soc.* **2016,** *138* (29), 9316-9324.

14. Xie, W.; Su, M.; Zheng, Z.; Wang, Y.; Gong, L.; Xie, F.; Zhang, W.; Luo, Z.; Luo, J.; Liu, P.; Xu, N.; Deng, S.; Chen, H.; Chen, J. Nanoscale Insights into the Hydrogenation Process of Layered α-MoO_3. *ACS Nano* **2016,** *10* (1), 1662-1670.

15. Borgschulte, A.; Sambalova, O.; Delmelle, R.; Jenatsch, S.; Hany, R.; Nüesch, F. Hydrogen reduction of molybdenum oxide at room temperature. *Sci. Rep.* **2017,** *7*, 40761.

16. Magneli, A.; Blomberg-Hansson, B.; Kihlborg, L.; Sundkvist, G. Studies on Molybdenum and Molybdenum Wolfram Oxides of the Homologous Series Me_nO_{3n-1}. *Acta Chem. Scand.* **1955,** *9*, 1382-1390.

17. Bouzidi, A.; Benramdane, N.; Tabet-Derraz, H.; Mathieu, C.; Khelifa, B.; Desfeux, R. Effect of substrate temperature on the structural and optical properties of MoO_3 thin films prepared by spray pyrolysis technique. *Mat. Sci. Eng. B* **2003,** *97* (1), 5-8.

18. Kröger, M.; Hamwi, S.; Meyer, J.; Riedl, T.; Kowalsky, W.; Kahn, A. P-type doping of organic wide band gap materials by transition metal oxides: A case-study on Molybdenum trioxide. *Org. Electron.* **2009,** *10* (5), 932-938.

19. Sian, T. S.; Reddy, G. B. Optical, structural and photoelectron spectroscopic studies on amorphous and crystalline molybdenum oxide thin films. *Sol. Energy Mater. Sol. Cells* **2004,** *82* (3), 375-386.

20. Greiner, M. T.; Chai, L.; Helander, M. G.; Tang, W.-M.; Lu, Z.-H. Transition Metal Oxide Work Functions: The Influence of Cation Oxidation State and Oxygen Vacancies. *Adv. Funct. Mater.* **2012,** *22* (21), 4557-4568.

21. Zacharopoulou, V.; Vasiliadou, E. S.; Lemonidou, A. A. Exploring the Reaction Pathways of Bioglycerol Hydrodeoxygenation to Propene over Molybdena-Based Catalysts. *ChemSusChem* **2018,** *11* (1), 264–275.

22. Shetty, M.; Murugappan, K.; Prasomsri, T.; Green, W. H.; Román-Leshkov, Y. Reactivity and stability investigation of supported molybdenum oxide catalysts for the hydrodeoxygenation (HDO) of m-cresol. *J. Catal.* **2015,** *331* (Supplement C), 86-97.

23. Labanowska, M. Paramagnetic defects in MoO_3-revisited. *Phys. Chem. Chem. Phys.* **1999,** *1* (23), 5385-5392.

24. Py, M. A.; Maschke, K. Intra- and interlayer contributions to the lattice vibrations in MoO_3. *Physica B+C* **1981,** *105* (1), 370-374.

25. Mestl, G.; Verbruggen, N. F. D.; Bosch, E.; Knözinger, H. Mechanically Activated MoO_3. 5. Redox Behavior. *Langmuir* **1996,** *12* (12), 2961-2968.

26. Vasilopoulou, M.; Douvas, A. M.; Georgiadou, D. G.; Palilis, L. C.; Kennou, S.; Sygellou, L.; Soultati, A.; Kostis, I.; Papadimitropoulos, G.; Davazoglou, D.; Argitis, P. The Influence of Hydrogenation and Oxygen Vacancies on Molybdenum Oxides Work Function and Gap States for Application in Organic Optoelectronics. *J. Am. Chem. Soc.* **2012,** *134* (39), 16178-16187.

27. Hanson, E. D.; Lajaunie, L.; Hao, S.; Myers, B. D.; Shi, F.; Murthy, A. A.; Wolverton, C.; Arenal, R.; Dravid, V. P. Systematic Study of Oxygen Vacancy Tunable Transport Properties of Few-Layer MoO_{3-x} Enabled by Vapor-Based Synthesis. *Adv. Funct. Mater.* **2017,** *27* (17), 1605380.

28. Scanlon, D. O.; Watson, G. W.; Payne, D. J.; Atkinson, G. R.; Egdell, R. G.; Law, D. S. L. Theoretical and Experimental Study of the Electronic Structures of MoO_3 and MoO_2. *J. Phys. Chem. C* **2010,** *114* (10), 4636-4645.

29. Akande, S. O.; Chroneos, A.; Vasilopoulou, M.; Kennou, S.; Schwingenschlögl, U. Vacancy formation in MoO_3: hybrid density functional theory and photoemission experiments. *J. Mater. Chem. C* **2016,** *4* (40), 9526-9531.

30. Rellán-Piñeiro, M.; López, N. The Active Molybdenum Oxide Phase in the Methanol Oxidation to Formaldehyde (Formox Process): A DFT Study. *ChemSusChem* **2015,** *8* (13), 2231-2239.

31. Mei, D.; Karim, A. M.; Wang, Y. Density Functional Theory Study of Acetaldehyde Hydrodeoxygenation on MoO_3. *J. Phys. Chem. C* **2011,** *115* (16), 8155-8164.

32. Choksi, T.; Greeley, J. Partial Oxidation of Methanol on MoO_3 (010): A DFT and Microkinetic Study. *ACS Cat.* **2016,** *6* (11), 7260-7277.

33. Shetty, M.; Buesser, B.; Román-Leshkov, Y.; Green, W. H. Computational Investigation on Hydrodeoxygenation (HDO) of Acetone to Propylene on α-MoO_3(010) Surface. *J. Phys. Chem. C* **2017,** *121* (33), 17848-17855.

34. Dudarev, S. L.; Botton, G. A.; Savrasov, S. Y.; Humphreys, C. J.; Sutton, A. P. Electron-energy-loss spectra and the structural stability of nickel oxide: An LSDA+U study. *Phys. Rev. B* **1998,** *57* (3), 1505-1509.

35. Inzani, K.; Grande, T.; Vullum-Bruer, F.; Selbach, S. M. A van der Waals Density Functional Study of MoO_3 and Its Oxygen Vacancies. *J. Phys. Chem. C* **2016,** *120* (16), 8959-8968.

36. Tahini, H. A.; Tan, X.; Lou, S. N.; Scott, J.; Amal, R.; Ng, Y. H.; Smith, S. C. Mobile Polaronic States in α-MoO_3: An ab Initio Investigation of the Role of Oxygen Vacancies and Alkali Ions. *ACS Appl. Mater. Inter.* **2016,** *8* (17), 10911-10917.

37. Kim, H. S.; Cook, J. B.; Lin, H.; Ko, J. S.; Tolbert, S. H.; Ozolins, V.; Dunn, B. Oxygen vacancies enhance pseudocapacitive charge storage properties of MoO_{3-x}. *Nat. Mater.* **2017,** *16* (4), 454.

38. Lei, Y.-H.; Chen, Z.-X. DFT+U Study of Properties of MoO_3 and Hydrogen Adsorption on MoO_3(010). *J. Phys. Chem. C* **2012,** *116* (49), 25757-25764.

39. Ding, H.; Lin, H.; Sadigh, B.; Zhou, F.; Ozoliņš, V.; Asta, M. Computational Investigation of Electron Small Polarons in α-MoO_3. *J. Phys. Chem. C* **2014,** *118* (29), 15565-15572.

40. Coquet, R.; Willock, D. J. The (010) surface of α-MoO_3, a DFT + U study. *Phys. Chem. Chem. Phys.* **2005,** *7* (22), 3819-3828.

41. Agarwal, V.; Metiu, H. Energy of Oxygen-Vacancy Formation on Oxide Surfaces: Role of the Spatial Distribution. *J. Phys. Chem. C* **2016,** *120* (4), 2320-2323.

42. Agarwal, V.; Metiu, H. Oxygen Vacancy Formation on α-MoO_3 Slabs and Ribbons. *J. Phys. Chem. C* **2016,** *120* (34), 19252-19264.

43. Lutfalla, S.; Shapovalov, V.; Bell, A. T. Calibration of the DFT/GGA+U Method for Determination of Reduction Energies for Transition and Rare Earth Metal Oxides of Ti, V, Mo, and Ce. *J. Chem. Theory Comput.* **2011,** *7* (7), 2218-2223.

44. Getsoian, A. B.; Bell, A. T. The Influence of Functionals on Density Functional Theory Calculations of the Properties of Reducible Transition Metal Oxide Catalysts. *J. Phys. Chem. C* **2013,** *117* (48), 25562-25578.

45. Kihlborg, L. Least-squares refinement of the crystal structure of Mo trioxide. *Ark. Kemi* **1963,** *21*, 357-64.

46. Camacho-López, M. A.; Escobar-Alarcón, L.; Picquart, M.; Arroyo, R.; Córdoba, G.; Haro-Poniatowski, E. Micro-Raman study of the m-MoO_2 to α-MoO_3 transformation induced by cw-laser irradiation. *Opt. Mater.* **2011,** *33* (3), 480-484.

47. Dieterle, M.; Weinberg, G.; Mestl, G. Raman spectroscopy of molybdenum oxides Part I. Structural characterization of oxygen defects in MoO_{3-x} by DR UV/VIS, Raman spectroscopy and X-ray diffraction. *Phys. Chem. Chem. Phys.* **2002,** *4* (5), 812-821.

48. Kresse, G.; Furthmüller, J. Efficient iterative schemes for ab initio total-energy calculations using a plane-wave basis set. *Phys. Rev. B: Condens. Matter* **1996,** *54*, 11169-11186.

49. Kresse, G.; Furthmüller, J. Efficiency of ab-initio total energy calculations for metals and semiconductors using a plane-wave basis set. *Comput. Mater. Sci.* **1996,** *6*, 15-50.

50. Perdew, J. P.; Burke, K.; Ernzerhof, M. Generalized gradient approximation made simple. *Phys. Rev. Lett.* **1996,** *77*, 3865-3868.

51. Grimme, S. Semiempirical GGA-type density functional constructed with a long-range dispersion correction. *J. Comput. Chem.* **2006,** *27*, 1787-1799.

52. Wellendorff, J.; Lundgaard, K. T.; Møgelhøj, A.; Petzold, V.; Landis, D. D.; Nørskov, J. K.; Bligaard, T.; Jacobsen, K. W. Density functionals for surface science: Exchange-correlation model development with Bayesian error estimation. *Phys. Rev. B* **2012,** *85* (23), 235149.

53. Lee, K.; Murray, É. D.; Kong, L.; Lundqvist, B. I.; Langreth, D. C. Higher-accuracy van der Waals density functional. *Phys.Rev. B* **2010,** *82* (8), 081101.

54. Heyd, J.; Scuseria, G. E.; Ernzerhof, M. Hybrid functionals based on a screened Coulomb potential. *J. Chem. Phys.* **2003,** *118* (18), 8207-8215.

55. Paier, J.; Marsman, M.; Hummer, K.; Kresse, G.; Gerber, I. C.; Ángyán, J. G. Erratum: "Screened hybrid density functionals applied to solids" [J. Chem. Phys. 124, 154709 (2006)]. *J. Chem. Phys.* **2006,** *125* (24), 249901.

56. Kresse, G.; Joubert, D. From ultrasoft pseudopotentials to the projector augmented-wave method. *Phys. Rev. B: Condens. Matter Mater. Phys.* **1999,** *59*, 1758-1775.

57. Makov, G.; Payne, M. C. Periodic boundary conditions in *ab initio* calculations. *Phys. Rev. B* **1995,** *51* (7), 4014-4022.

58. Álvarez-Moreno, M.; de Graaf, C.; López, N.; Maseras, F.; Poblet, J. M.; Bo, C. Managing the Computational Chemistry Big Data Problem: The ioChem-BD Platform. *J. Chem. Theory Comput.* **2015,** *55* (1), 95-103.

59. https://iochem-bd.iciq.es/browse/review-collection/100/8524/aa697702a88410b5295c5f64.

Green Chemistry

PAPER

View Article Online
View Journal

Cite this: DOI: 10.1039/c7gc02692g

A mechanism for the selective epimerization of the glucose mannose pair by Mo-based compounds: towards catalyst optimization†

M. Rellán-Piñeiro, [a] M. Garcia-Ratés [b] and N. López *[a]

The selective C^2 epimerization of the glucose/mannose pair on a set of Mo-based catalysts was studied by means of density functional theory. The process, known as the Bilik reaction, encompasses a 1,2 C-shift of the C^3 centers at the sugars. Molybdic acid was initially proposed as a catalyst in this reaction, and recent experimental studies have shown that the polyoxometalate (POM) Keggin cluster $H_3PMo_{12}O_{40}$ also presents a good performance. In the present work, we propose a reaction mechanism for the epimerization on the Keggin cluster with different heteroatoms and extend it to a larger POM, $H_6P_2Mo_{18}O_{62}$, and the continuous α-MoO_3(010) surface. We have found that in the transition state corresponding to the 1,2 C-shift the Mo center acts as an electron buffer that promotes the transformation of the aldehyde group in C^1 into an alkoxy group and the C^2 alkoxy into an aldehyde group. As a consequence, the activity of Mo-containing compounds can be traced back to the reducibility of the Mo center and a simple microkinetic model illustrates that this descriptor generates an activity volcano. This allows the identification of a new POM that shall be 4.7 times more active than the parent compound. We have thus shown that continuum models linking the properties of molecular cluster-like catalysts and oxide surfaces can be derived and this paves the way towards a unified theory in catalysis.

Received 4th September 2017,
Accepted 15th November 2017

DOI: 10.1039/c7gc02692g

rsc.li/greenchem

Introduction

Obtaining compounds with controlled chirality is a challenge to develop platform chemicals from biomass. Some of the target compounds could be easily generated from sugars but in some cases the natural abundance of the parent sugar is relatively small (rare sugars) whereas their epimers are widely abundant. The chemical toolbox now allows epimerization reactions,[1] that is, the rearrangement of a single stereogenic center in a molecule that contains several of them.[2] In nature, epimerases catalyze this reaction at multiple carbon positions providing a high specificity for products,[3,4] but their transfer to the industrial scale suffers from the very specific conditions of temperatures and pH as well as difficult recycling.[5] Therefore, there is a need to develop inorganic catalysts that can allow the successful epimerization avoiding these drawbacks.

Lobry de Bruyn–Alberda van Ekenstein observed that during the isomerization of aldoses to ketoses promoted by a base, epimers were obtained as byproducts.[6] Lewis acids like Ni^{+2} diamines in methanol are active and the equilibrium is reached only in 5 min at 60 °C.[7,8] However, the catalyst is complex and the reactivity is limited by the low solubility of sugars in methanol.[9] Other Lewis acids like metal(III) chlorides ($CrCl_3$, $AlCl_3$, $InCl_3$, $LaCl_3$, $DyCl_3$, and $YbCl_3$) epimerize glucose to fructose, giving mannose as a secondary product.[10] Alternatively, the Sn-Beta zeolite has also been proposed as an active catalyst for epimerization; framework Sn sites are active in methanol,[11] and partially hydrolyzed Sn sites catalyze the reaction when Na^+ is added to the reaction media.[12] Borate salts also activate the Sn-Beta zeolite for epimerization reactions.[13,14] Mechanistic investigations by ^{13}C and ^1H NMR showed that epimerization proceeds *via* 1,2 C-shift and, in some cases, also by C^1–C^2 hydride transfer. Generally, these catalysts perform the reaction *via* the coordination of the sugar to only one metal center.

However, the most prominent inorganic catalysts are based on Mo. Mo-Catalysts have found several applications in biomass conversion and, most recently, also when employed as single atoms or small clusters.[15–21] In the 1970s, Bilik and coworkers[22] reported the epimerization of aldoses at the C^2-position catalyzed by molybdates under acidic conditions and gave name to the reaction.[23] In their experiments, the thermodynamic equilibrium between the aldose pair was reached after 3 h at 90 °C, and the reaction was quite neat. In 1982,

[a]Institute of Chemical Research of Catalonia, ICIQ, and The Barcelona Institute of Science and Technology, Av. Països Catalans 16, 43007 Tarragona, Spain. E-mail: nlopez@iciq.es
[b]Max Planck Institute for Chemical Energy Conversion, Stiftstrasse 34-36, D-45470 Mülheim an der Ruhr, Germany

†Electronic supplementary information (ESI) available. See DOI: 10.1039/c7gc02692g

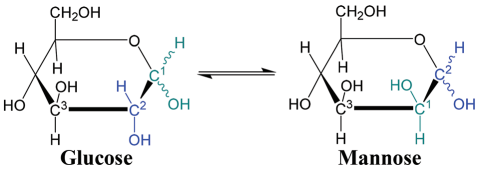

Scheme 1 Schematic representation of the epimerization of glucose to mannose. The carbons where the rearrangement occurs are marked in colors illustrating the chiral nature of the C^2 positions.

NMR-based mechanistic studies[24] with labeled $^{13}C^1$ and $^{13}C^2$ aldoses showed a stereospecific carbon-skeleton rearrangement during the reaction formally leading to the C^2 epimerization by C^1–C^2 carbon shift (Scheme 1).

The mechanistic studies with molybdates[24–26] indicate that the reaction is intramolecular and takes place through the open form of the aldose. The accepted molecular mechanism presented in Scheme 2 requires two Mo-centers to occur. The hydrated aldose coordinates through the four hydroxyl groups C^1–C^4 (the oxygen atoms on C^1 and C^4 are attached to Mo atoms, while the oxygen atoms on C^2 and C^3 form a bridge between Mo).[23,27] Then, in the transition state, the C^3–C^2 breaks while C^3–C^1 is simultaneously formed. This process is accompanied by the dehydration of C^1 and hydration of C^2. The chain rearrangement leads to the inversion of configuration in C^2 obtaining the epialdose-dimolybdate complex. The presence of a terminal aldehyde group and hydroxyl groups in C^2 and C^3 is essential, and the alcohol group is not needed in position C^4, although it enhances the rate. Using Density Functional Theory, DFT, only the epimerization step has been studied with Mo oxide dimers and tetramers and due to rigidity, the former was found to be better for this elementary step.[28]

Molecular oxides, like the molybdenum-based polyoxometalate (POM) $H_3PMo_{12}O_{40}$, are also active and highly selective catalysts, more than 90%, in aqueous solution and acid media (pH = 2.5–3.5).[19] By ^{13}C NMR the C^1–C^2 carbon shift reported in the Bilik reaction was found and XPS identified electron transfer from glucose to the Mo octahedra units. The kinetic studies reported apparent activation barriers between 95 and 100 kJ mol^{-1}, thus slightly lower than those reported for molybdic acid, 126 kJ mol^{-1}.[29] More importantly, the catalyst was stable under reaction conditions and could be recycled. Later, this catalyst was employed to transform glucose to mannose in aqueous solution as the first step to obtain mannitol,[30] and POM overperformed bulk molybdenum oxide, which suffered complete leaching. Other closely related applications like tandem reactions for the production of alkyl lactates from ketohexoses[31] in ethanol have been identified on bulk MoO_3. Finally, niobium molybdates ($LiNbMoO_6$ and $HNbMoO_6$) have been proposed as heterogeneous catalysts for the reaction.[32]

In this work, we study by first principles methods the epimerization reaction of glucose to mannose catalyzed by different Mo oxide species including two POMs:[33] the Keggin[34] $H_3PMo_{12}O_{40}$ (with a set of different heteroatoms), the Dawson $H_6P_2Mo_{18}O_{62}$ clusters and the bulk material α-MoO_3(010),[17] both as pristine and defective surfaces. We propose a mechanism for the Bilik reaction which explains the experimental observations and requires a single center. Finally, we have found that the reducibility of the Mo reaction centers is the unique descriptor for the activity of Mo oxides irrespective of their molecular or continuous nature.

Computational methods

Density Functional Theory (DFT) calculations were carried out with the 5.3.3 version of Vienna *ab initio* simulation package (VASP) for the molecular and continuous Mo-based catalyst.[35,36] The Perdew–Burke–Ernzerhof (PBE) functional[37] was chosen to describe the exchange correlation energy. To correctly describe the on-site Coulomb interactions of localized 4d electrons of molybdenum atoms the Hubbard U correction,[38] U_{eff}, with a value of 3.5 eV was introduced. The U_{eff} value was optimized to reproduce the correct reaction energy and electron localization for the dissociative H_2 adsorption. Gaussian smearing with smearing parameter σ = 0.1 eV was used. The van der Waals contributions were accounted for with Grimme's semiempirical vdW-D2 correction.[39] Projector-augmented wave (PAW) pseudopotentials[40] were used to replace the inner electrons. The kinetic cut-off energy to expand the valence electrons in plane-waves was set to 450 eV and spin polarization was taken into account.

For all the molecules present in this study, including polyoxometalates, $H_nXMo_{12}O_{40}$, a 19.5 × 20 × 20.5 $Å^3$ box was used. For the $H_6P_2Mo_{18}O_{62}$ cluster the simulation box volume was

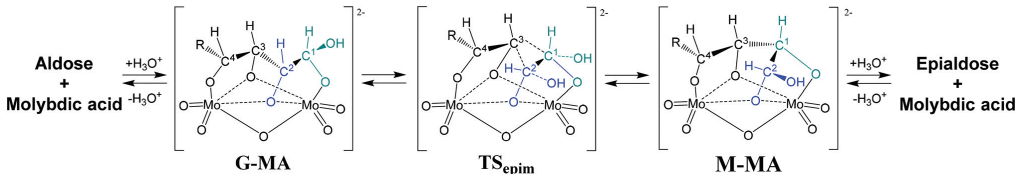

Scheme 2 Accepted mechanism for the epimerization of aldose pairs, Bilik reaction, catalyzed by molybdic acid. Adapted from ref. 23.

increased to 25.5 × 25 × 24.5 Å^3. All cells were large enough to avoid the interaction between structures of neighboring unit cells, which were sampled at the Gamma point. All atoms were allowed to relax. Benchmark calculations for these settings were done with the Gaussian code obtaining very similar values, see Table SI1.† A slab model was used to test the reactivity on the α-MoO_3(010) surface. A (3 × 3) supercell containing two bilayers with 3 × 3 × 1 *k*-point sampling was considered. The upper bilayer and adsorbates were relaxed. A vacuum gap of 15 Å was added between slabs. The use of asymmetric slabs causes spurious terms, which were avoided with the use of a dipole correction along the *z* axis.[41] The reaction path was tested both on the clean surface and on the terminal oxygen, O_t, defective surface with one vacancy per supercell. The climbing image nudged elastic band (CI-NEB)[42,43] method was used to find the transition states, which were then refined with the improved dimer method (IDM).[44,45] A vibrational analysis was applied to confirm all the minima and saddle points, and all energies were corrected by ZPVE. Solvation was included for $[H_{3-n}PMo_{12}O_{40}]^{-n}$, *n* between 0 and 3, through the VASP-MGCM continuum model[46,47] for an aqueous environment. To balance the charge of the Keggin cluster a cation with the equivalent valence Rb^{+1}, Sr^{+2} or Y^{+3} was added to the system. To minimize spurious electrostatic interactions the distance between the anion and the cation was set to its maxima within the box. For the three systems the multiplicity of the POM was singlet. All the structures are published in the ioChem-BD database[48] and can be retrieved in ref. 49.

Results

The energy profile for the epimerization reaction starting by open glucose was calculated for the reaction on $H_3PMo_{12}O_{40}$, $H_6P_2Mo_{18}O_{62}$ and the pristine and defective α-MoO_3(010) surfaces. The structures of these compounds are shown in Fig. 1.

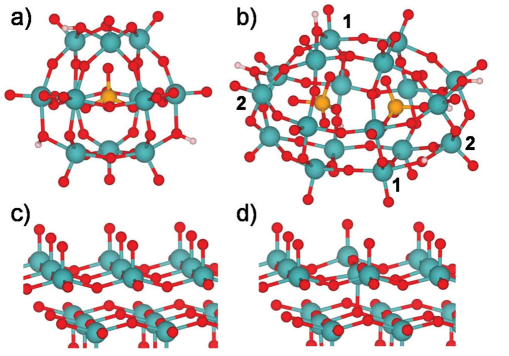

Fig. 1 Mo-Based systems where the Bilik reaction was investigated: (a) Keggin POM $H_3PMo_{12}O_{40}$; (b) Dawson POM $H_6P_2Mo_{18}O_{62}$, two different types of Mo centers are indicated by 1 and 2; (c) α-MoO_3; (d) α-MoO_{3-x}. Mo atoms in green, O in red, P in orange and H in white.

All Mo centers of deprotonated $[PMo_{12}O_{40}]^{3-}$ and pristine α-MoO_3(010) surfaces are equivalent whereas $H_6P_2Mo_{18}O_{62}$ has two different Mo environments (labelled as 1 and 2 in Fig. 1b). The molybdenum atoms in these three catalysts present a formal oxidation state of +6. In the defective α-MoO_{3-x}(010) surface two Mo^{+6} centers are reduced to Mo^{+5}.[50–52]

The coordination environments of the Mo centers in $H_3PMo_{12}O_{40}$ do not allow the two center glucose coordination observed in glucose-dimolybdate complexes.[23,27] Glucose coordinates to a single Mo, thus being similar to metal chlorides,[10] which results in the mechanism and reaction profiles shown in Fig. 2. Detailed reaction energies and energy barriers are shown in Table SI2;† and geometric parameters are provided in Table SI3.† Reaction free energy profiles including vibrational terms are shown in Fig. SI2.†

The overall reaction is almost thermoneutral, with the formation of mannose slightly favored by 0.09 eV. The barrier for non-catalyzed gas-phase epimerization of glucose to mannose is 1.37 eV. For $H_3PMo_{12}O_{40}$, the open form of the glucose is dissociatively adsorbed on a Mo center (R1) through the TS_{diss}. In the adsorbed state, G_{diss}, the hydroxyl group of C^2 is bonded to a Mo center whereas the C^1-aldehyde group interacts with the same Mo center forming a bidentate complex. This step is endothermic by 0.57 eV, with an activation barrier of 1.04 eV. Although glucose adsorption through other hydroxyl groups is possible, Fig. SI3,† it will not lead to the desired reactivity. The adsorbed glucose undergoes 1,2 C-shift (R2) through TS_{epim} where the C^2–C^3 bond is broken and C^1–C^3 is simultaneously formed. Concomitantly the C^1 aldehyde transforms into an alkoxy group and C^2 alkoxy into an aldehyde group. The corresponding final state is the dissociated mannose, M_{diss}, bonded to the Mo center through the oxygen of

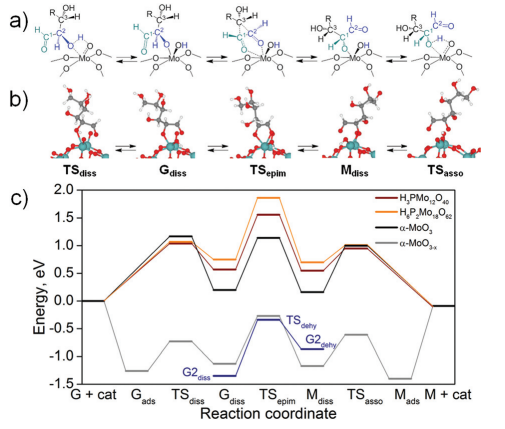

Fig. 2 (a) Proposed mechanism[10] for the epimerization reaction on $H_3PMo_{12}O_{40}$. (b) Optimized structures for reaction on $H_3PMo_{12}O_{62}$. (c) Reaction profile for the Bilik reaction for glucose on $H_3PMo_{12}O_{40}$, $H_6P_2Mo_{18}O_{62}$, α-MoO_3(010) and α-MoO_{3-x}(010). Dehydration step on α-MoO_{3-x}(010) is represented by the blue line.

the alkoxy group of C^1, with the aldehyde group of C^2 also interacting with the same Mo center. The forward energy barrier is 0.99 eV. Finally, the proton is transferred back to M_{diss} driving the associative desorption (R3) of the mannose through TS_{asso}. This process is exothermic by 0.64 eV with a barrier of 0.40 eV.

The reaction mechanism starts with the open form of the glucose, but in water aldoses are mainly in their ring configurations. The presence of Mo-based compounds in reaction media can catalyze glucose opening, see Fig. SI4.†

The Dawson cluster has two different Mo positions, Fig. 1b. Position 1 exhibits a better performance in both, binding and energy barriers for the reaction and, therefore, only the reactivity at this site will be discussed. The dissociative adsorption of glucose (R1) is endothermic by 0.75 eV, and the barrier is 1.07 eV. The 1,2 C-shift step (R2) is nearly thermoneutral, with M_{diss} formation slightly favored by 0.05 eV. The energy barrier is 1.10 eV and the associative desorption of mannose (R3) is exothermic, −0.79 eV, with a small barrier of 0.31 eV.

We extended the reaction path calculated for POMs to the bulk α-MoO_3 on the pristine and defective (010) surfaces.[15–18,21] The mechanism on the regular surface follows that found for POMs. However, the first step is only slightly endothermic by 0.20 eV, with a relatively low barrier of 1.17 eV. The reaction energy for the epimerization step is −0.04 eV, practically thermoneutral, and the forward activation energy is 0.94 eV. The desorption of mannose is exothermic, with a reaction energy of −0.24 eV and a barrier of 0.85 eV. Oxides might lose oxygen and thus the reaction on the reduced surface needs to be investigated. Unlike the Mo^{+6} centers, glucose adsorption on the Mo^{+5} center of α-MoO_{3-x}(010) through the –OH group of C^2 is non-dissociative, and it is highly exothermic, −1.26 eV. The adsorbed glucose is dissociated by transferring the hydrogen atom of the interacting –OH group to a neighboring O_t. This –OH dissociation is slightly endothermic by 0.14 eV. The energy barrier to this step is 0.53 eV. Most likely, this step corresponds to a proton coupled electron transfer as the images along the path belong to two different electron localizations. Again, the 1,2 C-shift step is close to thermoneutral, −0.04 eV, and its barrier is 0.87 eV. After this step, the hydrogen is transferred back from the surface to the mannose oxygen bonded to the Mo center. This process is exothermic by 0.23 eV with an energy barrier of 0.55 eV. Desorption of the mannose molecule formed in this step is highly endothermic, with a reaction energy of 1.40 eV. However, defective MoO_{3-x} has been reported as an active catalyst for the hydrodeoxygenation (HDO) of oxygenated compounds as alcohols and polyalcohols through the breaking of C–O bonds.[15,16,18] Glucose has five –OH groups that could undergo HDO. We have calculated the dehydration step for the $-O_5H$ group of glucose obtaining an energy barrier of 1.01 eV, Fig. SI5.† Similar values are expected for the other –OH groups. This result compromises the selectivity for epimerization on the defective MoO_{3-x}(010) surface towards dehydrated compounds and discards it as a catalyst for the reaction.

Theory also explains why in experiments vicinal hydroxyl groups have an important effect on the epimerization reaction.[23] In our path, the relevance of the C^2 alcohol group is evident, since it takes part directly in the mechanism, as glucose adsorbs on the Mo center through this alcohol group and its transformation into a ketone allows the chain rearrangement. In order to study the influence of $-O^3H$ and $-O^4H$ groups, we calculated the intermediates and transition states for the 1,2 C-shift step for glucoses without these groups on $H_3PMo_{12}O_{40}$. The energy profile of this step for three systems is shown in Fig. SI6.† The presence of $-O^3H$ and $-O^4H$ has a weak influence on the adsorption energy of molecules; they are between 0.47–0.57 eV for the three systems. However, the energy barriers increase from 0.99 eV, with glucose, to 1.08 eV without $-O^4H$ and to 1.23 eV without $-O^3H$, in agreement with the experiments with molybdates,[24] Table SI4.† Although these –OH groups do not play a direct role in the interaction with the POM, the presence of $-O^3H$ has a great influence on the stabilization of the transition state. In the adsorbed glucose the C^3–O^3 bond distance is 1.413 Å. This distance is reduced to 1.350 Å at the transition state, indicating the formation of a partial double bond C^3=O^3H that stabilizes the transition state. This effect could also be present in the reaction catalyzed by molybdates. In adsorbed glucose a hydrogen bond is formed between $-O^3H$ and $-O^4H$ with a distance of 2.432 Å. In the transition state structure, C^3 has partial sp^2 geometry reducing this distance to 2.259 Å, thus stabilizing the structure. In adsorbed glucose without $-O^4H$, the $-O^3H$ group forms a strong hydrogen bond with the $-O^5H$ group with a distance of 1.800 Å. In contrast, for glucose, this distance increases to 2.000 Å at the transition state due to the geometry change in C^3, increasing the activation energy. Thus, computed results explain previous experimental observations for molybdates.

The reaction is carried out in aqueous solution, and we have investigated the influence of the solvent only for the $H_3PMo_{12}O_{40}$ system. In gas-phase, the dissociative adsorption of sugars involves high energy barriers, but the presence of water molecules acting as hydrogen shuttles reduces this barrier to 0.54 and 0.55 eV for glucose and mannose, respectively, Fig. SI7.† In addition, in aqueous solution the Keggin cluster has a high solubility and is fully dissociated.[53] We have investigated how deprotonation and solvation affects the 1,2 C-shift. Binding energy for dissociated glucose and mannose and the energy barrier for this elementary step on solvated $[H_nMo_{12}O_{40}]^{3-n}$ are shown in Fig. 3 and Table SI5.† The dissociative binding energy of glucose and mannose on solvated $H_3PMo_{12}O_{40}$ is not affected by the presence of water. However, the energy barrier for 1,2 C-shift is reduced by 0.24 eV. This is due to the polarity of water that stabilizes the transition state structure. Binding and activation energies for 1,2 C-shift increase almost linearly with the overall charge of the deprotonated POMs, Fig. SI8,† the binding energy ranging from 0.57 to 1.05 eV and the activation barrier from 0.79 to 1.00 eV. The presence of a polar solvent smoothed this effect by the stabilization of the charge. The completely deprotonated POM,

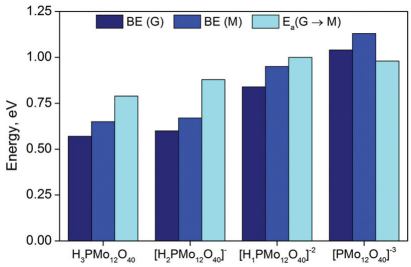

Fig. 3 Charge effects in the binding, BE, and activation energies, E_a, both in eV, for the 1,2 C-shift step at the Keggin cluster including solvation effects. Solvated POMs and solvated open form of glucose as reference.

$[PMo_{12}O_{40}]^{-3}$, has an energy barrier for the epimerization elementary step of 1.00 eV, very similar to the barrier calculated for $H_3PMo_{12}O_{40}$ in gas phase. Geometrical details are shown in Table SI6.† In order to have a better understanding of the role of the solvent in this step we performed a set of calculations with one and two explicit water molecules, Fig. SI9 and Table SI7.† One water molecule was adsorbed on the $-O_tH$ group bonded to the Mo reactive center through a hydrogen bond, the water molecule being the hydrogen donor. The presence of this water molecule reduces the activation energy by 0.12 eV. This water molecule weakens the O_t–Mo bond allowing a better stabilization of the transition state. Alternatively, if the water molecule is placed between $-O_3H$ and $-O_4H$, being the hydrogen acceptor of $-O_3H$ and the donor for $-O_4H$, the activation energy is reduced by 0.10 eV as water assists the formation of the partial double bond $C^3{=}O^3H$. We also calculated the system including simultaneously these two water molecules, and then the activation energy is reduced by 0.19 eV, and thus the value is very similar to that calculated with the solvation VASP-MGCM model.

Finally, we tested the influence of the heteroatom in the $H_nXMo_{12}O_{40}$ (X = P, As, Si, Ge) in the 1,2 C-shift elementary step. It is reported that the heteroatom does not participate directly in the reactivity, but these heteroatoms present different formal charges and thus induce different charge distribution over the POM structure which finely tunes the redox properties of the POM framework.[54,55] Intermediates and transition states on $H_nXMo_{12}O_{40}$ (X = S, P, As, Si, Ge) for this elementary step have been calculated. Energy profiles for this step are shown in Fig. SI10.† As is shown in Table 1 the heteroatom has a relatively mild influence. Binding energies range from 0.51 to 0.67 eV for glucose, and between 0.49 and 0.62 eV for mannose, see Tables SI8 and SI9.† Energy barriers for the glucose to mannose epimerization are between 0.95 and 1.07 eV. Binding and activation energies increase with the number of valence electrons in the heteroatom, and, for a given valence with the heteroatom size.

The lowest energy barriers for the epimerization step are on solid α-MoO_3(010), both pristine and defective surfaces. This

Table 1 Binding energy, BE, in eV, of glucose and mannose on $H_nXMo_{12}O_{40}$ (relative to gas-phase glucose and POM), activation energy, E_a, eV, for 1,2 C-shift, and Bader analysis of the charge transfer from the heteroanion to the $Mo_{12}O_{36}$ skeleton

X	BE (G)	BE (M)	E_a TS_{epim} (G → M)	Formal charge XO_4^{n-}	Bader charge XO_4^{n-}	Transferred charge
S	0.51	0.49	0.95	−2	−1.61	−0.39
P	0.57	0.55	0.99	−3	−2.23	−0.77
As	0.61	0.57	1.00	−3	−2.19	−0.89
Si	0.65	0.59	1.02	−4	−2.72	−1.28
G	0.67	0.62	1.07	−4	−2.69	−1.31

energy barrier on α-MoO_{3-x}(010) is 0.09 eV lower than that on α-MoO_3(010) and 0.16 eV lower than that on $H_3PMo_{12}O_{40}$. However the adsorption energies of glucose and mannose on α-MoO_{3-x}(010) are highly exothermic, −1.26 and −1.40 eV respectively, and therefore, the desorption of glucose/mannose is the most energy demanding step. α-MoO_3(010), $H_3PMo_{12}O_{40}$, and $H_6P_2Mo_{18}O_{62}$ have similar energy barriers for the dissociative adsorption of the glucose/mannose pair, Fig. 2. However, the binding energies of dissociated molecules and the energy barrier for the epimerization step increase in the order: α-MoO_3(010) < $H_3PMo_{12}O_{40}$ < $H_6P_2Mo_{18}O_{62}$.

As stability seems to be an issue for the Mo-based catalyst, we have investigated the thermodynamic stability of crystalline structures in terms of their cohesive energy, *i.e.* the energy required to separate the crystalline material into isolated molecular units. We have calculated the cohesive energy for $[PMo_{12}O_{40}]^{-3}$, the POM species present in aqueous solution, and for bulk α-MoO_3 in order to compare their stabilities. The monomer molybdic acid, H_2MoO_4, was used as a reference, as it is the smallest molybdenum compound present in aqueous solution. The dissolution of MoO_3 and $[PMo_{12}O_{40}]^{-3}$ can be written as:

$$nMoO_3 + nH_2O \rightarrow nH_2MoO_4 \quad (1)$$

$$[PMo_{12}O_{40}]^{-3} + 12H_2O \rightarrow 12H_2MoO_4 + PO_4^{3-} \quad (2)$$

The calculated cohesive energies are 1.06 eV per MoO_3 for bulk α-MoO_3, and 1.78 eV per MoO_3 for $[PMo_{12}O_{40}]^{-3}$. This higher thermodynamic stability of the POM is due to the electrostatic interactions between the encapsulated anion and the $Mo_{12}O_{36}$ framework that makes it stable against leaching in aqueous solution. The same strategy is used for the stability of layered niobium molybdates where the presence of Li^+ or H^+ atoms in the interlayer region has a similar effect as the encapsulated ion in POMs, avoiding leaching in aqueous solution by improving electrostatics.[32]

Discussion: descriptor analysis

Direct deprotonation of the POM affects the MoO-framework charge and similarly POMs with different heteroatoms present slightly different MoO-framework charges due to the charge

transfer between the anions and the MoO_6 POM units, see Table 1 and Table SI10.† Binding energies and the energy barrier for the 1,2 C-shift increase linearly with the POM MoO-framework charge, Fig. SI11.† The reduction potentials follow a similar trend as they decrease linearly with the degree of deprotonation.[55–57]

Analyzing our reaction network we find that during 1,2 C-shift the C^1 aldehyde group is transformed into an alkoxy group and a C^2 alkoxy group in an aldehyde group allowing the carbon chain rearrangement. Thus, the large electronic rearrangement in this step has been investigated by calculating the charge density difference of the TS_{epim} with respect to the $[C_6H_{11}O_6]^-$ anion and the protonated POM. This difference is shown in Fig. 4a illustrating the charge depletion from the lone pair of the isolated glucose and accumulation at the Mo center. This result indicates that Mo reducibility[58,59] is the controlling factor in the reaction. However, the direct calculation of single atom reducibility on the surface of MoO_3 is elusive and thus alternatives are needed.

Iglesia *et al.* have proposed the H-atom addition energy (HAE) as the descriptor for C–H activation for methanol oxidation on Keggin clusters[60,61] (other geometric and electronic parameters are discussed in descriptors[58,59] in Table SI11†). We used this parameter for glucose epimerization. HAE is calculated as the energy to add a hydrogen atom to an oxygen on the catalyst:

$$\mathrm{HAE} = E_{\mathrm{cat+H^{\cdot}}} - E_{\mathrm{cat}} \quad (3)$$

This descriptor combines both the reducibility of the metal center, by the addition of an electron, and the basicity of the oxygen atom, as a proton is retained on a neighboring oxygen. To minimize the influence of the different basicities of Mo-neighboring O atoms several O atoms were sampled, always ensuring that electron localization occurs at the desired center. The catalysts in the analysis were $H_nXMo_{12}O_{40}$ (X: S, P, As, Si, Ge), $H_6P_2Mo_{18}O_{62}$, α-MoO_3(010) and α-MoO_{3-x}(010). The results shown in Fig. 4b and c indicate that both the reactant (product) adsorption and the activation energy for the 1,2 C-shift elementary step depend on the HAE.

In addition, for POMs the reducibility can be extracted from the previous calculations as follows:

$$\mathrm{Red} = \mathrm{HAE} - (E_{\mathrm{cat+H^+}} - E_{\mathrm{cat}}) \quad (4)$$

where the second term eliminates the contribution from the basicity. As is shown in Fig. SI12† adsorption and activation energies correlate with the reducibility for the six studied POMs, showing how a higher reducibility results in a lower energy barrier. Thus, the redox properties of the catalyst are ultimately responsible for catalytic behavior, and reducibility is the single descriptor that correctly defines adsorption and activation energies for this process. The electronic descriptor has two advantages: (i) it maps the geometry of the Mo–O distance (Fig. SI13†) and more importantly (ii) it is very easy to measure experimentally as cyclic voltammetry could easily determine the reducibility.[62]

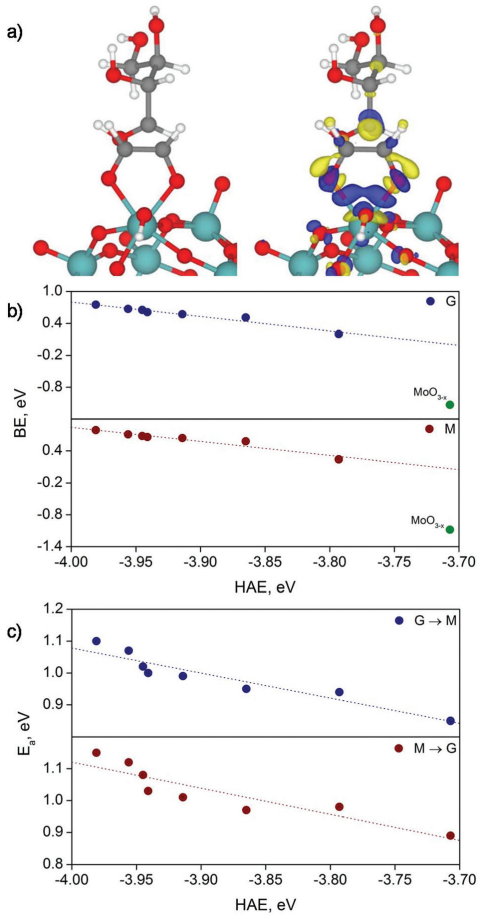

Fig. 4 (a) Structure of TS_{epim} for $H_3PMo_{12}O_{40}$ (left) and TS_{epim} charge density difference (right). The charge density difference was calculated with respect to the anion $[C_6H_{11}O_6]^-$ and cation $(H_4PMo_{12}O_{40})^+$ at the TS_{epim} geometry; same color code as Fig. 1. Blue color means depletion of charge density and yellow color means accumulation. (b) Binding energy, BE, of dissociated glucose and mannose as a function of HAE. E_{ads}(G) = −2.72 HAE − 10.08 eV, R^2 = 0.96, MAE = 0.03 eV. E_{ads}(M) = −2.65 HAE − 9.74 eV, R^2 = 0.93, MAE = 0.03 eV. Adsorption on defective MoO_{3-x}(010) surface is not included in the fittings. (c) Activation energy, E_a, of TS_{epim} as a function of HAE. E_a(G → M) = −0.79HAE − 2.06 eV, R^2 = 0.88, MAE = 0.02 eV. E_a(M → G) = −0.81HAE − 2.13 eV, R^2 = 0.81, MAE = 0.03 eV.

A microkinetic model was built in order to obtain the analytical equation for the reaction rate. The energies for the adsorption and 1,2 C-shifts are obtained from the linear fittings in Fig. 4b and c. From the reaction profile (Fig. 2) the epimeriza-

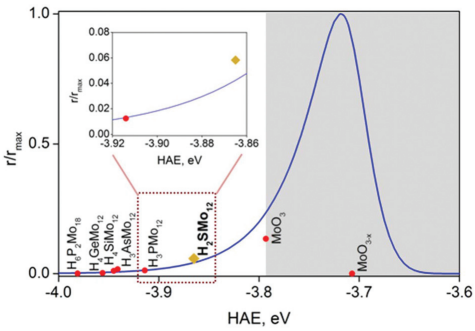

Fig. 5 Volcano plot of the normalized reaction rate as a function of the HAE. Conditions: T = 100 °C, [G] = 0.90 M, [M] = 0.10 M. Red points mark the calculated rate with eqn (5) for the catalyst used in the analysis. Catalysts in the shadow area present drawbacks for epimerization reaction.

tion step is the rate-determining step and using the quasi-equilibrium approximation the reaction rate can be expressed as:

$$r = k_2 K_G[G]\left(1 - \frac{[M]}{K_{global}[G]}\right)\frac{1}{1 + K_G[G] + \frac{1}{K_M}[M]} \qquad (5)$$

where K_i are the adsorption constants for glucose and mannose, i = G, M; k_2 is the coefficient for 1,2 C-shift (R2) starting from glucose, K_{global} is the constant for the epimerization reaction, and [M] and [G] are the corresponding concentrations of glucose and mannose. Dissociative adsorption and 1,2 C-shift energy barrier can be written in terms of the HAE. At 100 °C, for $[G]_i$ = 1 M and a conversion of 10% the reaction rate shows a volcano shape with the maximum placed in HAE = −3.72 eV, with TOF = 10.1 s^{-1}. In Fig. 5 the normalized reaction rate is plotted as a function of the HAE. The calculated rate for the defective surface is displaced from the rate fitting, as its adsorption energy does not adjust to the linear fitting. Pristine and defective MoO_3 surfaces are placed in a shadow zone, indicating that they present drawbacks for epimerization reaction; low stability in aqueous solution[30–32] or selectivity. Therefore, $H_2SMo_{12}O_{40}$ is the best catalyst for epimerization, and overperforming the activity of $H_3PMo_{12}O_{40}$. Calculated apparent activation energy using the reaction rate obtained from eqn (5), for $H_3PMo_{12}O_{40}$ is 1.04 eV, in good agreement with experimental value: 0.99 ± 0.04 eV.[19] The apparent activation energy calculated for $H_2SMo_{12}O_{40}$ is 1.00 eV, Fig. SI14.† The plot shows a narrow zone of reducibility where the Mo-based catalysts are active for epimerization. POMs are placed in the upper end of this zone and, therefore, a more active catalyst could be developed.

Conclusions

We have identified the mechanism behind the epimerization, the Bilik reaction, in the glucose/mannose pair on Mo-containing catalysts. The mechanism encompasses the adsorption of the aldose, the 1,2 C-shift and the recombination for desorption of the product. The same mechanism is valid for molecular and surface Mo oxides and no significant differences are found for the heteroatom or the curvature of the surface. The descriptor for the reaction corresponds to the reducibility of the Mo atoms on the surface/molecular catalyst that plays a crucial role in the 1,2 C-shift. When the reaction is written in terms of the HAE-descriptor (H addition energy) it is possible to optimize the composition thus indicating the most active system. The molecular catalyst also presents an excellent behavior in terms of the stability due to the electrostatic interaction between the heteroatom anion and the MoO_x shell. The bulk oxide shows a low cohesive energy. However, electrostatic interactions between the charged heteroatom unit and the $Mo_{12}O_{36}$ layer are larger which indicates the preeminent stability of the molecular catalyst. Finally, a more active POM, $H_2SMo_{12}O_{40}$, is proposed.

Conflicts of interest

There are no conflicts to declare.

Acknowledgements

The authors acknowledge the Spanish Ministerio de Economía y Competitividad (MINECO) for financial support (CTQ 2015-68770-R, Severo Ochoa Excellence Accreditation 2014–2018 SEV-2013-0319, and Severo Ochoa predoctoral grant SVP-2014-068237). In addition, we thank BSC-RES for providing computational resources.

References

1 Y.-C. Park, E. J. Oh, J.-H. Jo, Y.-S. Jin and J.-H. Seo, *Curr. Opin. Biotechnol.*, 2016, **37**, 105–113.
2 I. Delidovich and R. Palkovits, *ChemSusChem*, 2016, **9**, 547–561.
3 M. E. Tanner, *Acc. Chem. Res.*, 2002, **35**, 237–246.
4 J. Samuel and M. E. Tanner, *Nat. Prod. Rep.*, 2002, **19**, 261–277.
5 S.-C. Lu and S.-C. Lin, *Enzyme Microb. Technol.*, 2012, **50**, 65–70.
6 S. J. Angyal, *Carbohydr. Res.*, 1997, **300**, 279–281.
7 T. Tanase, F. Shimizu, S. Yano and S. Yoshikawa, *J. Chem. Soc., Chem. Commun.*, 1986, 1001–1003.
8 T. Tanase, F. Shimizu, M. Kuse, S. Yano, M. Hidai and S. Yoshikawa, *Inorg. Chem.*, 1988, **27**, 4085–4094.
9 A. M. Peres and E. A. Macedo, *Ind. Eng. Chem. Res.*, 1997, **36**, 2816–2820.
10 H. Nguyen, V. Nikolakis and D. G. Vlachos, *ACS Catal.*, 2016, **6**, 1497–1504.

11 R. Bermejo-Deval, R. Gounder and M. E. Davis, *ACS Catal.*, 2012, **2**, 2705–2713.
12 R. Bermejo-Deval, M. Orazov, R. Gounder, S.-J. Hwang and M. E. Davis, *ACS Catal.*, 2014, **4**, 2288–2297.
13 W. R. Gunther, Y. Wang, Y. Ji, V. K. Michaelis, S. T. Hunt, R. G. Griffin and Y. Roman-Leshkov, *Nat. Commun.*, 2012, **3**, 2122.
14 W. R. Gunther, Q. Duong and Y. Román-Leshkov, *J. Mol. Catal. A: Chem.*, 2013, **379**, 294–302.
15 T. Prasomsri, T. Nimmanwudipong and Y. Roman-Leshkov, *Energy Environ. Sci.*, 2013, **6**, 1732–1738.
16 T. Prasomsri, M. Shetty, K. Murugappan and Y. Roman-Leshkov, *Energy Environ. Sci.*, 2014, **7**, 2660–2669.
17 M. Rellán-Piñeiro and N. López, *ChemSusChem*, 2015, **8**, 2231–2239.
18 V. Zacharopoulou, E. S. Vasiliadou and A. A. Lemonidou, *Green Chem.*, 2015, **17**, 903–912.
19 F. Ju, D. VanderVelde and E. Nikolla, *ACS Catal.*, 2014, **4**, 1358–1364.
20 T. L. Lohr, A. R. Mouat, N. M. Schweitzer, P. C. Stair, M. Delferro and T. J. Marks, *Energy Environ. Sci.*, 2017, **10**, 1558–1562.
21 T. Choksi and J. Greeley, *ACS Catal.*, 2016, **6**, 7260–7277.
22 V. Bilik, *Chem. Zvesti*, 1972, **26**, 183–186.
23 L. Petruš, M. Petrušová and Z. Hricovíniová, in *Glycoscience: Epimerisation, Isomerisation and Rearrangement Reactions of Carbohydrates*, ed. A. E. Stütz, Springer Berlin Heidelberg, Berlin, Heidelberg, 2001, pp. 15–41.
24 M. L. Hayes, N. J. Pennings, A. S. Serianni and R. Barker, *J. Am. Chem. Soc.*, 1982, **104**, 6764–6769.
25 J. E. Godfrey and J. M. Waters, *Cryst. Struct. Commun.*, 1975, **4**, 5–8.
26 G. E. Taylor and J. M. Waters, *Tetrahedron Lett.*, 1981, **22**, 1277–1278.
27 M. Matulova and V. Bilik, *Chem. Pap.*, 1990, **44**, 257–265.
28 B. K. Chethana, D. Lee and S. H. Mushrif, *J. Mol. Catal. A: Chem.*, 2015, **410**, 66–73.
29 A. Cybulski, B. F. M. Kuster and G. B. Marin, *J. Mol. Catal.*, 1991, **68**, 87–103.
30 G. M. Lari, O. G. Gröninger, Q. Li, C. Mondelli, N. López and J. Pérez-Ramírez, *ChemSusChem*, 2016, **9**, 3407–3418.
31 M. Orazov and M. E. Davis, *Proc. Natl. Acad. Sci. U. S. A.*, 2015, **112**, 11777–11782.
32 A. Takagaki, S. Furusato, R. Kikuchi and S. T. Oyama, *ChemSusChem*, 2015, **8**, 3769–3772.
33 M. T. Pope and A. Müller, *Angew. Chem., Int. Ed. Engl.*, 1991, **30**, 34–48.
34 J. F. Keggin, *Proc. R. Soc. London, Ser. A*, 1934, **144**, 75–100.
35 G. Kresse and J. Furthmuller, *Comput. Mater. Sci.*, 1996, **6**, 15–50.
36 G. Kresse and J. Furthmueller, *Phys. Rev. B: Condens. Matter Mater. Phys.*, 1996, **54**, 11169–11186.
37 J. P. Perdew, K. Burke and M. Ernzerhof, *Phys. Rev. Lett.*, 1996, **77**, 3865–3868.
38 S. L. Dudarev, G. A. Botton, S. Y. Savrasov, C. J. Humphreys and A. P. Sutton, *Phys. Rev. B: Condens. Matter Mater. Phys.*, 1998, **57**, 1505–1509.
39 S. Grimme, *J. Comput. Chem.*, 2006, **27**, 1787–1799.
40 G. Kresse and D. Joubert, *Phys. Rev. B: Condens. Matter Mater. Phys.*, 1999, **59**, 1758–1775.
41 G. Makov and M. C. Payne, *Phys. Rev. B: Condens. Matter Mater. Phys.*, 1995, **51**, 4014–4022.
42 G. Mills, H. Jonsson and G. K. Schenter, *Surf. Sci.*, 1995, **324**, 305–337.
43 G. Henkelman, B. P. Uberuaga and H. Jónsson, *J. Chem. Phys.*, 2000, **113**, 9901–9904.
44 G. Henkelman and H. Jónsson, *J. Chem. Phys.*, 1999, **111**, 7010–7022.
45 A. Heyden, A. T. Bell and F. J. Keil, *J. Chem. Phys.*, 2005, **123**, 224101.
46 M. Garcia-Ratés and N. López, *J. Chem. Theory Comput.*, 2016, **12**, 1331–1341.
47 M. Garcia-Ratés, R. García-Muelas and N. López, *J. Phys. Chem. C*, 2017, **121**, 13803–13809.
48 M. Álvarez-Moreno, C. de Graaf, N. López, F. Maseras, J. M. Poblet and C. Bo, *J. Chem. Inf. Model.*, 2015, **55**, 95–103.
49 https://doi.org/10.19061/iochem-bd-1-44.
50 S. S. Sunu, E. Prabhu, V. Jayaraman, K. I. Gnanasekar, T. K. Seshagiri and T. Gnanasekaran, *Sens. Actuators, B*, 2004, **101**, 161–174.
51 A. Borgschulte, O. Sambalova, R. Delmelle, S. Jenatsch, R. Hany and F. Nüesch, *Sci. Rep.*, 2017, **7**, 40761.
52 K. Inzani, M. Nematollahi, F. Vullum-Bruer, T. Grande, T. W. Reenaas and S. M. Selbach, *Phys. Chem. Chem. Phys.*, 2017, **19**, 9232–9245.
53 I. V. Kozhevnikov, *Chem. Rev.*, 1998, **98**, 171–198.
54 J. Macht, M. J. Janik, M. Neurock and E. Iglesia, *J. Am. Chem. Soc.*, 2008, **130**, 10369–10379.
55 I.-M. Mbomekallé, X. López, J. M. Poblet, F. Sécheresse, B. Keita and L. Nadjo, *Inorg. Chem.*, 2010, **49**, 7001–7006.
56 K. Maeda, H. Katano, T. Osakai, S. Himeno and A. Saito, *J. Electroanal. Chem.*, 1995, **389**, 167–173.
57 M. Sadakane and E. Steckhan, *Chem. Rev.*, 1998, **98**, 219–238.
58 M. Capdevila-Cortada and N. López, *ACS Catal.*, 2015, **5**, 6473–6480.
59 M. Capdevila-Cortada, G. Vilé, D. Teschner, J. Pérez-Ramírez and N. López, *Appl. Catal., B*, 2016, **197**, 299–312.
60 P. Deshlahra and E. Iglesia, *J. Phys. Chem. C*, 2014, **118**, 26115–26129.
61 P. Deshlahra, R. T. Carr, S.-H. Chai and E. Iglesia, *ACS Catal.*, 2015, **5**, 666–682.
62 Notice that Mo^{5+} centers are outliers in the fit for adsorption *via* electrostatic contributions.

Appendix

Suplementary information

CHEMISTRY & SUSTAINABILITY
CHEMSUSCHEM
ENERGY & MATERIALS

Supporting Information

The Active Molybdenum Oxide Phase in the Methanol Oxidation to Formaldehyde (Formox Process): A DFT Study

Marcos Rellán-Piñeiro and Núria López*[a]

cssc_201500315_sm_miscellaneous_information.pdf

Table S1. Crystal structure and corresponding bulk parameters and comparison to experiments. Distances in Å.

System		Crystal group	a	b	c
α-MoO_3	**PBE-D2**	*Pbnm*	3.921	14.480	3.708
	Exp.	*Pbnm*	3.962	13.855	3.699
MoO_2*	PBE	$P2_1/c$	5.612	4.923	5.692
	Exp.	$P2_1/c$	5.611	4.856	5.629
r-MoO_2	**PBE**	*P4/mnm*	4.966	4.966	2.732

*Angle β^{PBE}=120.7º and β^{Exp}=121.0º

Table S2. Surface energies for α-MoO_3(010) and MoO_2 (110) surfaces, in eV/Å^2.

	α-MoO_3(010)	**r-MoO_2(110)**
γ	0.009	0.103

Figure S1. Structures of MoO_6 distorted octahedra for (a) α-MoO_3 and (b) r-MoO_2.

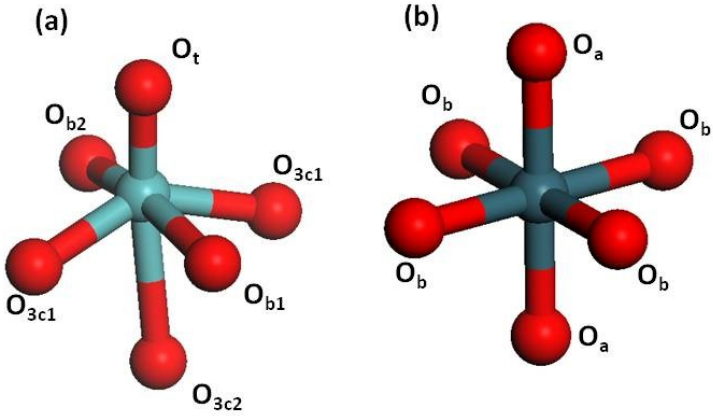

Table S3. Bond distances, in Å, between Mo and O in MoO_6 distorted octahedra for r-MoO_2 and α-MoO_3.

α -MoO_3(010)			
Oxygen	**Nº**	**Coord.**	**d (Mo-O)**
O_t	1	1	1.701
O_{b1}	1	2	2.176
O_{b2}	1	2	1.774
O_{3c1}	2	3	1.954
O_{3c2}	1	3	2.402

r-MoO_2			
Oxygen	**Nº**	**Coord.**	**d (Mo-O)**
O_a	2	3	1.986
O_b	4	3	2.047

Figure S2. Projected Density of States for α-MoO_3 and r-MoO_2 systems.

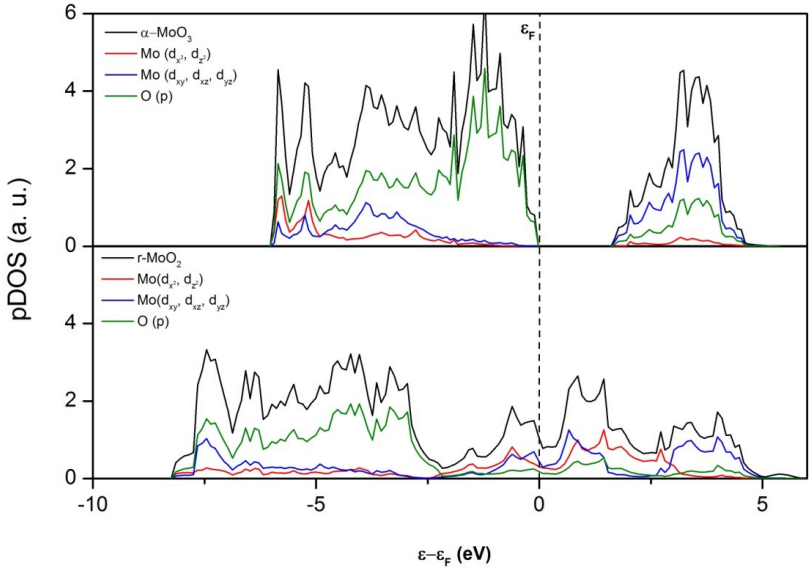

Figure S3. Relaxed structures of reduced α-MoO_3(010). Vacancies are placed in surface and subsurface positions.

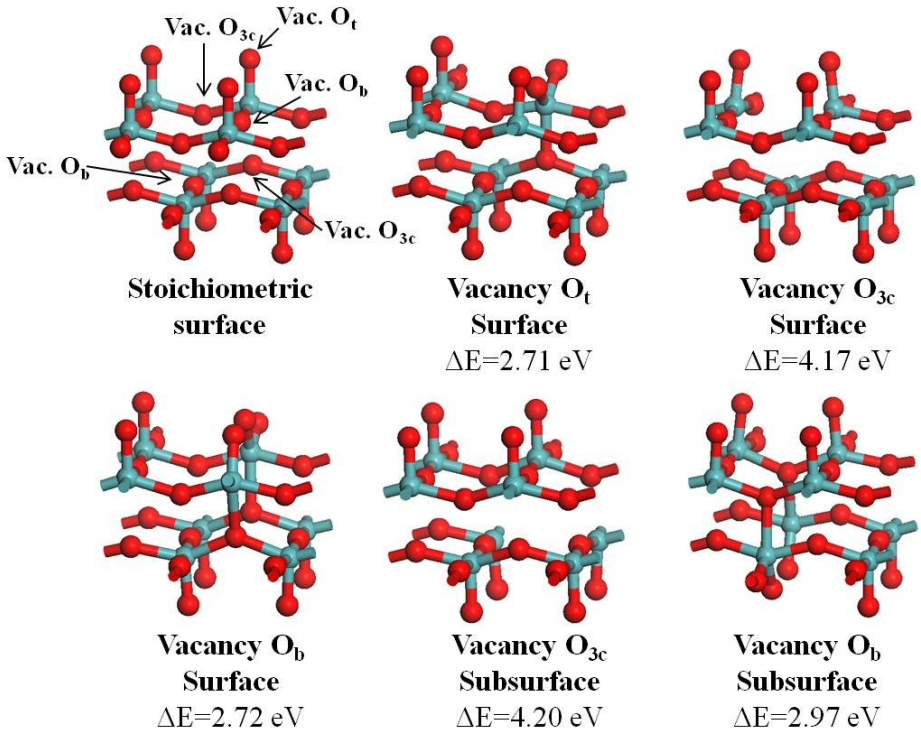

Table S4. Adsorption energies, E_{ads}, in eV, of CH_3OH, CH_2O and CO for all surfaces of this study.

	CH_3OH	CH_2O	CO
α-MoO_3(010)	-0.25	-0.05	-
α-MoO_3(010)-□	-1.16	-1.44	-1.21
r-MoO_2(110)	-2.06	-2.38	-1.30
r-MoO_2(110)- O_{cus}	-1.85	-2.29	-1.27
r-MoO_2/MoO_3	-0.22	-0.27	-
Fe_{ss}-MoO_3	-0.47	-0.01	-
Fe_{ss}-MoO_3-□	-1.44	-1.40	-
Fe_s-MoO_3-Mo□	0.02	-0.89	-
Fe_s-MoO_3-Fe□	-1.07	-1.24	-

Table S5. Adsorption energies, E_{ads} in eV, for CH_3OH and CH_2O on α-MoO_3(010), α-MoO_3-□(010) and r-MoO_2(110) with different cut-off energies.

	α-MoO_3(010)		**α-MoO_3-□(010)**		**r-MoO_2(110)**	
Cut-off eV	**CH_3OH**	**CH_2O**	**CH_3OH**	**CH_2O**	**CH_3OH**	**CH_2O**
400	-0.27	-0.05	-1.18	-1.46	-2.07	-2.39
450	-0.25	-0.05	-1.16	-1.44	-2.06	-2.38
500	-0.26	-0.05	-1.17	-1.44	-2.06	-2.37
600	-0.26	-0.05	-1.16	-1.44	-2.06	-2.38
700	-0.26	-0.06	-1.17	-1.45	-2.06	-2.38

Table S6. Reaction energies, ΔE**,** for CH_3OH and CH_2O oxidations in all systems. Energies in eV.

System	**Reaction**	**ΔE**
α -MoO_3(010)	$CH_3OH \rightarrow CH_2O + H_2O$	1.53
α -MoO_3(010)-□	$CH_3OH \rightarrow CH_2O + H_2$	1.34
r-MoO_2(110)	$CH_3OH \rightarrow CH_2O + H_2O$	1.97
r-MoO_2(110) -O_{cus}	$CH_3OH \rightarrow CH_2O + H_2O$	1.78
r-MoO_2/MoO_3	$CH_3OH \rightarrow CH_2O + H_2O$	1.14
Fe_{ss}-MoO_3(010)	$CH_3OH \rightarrow CH_2O + H_2O$	0.12
α -MoO_3(010)	$CH_2O \rightarrow CO + H_2O$	0.78
α -MoO_3(010)-□	$CH_2O \rightarrow CO + H_2$	0.59
r-MoO_2(110)	$CH_2O \rightarrow CO + H_2O$	1.23
r-MoO_2(110) -O_{cus}	$CH_2O \rightarrow CO + H_2O$	1.03
r-MoO_2/MoO_3	$CH_2O \rightarrow CO + H_2O$	0.39
Fe_{ss}-MoO_3(010)	$CH_2O \rightarrow CO + H_2O$	-0.63

Table S7. Reaction energies, ΔE, activation barriers, E_a, and imaginary frequencies for the transition states, ν_i, for all the reactions in this study. Energies in eV and frequencies in cm^{-1}.

α-MoO_3(010)			
Reaction	**ΔE**	**E_a**	**ν_i**
CH_3OH+*→CH_3OH*	-0.25	-	-
CH_3OH*+*→CH_3O*+OH*	0.38	1.13	941
(A) CH_3O*+*OH→CH_2O*+H_2O*	-0.33	1.04	667
(A) CH_2O*+ H_2O*→CH_2O+H_2O*	0.83	-	-
(A) CH_2O+*H_2O→CH_2O+H_2O	0.90	-	-
(B) CH_3O*+*OH→CH_2O*+2OH*	0.00	1.30	1245
(B) CH_2O*+*2OH→CH_2O+2OH*	0.28	-	-
(B) CH_2O+*2OH→CH_2O+H_2O	1.12	-	-
CH_2O+*→CH_2O*	-0.05		
CH_2O*+*→CHO*+OH*	-0.37	1.01	1327

α -MoO_3(010)-□			
Reaction	**ΔE**	**E_a**	**ν_i**
CH_3OH+*→CH_3OH*	-1.16	-	-
CH_3OH*+*→CH_3O*+H*	0.07	0.16	757
(A) CH_3O*+*OH→CH_2O*+H_2O*	0.15	1.28	1284
(A) CH_2O*+ H_2O*→CH_2O+H_2O*	1.99	-	-
(A) CH_2O+*H_2O→CH_2O+H_2	0.30	-	-
(B) CH_3O*+*OH→CH_2O*+2OH*	0.38	1.54	1345
(B) CH_2O*+*2OH→CH_2O+2OH*	1.83	-	-
(B) CH_2O+*2OH→CH_2O+H_2	0.23	-	-
CH_2O+*→CH_2O*	-1.44	-	-
CH_2O*+*→CHO*+H*	-0.17	1.08	1211
CHO*+OH*→CO*+2OH*	0.62	1.45	525
CO*+ 2OH*→CO+2OH*	1.21	-	-
CO+ 2OH*→CO+H_2	0.38	-	-

r-MoO_2(110)			
Reaction	**ΔE**	**E_a**	**ν_i**
CH_3OH+*→CH_3OH*	-2.06	-	-
CH_3OH*+*→CH_3O*+OH*	-0.25	0.12	984
CH_3O*+*OH→CH_2O*+2OH*	1.09	1.34	1435
CH_2O*+*2OH→CH_2O+2OH*	1.12	-	-
CH_2O+*2H→CH_2O+H_2O	2.06	-	-
CH_2O+*→CH_2O*	-2.38	-	-
CH_2O*+*→CHO*+OH*	0.14	1.45	1479
CHO*+OH*→CO*+2OH*	0.11	1.51	1464
CO*+2OH*→CO+2OH*	1.30	-	-
CO+2OH*→CO+H_2O	2.06	-	-

r-MoO_2(110)-O_{cus}			
Reaction	**ΔE**	**E_a**	**ν_i**
CH_3OH+*→CH_3OH*	-1.85	-	-
CH_3OH*+*→CH_3O*+OH*	-0.05	0.14	763
(A) CH_3O*+*OH→CH_2O*+H_2O*	0.75	1.27	1232
(A) CH_2O*+ H_2O*→CH_2O+H_2O*	1.43	-	-
(A) CH_2O+*H_2O→CH_2O+H_2O	1.50	-	-
(B) CH_3O*+*OH→CH_2O*+2OH*	0.46	1.07	1481
(B) CH_2O*+*2OH→CH_2O+2OH*	1.26	-	-
(B) CH_2O+*2OH→CH_2O+H_2O	1.96		
CH_2O+*→CH_2O*	-2.29	-	-
CH_2O*+*→CHO*+OH*	-1.10	1.10	1723
CHO*+OH*→CO*+2OH*	1.23	2.28	1376
CO*+2OH*→CO+2OH*	1.38	-	-
CO+2OH*→CO+H_2O	1.81	-	-

MoO_2/MoO_3(010)			
Reaction	**ΔE**	**E_a**	**ν_i**
CH_3OH+*→CH_3OH*	-0.22	-	-
CH_3OH*+*→CH_3O*+OH*	0.70	1.77	895
(A) CH_3O*+*OH→CH_2O*+H_2O*	-1.07	0.84	1544
(A) CH_2O*+ H_2O*→CH_2O+H_2O*	0.12	-	-
(A) CH_2O+*H_2O→CH_2O+H_2O	1.62	-	-
(B) CH_3O*+*OH→CH_2O*+2OH*	-0.90	1.05	1491
(B) CH_2O*+*2OH→CH_2O+2OH*	0.11	-	-
(B) CH_2O+*2OH→CH_2O+H_2O	1.45	-	-
CH_2O+*→CH_2O*	-0.27	-	-
CH_2O*+*→CHO*+OH*	-0.86	0.50	1176

Table S8. Bader charges for atoms of the topmost bilayer for α-MoO_3 surfaces and magnetization for relevant atoms.

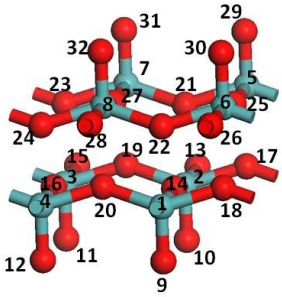

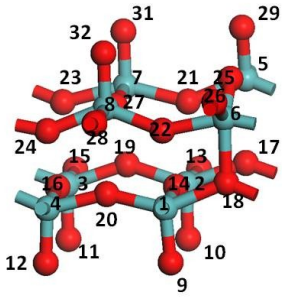

α -MoO_3(010)		
	q |e^-|	
Atom	α-MoO_3	α-MoO_3-□
Mo(8)	2.30	2.28
Mo(7)	2.30	2.24
Mo(6)	**2.30**	**2.21**
Mo(5)	2.30	2.25
Mo(4)	2.35	2.33
Mo(3)	2.35	2.31
Mo(2)	2.35	2.31
Mo(1)	2.35	2.33
O (32)	-0.54	-0.57
O (31)	-0.54	-0.53
O(30)	-0.54	-
O(29)	-0.54	-0.55
O(28)	-0.80	-0.83
O(27)	-0.80	-0.88
O(26)	-0.80	-0.85
O(25)	-0.80	-0.69
O(24)	-0.96	-0.96
O(23)	-0.96	-0.95
O(22)	-0.96	-0.96
O(21)	-0.96	-0.95
O(20)	-0.96	-0.90
O(19)	-0.96	-0.96
O(18)	-0.96	-0.98
O(17)	-0.96	-0.96
O(16)	-0.79	-0.84
O(15)	-0.79	-0.84
O(14)	-0.79	-0.84
O(13)	-0.79	-0.84
O(12)	-0.61	-0.62
O(11)	-0.61	-0.56
O(10)	-0.61	-0.56
O(9)	-0.61	-0.62

α -MoO_3(010)		
Atom	μ(μ_B)	
	α-MoO_3	α-MoO_3-□
Mo(8)	0.00	0.02
Mo(6)	**0.00**	**0.35**
Mo(5)	0.00	0.07
O(27)	0.00	0.02
O(26)	0.00	-0.01
O(25)	0.00	-0.02
O(24)	0.00	0.02
O(22)	0.00	0.02
O(21)	0.00	0.01

Table S9. Bader charges for the atoms of the two topmost trilayers for r-MoO_2 surfaces.

r-MoO_2(110)			
Atom	**q |e⁻|**		
	MoO_2	MoO_2-□	MoO_2-O_{cus}
Mo(12)	1.94	1.72	**2.06**
Mo(11)	1.95	1.72	1.79
Mo(10)	1.94	1.78	2.06
Mo(9)	1.82	1.79	1.79
Mo(8)	1.82	1.75	1.79
Mo(7)	1.83	1.79	2.02
Mo(6)	1.83	1.83	1.87
Mo(5)	1.83	1.83	1.87
Mo(4)	1.84	1.84	1.88
Mo(3)	1.89	1.92	1.96
Mo(2)	1.90	1.89	1.96
Mo(1)	1.90	1.89	1.92
O_{cus}*	-	-	-0.59
O(36)	-0.79	0.83	-0.75
O(35)	-0.79	-	-0.75
O(34)	-0.79	-0.83	-0.80
O(33)	-0.98	-0.99	-0.97
O(32)	-0.98	-1.00	-0.97
O(31)	-0.98	-0.97	-0.95
O(30)	-0.98	-0.98	-0.95
O(29)	-0.98	-0.97	-0.97
O(28)	-0.98	-1.00	-0.97
O(27)	-0.98	-1.04	-0.97
O(26)	-0.98	-0.91	-0.97
O(25)	-0.98	-0.92	-1.00
O(24)	-0.93	-0.91	-0.92
O(23)	-0.93	-0.90	-0.92
O(22)	-0.93	-0.91	-0.95
O(21)	-0.96	-0.96	-0.95
O(20)	-0.95	-0.95	-0.95
O(19)	-0.95	-0.95	-0.94
O(18)	-0.95	-0.95	-0.94
O(17)	-0.95	-0.95	-0.95
O(16)	-0.96	-0.96	-0.95
O(15)	-0.92	-0.92	-0.93
O(14)	-0.92	-0.92	-0.93
O(13)	-0.92	-0.92	-0.91

*O_{cus} on Mo(7)

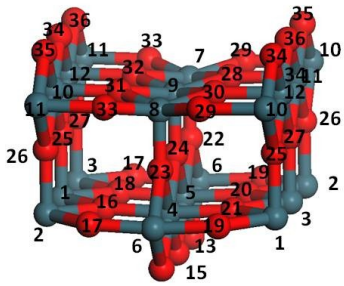

Table S10. Bader charges for the atoms of topmost bilayer for Fe-MoO_3 and magnetization for relevant atoms.

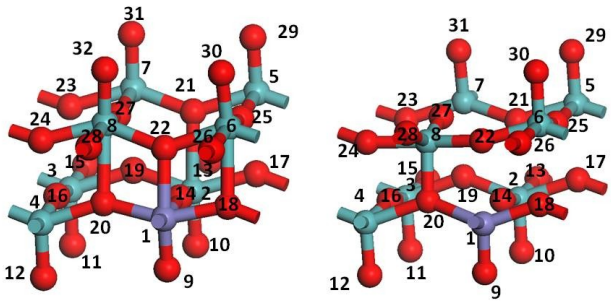

Fe-MoO_3(010)		
Atom	**q |e⁻|**	
	Fe-MoO_3	Fe-MoO_3-□
Mo(8)	**2.32**	**2.28**
Mo(7)	2.31	2.29
Mo(6)	2.33	2.30
Mo(5)	2.35	2.31
Mo(4)	2.32	2.26
Mo(3)	2.35	2.34
Mo(2)	2.32	2.28
Fe(1)	**1.64**	**1.58**
O(32)	-0.55	-
O(31)	-0.59	-0.56
O(30)	-0.55	-0.58
O(29)	-0.59	-0.56
O(28)	-0.80	-0.80
O(27)	-0.80	-0.77
O(26)	-0.80	-0.78
O(25)	-0.80	-0.81
O(24)	-0.94	-0.94
O(23)	-0.95	-0.95
O(22)	-0.91	-0.88
O(21)	-0.97	-0.95
O(20)	-0.89	-0.88
O(19)	-0.95	-0.97
O(18)	-0.89	-0.89
O(17)	-0.95	-0.96
O(16)	-0.79	-0.81
O(15)	-0.82	-0.82
O(14)	-0.74	-0.74
O(13)	-0.55	-0.78
O(12)	-0.60	-0.55
O(11)	-0.57	-0.60
O(10)	-0.60	-0.56
O(9)	-0.36	-0.48

Fe-MoO_3(010)		
Atom	**μ(μ_B)**	
	Fe-MoO_3	Fe-MoO_3-□
Mo(8)	**0.00**	**0.329**
Mo(7)	0.00	0.02
Mo(6)	0.00	0.03
Mo(5)	0.00	0.01
Mo(4)	0.03	0.07
Mo(3)	0.00	0.01
Mo(2)	0.00	0.02
Fe(1)	**1.29**	**2.33**
O(13)	0.23	0.20
O(9)	0.23	0.36

Figure S4. Projected Density of States for Fe atom on Fe-MoO_3 and Fe-MoO_3-□ surfaces.

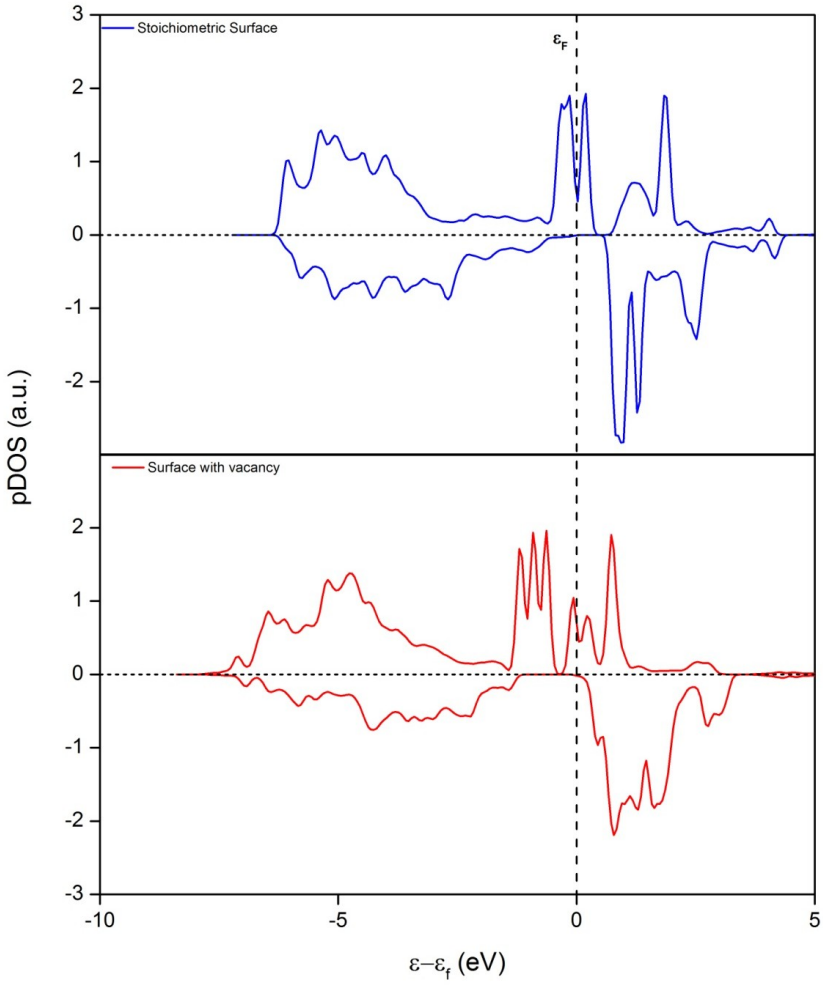

Figure S5. Optimized structures of all intermediates for methanol and formaldehyde decomposition in each system. Color code: red: oxygen, dark red: oxygen, light green: Mo(VI), dark green: Mo(IV) and white: H.

α-MoO_3(010)

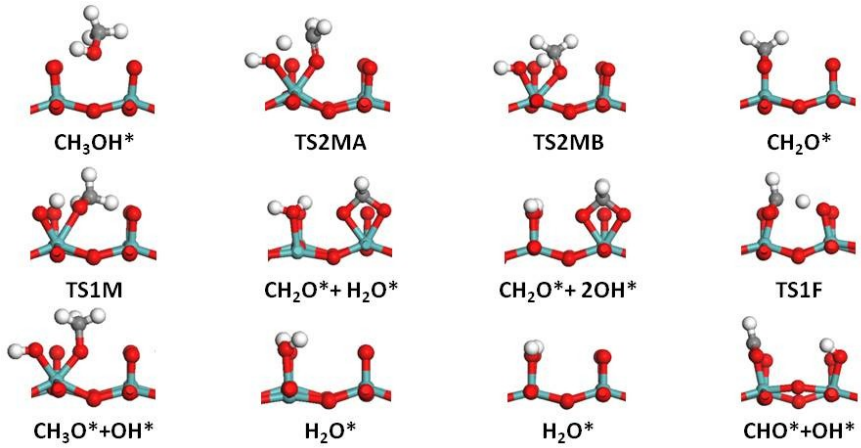

α-MoO_3(010)-□

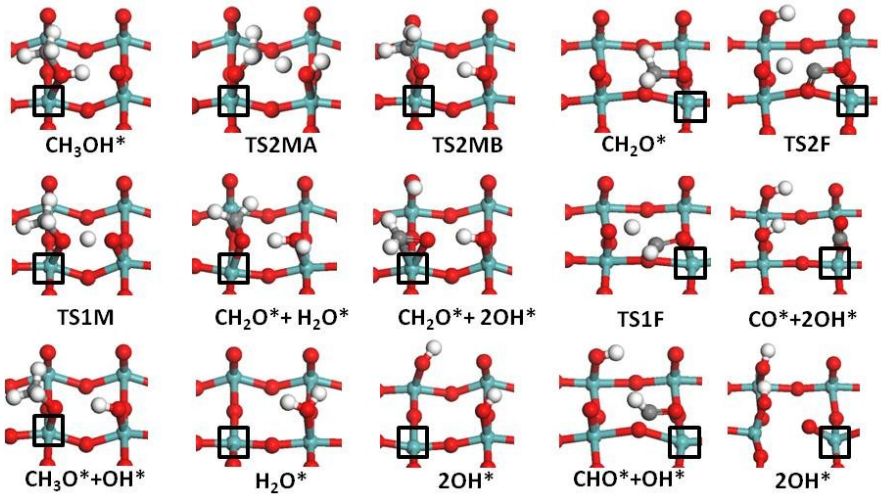

r-MoO_2(110)

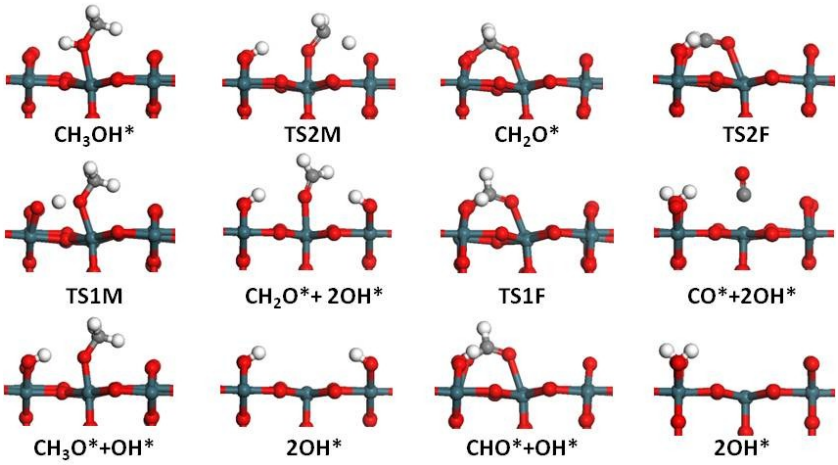

r-MoO_2(110)-O_{cus}

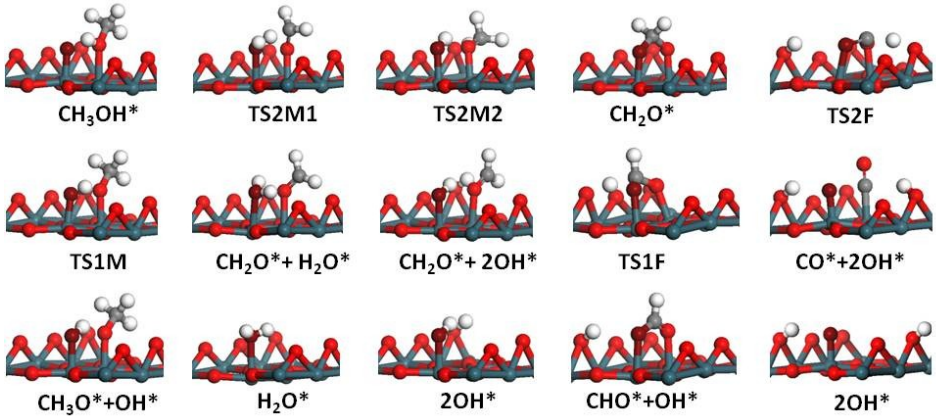

MoO_2/MoO_3

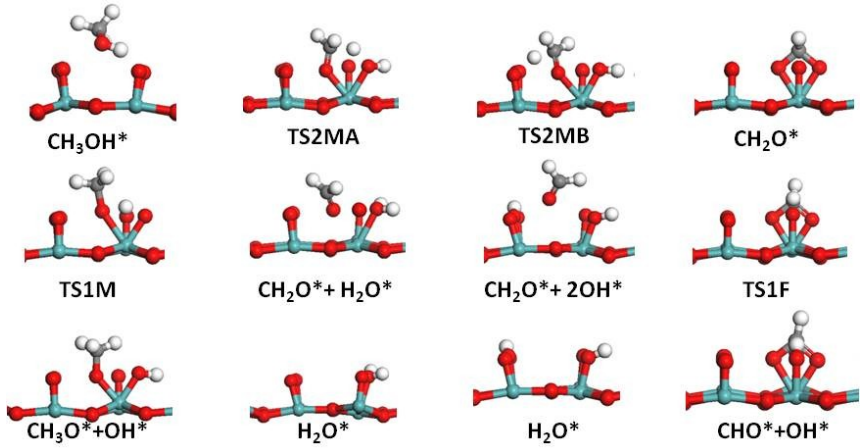
CH3OH*
TS2MA
TS2MB
CH2O*
TS1M
CH2O*+ H2O*
CH2O*+ 2OH*
TS1F
CH3O*+OH*
H2O*
H2O*
CHO*+OH*

Supporting Information

One oxygen vacancy, two charge states: characterization of reduced α-MoO_3(010) through theoretical methods

Marcos Rellán-Piñeiro and Núria López*

Institute of Chemical Research of Catalonia, ICIQ, and The Barcelona Institute of Science and Technology, Av. Països Catalans 16, 43007 Tarragona Spain

*E-mail: nlopez@iciq.es

Table of contents:

SI1. U_{eff} optimization

Density functional theory, DFT, has become an essential tool to study catalytic processes. Atomic simulations allow better understanding of catalytic properties and reaction mechanisms. For α-MoO_3 catalytic systems several theoretical works have been performed with pure GGA functionals.[1-3] However, these functionals are known to delocalizate *d* and *f* electrons, which results in scattered results for reaction energies and activation barriers. An alternative to solve this problem is the use of hybrid functionals, which include a portion of exact exchange from HF theory. This approximation is extended in the study of molecules but its computational cost is prohibitive for reactivity studies. In heterogeneous catalysis, the most common method used to correctly describe *d* and *f* electrons is the DFT+U approximation. The electron localization is reached by the introduction of an extra interelectron repulsion term, the Hubbard-like U_{eff}.[4] The U_{eff} is chosen either by fitting to a particular experimental property or reaction energy or by fitting to hybrid functional results.

Several values for U_{eff} have been reported in theoretical works on MoO_3. The most common was proposed by Willock,[5] 6.3 eV, that was widely used by others.[6-7] This value is very close to the value proposed by Asta,[8] 6 eV; both were fitted with cluster calculations with hybrid functionals. Metiu[9-10] and Bell[11-12] fitted U_{eff} to experimental reaction energies and proposed values of 2.0 and 8.6 eV respectively. Moreover, several studies used intermediate values.[13-15]

In order to obtain the U_{eff} that gives the most accurate results we have studied the reaction energies and electron localization as function of U_{eff} for a set of reactions. The methanol oxidation to formaldehyde on α-MoO_3(010) surface was used as example.[2, 16] In **Figure S1.a** the reaction energy for methanol dissociative adsorption is represented as function of U_{eff} = 0.0-7.0 eV range. This is an acid-base process, i.e., no electrons are transferred to the surface. The reaction energy is almost constant for all U_{eff} and no magnetization appears. Redox processes are known to behave differently. In **Figure 2.b** and **c** the reaction energies for the formation of ½CH_2O and CH_2O from methanol are shown. These reactions leave one and two hydrogen atoms on the surface respectively leading the one and two electrons surface reduction. These electrons are accommodated on surface cations. For small values of U_{eff} the reaction energies remain constant and no magnetization at Mo centers is observed. For U_{eff} higher than 3.0 eV the reaction energies decrease linearly with U_{eff}; the slope of the energy variation is proportional to the number of electrons localized on the surface. The same behavior was previously reported for redox processes on CeO_2.[17] In the same U_{eff} range magnetization values are close to 1 and

2, describing the single and double reduction to one Mo^{5+} and two Mo^{5+}. For the two electrons reduction system single electron localization is observed at low U_{eff} values (2.0 and 2.5 eV).

Single point calculations with the hybrid HSE06 functional at Γ-point were performed to obtain accurately reaction energies and electron localization, **Figure SI1**. Hybrid calculations were performed for PBE+U (U_{eff}= 0, 3.5 and 7.0 eV) on the converged geometries:

- For the acid-base reaction the hybrid calculations give almost constant reaction values between 0.43 and 0.54 eV. The PBE+U reaction energies at Γ-point are more similar to the obtained with HSE06 functional, and therefore, an influence of the k-point sampling cannot be neglected.
- For the redox systems the hybrid functional gives reaction energies similar to PBE+U when low U_{eff} values are employed and a magnetization close to 1 and 2 for the single and double Mo reduction reactions. High U_{eff} results in energies that depart from the benchmark values even if the single point HSE06 calculations are performed over the structures optimized with U_{eff}= 7.0 eV.

Therefore, a low U_{eff} should be used to obtain good reaction energies; and moreover, the U_{eff} value should give the correct electron localization. The reaction energies for U_{eff}= 3.5 eV are similar to obtained with the more accurate HSE06 functional and, in addition, the electron magnetization is the same as the hybrid functional. Therefore, U_{eff}= 3.5 eV is the most accurate U_{eff} value for our system.

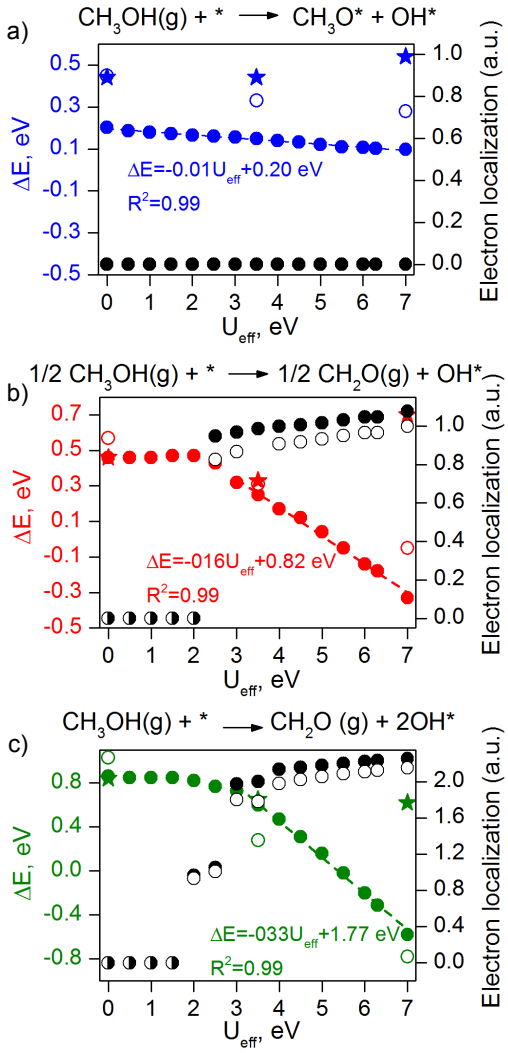

Figure SI1. Reaction energy as function of U_{eff} for: a) acid-base dissociative adsorption of methanol, b) one electron reduction of the surface by de adsorption of one hydrogen atom, and c) two electron reduction of the surface for the addition of two hydrogen atoms. Colored filled circles are PBE+U values at 5x5x1 k-point sampling. Colored circles are PBE+U energies at Γ-point. Colored stars are HSE06 reaction energies. Right axis: Black circles are the total magnetization and white circles the magnetization of reduced Mo centers.

In addition, benchmark calculations were performed for the 1,3-propanediol oxidation to hydroxypropanal on the cluster Mo_3O_9. Molecules and cluster Mo_3O_9 were calculated inside a 20x21x22 $Å^3$ box at Γ-point. This reaction leaves two hydrogen atoms on the cluster reducing two Mo^{6+} to Mo^{5+}. Dixon and collaborators reported the reaction energy for this system at the CCSD(T) level.[18] We performed single point calculations on their reported structures at PBE, PBE+U, BEEF-vdW and HSE06 level with VASP code. For PBE+U functional we used both our fitted U_{eff}= 3.5 eV and the most utilized value of 6.3 eV. In addition, we performed a test in Gaussian 09[19] with the B3LYP[20-21] functional with the base aug-cc-pVDZ[22] for O, C and H and aug-cc-pVDZ-pp coupled to relativistic effective core potentials (RECP)[23] for Mo. The results are shown in **Figure SI2**. The CCSD(T) reference value is 1.00 eV. PBE and BEEF-vdW overestimate the reaction energy by 0.22 and 0.25 eV respectively, and do not show any electron localization. Hybrid functionals give values similar to coupled cluster, 1.05 and 1.11 eV for B3LYP and HSE06 respectively. Finally, PBE+U gives a good value of 1.13 eV for U_{eff}= 3.5 eV. On the contrary, a U_{eff} value of 6.3 eV leads to 0.66 eV. Both hybrid and PBE+U functionals correctly localize the electrons resulting on two Mo^{5+} centers. These results further confirm that PBE+U with U_{eff}= 3.5 eV gives accurate values for both energy and electron localization for Mo oxides irrespectively of its cluster or continuous nature.

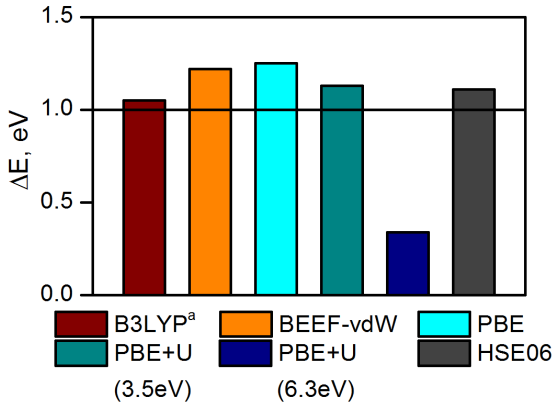

Figure SI2. Benchmark calculations for the reaction energy of $C_3O_2H_8(g)$ + Mo_3O_9 → $C_3O_2H_6$ + $Mo_3O_9H_2$ with different functionals. The horizontal line marks the value for the CCSD(T)/aug-cc-pVDZ/aug-cc-pVDZ-pp method.[18] [a]B3LYP calculations were performed with Gaussian 09 software.

SI2. Surface vacancy formation

Vacancies in O_b position were not possible to converge; all our attempts to optimize it converged in the O_t vacancy geometry. Moreover, the formation of an O_{3c} vacancy is highly energy demanding. Therefore, all the vacancies formed will be in O_t position. Vacancy formation energies at O_t and O_{3c} positions were calculated for different vacancy coverage, θ_{VOt}, see **Table S1** and **S2**. (1x2), (2x2), (3x2), (2x3), and (3x3) supercells were employed removing up to four oxygen atoms. When O_t are removed the formation of $2xMo^{5+}$ vacancies has a linear coverage dependence; whereas, the formation of Mo^{4+} vacancies is independent of the coverage until θ_{VOt}= 0.5. The formation of vicinal vacancies along [001]-axis is not allowed for $2xMo^{5+}$ surface oxidation state, since the two Mo^{5+} are placed on vicinal positions along this axis. However, for the formation of two Mo^{4+} vacancies along [001]-axis is possible and the formation energy is constant. In addition, the formation of two vacancies in contiguous Mo along the [100]-axis is avoided for both two oxidation states. The formation of a second vacancy in the (3x3) supercell requires an additional 0.36 and 0.24 eV for $2xMo^{5+}$ and Mo^{+4} oxidation states. This energy increment reaches 0.90 and 0.58 eV for the (2x2) supercell.

Table SI1. O_t vacancy formation energy, in eV, according to the reaction $MoO_3 \rightarrow MoO_{3-x} + x/2\ O_2(g)$, for all the cell size and vacancy coverage calculated in this work. Color code: Mo: green; O: red.

	Vacancies O_t			
	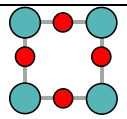	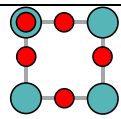	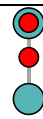	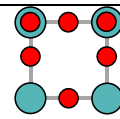
θ_{vac}	**1**	**3/4 (0.75)**	**1/2 (0.5)**	**2/4 (0.5)**
$2xMo^{5+}$	-	2.98	3.24	$2xMo^{5+}$: -
Mo^{4+}	3.05 (3.30)	2.96	3.13	3.10
	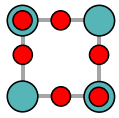	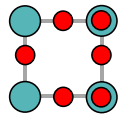	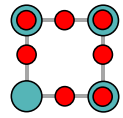	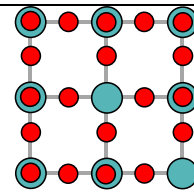
θ_{vac}	**2/4 (0.5)**	**2/4 (0.5)**	**1/4 (0.25)**	**2/9 (0.22)**
$2xMo^{5+}$	2.78	-	2.73	2.66
Mo^{4+}	2.83	2.81	2.87	2.85
	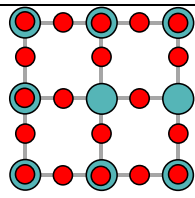	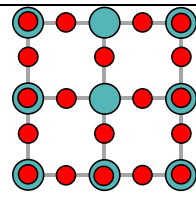	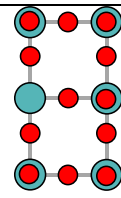	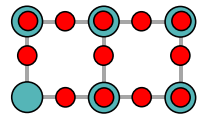
θ_{vac}	**2/9 (0.22)**	**2/9 (0.22)**	**1/6 (0.17)**	**1/6 (0.17)**
$2xMo^{5+}$	2.83	-	2.66	2.68
Mo^{4+}	2.94	2.82	2.85	2.86
	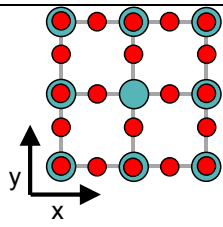			
θ_{vac}	**1/9 (0.11)**			
$2xMo^{5+}$	2.62			
Mo^{4+}	2.84			

Table SI2 . Scheme of O_{3c} vacancies and vacancy formation energy, in eV, according to the reaction $MoO_3 \rightarrow MoO_{3-x} + x/2\ O_2(g)$ for (2x2), (3x2), (2x3) and (3x3) cell size. Same color code as in Table SI1.

	Vacancies O_{3c}			
	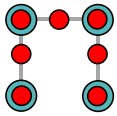	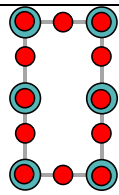	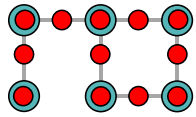	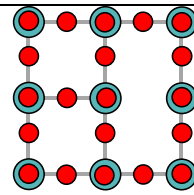
θ_{vac}	**1/4 (0.25)**	**1/6 (0.17)**	**1/6 (0.17)**	**1/9 (0.11)**
$2xMo^{5+}$	4.52	4.46	4.41	4.56

Table SI3. Population of Mo surface oxidation states (obtained by the Boltzmann distribution) as function of vacancy coverage, θ_{vac}, at 350ºC.

θ_{vac}	$\%Mo^{6+}$	$\%Mo^{5+}$	$\%Mo^{4+}$
1/9	77.9	21.9	0.2
1/6	67.1	32.4	0.5
2/9	57.1	42.4	0.5
1/4	52.0	45.9	2.1
1/2	14.6	70.8	14.6
3/4	14.3	21.4	64.3
1	0	0	100

SI3. Adsorbate structure

Figure SI3. Adsorption configurations of a) methanol and b) formaldehyde on the two electronic configurations of reduced α-MoO_3(010).

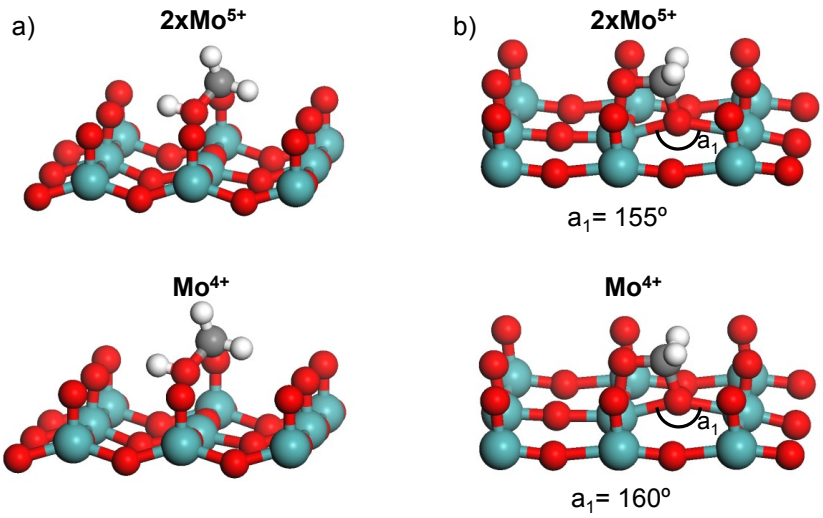

References

1. Mei, D.; Karim, A. M.; Wang, Y. Density Functional Theory Study of Acetaldehyde Hydrodeoxygenation on MoO_3. *J. Phys. Chem. C* **2011,** *115* (16), 8155-8164.

2. Choksi, T.; Greeley, J. Partial Oxidation of Methanol on MoO_3 (010): A DFT and Microkinetic Study. *ACS Cat.* **2016,** *6* (11), 7260-7277.

3. Shetty, M.; Buesser, B.; Román-Leshkov, Y.; Green, W. H. Computational Investigation on Hydrodeoxygenation (HDO) of Acetone to Propylene on α-MoO_3(010) Surface. *J. Phys. Chem. C* **2017,** *121* (33), 17848-17855.

4. Dudarev, S. L.; Botton, G. A.; Savrasov, S. Y.; Humphreys, C. J.; Sutton, A. P. Electron-energy-loss spectra and the structural stability of nickel oxide: An LSDA+U study. *Phys. Rev. B* **1998,** *57* (3), 1505-1509.

5. Coquet, R.; Willock, D. J. The (010) surface of α-MoO_3, a DFT + U study. *Phys. Chem. Chem. Phys.* **2005,** *7* (22), 3819-3828.

6. Lei, Y.-H.; Chen, Z.-X. DFT+U Study of Properties of MoO_3 and Hydrogen Adsorption on MoO_3(010). *J. Phys. Chem. C* **2012,** *116* (49), 25757-25764.

7. Hanson, E. D.; Lajaunie, L.; Hao, S.; Myers, B. D.; Shi, F.; Murthy, A. A.; Wolverton, C.; Arenal, R.; Dravid, V. P. Systematic Study of Oxygen Vacancy Tunable Transport Properties of Few-Layer MoO_{3-x} Enabled by Vapor-Based Synthesis. *Adv. Funct. Mater.* **2017,** *27* (17), 1605380.

8. Ding, H.; Lin, H.; Sadigh, B.; Zhou, F.; Ozoliņš, V.; Asta, M. Computational Investigation of Electron Small Polarons in α-MoO_3. *J. Phys. Chem. C* **2014,** *118* (29), 15565-15572.

9. Agarwal, V.; Metiu, H. Energy of Oxygen-Vacancy Formation on Oxide Surfaces: Role of the Spatial Distribution. *J. Phys. Chem. C* **2016,** *120* (4), 2320-2323.

10. Agarwal, V.; Metiu, H. Oxygen Vacancy Formation on α-MoO_3 Slabs and Ribbons. *J. Phys. Chem. C* **2016,** *120* (34), 19252-19264.

11. Lutfalla, S.; Shapovalov, V.; Bell, A. T. Calibration of the DFT/GGA+U Method for Determination of Reduction Energies for Transition and Rare Earth Metal Oxides of Ti, V, Mo, and Ce. *J. Chem. Theory Comput.* **2011,** *7* (7), 2218-2223.

12. Getsoian, A. B.; Bell, A. T. The Influence of Functionals on Density Functional Theory Calculations of the Properties of Reducible Transition Metal Oxide Catalysts. *J. Phys. Chem. C* **2013,** *117* (48), 25562-25578.

13. Inzani, K.; Grande, T.; Vullum-Bruer, F.; Selbach, S. M. A van der Waals Density Functional Study of MoO_3 and Its Oxygen Vacancies. *J. Phys. Chem. C* **2016,** *120* (16), 8959-8968.

14. Inzani, K.; Nematollahi, M.; Vullum-Bruer, F.; Grande, T.; Reenaas, T. W.; Selbach, S. M. Electronic properties of reduced molybdenum oxides. *Phys. Chem. Chem. Phys.* **2017,** *19* (13), 9232-9245.

15. Akande, S. O.; Chroneos, A.; Vasilopoulou, M.; Kennou, S.; Schwingenschlogl, U. Vacancy formation in MoO_3: hybrid density functional theory and photoemission experiments. *J. Mater. Chem. C* **2016,** *4* (40), 9526-9531.

16. Rellán-Piñeiro, M.; López, N. The Active Molybdenum Oxide Phase in the Methanol Oxidation to Formaldehyde (Formox Process): A DFT Study. *ChemSusChem* **2015,** *8* (13), 2231-2239.

17. Capdevila-Cortada, M.; Łodziana, Z.; López, N. Performance of DFT+U Approaches in the Study of Catalytic Materials. *ACS Catalysis* **2016,** *6* (12), 8370-8379.

18. Fang, Z.; Zetterholm, P.; Dixon, D. A. 1,2-Ethanediol and 1,3-Propanediol Conversions over $(MO_3)_3$ (M = Mo, W) Nanoclusters: A Computational Study. *J. Phys. Chem. A* **2016,** *120* (11), 1897-1907.

19. Frisch, M. J.; Trucks, G. W.; Schlegel, H. B.; Scuseria, G. E.; Robb, M.; A.; Cheeseman, J. R.; Scalmani, G.; Barone, V.; Mennucci, B.; Petersson, G. A.; Nakatsuji, H.; Caricato, M.; Li, X.; Hratchian, H. P.; Izmaylov, A. F.; Bloino, J.; Zheng, G.; Sonnenberg, J. L.; Hada, M.; Ehara, M.; Toyota, K.; Fukuda, R.; Hasegawa, J.; Ishida, M.; Nakajima, T.; Honda, Y.; Kitao, O.; Nakai, H.; Vreven, T.; Montgomery, J.; Peralta, J. A.; Ogliaro, J. E.; Bearpark, F.; M.; Heyd, J. J.; Brothers, E.; Kudin, K. N.; Staroverov, V. N.; Kobayashi, R.; Normand, J.; Raghavachari, K.; Rendell, A.; Burant, J. C.; Lyengar, S. S.; Tomasi, J.; Cossi, M.; Rega, N.; Millam, N. J.; Klene, M.; Knox, J. E.; Cross, J. B.; Bakken, V.; Adamo, C.; Jaramillo, J.; Gomperts, R.; Stratmann, R. E.; Yazyev, O.; Austin, A. J.; Cammi, R.; Pomelli, C.; Ochterski, J. W.; Martin, R. L.; Morokuma, K.; Zakrzewski, V. G.; Voth, G. A.; Salvador, P.; Dannenberg, J. J.; Dapprich, S.; Daniels, A. D.; Farkas, Ö.; Foresman, J. B.; Ortiz, J. V.; Cioslowski, J.; Fox, D.; . Gaussian 09, revision a. 02, gaussian. *Inc., Wallingford, CT* **2009,** *200*.

20. Becke, A. D. Density functional thermochemistry. III. The role of exact exchange. *J. Chem. Phys* **1993,** *98*, 5648-5652.

21. Lee, C.; Yang, W.; Parr, R. G. Development of the Colle-Salvetti correlation-energy formula into a functional of the electron density. *Phys. Rev. B* **1988,** *37* (2), 785.

22. Kendall, R. A.; Dunning Jr, T. H.; Harrison, R. J. Electron affinities of the first-row atoms revisited. Systematic basis sets and wave functions. *J. Chem. Phys.* **1992,** *96* (9), 6796-6806.

23. Peterson, K. A.; Figgen, D.; Dolg, M.; Stoll, H. Energy-consistent relativistic pseudopotentials and correlation consistent basis sets for the 4 d elements Y–Pd. *J. Chem. Phys.* **2007,** *126* (12), 124101.

UNIVERSITAT ROVIRA I VIRGILI
MOLYBDENUM OXIDES AS CATALYST FOR BIOMASS-DERIVED COMPOUNDS: A THEORETICAL APPROACH
Marcos Rellán Piñeiro

Supporting information

Propylene production from glycerol: a first principles study of hydrodeoxygenation (HDO) process on MoO_{3-x} catalysts

M. Rellán-Piñeiro and Núria López*

Institute of Chemical Research of Catalonia (ICIQ), The Barcelona Institute of Science and Technology, Avinguda Països Catalans 16, 43007 Tarragona, Spain

*nlopez@iciq.es

Table S.1 Reaction energies, ΔE; direct energy barriers, $E_{a,d}$; and reverser energy barriers, $E_{a,i}$ in eV, for all the elementary steps of the reaction network. Energies corrected by ZPVE. The imaginary frequency to all the transition states, ν_i , are in cm^{-1}.

Reaction list	ΔE	$E_{a,d}$	$E_{a,i}$	ν_i
Glycerol →1,2-Enol				
GlycerolH(g) + * → GlycerolH*(a)	-1.72			
GlycerolH*(a) + O_t → Glycerol*(a) + O_tH	0.51	0.72	0.21	861
Glycerol*(a) + O_b → 1,2-EnolH(a) + O_bH	-0.08	1.13	1.21	926
1,2-EnolH(a) → 1,2-EnolH(g) + O_t	0.60			
Glycerol → 1,3-Enol				
GlycerolH(g) + * → GlycerolH*(b)	-1.92			
GlycerolH*(b) + O_t → Glycerol*(b) + O_tH	0.45	0.80	0.35	964
Glycerol*(b) + O_b → 1,3-EnolH(b) + O_bH	0.15	1.29	1.14	926
1,3-EnoHl(b) → 1,3-EnolH(g) + O_t	0.65			
1,2-Enol → Acetol				
1,2-EnolH(g) + * → 1,2-EnolH*	-1.59			
1,2-EnolH * + O_t → 1,2-Enol* + O_tH	0.30	0.68	0.37	434
1,2 -Enol* + O_tH → Acetol* + O_t	-1.03	0.09	1.12	931
Acetol* → Acetol(g) + *	1.67			
1,3-Enol → Hydroxypropanal				
1,3-EnolH(g) + * → 1,3-EnolH*	-1.20			
1,3-EnolH * + O_t → 1,3-Enol* + O_tH	0.17	0.38	0.21	655
1,3-Enol* + O_tH → HPH*(a) + O_t	-0.86	-0.04	0.82	808
HPH*(a) → HPH(g) + *	1.69			
Acetol → Propylene Glycol				
Acetol(g) + * → Acetol*	-1.83			
Acetol* + O_tH → PG* + O_t	0.20	1.43	1.23	1322
PG* + O_tH → PGH*(b) + O_t	-0.46	0.25	0.71	783
PGH*(b) → PGH(g) + *	1.85			
Hydroxypropanal → 1,3-Propanediol				
HPH(g) + * → HPH*(a)	-2.16			
HPH*(a) + O_tH → 1,3-Propanediol* + O_t	0.22	1.45	1.22	1390
1,3-Propanediol* + O_tH → 1,3-PropanediolH* + O_t	-0.29	0.22	0.51	834
1,3-PropanediolH* → 1,3-PropanediolH(g) + *	1.59			
Hydroxypropanal → Acrolein				
HPH(g) + * → HPH*(b)	-1.55			
HPH*(b) + O_t → HP*(b) + O_tH	0.18	0.50	0.32	754
HP*(b) + O_b → Acrolein(a) + O_bH	0.23	1.42	1.19	1069
Acrolein*(a) → Acrolein(g) + O_t	0.52			
Propylene Glycol → Propen-2-ol				
PGH(g) + * → PGH*(a)	-1.51			
PGH*(a) + O_t → PG*(a) + O_tH	0.26	0.44	0.19	557
PG*(a) + O_b → Propen-2-olH(a) + O_bH	0.06	1.05	0.99	1174
Propen-2-olH(a) → Propen-2-olH(g) + O_t	0.42			
Propylene Glycol → 1-Propenol				
PGH(g) + * → PGH*(b)	-1.83			
PGH*(b) + O_t → PG*(b) + O_tH	0.46	0.67	0.22	941
PG*(b) + O_b → 1-Propenol(b) + O_bH	0.24	1.34	1.09	643
1-Propenol(b) → 1-PropenolH(g) + O_t	0.49			

Propylene Glycol → 2-Propenol				
PGH(g) + * → PGH*(b)	-1.83			
PGH*(b) + O_t → PG*(b) + O_tH	0.45	0.67	0.22	941
PG*(b) + O_b → 2-PropenolH(b) + O_bH + O_t	0.45	1.47	1.03	643
2-PropenolH(b) → 2-PropenolH(g)	0.66			
1,3-Propanediol → 2-Propenol				
1,3-PropanediolH(g) + * → 1,3-PropanediolH*	-1.62			
1,3-PropanediolH* + O_t → 1,3-Propanediol*+ O_tH	0.34	0.65	0.31	876
1,3-Propanediol* + O_b → 2-PropenolH(a) + O_bH	0.32	1.59	1.27	1055
2-PropenolH(a) → 2-PropenolH(g) + O_t	0.66			
Acrolein → 2-Propenol				
Acrolein(g) + * → Acrolein*	-1.90			
Acrolein* + O_tH → 2-Propenol* + O_t	0.33	1.09	0.76	949
2-Propenol* + O_tH → 2-PropenolH* + O_t	-0.20	0.25	0.46	693
2-PropenolH* → 2-PropenolH(g) + *	1.40			
Acrolein → 1-Propenol				
Acrolein(g) + * → Acrolein*	-1.90			
Acrolein* + O_tH → 1-Propenol* + O_t	-0.11	1.18	1.29	1096
1-Propenol * + O_tH → 1-PropenolH* + O_t	-0.12	0.26	0.38	615
1-PropenolH* → 1-PropenolH(g) + *	1.41			
Propen-2-ol → Propanone				
Propen-2-olH(g) + * → Propen-2-olH*	-1.37			
Propen-2-olH * + O_t → Propen-2-ol* + O_tH	0.04	0.42	0.38	863
Propen-2-ol * + O_tH → Propanone* + O_t	-0.95	0.54	1.49	864
Propanone* → Propanone(g) + *	1.73			
1-Propenol → Propanal				
1-PropenolH(g) + * → 1-PropenolH*	-1.41			
1-PropenolH * + O_t → 1-Propenol* + O_tH	0.12	0.38	0.26	615
1-Propenol * + O_tH → Propanal* + O_t	-0.68	0.01	0.68	926
Propanal* → Propanal (g) + *	1.61			
Propanone → 2-Propanol				
Propanone(g) + * → Propanone*	-2.02			
Propanone* + O_tH → 2-Propanol* + O_t	0.37	1.44	1.07	1227
2-Propanol * + O_tH → 2-PropanolH* + O_t	-0.34	0.40	0.74	1050
2-PropanolH* → 2-PropanolH(g) + *	1.74			
Propanal → 1-Propanol				
Propanal(g) + * → Propanal*	-1.85			
Propanal* + O_tH → 1-Propanol* + O_t	0.19	1.48	1.29	
1-Propanol * + O_tH → 1-PropanolH* + O_t	-0.26	0.20	0.46	751
1-PropanolH* → 1-PropanolH(g) + *	1.52			
2-Propanol → Propylene				
2-PropanolH(g) + * → 2-PropanolH*	-1.75			
2-PropanolH* + O_t → 2-Propanol* + O_tH	0.35	0.74	0.39	557
2-Propanol* + O_b → Propylene + O_bH	0.74	1.51	0.77	742
Propylene → Propylene(g) + O_t	0.23			
1-Propanol → Propylene				
1-PropanolH(g) + * → 1-PropanolH*	-1.51			
1-PropanolH* + O_t → 1-Propanol* + O_tH	0.25	0.44	0.19	816
1-Propanol* + O_b → Propylene + O_bH	0.42	1.25	0.82	945
Propylene → Propylene(g) + O_t	0.23			
2-Propenol → Propylene				
2-PropenolH(g) + * → 2-PropenolH*	-1.41			

2-PropenolH* + O_t → 2-Propenol* + O_tH	0.22	0.45	0.22	671
2-Propenol* + O_t → Propylene + O_tH	-0.14	1.03	1.17	1565
Propylene → Propylene(g) + O_t	0.05			
H_2O formation				
$H_2(g) + 2O_t \rightarrow 2O_tH$	-0.86	1.63	2.49	
$H_2(g) + O_t + O_b \rightarrow O_tH + O_bH$	-0.96	1.46	2.42	
$O_bH + O_t \rightarrow O_b + O_tH$	0.09	0.77	0.68	1148
$2O_tH \rightarrow H_2O_t + O_t$	-0.32	0.14	0.46	647
$H_2O_t \rightarrow H_2O(g) + *$	1.22			

Supplementary Information

Mechanism for the selective epimerization of the glucose mannose pair by Mo-based compounds: towards catalyst optimization

Marcos Rellan-Piñeiro, Miquel Garcia-Ratés, Núria López

Institute of Chemical Research of Catalonia, ICIQ, and The Barcelona Institute of Science and Technology, Av. Països Catalans 16, 43007 Tarragona Spain

Figure SI1. Structure of the reaction intermediates in the Glucose → Mannose epimerization reaction catalysed by $H_3PMo_{12}O_{40}$, $H_6P_2Mo_{18}O_{60}$, α-MoO_3 and α-MoO_{3-x}. Same colour code as in Figure 1.

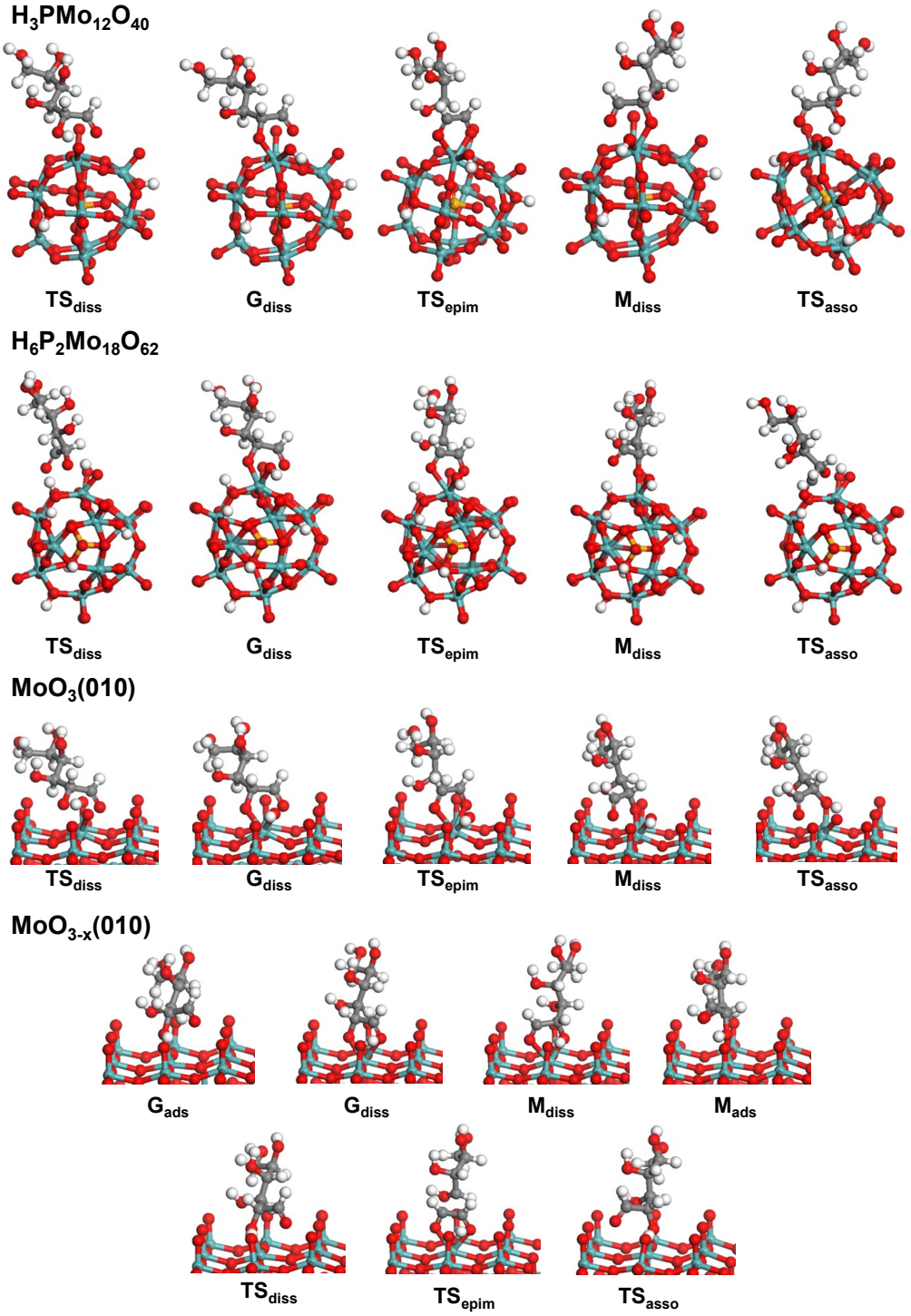

Table SI1. Reaction and activation energy, ΔE and E_a, in eV, for 1,2 C-shift elementary step on $H_3PMo_{12}O_{40}$.

Method/basis	ΔE	$E_{a,1}$	$E_{a,2}$
BP86-D2/set1	-0.04	0.98	1.02
BP86-D2/set2	-0.01	1.07	1.08
PBE-D2/set1	-0.04	0.97	1.01
PBE-D2/set2	-0.03	1.08	1.11
PBE-D2/PW	**-0.02**	**1.03**	**1.05**

set1: 6-311G* for P,O, C, H and LANL2TZ for Mo
set2: 6-311G* for P,O, C, H and TZVP for Mo

Table SI2. Reaction energies, ΔE, energy barriers, E_a (both in eV), and imaginary frequencies, ν_i (cm^{-1}) for all the reaction steps in the Glucose (G) → Mannose (M) epimerization reaction catalysed by $H_3PMo_{12}O_{40}$, $H_6P_2Mo_{18}O_{60}$, α-MoO_3 and α-MoO_{3-x}.

	ΔE	E_a^+	E_a^-	ν_i
$H_3PMo_{12}O_{40}$				
G(g) + * + O* ↔ G* + OH*	0.57	1.04	0.47	828
G* + OH* ↔ M* + OH*	-0.02	0.99	1.01	172
M* + OH* ↔ M(g) + * + O*	-0.64	0.40	1.04	715
$H_6P_2Mo_{18}O_{60}$				
G(g) + * + O* ↔ G* + OH*	0.75	1.07	0.31	739
G* + OH* ↔ M* + OH*	-0.05	1.10	1.15	202
M* + OH* ↔ M(g) + * + O*	-0.79	0.31	1.10	722
α-MoO_3				
G(g) + * + O* ↔ G* + OH*	0.20	1.17	0.97	1036
G* + OH* ↔ M* + OH*	-0.04	0.94	0.98	140
M* + OH* ↔ M(g) + * + O*	-0.24	0.85	1.09	990
α-MoO_{3-x}				
G(g) + * ↔ G*	-1.26	-	-	-
G* + O* ↔ G* + OH*	0.14	0.53	0.39	-
G* + OH* ↔ M* + OH*	-0.04	0.85	0.89	234
M* + OH* ↔ M* + O*	-0.23	0.55	0.78	-
M* ↔ M(g) + *	1.40	-	-	-

Table SI3. Relevant bond distances (Å) for all the reaction intermediates and transition states in the Glucose → Mannose epimerization reaction catalysed by $H_3PMo_{12}O_{40}$, $H_6P_2Mo_{18}O_{60}$, α-MoO_3 and α-MoO_{3-x}.

	Mo-O_1	**Mo-O_2**	**C_1-O_1**	**C_2-O_2**	**C_1-C_2**	**C_1-C_3**	**C_2-C_3**
$H_3PMo_{12}O_{40}$							
TS_{diss}	2.393	2.274	1.237	1.402	1.489	-	1.570
G_{diss}	2.456	1.911	1.230	1.397	1.497	-	1.576
TS_{epim}	2.089	2.137	1.314	1.289	1.407	2.162	2.377
M_{diss}	1.924	2.389	1.400	1.234	1.499	1.576	-
TS_{asso}	2.281	2.477	1.397	1.234	1.500	1.563	-
$H_6P_2Mo_{18}O_{62}$							
TS_{diss}	-	2.279	1.232	1.392	1.499	-	1.580
G_{diss}	2.544	1.922	1.227	1.398	1.504	-	1.565
TS_{epim}	2.109	2.184	1.312	1.236	1.409	2.119	2.268
M_{diss}	1.899	3.297	1.404	1.213	1.533	1.560	-
TS_{asso}	2.229	-	1.398	1.225	1.515	1.581	-
MoO_3							
TS_{diss}	2.475	2.250	1.234	1.420	1.495	-	1.564
G_{diss}	2.385	1.930	1.233	1.412	1.498	-	1.574
TS_{epim}	2.120	2.098	1.303	1.302	1.406	2.222	2.317
M_{diss}	1.919	2.453	1.397	1.231	1.509	1.554	-
TS_{asso}	2.296	2.317	1.403	1.237	1.500	1.556	-
MoO_{3-x}							
G_{ads}	4.079	2.239	1.220	1.444	1.524	-	1.535
TS_{diss}	3.455	1.972	1.219	1.408	1.522	-	1.559
G_{diss}	2.276	1.926	1.239	1.399	1.482	-	1.578
TS_{epim}	2.120	2.046	1.281	1.332	1.397	2.250	2.084
M_{diss}	1.919	2.259	1.398	1.238	1.488	1.567	-
TS_{asso}	1.988	3.605	1.408	1.218	1.526	1.548	-
M_{ads}	4.339	2.204	1.432	1.225	1.526	1.554	-

Figure SI2. Reaction profile, in terms of vibrational Gibbs free energy (Gibbs), for the Bilik reaction for glucose on $H_3PMo_{12}O_{40}$, $H_6P_2Mo_{18}O_{62}$, α-MoO_3(010) and α-MoO_{3-x}(010) at T= 100 ºC.

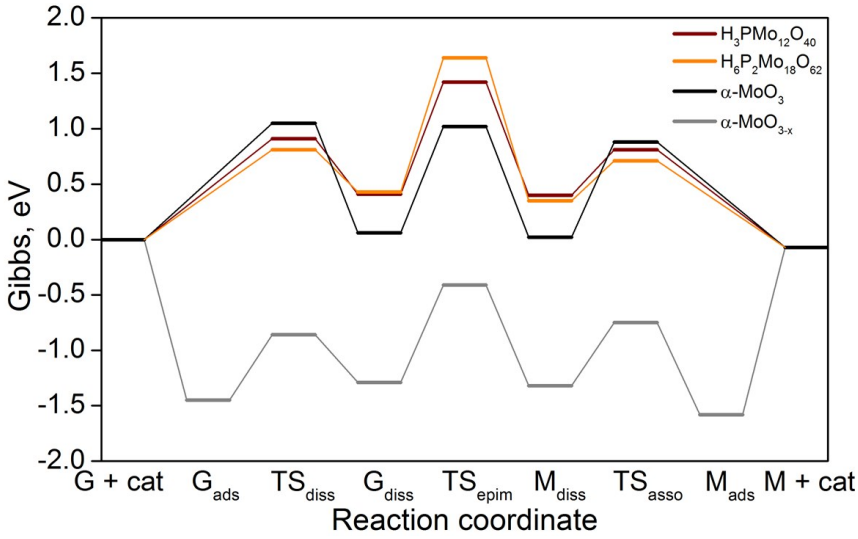

Figure SI3. a) Mechanism scheme for dissociative adsorption of glucose on $H_3PMo_{12}O_{40}$ through $-O^3H$ group. b) Optimized structures for reaction on $H_3PMo_{12}O_{40}$. c) Reaction and activation energies, ΔE and E_a, in eV, for the adsorption of glucose on $H_3PMo_{12}O_{40}$ through $-O^3H$ group.

a)

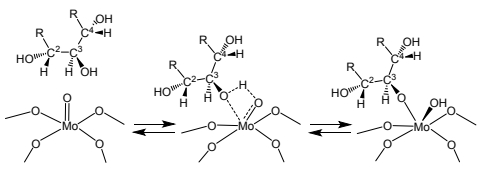

b)

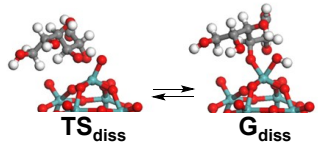

c)

ΔE	E_a^+	E_a^-
0.63	1.01	0.38

Figure SI4. a) Mechanism for the ring opening of glucose and mannose assisted by $H_3PMo_{12}O_{40}$. b) Optimized structures for reaction on $H_3PMo_{12}O_{40}$. c) Reaction profile of the reaction for glucose and mannose on $H_3PMo_{12}O_{40}$.

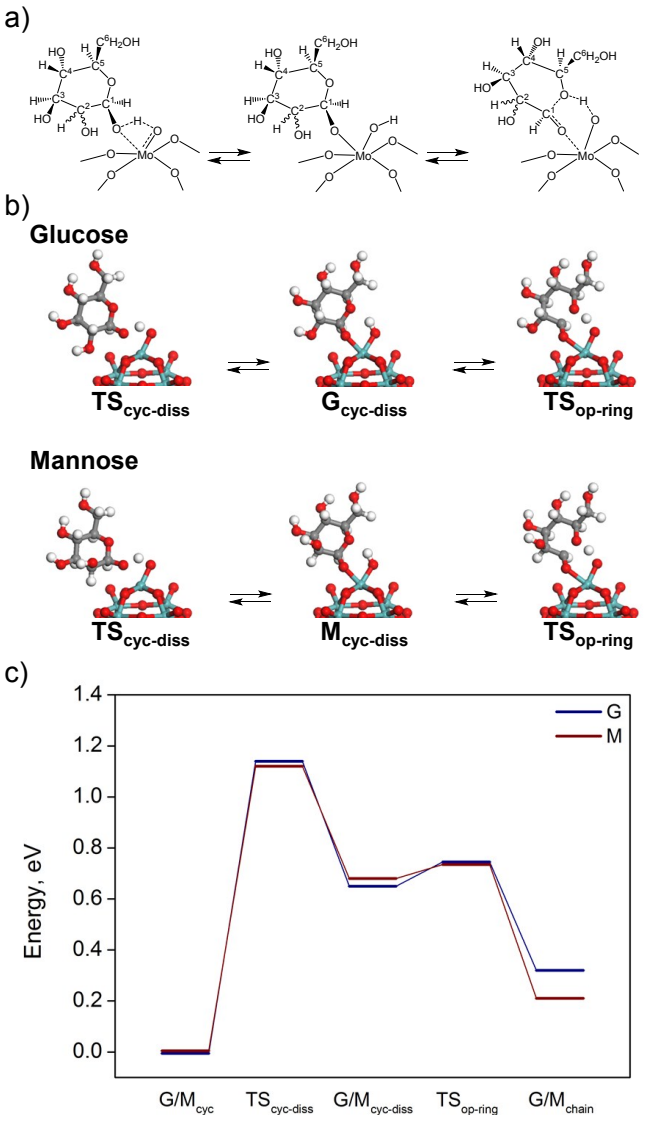

Figure SI5. a) Scheme and converged structures for the dehydration elementary step on the α-MoO_{3-x}(010) surface. b) Reaction path for this step. Energies are given relative to gas-phase glucose and defective surface.

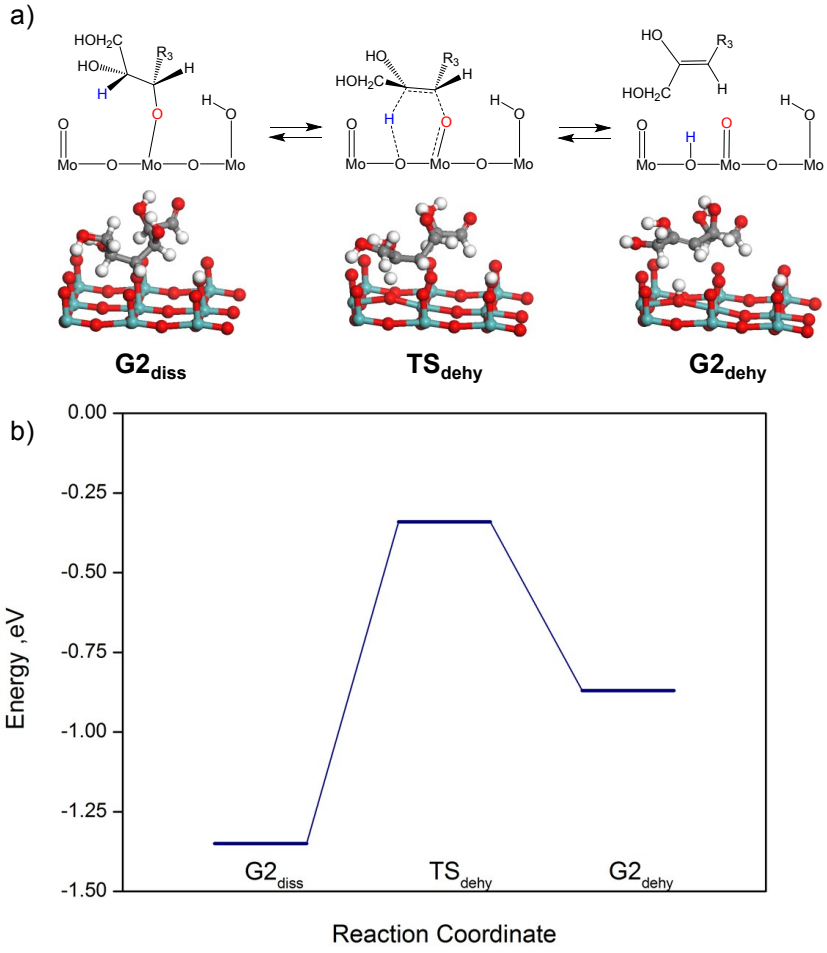

Figure SI6. Energy profile for the epimerization step of glucose to mannose for the case of complete molecules, molecules without $–O_3H$ group and molecules without $–O_4H$ group on $H_3PMo_{12}O_4$.

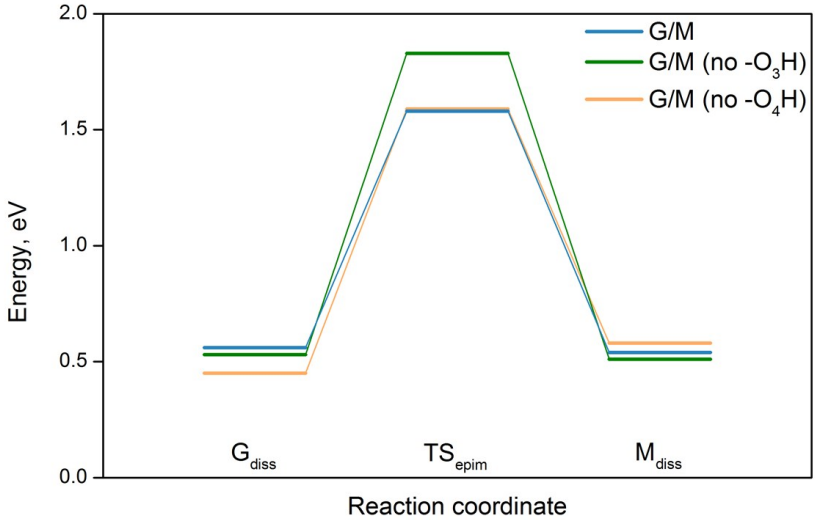

Table SI4. Binding energies, BE, reaction energies, ΔE, energy barriers, E_a, (all in eV) and imaginary frequencies, ν_i (cm^{-1}) for the epimerization step to complete molecules, molecules without $–O_3H$ group and molecules without $–O_4H$ group on $H_3PMo_{12}O_4$.

	BE(G)	BE(M)	ΔE	E_a^+	E_a^-	ν_i
G/M	0.57	0.55	-0.02	0.99	1.01	172
G/M (no $–O_3H$)	0.55	0.51	-0.04	1.23	1.27	351
G/M (no $–O_4H$)	0.47	0.60	0.12	1.07	0.95	120

Bibliography

[1] Marion, P.; Bernela, B.; Piccirilli, A.; Estrine, B.; Patouillard, N.; Guilbot, J.; Jérôme, F. Sustainable chemistry: how to produce better and more from less?, *Green Chem.* **2017,** *19,* 4973–4989.

[2] Röper, H. Renewable raw materials in Europe—industrial utilisation of starch and sugar [1], *Starch-Stärke* **2002,** *54,* 89–99.

[3] McKendry, P. Energy production from biomass (part 1): overview of biomass, *Bioresour. Technol.* **2002,** *83,* 37–46.

[4] Dapsens, P. Y.; Mondelli, C.; Pérez-Ramírez, J. Biobased chemicals from conception toward industrial reality: lessons learned and to be learned, *ACS Catal.* **2012,** *2,* 1487–1499.

[5] Zhang, Q.; Chang, J.; Wang, T.; Xu, Y. Review of biomass pyrolysis oil properties and upgrading research, *Energy Convers. Manag.* **2007,** *48,* 87–92.

[6] Sutton, D.; Kelleher, B.; Ross, J. Review of literature on catalysts for biomass gasification, *Fuel Process. Technol.* **2001,** *73,* 155–173.

[7] Kumar, P.; Barrett, D. M.; Delwiche, M. J.; Stroeve, P. Methods for pretreatment of lignocellulosic biomass for efficient hydrolysis and biofuel production, *Ind. Eng. Chem. Res.* **2009,** *48,* 3713–3729.

[8] Werpy, T.; Petersen, G.; Aden, A.; Bozell, J.; Holladay, J.; White, J.; Manheim, A.; Eliot, D.; Lasure, L.; Jones, S. "Top value added chemicals from biomass. Volume 1-Results of screening for potential candidates from sugars and synthesis gas", Technical Report, U.S. Department of Energy, 2004.

[9] Bozell, J, J.; Petersen, G. R. Technology development for the production of biobased products from biorefinery carbohydrates—the US Department of Energy's "Top 10" revisited, *Green Chem.* **2010,** *12,* 539–554.

[10] Lichtenthaler, F. W.; Peters, S. Carbohydrates as green raw materials for the chemical industry, *C. R. Chim.* **2004,** *7,* 65–90.

[11] Besson, M.; Gallezot, P.; Pinel, C. Conversion of biomass into chemicals over metal catalysts, *Chem. Rev.* **2013,** *114,* 1827–1870.

[12] Corma, A.; Iborra, S.; Velty, A. Chemical routes for the transformation of biomass into chemicals, *Chem. Rev.* **2007,** *107,* 2411–2502.

[13] Climent, M. J.; Corma, A.; Iborra, S. Converting carbohydrates to bulk chemicals and fine chemicals over heterogeneous catalysts, *Green Chem.* **2011,** *13,* 520–540.

[14] Ju, F.; VanderVelde, D.; Nikolla, E. Molybdenum-based polyoxometalates as highly active and selective catalysts for the epimerization of aldoses, *ACS Catal.* **2014,** *4,* 1358–1364.

[15] Orazov, M.; Davis, M. E. Tandem catalysis for the production of alkyl lactates from ketohexoses at moderate temperatures, *Proc. Nat. Acad. Sci.* **2015,** *112,* 11777–11782.

[16] Alamillo, R.; Tucker, M.; Chia, M.; Pagán-Torres, Y.; Dumesic, J. The selective hydrogenation of biomass-derived 5-hydroxymethylfurfural using heterogeneous catalysts, *Green Chem.* **2012,** *14,* 1413–1419.

[17] Ruberu, T. P. A.; Nelson, N. C.; Slowing, I. I.; Vela, J. Selective alcohol dehydrogenation and hydrogenolysis with semiconductor-metal photocatalysts: toward solar-to-chemical energy conversion of biomass-relevant substrates, *J. Phys. Chem. Lett.* **2012,** *3,* 2798–2802.

[18] Ruppert, A. M.; Weinberg, K.; Palkovits, R. Hydrogenolysis goes bio: from carbohydrates and sugar alcohols to platform chemicals, *Angew. Chem. Int. Ed.* **2012,** *51,* 2564–2601.

[19] Prasomsri, T.; Nimmanwudipong, T.; Román-Leshkov, Y. Effective hydrodeoxygenation of biomass-derived oxygenates into unsaturated hydrocarbons by MoO_3 using low H_2 pressures, *Energy Environ. Sci.* **2013,** *6,* 1732–1738.

[20] Davis, S. E.; Ide, M. S.; Davis, R. J. Selective oxidation of alcohols and aldehydes over supported metal nanoparticles, *Green Chem.* **2013,** *15,* 17–45.

[21] Chorkendorff, I.; Niemantsverdriet, J. W. *Concepts of modern catalysis and kinetics;* Wiley-VCH: 2005.

[22] de Vries, J. G.; Jackson, S. D. Homogeneous and heterogeneous catalysis in industry, *Catal. Sci. Technol.* **2012,** *2,* 2009–2009.

[23] Moulijn, J. A.; van Leeuwen, P.; van Santen, R. A. *Catalysis: an integrated approach to homogeneous, heterogeneous and industrial catalysis;* volume 79 Elsevier: 1993.

[24] Medford, A. J.; Vojvodic, A.; Hummelshøj, J. S.; Voss, J.; Abild-Pedersen, F.; Studt, F.; Bligaard, T.; Nilsson, A.; Nørskov, J. K. From the Sabatier principle to a predictive theory of transition-metal heterogeneous catalysis, *J. Catal.* **2015,** *328,* 36–42.

[25] Nokkosmäki, M. I.; Kuoppala, E. T.; Leppämäki, E. A.; Krause, A. O. I. Catalytic conversion of biomass pyrolysis vapours with zinc oxide, *J. Anal. Appl. Pyrolysis* **2000,** *55,* 119–131.

[26] Singh, A. K.; Xu, Q. Synergistic catalysis over bimetallic alloy nanoparticles, *ChemCatChem* **2013,** *5,* 652–676.

[27] Wachs, I. E. Recent conceptual advances in the catalysis science of mixed metal oxide catalytic materials, *Catal. Today* **2005,** *100,* 79–94.

[28] McFarland, E. W.; Metiu, H. Catalysis by doped oxides, *Chem. Rev.* **2013,** *113,* 4391–4427.

[29] Nilius, N.; Freund, H. J. Activating nonreducible oxides via doping, *Acc. Chem. Res.* **2015,** *48,* 1532–1539.

[30] Albonetti, S.; Cavani, F.; Trifiro, F. Key aspects of catalyst design for the selective oxidation of paraffins, *Catal. Rev.* **1996,** *38,* 413–438.

[31] Vining, W. C.; Goodrow, A.; Strunk, J.; Bell, A. T. An experimental and theoretical investigation of the structure and reactivity of bilayered $VO_x/TiO_x/SiO_2$ catalysts for methanol oxidation, *J. Catal.* **2010,** *270,* 163–171.

[32] Chen, L.; Li, J.; Ge, M.; Zhu, R. Enhanced activity of tungsten modified CeO_2/TiO_2 for selective catalytic reduction of NO_x with ammonia, *Catal. Today* **2010,** *153,* 77–83.

[33] Bowker, M.; Carley, A. F.; House, M. Contrasting the Behaviour of MoO_3 and MoO_2 for the Oxidation of Methanol, *Catal. Lett.* **2008,** *120,* 34.

[34] Keulks, G. W.; Rosynek, M. P.; Daniel, C. Bismuth molybdate catalysts. Kinetics and mechanism of propylene oxidation, *Ind. Eng. Chem. Prod. Res. Dev.* **1971,** *10,* 138–142.

[35] Al-Kandari, H.; Al-Kharafi, F.; Katrib, A. Isomerization reactions of n-hexane on partially reduced MoO_3/TiO_2, *Catalysis Communications* **2008,** *9,* 847–852.

[36] Al-Kandari, H.; Al-Kharafi, F.; Katrib, A. Catalytic activity-surface structure correlation of molybdenum-based catalysts, *J. Mol. Catal. A: Chem.* **2008,** *287,* 128–134.

[37] Beuther, H.; Flinn, R. A.; McKinley, J. B. For Better Hydrodesulfurization Activity of Promoted Molybdenum Oxide–Alumina Catalysts, *Ind. Eng. Chem. Res.* **1959,** *51,* 1349–1350.

[38] Prasomsri, T.; Shetty, M.; Murugappan, K.; Román-Leshkov, Y. Insights into the catalytic activity and surface modification of MoO_3 during the hydrodeoxygenation of lignin-derived model compounds into aro-

matic hydrocarbons under low hydrogen pressures, *Energy Environ. Sci.* **2014,** *7,* 2660–2669.

[39] Shetty, M.; Murugappan, K.; Prasomsri, T.; Green, W. H.; Roman-Leshkov, Y. Reactivity and stability investigation of supported molybdenum oxide catalysts for the hydrodeoxygenation (HDO) of m-cresol, *J. Catal.* **2015,** *331,* 86–97.

[40] Zacharopoulou, V.; Vasiliadou, E. S.; Lemonidou, A. A. One-step propylene formation from bio-glycerol over molybdena-based catalysts, *Green Chem.* **2015,** *17,* 903–912.

[41] Ranga, C. *et al.* Effect of composition and preparation of supported MoO_3 catalysts for anisole hydrodeoxygenation, *Chem. Eng. J.* **2018,** *335,* 120–132.

[42] Greenwood, N. N.; Earnshaw, A. *Chemistry of the Elements (Second Edition);* Butterworth-Heinemann: 1997.

[43] Bouzidi, A.; Benramdane, N.; Tabet-Derraz, H.; Mathieu, C.; Khelifa, B.; Desfeux, R. Effect of substrate temperature on the structural and optical properties of MoO_3 thin films prepared by spray pyrolysis technique, *Mat. Sci. Eng. B* **2003,** *97,* 5–8.

[44] Kröger, M.; Hamwi, S.; Meyer, J.; Riedl, T.; Kowalsky, W.; Kahn, A. P-type doping of organic wide band gap materials by transition metal oxides: A case-study on Molybdenum trioxide, *Org. Electron.* **2009,** *10,* 932–938.

[45] Sian, T. S.; Reddy, G. B. Optical, structural and photoelectron spectroscopic studies on amorphous and crystalline molybdenum oxide thin films, *Sol. Energy Mater. Sol Cells* **2004,** *82,* 375–386.

[46] Greiner, M. T.; Chai, L.; Helander, M. G.; Tang, W. M.; Lu, Z. H. Transition metal oxide work functions: the influence of cation oxidation state and oxygen vacancies, *Adv. Funct. Mater.* **2012,** *22,* 4557–4568.

[47] Meyer, J.; Hamwi, S.; Kröger, M.; Kowalsky, W.; Riedl, T.; Kahn, A. Transition metal oxides for organic electronics: energetics, device physics and applications, *Adv. Mater.* **2012,** *24,* 5408–5427.

[48] Qu, Q.; Zhang, W. B.; Huang, K.; Chen, W. M. Electronic structure, optical properties and band edges of layered MoO_3: A first-principles investigation, *Comp. Mater. Sci.* **2017,** *130,* 242–248.

[49] de Castro, I. A.; Datta, R. S.; Ou, J. Z.; Castellanos-Gomez, A.; Sriram, S.; Daeneke, T.; Kalantar-zadeh, K. Molybdenum Oxides–From Fundamentals to Functionality, *Adv. Mater.* **2017,** 1701619.

[50] *Merchant Research & Consulting*, `https://mcgroup.co.uk/news/20140627/formaldehyde-production-exceed-52-mln-tonnes.html`, Accessed: 2017-11-18.

[51] Bowker, M.; Holroyd, R.; Elliott, A.; Morrall, P.; Alouche, A.; Entwistle, C.; Toerncrona, A. The selective oxidation of methanol to formaldehyde on iron molybdate catalysts and on component oxides, *Catal. Lett.* **2002,** *83,* 165–176.

[52] Soares, A. P. V.; Portela, M. F.; Kiennemann, A.; Millet, J. M. M. Iron-molybdate deactivation during methanol to formaldehyde oxidation: effect of water, *Reac. Kin. Catal. Lett.* **2002,** *75,* 13–20.

[53] Brookes, C.; W.,; Cibin, G.; Dimitratos, N.; Jones, W.; Morgan, D. J.; Bowker, M. Molybdenum Oxide on Fe_2O_3 Core–Shell Catalysts: Probing the Nature of the Structural Motifs Responsible for Methanol Oxidation Catalysis, *ACS Catal.* **2013,** *4,* 243–250.

[54] Brookes, C.; Wells, P. P.; Dimitratos, N.; Jones, W.; Gibson, E. K.; Morgan, D. J.; Cibin, G.; Nicklin, C.; Mora-Fonz, D.; Scanlon, D. O.; Catlow, C. R. A.; Bowker, M. The nature of the molybdenum surface in iron molybdate. The active phase in selective methanol oxidation, *J. Phys. Chem. C* **2014,** *118,* 26155–26161.

[55] Soares, A. P.; Montemor, F.; Portela, M. F.; Kiennemann, A. The role of the suprastoichiometric molybdenum during methanol to formaldehyde oxidation over Mo–Fe mixed oxides, *J. Mol. Catal. A: Chem.* **2015,** *397,* 93–98.

[56] Brookes, C.; Bowker, M.; Wells, P. P. Catalysts for the selective oxidation of methanol, *Catalysts* **2016,** *6,* 92.

[57] Deshlahra, P.; Iglesia, E. Methanol Oxidative Dehydrogenation on Oxide Catalysts: Molecular and Dissociative Routes and Hydrogen Addition Energies as Descriptors of Reactivity, *J. Phys. Chem. C* **2014,** *118,* 26115–26129.

[58] Coquet, R.; Willock, D. J. The (010) surface of α-MoO_3, a DFT+U study, *Phys. Chem. Chem. Phys.* **2005,** *7,* 3819–3828.

[59] Scanlon, D. O.; Watson, G. W.; Payne, D. J.; Atkinson, G. R.; Egdell, R. G.; Law, D. S. L. Theoretical and experimental study of the electronic structures of MoO_3 and MoO_2, *J. Phys. Chem. C* **2010,** *114,* 4636–4645.

[60] Getsoian, A.; Bell, A. T. The influence of functionals on density functional theory calculations of the properties of reducible transition metal oxide catalysts, *J. Phys. Chem. C* **2013,** *117,* 25562–25578.

[61] Ding, H.; Lin, H.; Sadigh, B.; Zhou, F.; Ozolinš, V.; Asta, M. Computational investigation of electron small polarons in α-MoO_3, *J. Phys. Chem. C* **2014,** *118,* 15565–15572.

[62] Agarwal, V.; Metiu, H. Energy of Oxygen-Vacancy Formation on Oxide Surfaces: Role of the Spatial Distribution, *J. Phys. Chem. C* **2016,** *120,* 2320–2323.

[63] Inzani, K.; Grande, T.; Vullum-Bruer, F.; Selbach, S. M. A van der Waals density functional study of MoO_3 and its oxygen vacancies, *J. Phys. Chem. C* **2016,** *120,* 8959–8968.

[64] Mei, D.; Karim, A. M.; Wang, Y. Density functional theory study of acetaldehyde hydrodeoxygenation on MoO_3, *J. Phys. Chem. C* **2011,** *115,* 8155–8164.

[65] Choksi, T.; Greeley, J. Partial Oxidation of Methanol on MoO_3 (010): A DFT and Microkinetic Study, *ACS Catal.* **2016,** *6,* 7260–7277.

[66] Shetty, M.; Buesser, B.; Román-Leshkov, Y.; Green, W. H. Computational Investigation on Hydrodeoxygenation (HDO) of Acetone to Propylene on α-MoO_3(010) Surface, *J. Phys. Chem. C* **2017,** *121,* 17848–17855.

[67] Kihlborg, L. Least squares refinement of crystal structure of molybdenum trioxide, *Ark. Kem.* **1963,** *21,* 357–364.

[68] Smith, M. R.; Ozkan, U. S. Transient isotopic labeling studies under steady-state conditions in partial oxidation of methane to formaldehyde over MoO_3 catalysts, *J. Catal.* **1993,** *142,* 226–236.

[69] Nørskov, J. K.; Bligaard, T.; Rossmeisl, J.; Christensen, C. H. Towards the computational design of solid catalysts, *Nat. Chem.* **2009,** *1,* 37.

[70] López, N.; Almora-Barrios, N.; Carchini, G.; Błoński, P.; Bellarosa, L.; García-Muelas, R.; Novell-Leruth, G.; García-Mota, M. State-of-the-art and challenges in theoretical simulations of heterogeneous catalysis at the microscopic level, *Catal. Sci. Technol.* **2012,** *2,* 2405–2417.

[71] Dudarev, S. L.; Botton, G. A.; Savrasov, S. Y.; Humphreys, C. J.; Sutton, A. P. Electron-energy-loss spectra and the structural stability of nickel oxide: An LSDA+U study, *Phys. Rev. B* **1998,** *57,* 1505–1509.

[72] Lei, Y. H.; Chen, Z. X. DFT+ U study of properties of MoO_3 and hydrogen adsorption on MoO_3(010), *J. Phys. Chem. C* **2012,** *116,* 25757–25764.

[73] Grimme, S. Semiempirical GGA-type density functional constructed with a long-range dispersion correction, *J. Comput. Chem.* **2006,** *27,* 1787–1799.

[74] Grimme, S.; Antony, J.; S., E.; Krieg, H. A consistent and accurate ab initio parametrization of density functional dispersion correction (DFT-D) for the 94 elements H-Pu, *J. Chem. Phys.* **2010,** *132,* 154104.

[75] Schrödinger, E. An undulatory theory of the mechanics of atoms and molecules, *Phys. Rev.* **1926,** *28,* 1049–1070.

[76] Born, M.; Oppenheimer, R. Zur quantentheorie der molekeln, *Ann. Phys.* **1927,** *389,* 457–484.

[77] Valatin, J. G. Generalized Hartree-Fock method, *Phys. Rev.* **1961,** *122,* 1012–1020.

[78] Lieb, E. H. Thomas-Fermi and related theories of atoms and molecules, *Rev. Mod. Phys.* **1981,** *53,* 603–641.

[79] Kohn, W. Nobel lecture: Electronic structure of matter-wave functions and density functionals, *Rev. Mod. Phys.* **1999,** *71,* 1253–1266.

[80] Hohenberg, P.; Kohn, W. Inhomogeneous electron gas, *Phys. Rev.* **1964,** *136,* B864–B871.

[81] Kohn, W.; Sham, L. J. Self-consistent equations including exchange and correlation effects, *Phys. Rev.* **1965,** *140,* A1133–A1138.

[82] Ceperley, D. M.; Alder, B. J. Ground state of the electron gas by a stochastic method, *Phys. Rev. Lett.* **1980,** *45,* 566–569.

[83] Perdew, J. P.; Burke, K.; Ernzerhof, M. Generalized gradient approximation made simple, *Phys. Rev. Lett.* **1996,** *77,* 3865–3868.

[84] Perdew, J. P.; Wang, Y. Accurate and simple analytic representation of the electron-gas correlation energy, *Phys. Rev. B* **1992,** *45,* 13244–13249.

[85] Hammer, B.; Hansen, L. B.; Nørskov, J. K. Improved adsorption energetics within density-functional theory using revised Perdew-Burke-Ernzerhof functionals, *Phys. Rev. B* **1999,** *59,* 7413–7421.

[86] Tkatchenko, A.; Scheffler, M. Accurate molecular van der Waals interactions from ground-state electron density and free-atom reference data, *Phys. Rev. Lett.* **2009,** *102,* 073005.

[87] Becke, A. D. Density-functional exchange-energy approximation with correct asymptotic behavior, *Phys. Rev. A* **1988,** *38,* 3098–3100.

[88] Lee, C.; Yang, W.; Parr, R. G. Development of the Colle-Salvetti correlation-energy formula into a functional of the electron density, *Phys. Rev. B* **1988,** *37,* 785–789.

[89] Adamo, C.; Barone, V. Toward reliable density functional methods without adjustable parameters: The PBE0 model, *J. Chem. Phys.* **1999,** *110,* 6158-6170.

[90] Heyd, J.; Scuseria, G. E.; Ernzerhof, M. Hybrid functionals based on a screened Coulomb potential, *J. Chem. Phys.* **2003,** *118,* 8207-8215.

[91] Capdevila-Cortada, M.; Łodziana, Z.; López, N. Performance of DFT+U Approaches in the Study of Catalytic Materials, *ACS Catal.* **2016,** *6,* 8370-8379.

[92] Ashcroft, N. W.; Mermin, N. D. *Solid State Physics;* Saunders College: Philadelphia, 1976.

[93] Monkhorst, H. J.; Pack, J. D. Special points for Brillouin-zone integrations, *Phys. Rev. B* **1976,** *13,* 5188.

[94] Blöchl, P. E. Projector augmented-wave method, *Phys. Rev. B* **1994,** *50,* 17953–17979.

[95] Kresse, G.; Joubert, D. From ultrasoft pseudopotentials to the projector augmented-wave method, *Phys. Rev. B* **1999,** *59,* 1758–1775.

[96] Payne, M. C.; Teter, M. P.; Allan, D. C.; Arias, T. A.; Joannopoulos, J. D. Iterative minimization techniques for ab initio total-energy calculations: molecular dynamics and conjugate gradients, *Rev. Mod. Phys.* **1992,** *64,* 1045–1097.

[97] Makov, G.; Payne, M. C. Periodic boundary conditions in ab initio calculations, *Phys. Rev. B* **1995,** *51,* 4014–4022.

[98] Jónsson, H.; Mills, G.; Jacobsen, K. W. Nudged elastic band method for finding minimum energy paths of transitions, **1998,** 385–404.

[99] Henkelman, G.; Jónsson, H. Improved tangent estimate in the nudged elastic band method for finding minimum energy paths and saddle points, *J. Chem. Phys.* **2000,** *113,* 9978–9985.

[100] Henkelman, G.; Uberuaga, B. P.; Jónsson, H. A climbing image nudged elastic band method for finding saddle points and minimum energy paths, *J. Chem. Phys.* **2000,** *113,* 9901–9904.

[101] Eyring, H. The activated complex in chemical reactions, *J. Chem. Phys.* **1935,** *3,* 107-115.

[102] Evans, M. G.; Polanyi, M. Some applications of the transition state method to the calculation of reaction velocities, especially in solution, *Trans. Faraday Soc.* **1935,** *31,* 875-894.

[103] Rellán-Piñeiro, M.; López, N. The Active Molybdenum Oxide Phase in the Methanol Oxidation to Formaldehyde (Formox Process): A DFT Study, *ChemSusChem* **2015,** *8,* 2231–2239.

[104] Andersson, A.; Hernelind, M.; Augustsson, O. A study of the ageing and deactivation phenomena occurring during operation of an iron molybdate catalyst in formaldehyde production, *Catal. Today* **2006,** *112,* 40–44.

[105] Ivanov, K. I.; Dimitrov, D. Y. Deactivation of an industrial iron-molybdate catalyst for methanol oxidation, *Catal. Today* **2010,** *154,* 250–255.

[106] O'Brien, M. G.; Beale, A. M.; Jacques, S. D. M.; Buslaps, T.; Honkimaki, V.; Weckhuysen, B. M. On the active oxygen in bulk MoO_3 during the anaerobic dehydrogenation of methanol, *J. Phys. Chem. C* **2009,** *113,* 4890–4897.

[107] Gai, P. L.; Labun, P. A. Electron microscopy studies relating to methanol oxidation over ferric molybdate and molybdenum trioxide catalysts, *J. Catal.* **1985,** *94,* 79–96.

[108] Fernández, E.; Moses, P.; Toftelund, A.; Hansen, H. A.; Martínez, J. I.; Abild-Pedersen, F.; Kleis, J.; Hinnemann, B.; Rossmeisl, J.; Bligaard, T.; Nørskov, J. K. Scaling relationships for adsorption energies on transition metal oxide, sulfide, and nitride surfaces, *Angew. Chem. Int. Ed.* **2008,** *47,* 4683-4686.

[109] Martínez, J. I.; Hansen, H. A.; Rossmeisl, J.; Nørskov, J. K. Formation energies of rutile metal dioxides using density functional theory, *Phys. Rev. B* **2009,** *79,* 045120.

[110] M, T. J. Methanol oxidation as a catalytic surface probe, *App. Catal. A* **1997,** *148,* 213 - 252.

[111] Pernicone, N.; Lazzerin, F.; Liberti, G.; Lanzavecchia, G. On the mechanism of CH_3OH oxidation to CH_2O over MoO_3-$Fe_2(MoO_4)_3$ catalyst, *J. Catal.* **1969,** *14,* 293–302.

[112] Farneth, W. E.; Ohuchi, F.; Staley, R. H.; Chowdhry, U.; Sleight, A. W. Mechanism of partial oxidation of methanol over molybdenum (VI) oxide as studied by temperature-programmed desorption, *J. Phys. Chem.* **1985,** *89,* 2493–2497.

[113] Yang, T. J.; Lunsford, J. H. Partial oxidation of methanol to formaldehyde over molybdenum oxide on silica, *J. Catal.* **1987,** *103,* 55–64.

[114] Chung, J. S.; Miranda, R.; Bennett, C. O. Mechanism of partial oxidation of methanol over MoO_3, *J. Catal.* **1988,** *114,* 398–410.

[115] Machiels, C. J.; Sleight, A. W. Kinetic isotope effect in the selective oxidation of methanol to formaldehyde over some molybdate catalysts, *J. Catal.* **1982,** *76,* 238–239.

[116] Guidot, J.; Germain, J. E. Continuous recording of the X-ray diffraction pattern during catalysis: Methanol on molybdenum trioxide, *React. Kinet. Catal. Lett.* **1981,** *15,* 389–393.

[117] Doornkamp, C.; Ponec, V. The universal character of the Mars and Van Krevelen mechanism, *J. Mol. Catal. A: Chem.* **2000,** *162,* 19–32.

[118] Pernicone, N.; Lazzerin, F.; Liberti, G.; Lanzavecchia, G. The oxidation of methanol over pure MoO_3 catalyst, *J. Catal.* **1969,** *14,* 391–393.

[119] Cheng, W. H. Methanol and formaldehyde oxidation study over molybdenum oxide, *J. Catal.* **1996,** *158,* 477–485.

[120] Capdevila-Cortada, M.; García-Melchor, M.; López, N. Unraveling the structure sensitivity in methanol conversion on CeO_2: A DFT+U study, *J. Catal.* **2015,** *327,* 58–64.

[121] Ressler, T.; Wienold, J.; Jentoft, R. E.; Neisius, T. Bulk structural investigation of the reduction of MoO_3 with propene and the oxidation of MoO_2 with oxygen, *J. Catal.* **2002,** *210,* 67–83.

[122] Kim, H. S.; Cook, J. B.; Lin, H.; Ko, J. S.; Tolbert, S. H.; Ozolins, V.; Dunn, B. Oxygen vacancies enhance pseudocapacitive charge storage properties of MoO_{3-x}, *Nat. Mater.* **2017,** *16,* 454–460.

[123] Rellán-Piñeiro, M.; López, N. One oxygen vacancy, two charge states: characterization of reduced α-MoO_3(010) through theoretical methods, *Submitted* **2018,** .

[124] Lee, S. H.; Kim, Y. H.; Deshpande, R.; Parilla, P. A.; Whitney, E.; Gillaspie, D. T.; Jones, K. M.; Mahan, A.; Zhang, S.; Dillon, A. C. Reversible Lithium-Ion Insertion in Molybdenum Oxide Nanoparticles, *Adv. Mater.* **2008,** *20,* 3627–3632.

[125] Cheng, H.; Wen, M.; Ma, X.; Kuwahara, Y.; Mori, K.; Dai, Y.; Huang, B.; Yamashita, H. Hydrogen Doped Metal Oxide Semiconductors with Exceptional and Tunable Localized Surface Plasmon Resonances, *J. Am. Chem. Soc.* **2016,** *138,* 9316–9324.

[126] Magneli, A.; Blomberg-Hansson, B.; Kihlborg, L.; Sundkvist, G. Studies on Molybdenum and Molybdenum Wolfram Oxides of the Homologous Series Me_mO_{3n-1}, *Acta Chem. Scand.* **1955,** *9,* 1382–1390.

[127] Carrasco, J.; López, N.; Illas, F. First principles analysis of the stability and diffusion of oxygen vacancies in metal oxides, *Phys. Rev. Lett.* **2004,** *93,* 225502.

[128] Kowalski, P. M.; Camellone, M. F.; Nair, N. N.; Meyer, B.; Marx, D. Charge localization dynamics induced by oxygen vacancies on the TiO_2(110) surface, *Phys. Rev. Lett.* **2010,** *105,* 146405.

[129] Walsh, A.; Da Silva, J. L. F.; Wei, S. H.; Körber, C.; Klein, A.; Piper, L. F. J.; DeMasi, A.; Smith, K. E.; Panaccione, G.; Torelli, P. Nature of the band gap of In_2O_3 revealed by first-principles calculations and X-ray spectroscopy, *Phys. Rev. Lett.* **2008,** *100,* 167402.

[130] Zacharopoulou, V.; Vasiliadou, E. S.; Lemonidou, A. A. Exploring the Reaction Pathways of Bioglycerol Hydrodeoxygenation to Propene over Molybdena-Based Catalysts, *ChemSusChem* **2018,** 264–275.

[131] Fang, Z.; Zetterholm, P.; Dixon, D. A. 1,2-Ethanediol and 1,3-Propanediol Conversions over $(MO_3)_3$ (M= Mo, W) Nanoclusters: A Computational Study, *J. Phys. Chem. A* **2016,** *120,* 1897–1907.

[132] Frisch, M. J. *et al.* Gaussian 09, revision A. 2, *Gaussian, Inc., Wallingford, CT* **2009,** .

[133] Mestl, G.; Verbruggen, N. F. D.; Bosch, E.; Knözinger, H. Mechanically activated MoO_3. 5. Redox behavior, *Langmuir* **1996,** *12,* 2961–2968.

[134] Vasilopoulou, M. *et al.* The influence of hydrogenation and oxygen vacancies on molybdenum oxides work function and gap states for application in organic optoelectronics, *J. Am. Chem. Soc.* **2012,** *134,* 16178–16187.

[135] Bridgwater, A. V. Review of fast pyrolysis of biomass and product upgrading, *Biomass Bioenergy* **2012,** *38,* 68–94.

[136] Furimsky, E. Catalytic hydrodeoxygenation, *Appl. Catal. A: General* **2000,** *199,* 147–190.

[137] Saidi, M.; Samimi, F.; Karimipourfard, D.; Nimmanwudipong, T.; Gates, B. C.; Rahimpour, M. R. Upgrading of lignin-derived bio-oils by catalytic hydrodeoxygenation, *Energy Environ. Sci.* **2014,** *7,* 103–129.

[138] Wang, H.; Male, J.; Wang, Y. Recent advances in hydrotreating of pyrolysis bio-oil and its oxygen-containing model compounds, *ACS Catal.* **2013,** *3,* 1047–1070.

[139] Sitthisa, S.; Resasco, D. E. Hydrodeoxygenation of furfural over supported metal catalysts: a comparative study of Cu, Pd and Ni, *Catal. Lett.* **2011,** *141,* 784–791.

[140] González, C.; Marín, P.; Díez, F. V.; Ordóñez, S. Hydrodeoxygenation of Acetophenone over Supported Precious Metal Catalysts at Mild Conditions: Process Optimization and Reaction Kinetics, *Energy Fuels* **2015,** *29,* 8208–8215.

[141] Ramos, R.; Tišler, Z.; Kikhtyanin, O.; Kubička, D. Towards understanding the hydrodeoxygenation pathways of furfural–acetone aldol condensation products over supported Pt catalysts, *Catal. Sci. Technol.* **2016,** *6,* 1829–1841.

[142] Zhou, L.; Lawal, A. Hydrodeoxygenation of microalgae oil to green diesel over Pt, Rh and presulfided NiMo catalysts, *Catal. Sci. Technol.* **2016,** *6,* 1442–1454.

[143] Nelson, R. C.; Baek, B.; Ruiz, P.; Goundie, B.; Brooks, A.; Wheeler, M. C.; Frederick, B. G.; Grabow, L. C.; Austin, R. N. Experimental and theoretical insights into the hydrogen-efficient direct hydrodeoxygenation mechanism of phenol over Ru/TiO_2, *ACS Cat.* **2015,** *5,* 6509–6523.

[144] Lari, G. M.; Gröninger, O. G.; Li, Q.; Mondelli, C.; López, N.; Pérez-Ramírez, J. Catalyst and Process Design for the Continuous Manufacture of Rare Sugar Alcohols by Epimerization–Hydrogenation of Aldoses, *ChemSusChem* **2016,** *9,* 3407–3418.

[145] Witsuthammakul, A.; Sooknoi, T. Selective hydrodeoxygenation of bio-oil derived products: ketones to olefins, *Catal. Sci. Technol.* **2015,** *5,* 3639–3648.

[146] Khromova, S. A.; Smirnov, A. A.; Bulavchenko, O. A.; Saraev, A. A.; Kaichev, V. V.; Reshetnikov, S. I.; Yakovlev, V. A. Anisole hydrodeoxygenation over Ni–Cu bimetallic catalysts: The effect of Ni/Cu ratio on selectivity, *App. Cat. A: General* **2014,** *470,* 261–270.

[147] Popov, A.; Kondratieva, E.; Mariey, L.; Goupil, J. M.; El-Fallah, J.; Gilson, J. P.; Travert, A.; Maugé, F. Bio-oil hydrodeoxygenation: Adsorption of phenolic compounds on sulfided (Co) Mo catalysts, *J. Catal.* **2013,** *297,* 176–186.

[148] Wang, W.; Li, L.; Wu, K.; Zhu, G.; Tan, S.; Li, W.; Yang, Y. Hydrothermal synthesis of bimodal mesoporous MoS_2 nanosheets and their hydrodeoxygenation properties, *RSC Adv.* **2015,** *5,* 61799–61807.

[149] Chen, C. J.; Lee, W. S.; Bhan, A. Mo_2C catalyzed vapor phase hydrodeoxygenation of lignin-derived phenolic compound mixtures to aromatics under ambient pressure, *Appl. Catal. A: General* **2016,** *510,* 42–48.

[150] Li, Z.; Fang, Z.; Kelley, M. S.; Kay, B. D.; Rousseau, R.; Dohnálek, Z.; Dixon, D. A. Ethanol conversion on cyclic $(MO_3)_3$ (M= Mo, W) clusters, *J. Phys. Chem. C* **2014,** *118,* 4869–4877.

[151] Rousseau, R.; Dixon, D. A.; Kay, B. D.; Dohnálek, Z. Dehydration, dehydrogenation, and condensation of alcohols on supported oxide catalysts based on cyclic $(WO_3)_3$ and $(MoO_3)_3$ clusters, *Chem. Soc. Rev.* **2014,** *43,* 7664–7680.

[152] Matsuda, T.; Hirata, Y.; Suga, S.; Sakagami, H.; Takahashi, N. Effect of H_2 reduction on the catalytic properties of molybdenum oxides for the conversions of heptane and 2-propanol, *Appl. Catal. A: General* **2000,** *193,* 185–193.

[153] Yang, F.; Hanna, M. A.; Sun, R. Value-added uses for crude glycerol–a byproduct of biodiesel production, *Biotechnol. Biofuels* **2012,** *5,* 13.

[154] Quispe, C. A. G.; Coronado, C. J.; Carvalho Jr, J. Glycerol: production, consumption, prices, characterization and new trends in combustion, *Renew. Sust. Energ. Rev.* **2013,** *27,* 475–493.

[155] Thurmond, W. "Biodiesel 2020: Global Market Survey, Feedstock Trends and Market Forecasts", Technical Report, Emerging Markets Online., 2008.

[156] Calamur, N.; Carrera, M. Propylene in Kirk-Othmer Encyclopedia of Chemical Technology. In ; John Wiley & Sons, Inc.: 2000.

[157] Carr, C. "IHS Chemical North American Supply Propylene Study", Technical Report, IHS Markit, 2013.

[158] Yu, L.; Yuan, J.; Zhang, Q.; Liu, Y. M.; He, H. Y.; Fan, K. N.; Cao, Y. Propylene from renewable resources: catalytic conversion of glycerol into propylene, *ChemSusChem* **2014,** *7,* 743–747.

[159] Sousa Fadigas, J. C.; Gambetta, R.; Araujo Mota, C. J.; Conceicao Goncalves, V. L. D. *Preparation of heterogeneous catalysts used in selective hydrogenation of glycerin to propylene and hydrogenation process*, 2011 US 20110184216 A1 20110728.

[160] Mota, C. J.; Gonçalves, V. L.; Mellizo, J. E.; Rocco, A. M.; Fadigas, J. C.; Gambetta, R. Green propene through the selective hydrogenolysis of glycerol over supported iron-molybdenum catalyst: The original history, *Journal of Molecular Catalysis A: Chemical* **2016,** *422,* 158–164.

[161] Moberg, D. R.; Thibodeau, T. J.; Amar, F. G.; Frederick, B. G. Mechanism of hydrodeoxygenation of acrolein on a cluster model of MoO_3, *J. Phys. Chem. C* **2010,** *114,* 13782–13795.

[162] Kresse, G.; Furthmüller, J. Efficiency of ab-initio total energy calculations for metals and semiconductors using a plane-wave basis set, *Comput. Mater. Sci.* **1996,** *6,* 15–50.

[163] Kresse, G.; Furthmüller, J. Efficient iterative schemes for ab initio total-energy calculations using a plane-wave basis set, *Phys. Rev. B* **1996,** *54,* 11169–11186.

[164] Henkelman, G.; Jónsson, H. A dimer method for finding saddle points on high dimensional potential surfaces using only first derivatives, *J. Chem. Phys.* **1999,** *111,* 7010–7022.

[165] Heyden, A.; Bell, A. T.; Keil, F. J. Efficient methods for finding transition states in chemical reactions: Comparison of improved dimer method and partitioned rational function optimization method, *J. Chem. Phys.* **2005,** *123,* 224101.

[166] Rellán-Piñeiro, M.; Garcia-Ratés, M.; López, N. Mechanism for the selective epimerization of the glucose mannose pair by Mo-based compounds: towards catalyst optimization, *Green Chem.* **2017,** 5932–5939.

[167] Delidovich, I.; Palkovits, R. Catalytic Isomerization of Biomass-Derived Aldoses: A Review, *ChemSusChem* **2016,** *9,* 547–561.

[168] Tanner, M. E. Understanding nature's strategies for enzyme-catalyzed racemization and epimerization, *Acc. Chem. Res.* **2002,** *35,* 237–246.

[169] Samuel, J.; Tanner, M. E. Mechanistic aspects of enzymatic carbohydrate epimerization, *Nat. Prod. Rep.* **2002,** *19,* 261–277.

[170] Lu, S.-C.; Lin, S.-C. Recovery of active N-acetyl-D-glucosamine 2-epimerase from inclusion bodies by solubilization with non-denaturing buffers, *Enzyme Microb. Technol.* **2012,** *50,* 65–70.

[171] Angyal, S. J. A short note on the epimerization of aldoses, *Carbohyd. Res.* **1997,** *300,* 279–281.

[172] Tanase, T.; Shimizu, F.; Yano, S.; Yoshikawa, S. Novel C-2 epimerization of aldoses and stereoselective uptake of one of the epimeric aldoses by nickel (II) complexes, *J. Chem. Soc., Chem. Commun.* **1986,** 1001–1003.

[173] Tanase, T.; Shimizu, F.; Kuse, M.; Yano, S.; Hidai, M.; Yoshikawa, S. Novel C-2 epimerization of aldoses promoted by nickel (II) diamine complexes, involving a stereospecific pinacol-type 1, 2-carbon shift, *Inorg. Chem.* **1988,** *27,* 4085–4094.

[174] Nguyen, H.; Nikolakis, V.; Vlachos, D. G. Mechanistic insights into Lewis acid metal salt-catalyzed glucose chemistry in aqueous solution, *ACS Catal.* **2016,** *6,* 1497–1504.

[175] Bermejo-Deval, R.; Gounder, R.; Davis, M. E. Framework and extraframework tin sites in zeolite beta react glucose differently, *ACS Catal.* **2012,** *2,* 2705–2713.

[176] Bermejo-Deval, R.; Orazov, M.; Gounder, R.; Hwang, S. J.; Davis, M. E. Active sites in Sn-Beta for glucose isomerization to fructose and epimerization to mannose, *ACS Catal.* **2014,** *4,* 2288–2297.

[177] Gunther, W. R.; Wang, Y.; Ji, Y.; Michaelis, V. K.; Hunt, S. T.; Griffin, R. G.; Román-Leshkov, Y. Sn-Beta zeolites with borate salts catalyse the epimerization of carbohydrates via an intramolecular carbon shift, *Nat. Commun.* **2012,** *3,* 1109.

[178] Gunther, W. R.; Duong, Q.; Román-Leshkov, Y. Catalytic consequences of borate complexation and pH on the epimerization of L-arabinose to L-ribose in water catalyzed by Sn-Beta zeolite with borate salts, *J. Mol. Catal. A: Chem.* **2013,** *379,* 294–302.

[179] Bilik, V. Reactions of saccharides catalyzed by molybdate ions. II. Epimerization of D-glucose and D-mannose, *Chem. Zvesti* **1972,** *26,* 183–186.

[180] Cybulski, A.; Kuster, B. M.; Marin, G. B. The kinetics of the molybdate-catalysed epimerization of D-glucose and D-mannose in aqueous solutions, *J. Mol. Catal.* **1991,** *68,* 87–103.

[181] Hayes, M. L.; Pennings, N. J.; Serianni, A. S.; Barker, R. Epimerization of aldoses by molybdate involving a novel rearrangement of the carbon skeleton, *J. Am. Chem. Soc.* **1982,** *104,* 6764–6769.

[182] Godfrey, J. E.; Waters, J. M. Ammonium μ-Oxo-μ-Mannitolate-Tetraoxodimolybdate (VI) Monohydrate $[C_6H_{11}O_{11}Mo_2]$ $NH_4 \cdot$ H_2O, *Cryst. Struct. Comm* **1975,** *4,* 5–8.

[183] Taylor, G. E.; Waters, J. M. The structure of a compound of unexpected conformation involved in the xylose-lyxose epimerization, *Tetrahedron Lett.* **1981,** *22,* 1277–1278.

[184] Bilik, V.; Matulova, M. Reactions of saccharides catalyzed by molybdate ions. 42. Epimerization and the molybdate complexes of the aldoses, *Chem. Pap.* **1990,** *44,* 257–265.

[185] Petruš, L.; Petrušova, M.; Hricovíniová, Z. The Bilik reaction, *Top. Curr. Chem.* **2001,** *215,* 15–41.

[186] Takagaki, A.; Furusato, S.; Kikuchi, R.; Oyama, S. T. Efficient Epimerization of Aldoses Using Layered Niobium Molybdates, *ChemSusChem* **2015,** *8,* 3769–3772.

[187] Yang, G.; Pidko, E. A.; Hensen, E. J. M. The Mechanism of Glucose Isomerization to Fructose over Sn-BEA Zeolite: A Periodic Density Functional Theory Study, *ChemSusChem* **2013,** *6,* 1688–1696.

[188] Macht, J.; Janik, M. J.; Neurock, M.; Iglesia, E. Mechanistic consequences of composition in acid catalysis by polyoxometalate Keggin clusters, *J. Am. Chem. Soc.* **2008,** *130,* 10369–10379.

[189] Mbomekallé, I. M.; López, X.; Poblet, J. M.; Sécheresse, F.; Keita, B.; Nadjo, L. Influence of the heteroatom size on the redox potentials of selected polyoxoanions, *Inorg. Chem.* **2010,** *49,* 7001–7006.

[190] Garcia-Ratés, M.; López, N. Multigrid-based methodology for implicit solvation models in periodic DFT, *J. Chem. Theory Comput.* **2016,** *12,* 1331–1341.

[191] Garcia-Ratés, M.; García-Muelas, R.; López, N. Solvation Effects on Methanol Decomposition on Pd (111), Pt (111) and Ru (0001), *J. Phys. Chem. C* **2017,** 13803–13809.

[192] Kozhevnikov, I. V. Catalysis by heteropoly acids and multicomponent polyoxometalates in liquid-phase reactions, *Chem. Rev.* **1998,** *98,* 171–198.

[193] Capdevila-Cortada, M.; López, N. Descriptor Analysis in Methanol Conversion on Doped CeO_2 (111): Guidelines for Selectivity Tuning, *ACS Catal.* **2015,** *5,* 6473–6480.

[194] Capdevila-Cortada, M.; Vilé, G.; Teschner, D.; Pérez-Ramírez, J.; López, N. Reactivity descriptors for ceria in catalysis, *Appl. Catal. B* **2016,** *197,* 299–312.

[195] Maeda, K.; Katano, H.; Osakai, T.; Himeno, S.; Saito, A. Charge dependence of one-electron redox potentials of Keggin-type heteropolyoxometalate anions, *J. Electroanal. Chem.* **1995,** *389,* 167–173.

[196] Sadakane, M.; Steckhan, E. Electrochemical properties of polyoxometalates as electrocatalysts, *Chem. R.* **1998,** *98,* 219–238.

[197] Deshlahra, P.; Carr, R. T.; Chai, S. H.; Iglesia, E. Mechanistic details and reactivity descriptors in oxidation and acid catalysis of methanol, *ACS Catal.* **2014,** *5,* 666–682.

UNIVERSITAT
ROVIRA i VIRGILI